



**Università
degli Studi
di Palermo**

AREA QUALITÀ, PROGRAMMAZIONE E SUPPORTO STRATEGICO
SETTORE STRATEGIA PER LA RICERCA
U. O. DOTTORATI

Dottorato in Energia e Tecnologie per l'Informazione
Dipartimento di Ingegneria
ING-IND/31 Elettrotecnica

**DESIGN AND SIMULATION OF FAST DISCHARGE UNITS
(FDUs) FOR TOROIDAL FIELD COILS OF
DIVERTOR TOKAMAK TEST (DTT)**

**IL DOTTORE
CARMELO RICCARDO LOPES**

**IL COORDINATORE
PROF. ING. MAURIZIO CELLURA**

**TUTOR UNIPA
PROF. ING. GUIDO ALA**

**CO-TUTOR UNIPA
PROF. ING. GAETANO ZIZZO**

**TUTOR ENEA
PHD. ING. PIETRO ZITO**

**TUTOR ITER
ING. YULONG YE
ING. IVONE BENFATTO**

CICLO XXXV
2021-2022

Summary

1	<i>PhD Thesis Introduction</i>	1
2	<i>Introduction to nuclear fusion</i>	7
2.1	General introduction	7
2.2	Strategic Energy Technology Plan	10
2.2.1	First period: start ITER operation with other parties and complete DEMO conceptual design (2030)	10
2.2.2	Second period: burning plasma on ITER and DEMO engineering design (2030-2040)	10
2.2.3	Third period: plasma and technology optimization on ITER and construction of DEMO (2040 and on)	11
2.3	ITER and DEMO facilities	12
2.4	Brief review of nuclear physics	14
3	<i>Introduction to Tokamaks</i>	17
3.1	Fusion reactions	17
3.2	Plasma definition and main processes	20
3.3	Fusion confinement	21
3.3.1	Material confinement	21
3.3.2	Gravitational confinement	21
3.3.3	Inertial confinement	22
3.3.4	Magnetic confinement	23
3.4	Structure of a Tokamak and particle trapping principle	25
3.5	Power balance in a nuclear fusion reactor	30
3.6	Ignition	32
3.7	Tokamak Equilibrium	34
3.8	Heat dissipation	36
3.9	Tritium breeding	38
3.10	First wall	42

4	<i>Superconductivity</i>	43
4.1	Introduction to superconductivity	43
4.2	Superconductor materials' evolution	46
4.3	Necessary conditions for superconductivity	47
4.4	High temperature superconducting materials	49
4.5	Quench	51
4.6	Use of superconductors.....	55
4.6.1	Magnetic Resonance Imaging.....	55
4.6.2	Particle accelerators	55
4.6.3	Energy Storage systems and transports	56
4.6.4	Nuclear fusion.....	57
5	<i>Existing Tokamaks</i>	58
5.1	Introduction.....	58
5.2	JT-60SA.....	58
5.2.1	Research plan	58
5.2.2	Magnet system	61
5.2.3	Vacuum Vessel.....	64
5.2.4	Thermal Shield	65
5.2.5	In-Vessel components	65
5.2.6	Cryostat	68
5.2.7	Magnet Shared Components.....	69
5.2.8	Auxiliary Plant – Heating.....	69
5.2.9	Auxiliary Plant – Power Supply	69
5.2.10	Auxiliary Plant – Cryogenics.....	71
5.2.11	Auxiliary Plant – Cooling System	72
5.2.12	Auxiliary Plant – Control System.....	72
5.3	JET.....	74
5.3.1	Research Plan	74
5.3.2	Magnet System.....	75
5.3.3	Auxiliary Plant – Heating.....	77
5.3.4	Auxiliary Plant – Power Supply	77
5.3.5	Auxiliary Plant – Control System.....	78

5.4	FTU	80
5.4.1	Research Plan	80
5.4.2	Vacuum system.....	80
5.4.3	Cryogenics	80
5.4.4	Power Supply	81
5.5	DTT	86
5.5.1	Research Plan	86
5.5.2	Main Parameters	87
5.5.3	ENEA Frascati Research Center	87
5.5.4	Magnet System	88
5.5.5	Quench detection	92
5.5.6	Vacuum Vessel.....	92
5.5.7	Additional Heating.....	93
5.5.8	Divertor.....	94
5.5.9	First wall	95
5.5.10	Cryostat	95
5.5.11	Cryogenic System.....	96
5.5.12	Thermal Shield	97
5.5.13	Electrical components – Power Supply.....	98
5.5.14	Electrical components – Fast Discharge Units	101
5.5.15	Electrical components – Grounding system	107
5.5.16	Cooling system.....	107
5.5.17	CODAS.....	108
5.6	ITER	110
5.6.1	Research Plan	110
5.6.2	Magnet System.....	111
5.6.3	Vacuum Vessel.....	114
5.6.4	Blanket	114
5.6.5	Divertor.....	115
5.6.6	Cryostat	116
5.6.7	Fast Discharge Units	117
6	<i>Fast Discharge Units</i>	120
6.1	Fast Discharge Units on DTT	121
6.1.1	FDU Simulink model	123
6.1.2	Preliminary study with Fixed DR and Variable DR	127

6.1.3	Study with updated value of DR	132
6.1.4	Guided User Interface for IGCT MTTF study	141
6.1.5	Arc voltage and current transient modelling	142
6.1.6	Ansys-Simplorer Model for electric transient during a Fast Discharge	148
6.2	Conceptual design of the Grounding System of DTT	167
6.3	Fast Discharge Units on ITER.....	176
6.3.1	Matlab-Simulink electrical model.....	176
6.3.2	TFCs model detailed configuration.....	181
6.4.2	Results for TFC configuration model	194
6.4.3	Results for DL configuration Model	195
6.4.4	Fault analysis of FDUs in DL configuration.....	197
6.4.5	FDU control logic description	214
6.5	Fast Discharge Units on DEMO.....	219
6.5.1	TF FDU Dump Resistors study.....	223
6.5.2	Dump Resistor optimization model.....	227
6.5.3	Final Matlab-Simulink model.....	231
6.5.4	Final Matlab-Simulink model results	233
6.5.5	Discharge of TFC with Varistor study.....	235
7	Conclusions	239
8	Appendix.....	247
8.1	Scenario 1.....	247
8.1.1	Simulation 1.....	247
8.1.2	Simulation 2.....	249
8.2	Scenario 2	251
8.2.1	Simulation 1.....	251
8.2.2	Simulation 2.....	253
8.3	Scenario 3.....	255
8.4	Scenario 4.....	257
8.4.1	Simulation 1.....	257
8.4.2	Simulation 2.....	259
8.5	Scenario 5	261
8.5.1	Simulation 1.....	261

8.5.2	Simulation 2.....	263
8.6	Scenario 6.....	265
8.6.1	Simulation 1.....	265
8.6.2	Simulation 2.....	267
8.7	Scenario 7.....	269
8.8	Scenario 8.....	271
8.9	Scenario 9.....	273
8.10	Scenario 10.....	275
8.11	Scenario 11.....	277

FIGURE LIST

Figure 1: European roadmap in a nutshell [10].	8
Figure 2: Mass number (A) and atomic number (Z).	14
Figure 3: Binding energy per nucleon (MeV).	15
Figure 4: List of the most favorable fusion reactions [45].	18
Figure 5: Cross section of the main nuclear fusion reactions.	18
Figure 6: Helical motion of a charged particle subjected to a magnetic field.	20
Figure 7: Compression and heating of a spherical pellet by external laser [44].	22
Figure 8: Poloidal and Toroidal magnetic field used for magnetic confinement.	24
Figure 9: Schematic representation of TF, PF, CS, and the magnetic flux [45]	25
Figure 10: Components of a tokamak [45].	26
Figure 11: Driving center motion of a charged particle inside an electric and magnetic field.	27
Figure 12: Poloidal variation of the overall magnetic field in a tokamak [12]	28
Figure 13: Schematic projection of particle orbits in a tokamak onto a poloidal plane [12]	29
Figure 14: reactivity related to temperature in keV and billion kelvins. [46]	30
Figure 15: The value of density and time confinement required to obtain ignition as a function of temperature.	32
Figure 16: Sketch of the divertor configuration inside the tokamak [54]	36
Figure 17: SOL simplified model [55]	37
Figure 18: General scheme for the blanket [58].	39
Figure 19: General scheme for tritium breeding with neutron multipliers [57].	40
Figure 20: Temperature scales: Fahrenheit (left), Celsius (center), Kelvin (right) [14].	45
Figure 21: 3D illustration of the superconducting region, where the critical parameters are represented [16]	48

Figure 22: Perovskite structure.....	49
Figure 23:Critical temperature trend as a function of material and year [49]..	50
Figure 24: Normal propagation zone.....	52
Figure 25: Target regimes of JT-60SA [23].....	59
Figure 26: JT-60SA TFCs	61
Figure 27: JT-60SA CS	62
Figure 28: JT-60SA EFs.....	62
Figure 29: JT-60SA Magnets system top view	63
Figure 30: JT-60SA Total Magnet System.....	63
Figure 31: JT-60SA Vacuum Vessel [24]	64
Figure 32: JT-60SA Thermal Shield [24].....	65
Figure 33: JT-60SA Section with in-vessel components [24].....	66
Figure 34: Cryopump under the Divertor Cassette in JT-60SA [24].	67
Figure 35: JT-60SA Cryostat real view [24]	68
Figure 36: JT-60SA Cryostat [24].....	68
Figure 37: Toroidal Field Circuit with Power Supply [24].....	70
Figure 38: Poloidal Field Coil Circuits (CS2 and EF1) [24].....	71
Figure 39: JT-60SA Overall Status Monitor [24].	73
Figure 40: Configuration of SCSDAS for JT-60SA [24].....	73
Figure 41: JET TFCs [26]	75
Figure 42: Detail on one TFC of JET [26]	76
Figure 43: JET PFCs. [26].....	76
Figure 44: JET Main Power Supply Scheme [26].....	78
Figure 45: JET Diagnostics general view [26].	79
Figure 46: MFG1 (left) and MFG3 (right) electrical scheme [27].....	82
Figure 47: AL-T (left) and AL-V (right) Converters electrical scheme [27]... ..	83
Figure 48: AL-H Converter Electrical Scheme [27].	84
Figure 49: AL-F Converter Electrical Scheme [27].....	85
Figure 50: ENEA Frascati Research Center [28].	87
Figure 51: TFCs in blue, PFCs in white, CSs in pink [29].....	88
Figure 52: TFC cross section [30].	89
Figure 53: Cross section of TFC with details on the Double Pancakes [30]....	90

Figure 54: 3D CAD view of the vacuum vessel and ports [31].	93
Figure 55: Overall view of the Cryostat [28]	96
Figure 56: Simplified circuit for TFC PS [28]	99
Figure 57: Reference scheme for the TFPS for DTT [28].	100
Figure 58: Reference scheme of the single FDU of DTT [28].	101
Figure 59: Reference scheme for each of the 6 PF PSs [28].	103
Figure 60: General electrical circuit for CS PSs [6].	104
Figure 61: EDS block diagram of DTT [28]	106
Figure 62: DTT substation foreseen position [28]	106
Figure 63: Conceptual scheme of Cooling Water System during plasma discharge [29].	108
Figure 64: Schematic schedule for the first 10 years of ITER operations within the Staged Approach [32].	110
Figure 65: TFCs system in ITER [33]	112
Figure 66: PFCs system in ITER [33]	112
Figure 67: CS magnet system in ITER [33]	113
Figure 68: ITER Blanket design [34]	115
Figure 69: Cryostat in ITER [34]	116
Figure 70: ITER FDU.	118
Figure 71: ITER TF FDUs simplified scheme	118
Figure 72: Opening sequence of TFC's FDU for DTT [4]	122
Figure 73: Complete electrical circuit on Matlab-Simulink for DTT [4] (up) and simplified block scheme for more legibility (down).	123
Figure 74: Crowbar circuit Simulink model [4]	124
Figure 75: Self and mutual inductance matrix of Matlab-Simulink simulation [4]	125
Figure 76: TFC characteristics (2020) [4].	125
Figure 77: FDU characteristics [4]	125
Figure 78: Dump Resistor simulated with IGCTs [4]	126
Figure 79: Zoom of the previous figure	126
Figure 80: Matlab Simulink model of the FDU [4].	127
Figure 81: Variable DR electric simplified scheme [4]	128

Figure 82: Voltage on fixed DR (up) and variable DR (down) [4].....	129
Figure 83: Opening sequence with fixed DR (up) and variable DR (down) [4]	130
Figure 84: Voltage trend for exponential discharge (up) and linear discharge (down) with DR updated value.	133
Figure 85: Different simulations with variable DR by changing the initial value of time constant [3]	134
Figure 86: Voltage trends as a function of the time constant initial value [3]	134
Figure 87: Main results for changing time constant value with linear discharge [3].....	135
Figure 88: Example of Scenario 3 with 2 faults [3]	138
Figure 89: Example of Scenario 1 with single IGCT fault [3].....	138
Figure 90: Fault scenarios for $\tau = 6.2$ s [3].....	139
Figure 91: Scenario 5	139
Figure 92: Fault scenarios with $\tau = 5.9$ s [3]	140
Figure 93: IGCT MTTF calculation GUI.....	141
Figure 94: MTTF values for proposed Switched DR and BPS [3]	142
Figure 95: Matlab-Simulink block for implementation of Mayr-Cassie model [1]	146
Figure 96: FDU Opening sequence (SCB opening at t=2 s) [1]	146
Figure 97: Zoom on opening sequence at t=2 s [1].....	147
Figure 98: 2D axialsymmetric model of the Winding Pack (WP) in Ansys Maxwell [5].....	150
Figure 99: Mutual inductance coefficients comparison for some WP [5]	151
Figure 100: Electrical circuit of one coil [5]	151
Figure 101: Simplified scheme of TF coil [5].....	152
Figure 102: FDU model in Ansys Simplorer [5], this model is coherent with the one reported in Figure 80.	153
Figure 103: FDU generator detail	155
Figure 104: BPS detail	155
Figure 105: Command logic of SCB.....	156

Figure 106: SCB control: closing command (left) and opening command (right)	156
.....	
Figure 107: Control detail of DR.	157
Figure 108: Dump Resistor detail.	157
Figure 109: Final Ansys Simplorer FDU model.	158
Figure 110: Detail on the control of the DR.....	158
Figure 111: Simplified electrical scheme with TFCs and FDUs [5].....	159
Figure 112: Terminal voltage on the 3 groups with $R_{case} - to - ground = 100\ m\Omega$ [5]	160
Figure 113: Terminal voltage on group 1 with resistance of 100 mOhm [5].	161
Figure 114: Voltage at the terminals of the DP of coil 1 with resistance case to ground of 100 mOhm [5]	161
Figure 115: Terminal to ground voltage for all the DPs of TF01 coil [5].....	162
Figure 116: Terminal voltage on TFC groups (up) and terminal voltage of coils inside group 1 (down). Both with fault resistance of 1 Ohm [5]	163
Figure 117: Terminal voltage on DPs of TF01 with fault resistance of 1 Ohm [5]	164
.....	
Figure 118: Terminal to ground voltage of each group for fault resistance of 1 Ohm [5].....	164
Figure 119: Terminal to ground voltage for all the DPs in TF16 coil for fault scenario [5].....	165
Figure 120: Terminal voltage on group 1 for different fault resistances [5]..	166
Figure 121: Buildings in ENEA to be demolished (left) and to be built (right) [2]	170
.....	
Figure 122: ENEA research center grounding system [2]	170
Figure 123: General model with DL configuration (up) and simplified diagram block for more legibility (down).	177
Figure 124: General electrical scheme with DL configuration	178
Figure 125: General model with TFCs configuration	179
Figure 126: General electrical scheme with TFCs configuration.....	180
Figure 127: TFCs connections with grounding system.....	181
Figure 128: ERU details with ER1, ER2 and EC.....	182

Figure 129: Grounding system details.....	182
Figure 130: Scopes signals of the model.....	183
Figure 131: FDU's controls	184
Figure 132: FDU logic control electrical scheme	185
Figure 133: Logic control for BPS, VCB, and CPC	186
Figure 134: Logic control for PB	187
Figure 135: Logic control for BPS, VCB, CPC	188
Figure 136: Logic control for PB	188
Figure 137: Fault to GND block.....	189
Figure 138: Fault blocks.....	189
Figure 139: Ideal Switch for opening the PS circuit branch	190
Figure 140: Ideal circuit for simulation of Crowbar	190
Figure 141: Dummy Load circuit.....	191
Figure 142: DC busbar for PS - Stray resistance and capacitance	192
Figure 143: DC busbar for PS - Line resistance and inductance.....	192
Figure 144: DC busbar for FDU - Stray resistance and capacitance.....	193
Figure 145: DC busbar for FDU - Line resistance and inductance	193
Figure 146: FDU1 opening sequence	194
Figure 147: FDU1 voltages T2T and T2G	195
Figure 148: Dummy Load signals	195
Figure 149: FDU2 opening sequence	196
Figure 150: FDU2 voltages T2T and T2G	196
Figure 151: Electrical scheme with DL config. without faults	199
Figure 152: Current path before triggering	200
Figure 153: Zoom on electrical scheme of FDU2 (current flowing in BPS) .	200
Figure 154: Current flowing in the VCB of FDU2 (t=0.36 s).....	201
Figure 155: Electrical path of current flowing in the VCB of FDU2.....	201
Figure 156: Current path in DR of FDU2	202
Figure 157: Activation of CPC of FDU2 (t=0.56 s).....	202
Figure 158: Electrical path of the current in FDU2 (t>0.56 s).....	203
Figure 159: Scenario 1, Simulation 2.....	204
Figure 160: Scenario 1, Simulation 1.....	204

Figure 161: Scenario 2, Simulation 2	205
Figure 162: Scenario 2, Simulation 1	205
Figure 163: Scenario 3	206
Figure 164: Scenario 4, Simulation 2	207
Figure 165: Scenario 4, Simulation 1	207
Figure 166: Scenario 5, Simulation 2	208
Figure 167: Scenario 5, Simulation 1	208
Figure 168: Scenario 6, Simulation 2	209
Figure 169: Scenario 6, Simulation 1	209
Figure 170: Scenario 7	210
Figure 171: Scenario 8	210
Figure 172: Scenario 9	211
Figure 173: Scenario 11 opening sequence not completed	213
Figure 174: FDU1 Control Status	215
Figure 175: FDU normal opening sequence.....	215
Figure 176: PB control status	215
Figure 177: PB activation report	216
Figure 178: Opening sequence with BPS fault and PB activation	216
Figure 179: PB control status zoom on PB activation.....	217
Figure 180: FDU1 control status with BPS fault	217
Figure 181: Opening sequence with VCB fault and PB activation.....	217
Figure 182: PB control status zoom on PB activation.....	218
Figure 183: Opening sequence with CPC fault activation and PB activation	218
Figure 184: Circuit topologies: A is ITER-like, B, C and D (left). Conceptual waveforms of main currents and voltages in TFC circuit in case of FDU intervention in normal conditions (right) [42].....	220
Figure 185: ITER-like circuit configuration with 16 FDU's [42]	221
Figure 186: ITER-like circuit configuration with 8 FDU's [42]	222
Figure 187: Unified resistor section of ITER FDU resistors [42].....	224
Figure 188: Model of the FDU with temperature-dependent discharge resistor [42]	226
Figure 189: Temperature-dependant resistor and temperature limit.....	228

Figure 190: Model with single inductance and single FDU (equivalent to 16FDUs).....	228
Figure 191: Imported signals on Simulink Design Optimization tool	229
Figure 192: Specific energy through limit (blue line after optimization)	229
Figure 193: Minimum temperature limit (blue line after optimization).....	230
Figure 194: Maximum temperature limit (blue line after optimization).....	230
Figure 195: Optimization results	231
Figure 196: Detail of 16 FDU simulation block.....	232
Figure 197: General model.....	232
Figure 198: Detail of Temperature dependant resistor.....	233
Figure 199: Current on TF magnets of DTT 16 and 8 FDU's (overlapped) ...	233
Figure 200: Specific energy through for 16 and 8 FDU's expressed in $[A^2t]$	234
Figure 201: Resistance value during the discharge 16 and 8 FDU's.....	234
Figure 202: DR voltage Terminal to Terminal 16 and 8 FDU's	234
Figure 203: Temperature of the resistors during the discharge.....	235
Figure 204: Example of VI responses for linear resistors and varistors [43].	236
Figure 205: Varistor block simulation model on Matlab-Simulink	236
Figure 206: Detailed model for Varistor simulation of DEMO	237
Figure 207: TFC current on DEMO during discharge with varistor.....	237
Figure 208: Specific energy through during discharge on one TFC of DEMO with varistor expressed in $[A^2 s]$	238
Figure 209: Voltage across varistor terminals during discharge of one TFC of DEMO	238
Figure 210: Resistance value of the varistor during TFC discharge of DEMO	238

This Thesis is a collaboration with the **International Thermonuclear Experimental Reactor (ITER)** Organization.

Disclaimer: The views and opinions expressed herein do not necessarily reflect those of the ITER Organization.

The ITER Organization is an intergovernmental organization among:

The People's Republic of China,

The European Atomic Energy Community (Euratom),

The Republic of India,

Japan,

The Republic of Korea,

The Russian Federation,

The United States of America.

The ITER Project (<https://www.iter.org>) is under construction in St. Paul Lez Durance, France.



ACKNOWLEDGEMENT

This Thesis is the result of a strong synergy between the University of Palermo and ENEA. International experimental infrastructure on nuclear fusion DTT in Frascati has been co-funded by European Investment Bank (EIB), Eurofusion, Research and University Ministry, Economic Development Ministry and Lazio Region in 2019.

In this framework ENEA has funded a PhD fellowship in electrical engineering at UniPa to support the R&D activities connected to the design of the Fast Discharge Units for DTT.

The last five months of the PhD has been attended as PhD Student Internship at ITER Organization, Cadarache (France).

Words cannot express the gratitude to the professors, ENEA tutor and ITER tutors for the invaluable patience and feedback. It couldn't be also possible to undertake this journey without them, who generously provided knowledge and expertise.

Special thanks also to ENEA colleagues Giuseppe Messina and Luigi Morici.

I'm also grateful to all the people I met during the course for their editing help, moral support and also for letting me know their different fascinating cultures all over the world.

A particular mention should be given to Marzia for her constant presence during all my PhD course, Giuseppe for his moral support during ITER Internship and to the other colleagues of ITER: Cooper, Joep, Liza, Athenais, Nicolas, Gabriele, Ian, James, Hugo, Timote, Ricarda, Takumi, Dean, Enrique, Federico, Peter, Pavel, Vishal, Ansh, Chirag.

I'm so grateful I had the opportunity to meet different cultures, in particular people coming from: USA, Netherlands, Sweden, Japan, France, Germany, Spain, Hungary, Russia, India.

I would also like to thank Florian and my cat for all the entertainment and emotional support.

Acronym list	
AC	Alternate Current
AMU	Atomic Mass Unit
AVD	Arc Voltage Detector
BPS	Bypass Switch
CCU	Current Commutation Unit
CPC	Counter Pulse Circuit
CS	Central Solenoid
DB	Double Pancake
DC	Direct Current
DEMO	DEMONstration power plant
DL	Dummy Load
DPA	Displacement Per Atom
DR	Discharge Resistor / Dump Resistor
DTT	Divertor Tokamak Test
EC	Earth Contactor
ECRH	Electron Cyclotron Resonance Heating
EF	Equilibrium Field
ER	Earth Resistor
ERU	Earth Resistor Unit
FDU	Fast Discharge Unit
FPG	Firing Pulse Generator
FTU	Frascati Tokamak Upgrade
HL-LHC	High Luminosity Large Hadron Collider
HTS	High Temperature Superconductor
HV	High Voltage
ICRH	Ion Cyclotron Resonance Heating
IGCT	Insulated Gate Commutated Thyristor
ITER	International Thermonuclear Experimental Reactor
JET	Joint European Torus
JT-60SA	Japan Torus 60 Super Advanced
LCC	Local Center Cubicle
LHC	Large Hadron Collider
LTS	Low Temperature Superconductor
LV	Low Voltage
MQE	Minimum Quench Energy
MRI	Magnetic Resonance Image
MTTF	Mean Time to Failure
MV	Medium Voltage
NB	Neutron Beam
PB	Pyrobreaker
PFC	Poloidal Field Coil
PKA	Primary Knock-on Atom
PSS	Power Supply System
QPC	Quench Protection Circuit
QPC	Quench Protection Circuit
SC	Snubber Circuit
SCB	Static Circuit Breaker
SNU	Switching Network Unit
SOL	Scrape Off Layer

SWG	Switch Gear
T2G	Terminal To Ground
T2T	Terminal To Terminal
TBR	Tritium Breeding Ratio
TFC	Toroidal Field Coil
TR	Terminal Resistor
TS	Thermal Shield
VCB	Vacuum Circuit Breaker
VV	Vacuum Vessel
WP	Winding Pack
ZCD	Zero Current Detector

1 PhD Thesis Introduction

This thesis summarizes the work carried out during the 3-year PhD course in the period between 2019 and 2022.

As is well known in the scientific community, the very ambitious nuclear fusion project has required and still requires considerable resources and investments; The roadmap for large-scale nuclear fusion power generation is comprised of challenging missions.

This mission will be completed by the ITER (*International Thermonuclear Experimental Reactor*) project by 2030, providing what will then be the basis for a fusion thermal power plant. The tokamak configuration of the reactor is the one that at the moment turned out to be the best available; it has a toroidal shape and a "D" section within which the plasma is kept at a temperature of $1,5 * 10^8 K$

The ITER project aims to build an experimental reactor in which nuclear fusion can be carried out in *steady state* (500 MW produced for 60 minutes).

The main "fuel" used is tritium, *an isotope of hydrogen*, and the main role in ensuring tritium self-sufficiency will be played by ITER's Test Blanket Module (TBM) program which will demonstrate the ability to produce high-quality tritium and heat.

In 2012, the European *Fusion Development Agreement* (EFDA) based in Garching, Germany, proposed a roadmap for the construction of a new reactor, renamed to DEMO (short for *DEMONstrating fusion power reactor*). This project is similar to the ITER one but with the substantial difference that the main purpose of DEMO is to demonstrate the possibility of producing electricity from the nuclear fusion reaction with orders of magnitude of 1.33-1.55 GW.

In this field, the main differences between ITER and DEMO will be tritium management, with a greater amount of tritium and stocks in DEMO, as well as a greater neutron flux on the *blanket*; the latter is a component of the reactor that has two fundamental functions: to generate the tritium that will subsequently be used in the fusion reaction and to transfer to a refrigerant the energy removed from the plasma by neutrons.

The experience gained for ITER will be poured directly for the design of the DEMO project and in particular specific emphasis must be given on maintainability and reliability of the components as any damage to even the smallest component involves a considerable replacement or repair cost with particular reference to superconducting magnets in Nb_3Sn .

From simulations and already from the first experimental results it has been seen that in the plasma, in addition to the atoms of hydrogen isotopes, there are also heavier nuclei from structural materials or other gases in a vacuum. These nuclei must necessarily be removed to avoid poisoning the plasma with foreign materials that would lead to the instability of the same; this operation is done by exploiting their mass (certainly higher than hydrogen atoms) bringing them to a well-determined area of the plasma where they then interact with *the divertors* that serve precisely to extract these particles from the reactor.

It has been demonstrated that conventional divertors (which will still be tested on ITER) cannot be used for the DEMO project.

The ITER and DEMO projects, being international projects, require the collaboration (both from an economic and technical point of view) of different countries at European and non-European level; for this reason, the various technological aspects, which will then be implemented and applied in the final fusion reactors, are first analyzed, simulated, and managed by various bodies of the project member states (including Italy).

One of the most important research facilities for these projects is located at the ENEA headquarters in Frascati (RM) and is called DTT (*divertor tokamak test facility*).

The DTT structure is designed to explore all lines of plasma operating regimes relevant to ITER and DEMO; In particular, it will be possible to demonstrate the physical and technological feasibility of various divertor configurations. In this way it will be possible to integrate knowledge on alternative divertor concepts already tested on existing machines.

In the project proposal the parameters are chosen to be faithful to the conditions on the plasma frontier similar to those of DEMO. The main parameters of the

machine have been chosen in order to guarantee maximum flexibility, even within the limits of a budget and a time program consistent with the European roadmap.

The main objectives of DTT can be classified as follows:

1. Demonstrate that the heat removal system proposed for DEMO can withstand the high thermal load that would occur if the radiated power turned out to be higher than expected.
2. Enrich experimental knowledge in the field of heat and particle disposal with those not obtainable with existing machines.
3. Demonstrate that possible alternative or complementary solutions for the divertor can be adopted for the DEMO project.

It will be possible to evaluate whether:

1. Alternative magnetic configurations of divertor are acceptable in terms of heat removal.
2. The magnetic configurations of the divertor are compatible with the current engineering limits for the generation of the poloidal magnetic field.
3. The configurations of the divertors are compatible with the engineering constraints of DEMO.

Superconducting materials are of key importance in nuclear fusion projects. These materials are used for the generation of the magnetic field that has the role of confining the plasma within the *tokamak* structure and allowing fusion itself. The values of currents circulating inside the superconductor are around *40-70 kA*.

For a specific superconducting material, three parameters can be defined:

1. Critical magnetic field corresponding to zero current and temperature B_{c0} .
2. Critical temperature corresponding to zero current and magnetic field T_{c0} .
3. Critical current density corresponding to zero temperature and magnetic field J_{c0} .

A superconducting material is in the *superconducting state* when the following three conditions occur:

1. The temperature T of the superconductor must be lower than the critical temperature of the material.
2. The magnetic field B of the superconductor must be less than the critical magnetic field.

3. The current density J of the superconductor must be less than the critical current density.

The BJT is the surface that combines the trend of the three parameters. This surface is called the critical surface and determines the region of operation of the material as a superconductor; in particular, the material has almost zero resistance if it is operating below the critical surface. An observation that can be made is that as one of the three parameters increases, there is a decrease in the other two.

In order to better address the topic of the research project, it is necessary to introduce a magnetic phenomenon that is particularly relevant in failure conditions; this phenomenon is called quench.

The quench of a superconducting magnet consists in the overheating of a part of its winding that leads to the loss of superconductivity: when this happens, the circulating current is rapidly dissipated in the form of energy by Joule effect and the magnet ceases to function with catastrophic effects on the material itself (breakage and explosion due to the Lorentz forces generated in the transient) and demanding economic consequences.

What happens is therefore a local transition from a *superconducting state* to a *normal state* that is very fast (depending on the natural frequencies of the *RLC* circuit that is determined) and causes a complete transformation of the magnetic energy stored in the coils into heat. This process is called magnetic *quench*.

Since the magnetic energy stored in superconducting magnets is of the order of 2GJ-4GJ (for DTT), in the event of a failure or *quench* there must be the possibility to extract it very quickly to safeguard the integrity of the Tokamak and superconductors.

In this case, the so-called *FDU systems* (*fast discharge unit*) intervene, which basically consist of resistors to allow discharge and fast dissipation of energy. Protection is carried out by connecting a discharge resistor in series to each block of magnets divided into various groups depending on their electrical configuration.

The structure of the FDU with the details of his functioning system is described in Chapter 6 Fast Discharge Units.

The FDU system allows a rapid discharge (in the order of a few seconds) of energy of the magnetic field of the superconducting coil (up to 4.5 GJ) *in case of failure*.

In line with the objectives of DTT set out above, this research project therefore reports the analysis and modelling of the transient dynamic behavior of the electrical circuit of the FDU.

The goal is to avoid the replacement of magnets with related economic commitments as a possible failure would result not only in damage to superconductors but also to nearby metal structures (*vessels, auxiliary systems, etc.*) due to the Lorentz forces generated by the very high magnetic fields.

The results achieved in the three years of PhD will then be available to the scientific community to then be applied to the ITER and DEMO projects and thus ensuring the safety of superconducting magnets in the presence of failure.

The main objective of this thesis so is to report all the models, simulations and results processed for the entire duration of the course of study as part of the development of Fast Discharge Units (FDU).

For the purpose of understanding the thesis, it was considered appropriate to initially provide hints of nuclear physics while not going into too much detail as it is outside the ultimate purpose of the document.

Subsequently, the Strategic Energy Technology Plan and all that follows from it as a result of the agreements stipulated by the EU between the member countries and also with the countries outside the EU are addressed.

Continuing in the document there will be the description of the operation of a Tokamak type nuclear fusion reactor with reference to plasma confinement, its structure, and the key points to support the fusion reaction autonomously without intervention from the outside.

After this premise on these topics there is a focus on all the models built for the simulation of the behavior of DTT FDUs making full reference to the conference articles and published in the journal.

The original content of this thesis is to be searched on the Chapter 6 Fast Discharge Units, in particular there will be a description of all the work developed during the first 2 years of PhD Course related to DTT FDUs, then on Section 6.3

there will be a description of the FDUs model developed at ITER Organization with description of subtasks and finally on 6.5 there will be a description of FDUs model for DEMO.

The publications related to the original work realized during the PhD course can be found on the following references: [1] [2] [3] [4] [5] [6] [7] [8].

It is extremely important to remark that all the information related to ITER Tokamak can be found on ITER website and all the parameters of the FDUs are not reported in this document due to the policy of the Organization.

The scope of this document is to report the research during the PhD course and related to the ITER Internship, only the original research results are reported here thus avoiding reporting sensible data.

2 Introduction to nuclear fusion

2.1 General introduction

With “Nuclear fusion” is meant the fusion reaction of two atoms (generally hydrogen atoms) within special reaction chambers called Tokamak.

Currently in the world there is an increasing demand for electricity and now, even if part is produced from renewable sources, it is still heavily dependent on fossil fuels.

To make a significant contribution worldwide, it is estimated that fusion must generate an average of 1 TW of long-term electricity, i.e., at least several hundred nuclear fusion power plants during the 22nd century. Today, Europe is a leader in fusion research and development and can aim to be a key player in the fusion market. (“European Research Roadmap - EUROfusion”)

The main milestones that need to be achieved in the coming years are the following:

1. Technical demonstration that it is possible to build a large-scale nuclear fusion reactor (ITER aims to produce 500 MW in 400 s [9]).
2. Feeding the grid with electrical power coming directly from a nuclear fusion plant (DEMO¹) whose objective is to produce several hundred MW of power sustained for several hours.
3. Transition of the fossil fuel-based energy production model to reliable, large-scale power plants.
4. World production of energy from nuclear fusion.

The European Fusion Roadmap addresses the first three of these objectives, all in the context of the final objective.

This plan leads to the first conception or conceptual projects of DEMO around 2027.

The plan will form an engineering design activity by focusing on a decision to build DEMO a few years after a high-performance Deuterium Tritium (D-T) operation of ITER and the first results of the ITER Test.

¹ DEMOnstration fusion power plant

DEMO will be operational about 20 years after high-power plasmas are demonstrated as possible in ITER.

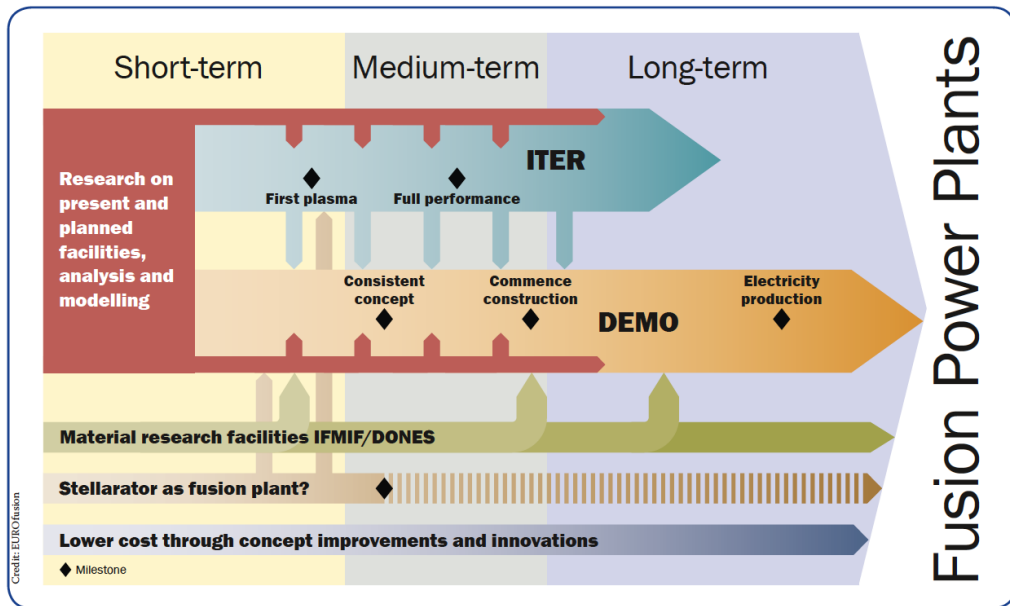


Figure 1: European roadmap in a nutshell [10].

ITER will allow science to broaden its horizons and focus all its forces on the exploitation of nuclear fusion energy.

To ensure its success, however, it is necessary that engineers from all over the world collaborate to obtain the fusion a concrete and achievable result as a deep understanding of the critical issues behind plasma physics is necessary.

The main structures that are currently producing results that will support ITER are JET (UK) and JT-60SA (Japan).

There are also other projects in Europe that will deal with more specific topics (like DTT in Frascati, Italy). The Wendelstein 7-X stellarator will also contribute to ITER's physics and technology.

The road to the realization of nuclear fusion on a large scale is fraught with obstacles and problems, here are summarized only some of them:

- Problem of heat exhaust inside the tokamak: now different configurations of divertor are being studied, a component that allows the disposal of impurities and heat coming from the fusion reaction (this, for example, is one of the main objectives of DTT in Frascati).

- Very high neutron irradiation problem for components at the interface with plasma: the walls of any nuclear fusion reactor, and especially DEMO, are subjected to a very high amount of neutron radiation (each neutron coming from the reaction has 14 MeV of energy).
- Self-production of tritium: this problem is related to the self-production of fuel that is not to be forgotten as tritium, having a very short half-life, is not present in nature and must therefore be produced artificially. So, it's necessary to produce the tritium to start the fusion reaction and then it will be produced in the so-called *blanket* inside which there is lithium that reacts with the fusion products (seen later). In this regard, it is necessary to try to optimize the tritium production process as much as possible by improving the production techniques and the layout of the blanket itself.
- The need to bring industries into the nuclear fusion market: to date, it is perhaps one of the biggest problems when dealing with the issue of the commission of the final version of a component. Industries should gradually enter this market as only in this way the research can move from prototype components to components in accordance with the safety standards that have been present for decades for all other types of power plants.

2.2 Strategic Energy Technology Plan

The European Commission has written and updated the Strategic Technology Plan, this document stresses the importance of having a new energy source in the next few years towards the end of the century and it also stresses the importance of ITER.

The first part of the document obviously takes up what are the main objectives in the short and medium term of ITER as only after its construction it can be considered as fully started the career of nuclear fusion.

2.2.1 First period: start ITER operation with other parties and complete DEMO conceptual design (2030)

All the steps of the first period are listed as follow [10]:

- Construct and commission of ITER with industry.
- Secure the success of future ITER operation via preparation and early experiments; this will also include D-T operation of JET (UK).
- Prepare the ITER generation of scientists, engineers, and operators.
- Finalize the design and construct a fusion spectrum neutron source (IFMIF-DONES)
- Lay the foundation of a DEMO fusion power plant.
- Explore the stellarator as an alternate approach to power plants.
- Promote innovation and European industry competitiveness in fusion technology and beyond.

2.2.2 Second period: burning plasma on ITER and DEMO engineering design (2030-2040)

- Exploit ITER with hydrogen, helium, and deuterium to prepare for high performance D-T operation.
- Optimize ITER performance with operation in D-T plasmas at $Q=10^2$.
- Acquire other information from ITER operation to support DEMO design.

² Gain factor which determines the energy gain from the reactions related to the input energy

- Exploitation of the IFMIF-DONES fusion materials testing facility and collect critical data for DEMO.
- Carry out the detailed engineering design of DEMO, with industry, and prepare for construction.
- Targeted development of long lead-time, power plant relevant materials and technologies.
- Depending on progress of Wendelstein 7-X and any decision taken regarding any next-step device, develop a pre-conceptual design for a stellarator power plant.
- Promote innovation and European industry competitiveness.
- Establish industrial involvement in DEMO, building on the ITER experience.
- Prepare the DEMO generation of scientists, technologists, and engineers.

2.2.3 Third period: plasma and technology optimization on ITER and construction of DEMO (2040 and on)

- Steady state and technology testing on fusion power plant plasmas.
- Exploitation of the DONES fusion materials testing facility and its upgrade to IFMIF to develop and qualify materials for long life in DEMO and commercial power plants.
- Finalization of the design and then construction of DEMO.
- Demonstration of electricity generation at the beginning of the second half of the century.
- Qualification of power plants relevant technologies and materials for the commercial phase.
- Cooperate with industry for the later deployment of fusion via either tokamak or stellarator power plants.

2.3 ITER and DEMO facilities

ITER and DEMO are plants that will therefore allow to test the actual feasibility of nuclear fusion on a large scale: ITER will demonstrate that it is possible to create and support plasma by generating hundreds of megawatts of output power and above all by developing the possible know-how to continue and develop research towards new perspectives. DEMO will bring all the results of ITER towards the effective integration of nuclear fusion with electricity grids.

Referring to the roadmap expressed above, it can be noted that ITER is the fundamental project for the first phase as it will allow to have a robust plasma maintenance system for long periods of time and to develop technologies for heat disposal; for this reason, a large part of European resources, at the moment, are directed precisely towards ITER and it is expected to have a gain factor of the merger $Q = 10$ by 2040.

On the other hand, within the European strategy, there is a DEMO whose objectives are as follows:

1. Net power production of 300-500 MW and to supply it to the electricity grid.
2. Safety and environmental sustainability.
3. Self-sufficiency in the production of tritium.
4. Resolution of any problems that may arise with ITER
5. To lay the foundations for the consolidation of nuclear fusion as a new source of energy.

One of the main problems that will have to be faced in the relative immediate future (and which was also one of the main problems faced in the doctoral course) is certainly the lack of presence on the market of standards, codes and all the know-how present in other sectors of the industry.

The industry will have to be able to update itself and adapt to the new needs of the entire nuclear fusion sector as DEMO cannot be designed solely and exclusively by research laboratories but requires a complete inclusion of the entire industrial sector, from the energy sector to the mechanical one (present in each design element of a nuclear fusion reactor).

The main sectors in which the industry will be most involved are the following [10]:

- Industrial Project Management;
- Plant architect engineering.
- Plant engineering tools, modelling and simulation.
- Design for robustness and manufacturing of critical components, including design simplification and reduction of fabrication costs.
- Standardization of parts and components.
- Materials development.
- Cost, risk, safety analysis.
- Development of codes and standards.

There are about 50 nuclear fusion reactors operating nowadays [11], all of them are built in order to evaluate different shapes and configurations but in this thesis there will be a major focus mainly on JT60-SA (Japan), FTU (Frascati Tokamak Upgrade, Italy), DTT (Italy), ITER (France) as they are strongly influenced each other from a purely technical point of view.

2.4 Brief review of nuclear physics

The nucleus is made up of Z protons, N neutrons and Z electrons that orbit the nucleus. By convention, Z is the atomic number, while $A = Z + N$ indicates the mass number.

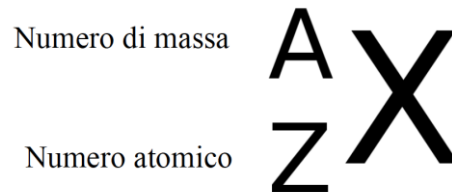


Figure 2: Mass number (A) and atomic number (Z).

The periodic table sorts the elements according to their atomic number Z which is also equal to the number of electrons in the orbitals. The mass number A is also defined as the number of nucleons.

Mass is conventionally measured in atomic mass units AMU: 1 AMU is equal to $1/12$ of the atom mass of ${}^{12}\text{C}$.

For each subatomic particle, masses per unit of energy are shown below:

- 1) Proton: $938,272 \text{ MeV}/c^2$
- 2) Neutron: $939,565 \text{ MeV}/c^2$
- 3) Electron: $0,511 \text{ MeV}/c^2$

In nature there are also atoms of the same element, but which differ only in the number of neutrons, in more rigorous terms it is said that they are nuclei with the same number of protons Z but different number of neutrons N .

Isotopes are not widespread in nature in equal percentages as they can sometimes be much more unstable, for example the case of Carbon C-12 which has an abundance of 98.93% while C-13 only 1.07%.

Another isotope is that of hydrogen with deuterium and tritium (the latter is radioactive and has a half-life of 12 years, which is why it cannot be found in nature), which will be explored later.

As the mass number A changes, there is a variation in the binding energy per nucleon according to the graph in the next figure (note that the y axis varies between 7 and 9).

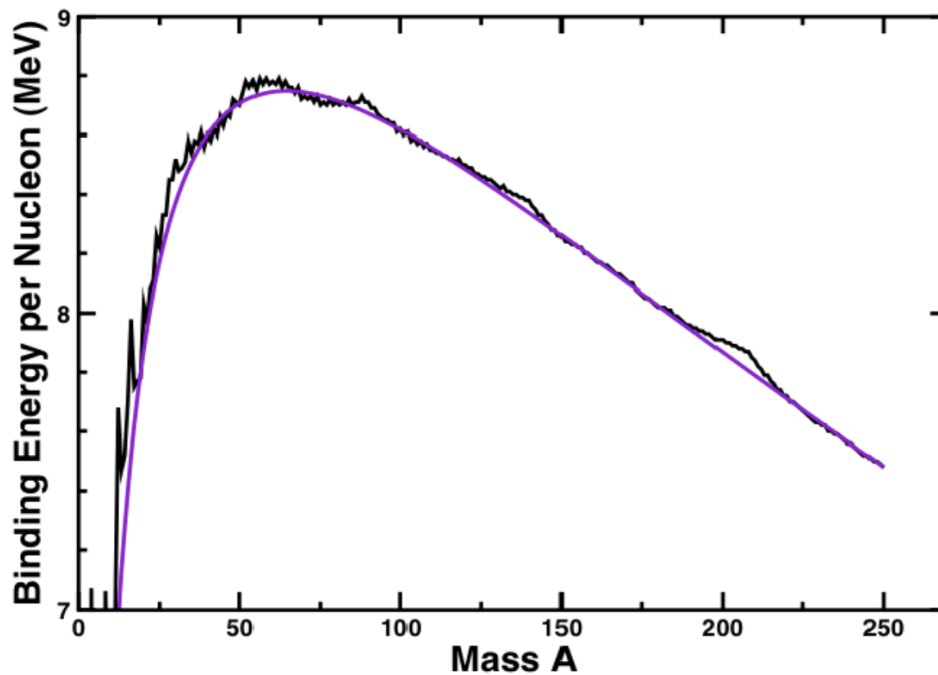


Figure 3: Binding energy per nucleon (MeV).

The oscillation of this energy around 8 MeV with the variation of the mass is the key to the exploitation of nuclear energy as for the fusion the nuclei are fused from light nuclei to heavier nuclei with consequent release of energy, as opposed to fission (in any case, both reactions are advantageous from the energetic point of view up to the maximum point, corresponding to the element of iron ($A = 56$) beyond which the nuclear fusion reaction is no longer advantageous).

Elementary particles are classified based on the following properties:

- 1) Mass
- 2) Electric charge
- 3) Spin
 - a. Semi-integer spin (fermions) in which the Pauli Exclusion Principle applies³.
 - b. Integer spin (bosons) in which the exclusion principle does not hold.

More in detail in the subatomic structure even smaller particles called *quarks* can be identified: they combine to form baryons (another name for identifying

³ The Pauli Exclusion Principle is a principle of quantum mechanics which states that two identical fermions cannot simultaneously occupy the same quantum state.

protons and neutrons); depending on the combination of quarks, u-u-d (proton) or u-d-d (neutron) are obtained.

The electrons belong instead to the category of leptons together with electronic neutrinos, muons, muon neutrinos, taus, tau neutrinos.

3 Introduction to Tokamaks

3.1 Fusion reactions

The term Tokamak is a term whose etymology is Russian, its meaning is to (*roidál'naja ká (mera) (s) ma (gnítnymi) k (atúškami)*), it can be translated into English as "toroidal chamber with magnetic coils".

A tokamak is an electric machine with magnetic confinement made up of different magnets (whose number and shape is variable according to the type of machine, as will be seen later); this machine is currently used for experimental nuclear fusion projects that are of great international interest, especially following the acceptance of the climate crisis by international politics and the increasing need to produce energy no longer from fossil fuels but from renewable sources (nuclear fusion, in this sense, can be understood as a renewable energy source).

The physical principle underlying Tokamak's functioning is that of the fusion of a deuterium nucleus with a tritium nucleus with consequent formation of a particle and release of energy; however, there are other nuclear fusion reactions whose energy characteristics will be analyzed in more detail however, today, the D-T reaction seems to be the most advantageous and it is the one on which the nuclear fusion reactors object of this thesis work (DEMO, ITER, DTT⁴).

From the D-T reaction an energy equal to 17 MeV⁵ will be released distributed in 14 MeV to the neutron and 3.5 MeV to the Helium atom according to the following reaction [12]:



For the sake of completeness, the other possible main fusion reactions will be reported in the figure below:

⁴ Divertor Tokamak Test (Frascati, Italia), International Thermonuclear Experimental Reactor (Cadarache, Francia), DEMONstration Power Plant.

⁵ Mega Electron Volt

1.	D + T	→	⁴ He (3.5 MeV) + n (14.1 MeV)
2.	D + D	→	T (1.01 MeV) + p (3.02 MeV) (50%)
		→	³ He (0.82 MeV) + n (2.45 MeV) (50%)
3.	D + ³ He	→	⁴ He (3.6 MeV) + p (14.7 MeV)
4.	T + T	→	⁴ He + 2 n + 11.3 MeV
5.	³ He + ³ He	→	⁴ He + 2 p
6.	³ He + T	→	⁴ He + p + n + 12.1 MeV (51%)
		→	⁴ He (4.8 MeV) + D (9.5 MeV) (43%)
		→	⁴ He (0.5 MeV) + n (1.9 MeV) + p (11.9 MeV) (6%)
7.	D + ⁶ Li	→	2 ⁴ He + 22.4 MeV
8.	p + ⁶ Li	→	⁴ He (1.7 MeV) + ³ He (2.3 MeV)
9.	³ He + ⁶ Li	→	2 ⁴ He + p + 16.9 MeV
10.	p + ¹¹ B	→	3 ⁴ He + 8.7 MeV

Figure 4: List of the most favorable fusion reactions [45]

The D +T reaction is the one with the highest cross section at lower temperatures.

The cross section has the dimensions of the square of a length and measures the effectiveness of interaction between beam and target and it's indicated with the letter σ [m^2]; if σ is high, there is a small attenuation length and therefore the beam is rapidly attenuated as it passes through the target and vice versa.

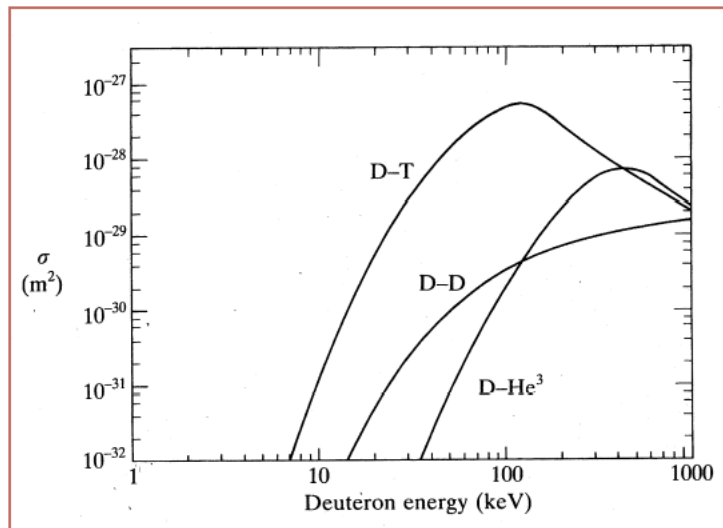


Figure 5: Cross section of the main nuclear fusion reactions.

The cross section is generally indicated in barn where $1 \text{ barn} = 10^{-28} m^2$ and in Figure 5 it's represented the cross section of the major nuclear fusion reactions

D-T, D-D, D-He; it can be noted that the D-T reaction is the one most easily obtainable at lower temperatures.

3.2 Plasma definition and main processes

In physics, plasma is defined as a strongly ionized gas in which most of the atoms or molecules are decomposed into positively charged ions and negatively charged electrons; this condition occurs when the gas reaches very high temperatures (as inside the stars), or because of electrical discharges of great intensity (as in arc or neon lamps).

Plasma is therefore defined as the fourth state of matter and there can be very variable temperatures ranging from 5,000 ° C to 100,000,000 ° C for thermonuclear plasmas and has the characteristic of being locally neutral (no positive or negative charge).

If a plasma is subjected to the action of a magnetic field, the electrons that are lighter than the ions will be accelerated, and these will assume a speed called drift speed.

The resistivity of the plasma can be written as follow:

$$\eta \propto \frac{1}{T_e^{\frac{2}{3}}}$$

A thermonuclear plasma has a temperature dependence opposite to that of conductive solid materials: the hotter it is, the less resistive it is.

A charged particle in a magnetic field is constrained to travel a helical trajectory as in the figure that can be moved away by more than a finite quantity (called the Larmor radius) from the magnetic field line. The motion of the helix center is called the guide center mode.

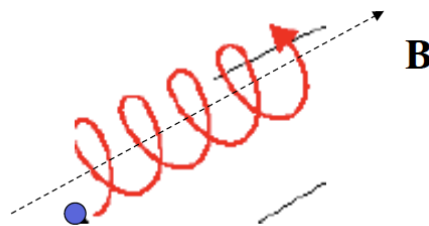


Figure 6: Helical motion of a charged particle subjected to a magnetic field.

3.3 Fusion confinement

One of the main problems of nuclear fusion is that of having to keep the plasma in critical confinement for a period and for temperatures sufficient to trigger the fusion reaction.

For this reason, the interacting particles must be endowed with a kinetic energy that allows them to overcome the Coulomb barrier.

Over the years various methods for plasma confinement have been hypothesized and they will be analyzed in this section.

For a D-T reaction, the ion energy which should be reached is about 370 keV and this is extremely challenging for the actual technology, and it requires a sufficiently high stable temperature which is about 10^8 K in a practical reaction volume (for a sufficient time to render the entire process energetically available) [12].

3.3.1 Material confinement

The first method which could be considered is certainly that of physical confinement by inserting the fuel into a combustion chamber. However, this approach is immediately to be discarded as the technical requirements of the fusion reaction do not allow the use of any type of material, even those with very high melting temperatures (generally metals melt at 5000 K which is an infinitely lower temperature than that necessary to support the fusion reaction).

Even if the material is not in direct contact with the plasma, problems arise in the same way due to the presence of atoms "sputtered" from the metal and consequently ended up in the plasma; this phenomenon could lead to the concentration of high amounts of impurities in the plasma and thus lowering its temperature.

3.3.2 Gravitational confinement

This is the method by which nuclear fusion occurs in nature within the cores of stars. This is possible because the very high density of the nuclei of the stars allows

the fuel to create a plasma at a sufficient temperature to trigger the fusion reaction while the particles that are in the most superficial layers instead manage to escape the gravitational attraction.

It is evident that this method of gravitational confinement is not among the possible options applicable on earth as it is not possible to obtain it in our environment.

3.3.3 Inertial confinement

Inertial confinement involves the compression of a small fuel pellet to such densities and temperatures as to trigger the reaction.

This compression process takes place by means of lasers or ion beams and theoretically a certain amount of energy is expected to be output due to the fusion reaction before the destruction of the pellet itself.

The main problem of this confinement technique is the need to bring the density of the 10^3 pellets times greater than that equivalent to the solid state, and it must also be considered that not all the atoms contained in the pellets will produce fusion energy but much of the fuel will be burned even before it can happen.

This technique, to date, is not the one mainly followed by the scientific community.

In the next figure is represented a general scheme for this technique.

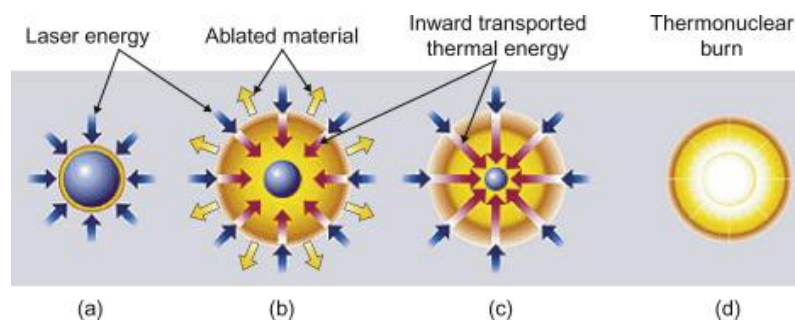


Figure 7: Compression and heating of a spherical pellet by external laser [44].

3.3.4 Magnetic confinement

One of the most promising methods for plasma confinement is magnetic confinement by exploiting the Lorentz force.

It is recalled that a particle of charge q and mass m in a magnetic field of density \mathbf{B} moves according to Lorentz's law:

$$m \frac{dv}{dt} = q (\mathbf{v} \times \mathbf{B})$$

Where:

- v is the velocity vector.
- B is the magnetic field.
- q is the charge of the particle.
- m is the mass of the particle.
- t is the time.

In the case of a magnetic field generated by a solenoid, it is recalled that the particles will travel a trajectory that is parallel to the field lines (the direction will be dependent on the charge of the particle) and following a spiral with a certain radius called gyro-motion radius equal to:

$$r_g \propto \frac{1}{|B|} [12]$$

In the case of the solenoid applied to fusion, however, the main problem is that of the leakage of fuel at the two ends of the solenoid, this determines a poor prospect of use in the nuclear fusion sector.

In a reactor that exploits this type of confinement, the main magnetic field is that generated by TFCs (Toroidal Field Coils), but this magnetic field is not able, by itself, to generate the total field capable of trapping all charged particles and bringing the plasma to the desired temperature and pressure condition.

For this reason, it is necessary to introduce a poloidal magnetic field that serves to create a total stabilizing magnetic field for the plasma even if, much of this magnetic field, is generated mainly by the plasma itself flowing in the toroidal direction (Figure 8).

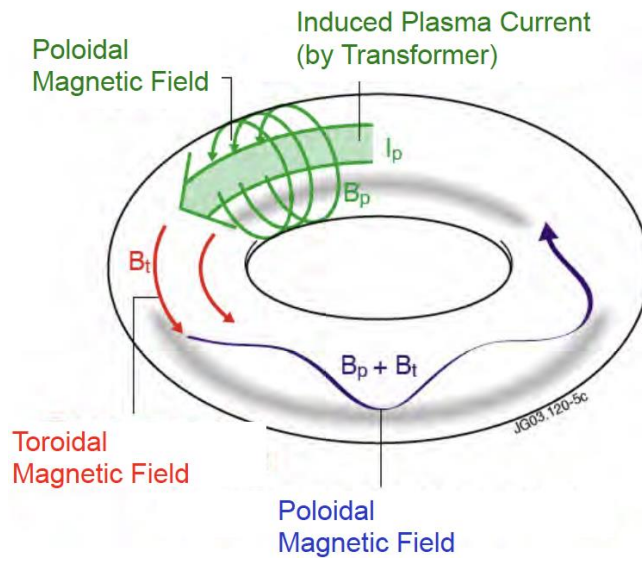


Figure 8: Poloidal and Toroidal magnetic field used for magnetic confinement.

3.4 Structure of a Tokamak and particle trapping principle

The general structure of a nuclear fusion reactor is illustrated in Figure 9.

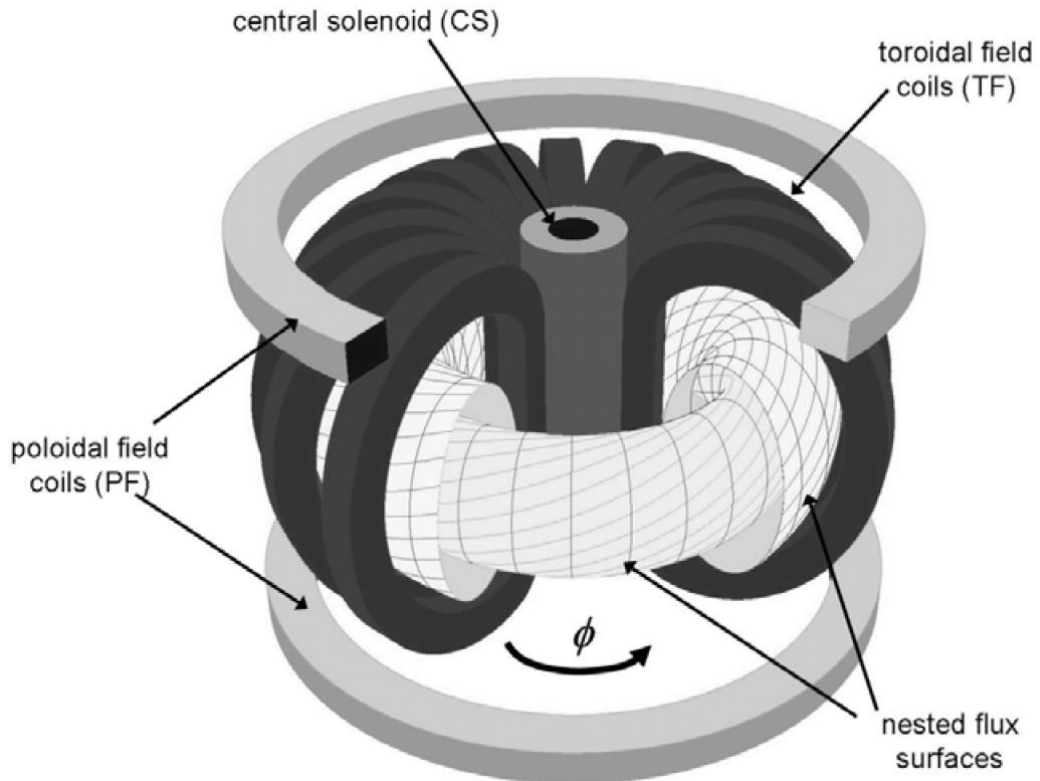


Figure 9: Schematic representation of TF, PF, CS, and the magnetic flux [45]

The Tokamak is mainly composed by the following coils:

- TFC or TF: Toroidal field coils (to generate the toroidal magnetic field).
- PFC or PF: Poloidal field coils (to generate the poloidal magnetic field).
- CS: Central solenoid (to give a magnetic pulse during the operating scenario).

The plasma is all surrounded by a blanket (not in figure) which has three roles:

- It absorbs the 14 MeV neutrons, transforming their energy into heat which is then transferred to a coolant to provide the power output.
- It shields the superconducting coils and outer components from neutrons.
- It allows the tritium breeding to fuel the reactor according to the reactions seen in previous sections.

The plasma torus, by a physically meaning, is viewed as a single-winding secondary circuit of a transformer.

A current flow in the primary transformer winding will therefore induce a current in the plasma torus by transformer action.

The resultant toroidal plasma current generates a poloidal magnetic field B_θ which is perpendicular to the toroidal field B_ϕ generated by the TFCs.

These two magnetic fields are combined by vector addition:

$$\vec{B} = \vec{B}_\phi + \vec{B}_\theta$$

Those magnetic fields combined generate the basis for the rotational transform effect in Figure 8.

However, there is a need to introduce stabilizing coils that do not allow the plasma to expand and disperse, this is because the poloidal magnetic field is not homogeneous throughout the section of the torus but will be greater in the inner part due to the geometric configuration of the magnetic chamber.

So, there is the need of adding a vertical magnetic field \vec{B}_v produced by the stabilizing coils to produce an inward directed force due to the interaction between the charged plasma and the magnetic field which prohibits the outward expansion (Figure 10).

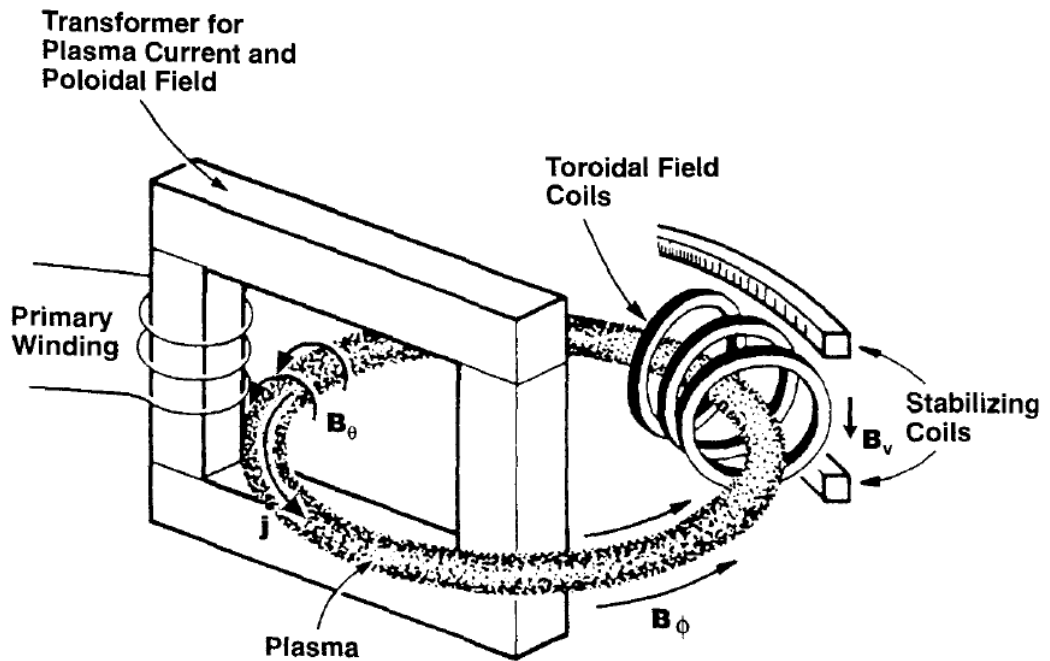


Figure 10: Components of a tokamak [45]

The main aim of creating such a complex system is to trap particles in order to achieve the nuclear fusion.

A charged particle with a specified velocity inside a magnetic field is forced to move according to the Lorentz law:

$$m \frac{dv}{dt} = e \vec{v} \times \vec{B}(r)$$

The kinetic energy is conserved and if the magnetic field is homogeneous the component of the velocity parallel to the magnetic field and the modulus of the perpendicular component are constants of motion.

Inside the plasma there are negatively and positively charged particles and therefore rotate in the opposite direction thus generating a demagnetizing effect in the plasma such as to oppose the equilibrium field (diamagnetic effect).

In the next figure can be seen the driving center motion of a charged particle inside an electric and magnetic field.

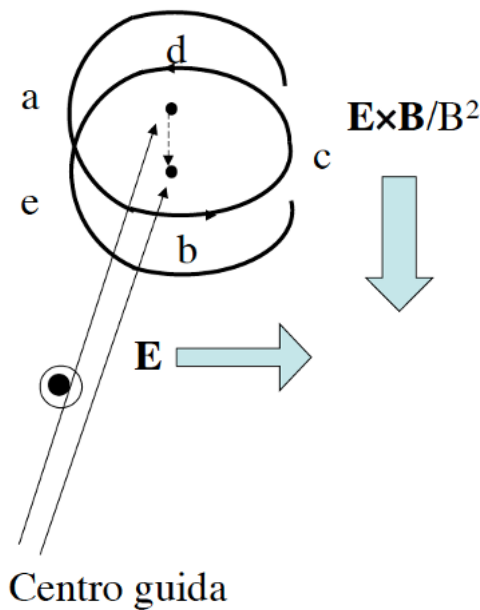


Figure 11: Driving center motion of a charged particle inside an electric and magnetic field.

While most of the particles are free to spiral around the helical field lines as they encircle both the major and minor axis of the torus, there is a part of the total particles which is trapped in a specific region inside the plasma due to the variation of the magnetic field itself depending on the plasma radius.

The explanation of this phenomenon is because the magnetic field is not constant as the radius varies but has a trend like that in Figure 12 and therefore a phenomenon like that of the magnetic mirror occurs.

For this reason, some of the plasma particles with a $v_{||}$ lower than a threshold are trapped by these mirrors (the other particles are called *passing particles*) by creating a path shape orbit called *banana orbit* (see above).

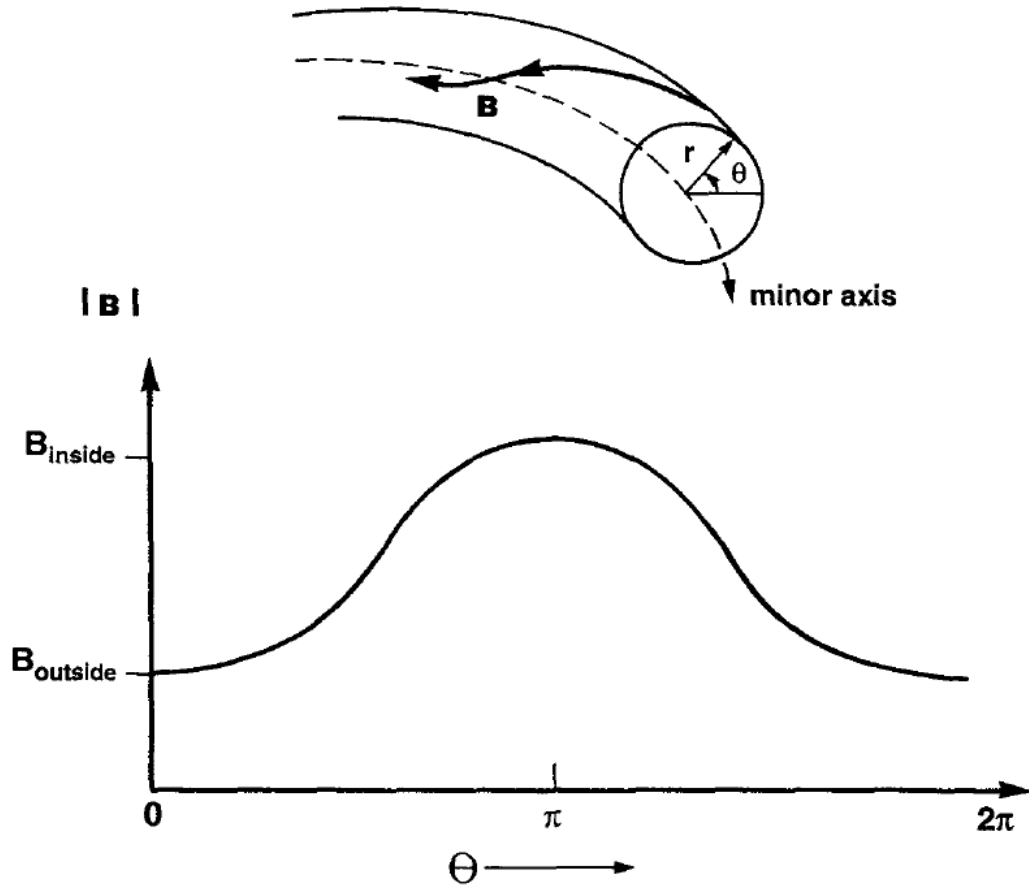


Figure 12: Poloidal variation of the overall magnetic field in a tokamak [12]

The fraction of trapped particles in a mirror field is given by [12]:

$$f_{trap} = \sqrt{1 - \frac{B_{min}}{B_{max}}}$$

And assuming $B_{\theta} \ll B_{\phi}$ such that

$$B \approx B_{\phi} \propto \frac{1}{R_0 + r \cos \theta}$$

It can be found the ratio

$$\frac{B_{\min}}{B_{\max}} = \frac{B_{\text{outboard}}}{B_{\text{inboard}}} = \frac{B(r = a)}{B(r = -a)} = \frac{\frac{1}{R_0 + a}}{\frac{1}{R_0 - a}} = \frac{1 - \varepsilon}{1 + \varepsilon}$$

Where

$$\varepsilon = \frac{a}{R_0}$$

Is the inverse aspect ratio of the tokamak.

So, the fraction of trapped particles is given by:

$$f_{\text{trap}} \approx \sqrt{1 - \frac{1 - \varepsilon}{1 + \varepsilon}} = \sqrt{\frac{2\varepsilon}{1 + \varepsilon}}$$

For a tokamak with aspect ratio of 1/3, approximately 70% of particles are trapped.

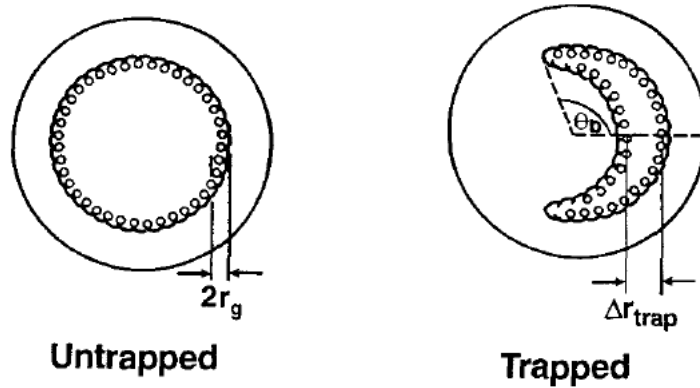


Figure 13: Schematic projection of particle orbits in a tokamak onto a poloidal plane [12]

The trapped particles bounce back and forth between poloidal angles $\pm \theta_b$ avoiding the inner torus region.

It is demonstrated that trapped particles can escape more rapidly from a tokamak plasma than the untrapped ones. Evidently, if the fraction of trapped particles is large, this leakage enhancement constitutes a substantial problem in tokamak confinement.

3.5 Power balance in a nuclear fusion reactor

The thermonuclear power per unit volume in D-T plasma is given by:

$$p_{T_n} = n_d n_t \langle \sigma v \rangle \varepsilon$$

Where:

- n_d is the deuterium density.
- n_t is the tritium density.
- $\langle \sigma v \rangle$ is the reactivity for a D-T reaction and it's calculated in $\left[\frac{m^3}{s}\right]$ (see next figure).
- ε is the energy released per reaction.

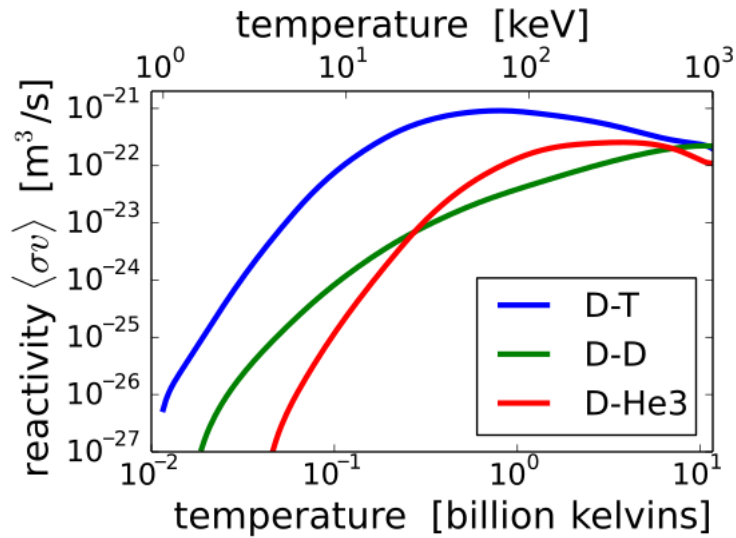


Figure 14: reactivity related to temperature in keV and billion kelvins. [46]

The total ion density is:

$$n = n_d + n_t$$

So, the previous equation can be written as:

$$p_{T_n} = n_d (n - n_d) \langle \sigma v \rangle \varepsilon$$

It can be demonstrated that for a given n the power is maximized when $n_d = \frac{1}{2}n$ which means that deuterium and tritium densities are the same. In this case the power is:

$$p_{T_n} = \frac{1}{4} n^2 \langle \sigma v \rangle \varepsilon$$

The total energy loss in the plasma can be written as:

$$W = 3\overline{nT}V$$

Where the bar represents the average value and V is the plasma volume.

The rate of energy loss is related to a parameter called energy confinement time represented by τ_E defined by the relation:

$$P_L = \frac{W}{\tau_E}$$

The thermonuclear power in the case of same densities for deuterium and tritium consists of two parts: 80% of energy is carried out by neutrons which leave the plasma without interacting with other particles and the remaining 20% of energy is carried by α -particles which transfer 3.5 MeV of energy through collisions.

The total α -particles heating power is:

$$P_\alpha = \frac{1}{4} \overline{n^2 \langle \sigma v \rangle} \epsilon_\alpha V$$

The overall power balance considers the externally supplied power P_H , the power due to α particles and the power loss P_L as following:

$$P_H + P_\alpha = P_L$$

Replacing all the terms, it can be obtained the power balance formula:

$$P_H + \frac{1}{4} \overline{n^2 \langle \sigma v \rangle} \epsilon_\alpha V = \frac{3\overline{nT}V}{\tau_E}$$

3.6 Ignition

During the D-T plasma heating process, alpha particles provide a certain amount of the power needed to heat the plasma.

If the optimal confinement conditions are reached, the plasma can be kept at a certain temperature and thus make up for the lost power seen in the previous section thanks to the heating provided by the alpha particles (thus allowing to remove the power provided from the outside). Taking up the power balance equation and considering constant density and temperature it can be written:

$$P_H = \left(\frac{3nT}{\tau_E} - \frac{1}{4} n^2 \langle \sigma v \rangle \varepsilon_\alpha \right) V$$

From this equation it can be obtained the requirement for the plasma to be self-sustained:

$$n\tau_E > \frac{12}{\langle \sigma v \rangle} \frac{T}{\varepsilon_\alpha}$$

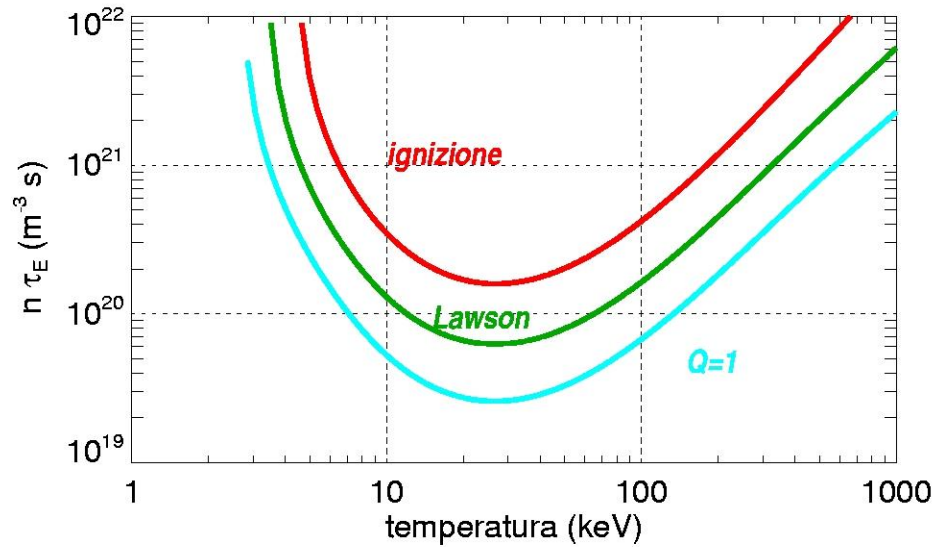


Figure 15: The value of density and time confinement required to obtain ignition as a function of temperature.

It can be seen from the graph a minimum peak around $T=30$ keV with a corresponding value to:

$$n\tau_E > 1.5 \cdot 10^{20} m^{-3}s$$

τ_E is however function itself of the temperature and so the temperature at the minimum peak is not to be taken in consideration as possible optimum condition.

With appropriate corrections the ignition condition becomes:

$$nT\tau_E > 3 \cdot 10^{21} m^{-3} keVs$$

In Figure 15 it can be also seen the curve related to the Lawson's criterion; this curve was replaced by the one described above since the Lawson didn't consider some considerations about the plasma physics like the energy released from alpha particles.

3.7 Tokamak Equilibrium

In the first approximation one can schematize the equilibrium of a tokamak by the interaction of n R-L circuits although this description is not sufficient to understand the function of the magnetic system of a tokamak.

The expression of magnetic energy can be written as:

$$U_{ik} = \frac{1}{2} \sum_{ik} M_{ik} I_i I_k = \frac{1}{2} \sum_i I_i \Phi_i$$

Where M_{ik} is the mutual inductance between the circuits i and k and the diagonal elements correspond to the self-inductances while those out of diagonal the mutual inductances.

In a magnetic surface there is an equilibrium condition whereby:

$$\nabla p = J \times B$$

Where p is the pressure on the magnetic surface and the current density lies on the magnetic surface ($J \cdot \nabla p = 0$); if magnetic surfaces exist the condition implies $B \cdot \nabla p = 0$ that the pressure is constant on the magnetic surface.

Through appropriate mathematical calculations the Grad-Shafranov equation can be obtained which describes an equilibrium condition in ideal magnetohydrodynamics for a two-dimensional plasma such as axialsymmetric toroidal plasma in a tokamak:

$$\Delta^* \psi + \mu_0 R^2 \frac{dp}{d\psi} + F \frac{dF}{d\psi} = 0$$

Where:

1. ψ is the flow and associated with that nabla written that way is in cylindrical coordinates $\Delta^* \psi = \frac{\partial^2 \psi}{\partial r^2} - \frac{1}{r} \frac{\partial \psi}{\partial r} + \frac{\partial^2 \psi}{\partial z^2}$ and emerges from the product of toroidal current by poloidal magnetic field.
2. F emerges from the product between poloidal current and toroidal field.

Through the equation of Grad Shafranov the function ψ and to follow $\vec{B}_p = \vec{\nabla} \psi \times \vec{\nabla} \phi \rightarrow \vec{B} = \vec{B}_T + \vec{B}_p$ can be obtained but it also allows to characterize the magnetic surfaces and their center which is the center of the real plasma in general not coinciding with the center of the section of the vacuum chamber.

A plasma in ideal magnetohydrodynamic equilibrium cannot be confined with only self-generated currents; this is because self-generated currents generate magnetic fields that tend to unbalance the system that is generating the current.

To achieve magnetohydrodynamic equilibrium it is necessary to have:

1. Active conductors (coils)
2. Passive conductors (conductive walls)

It should be noted that a tokamak is an axialsymmetric system and the equilibrium conditions are two-dimensional, that is, they can be studied on a section of the tokamak assuming that every other section of the tokamak assumes the same behavior (which does not happen for the stellarator that is not axialsymmetric).

3.8 Heat dissipation

The heat produced inside the plasma and lost by conduction must be disposed of on a component inside the reaction chamber, this component is called *divertor* and is also one of the main components of DTT as the Italian project will have as its main objective to study the dissipation of heat as the plasma configuration inside the reaction chamber changes (different scenarios).

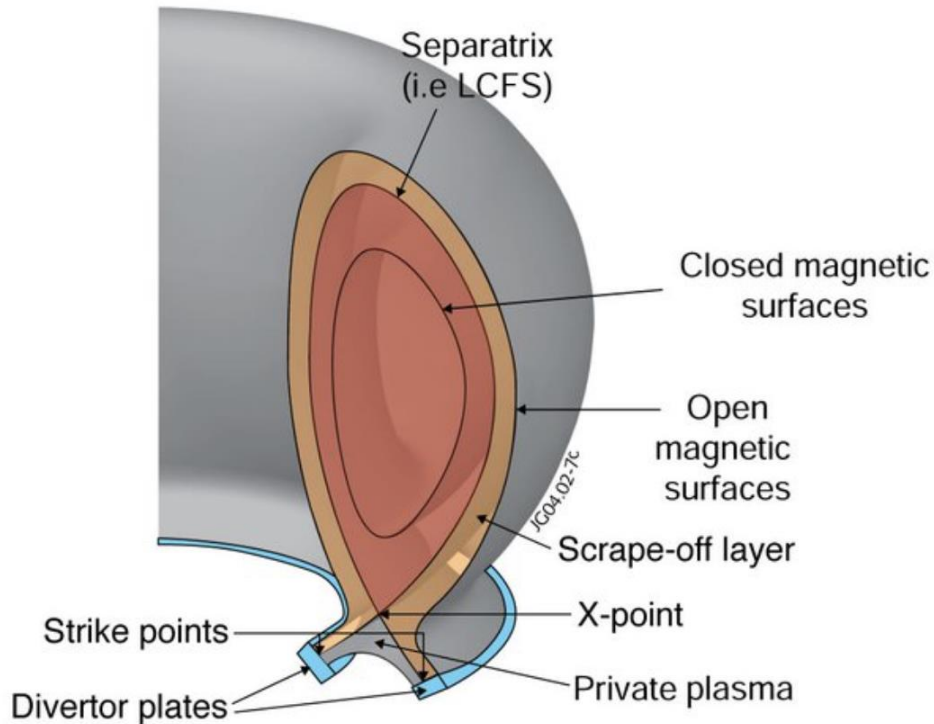


Figure 16: Sketch of the divertor configuration inside the tokamak [54]

The divertor, as a subject to high heat flux, must be designed considering the fact that it must not introduce into the plasma impurities due to the deterioration of the material that composes it.

The main reason why the divertor is used is to have a maximum removal of helium molecules from the reaction chamber as they contribute to the slowing down of the fusion reaction with possible shutdown.

If all the heating power were irradiated uniformly, there would be a limited thermal load on the *first wall* (the first wall that the plasma would encounter outside the magnetic field lines); in the case of ITER there would be about $200 \frac{kW}{m^2}$.

Much of the power that passes through the last closed magnetic field surface flows along it in a thin layer of plasma called *Scrape Off Layer (SOL)* and this power is disposed of on a plate that is consequently subject to high thermal load.

The plasma ions that interact with the plate extract impurities that also lead to plasma contamination (as well as erosion of the plates themselves).

In scrape off layer the power decays exponentially in the r direction and with length λ_q . In a layer of 5 mm there are about 100 MW of power which, depending on the size of the divertor for ITER coincides with a thermal load of $20 \frac{MW}{m^2}$.

For the study of the behavior of the particles close to the divertor, it can be considered a rectified SOL model in Figure 17.

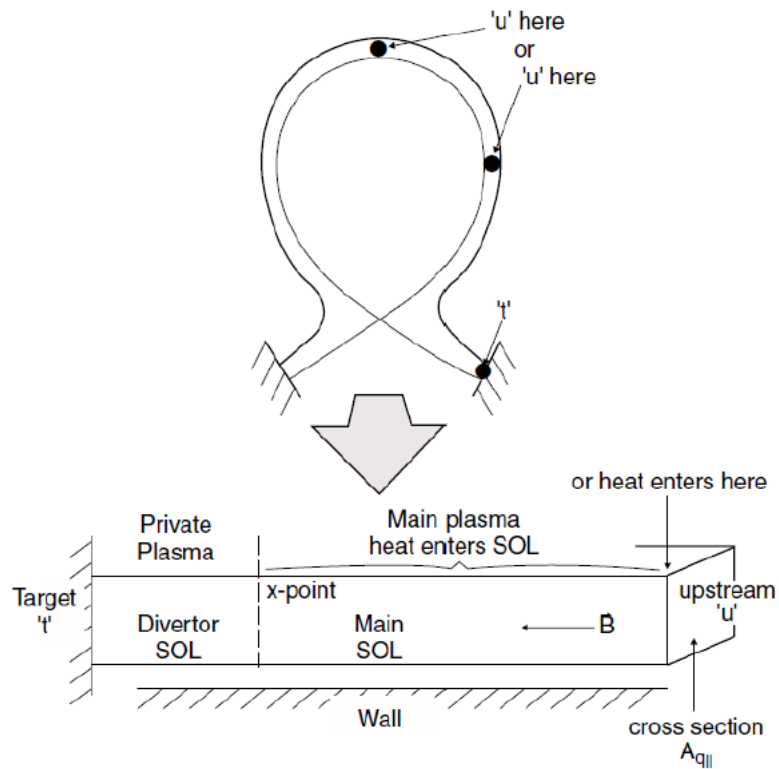


Figure 17: SOL simplified model [55]

The particles move along the open field lines and intercept the divertor plates. Electrons that are more mobile are lost more easily; the plates charge negatively, and a layer of positive charge is formed in front of the plate. The ions are then accelerated by the negative potential of the plates until they reach the speed of sound and the friction force between ions and impurities keeps these confined to the divertor.

3.9 Tritium breeding

The blanket is used to produce tritium through a process called *tritium breeding* with simple extraction methods; it also serves to shield the chamber and the magnet from neutrons (*shielding*) as the insulator of the magnet could deteriorate for sufficiently large absorbed doses and finally serves to convert the energy of neutrons into thermal energy.

Tritium has a half-life of the order of ten years so it is not found in nature but must be produced artificially unlike deuterium which is instead quite abundant on earth; to date it is produced by neutron capture in particular systems called *CANDU* (currently there are 20 *CANDU* in the world in Canada and 4 in Korea) with an estimated production of 1.8 kg per year until 2025.

Currently there are 20-25kg of tritium available which, although they may seem a sufficient quantity, may present one of the first obstacles to the start-up of new nuclear fusion reactors as tritium, precisely because of its difficulty of artificial creation, turns out to be one of the most expensive materials in the world to produce: the cost of tritium production is about 30.000\$/g [13].

ITER will use 20kg of tritium so for DEMO the production of tritium is of paramount importance.

The blanket consists of (see Figure 18):

1. Breeder (solid or liquid)
2. Neutron multiplier
3. Structural material and first wall
4. Coolant fluid (helium, water, or liquid metals)

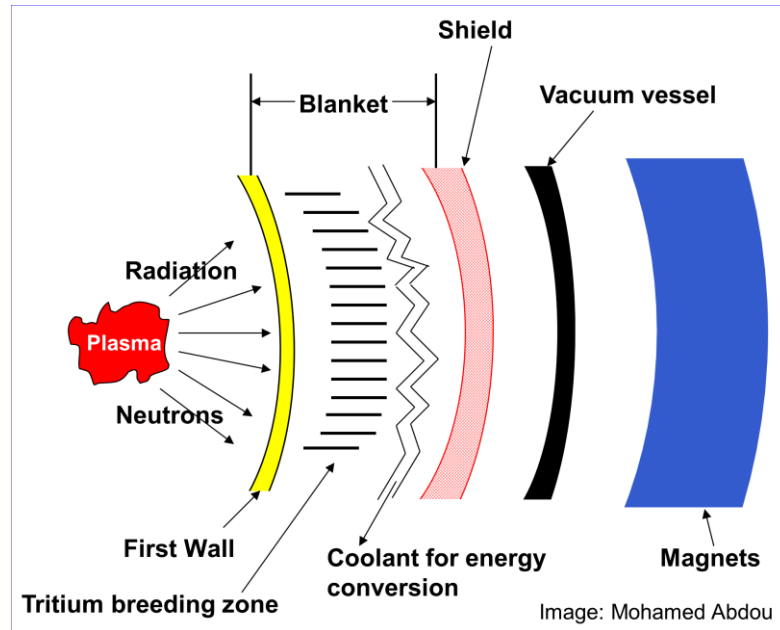


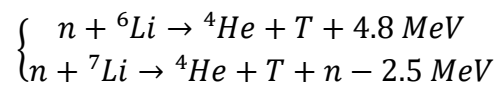
Figure 18: General scheme for the blanket [58].

Components must be chosen based on their ability to have a Tritium Breeding Ratio (TBR) greater than 1, their compatibility with high neutron fluxes and the demand for high operating temperatures.

The blanket is classified according to:

1. Physical state of the breeder: solid or liquid
2. Type of breeder
3. Refrigerant type
4. Type of structural material

Tritium is produced by the following reactions:



To achieve a $\text{TBR} > 1$, compounds with a high percentage of Li and in general enriched ${}^6\text{Li}$ by 30% to 90% must be used.

Not all neutrons that are produced by the nuclear fusion reaction then actually contribute to the production of tritium through the reactions that have just been exposed but part of the neutrons is lost anyway; for example, they are absorbed by structural materials (10-20%), for leaks through the blanket (5%) and through the ports or on the divertor (10-20%). To compensate for these losses, it is necessary to use special materials that are also called neutron multipliers such as ${}^9\text{Be}(n, 2n)$; ${}^{208}\text{Pb}(n, 2n)$; ${}^7\text{Li}(n, n')$.

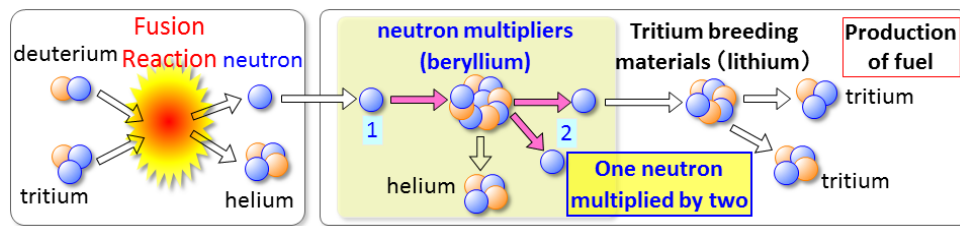


Figure 19: General scheme for tritium breeding with neutron multipliers [57].

These materials, as set out in the formula, absorb one neutron and release two or, as in the case of lithium, release a more excited one.

The breeder can be liquid and in this case it is built in such a way as to incorporate the neutron multiplier and the refrigerant can be Helium or water; a eutectic mixture of Lithium and Lead, pure Lithium or Molten Salts always based on Lithium is also used.

The solid breeder is usually a breeder in which there is a separation between multiplier (Be) and coolant (only He as above 600 ° C the Be reacts with water); in the solid breeder, sintered ceramic compounds also based on lithium are used.

As for refrigerants: they must have a high exchange coefficient, low pressure drops, high heat capacity, compatibility with mantle materials, good nuclear properties, and low working pressures.

Refrigerants can be of two types:

1. Water:
 1. High heat exchange
 2. Low pressure drops
 3. Compatibility problems with the breeder and with the materials inside the chamber in case of leaks

2. Helium:
 1. Low heat exchange
 2. High pressure drops
 3. Excellent compatibility with the breeder and with the materials of the room

3.10 First wall

The first wall is actually the first solid containment system that is located at the interface with the plasma (see Figure 18); it is characterized by high neutron flows more than $1 \frac{MW}{m^2}$ which can cause hardening, swelling, loss of ductility, embrittlement and high radiative flows of $q = 0,15 \frac{MW}{m^2}$

The materials used are mainly tungsten due to the high melting temperature and beryllium due to the low plasma contamination.

Damage to structural materials is due to the transfer of energy from the neutron to an atom in the lattice that produces a primary knock-on atom; this PKA moves the neighboring atoms creating a cascade of energy up to a few 100 keV resulting in the production of holes and interstitial defects that migrate within the lattice.

The damage to the material is quantified by the number of displacements per atom *dpa* and for high *dpa* values the material is brought to a transition from ductile to brittle with consequent loss of the original mechanical characteristics.

Materials used for the first wall can be the following:

1. AISI austenitic steels (used for the vacuum chamber but not for the blanket for rapid degradation under neutron flux).
2. Ferritic-martensitic steels with low RAFMS activation: maximum working temperature around 550 °C so it is a temperature that strongly limits the operating conditions.
3. Oxide dispersion Strengthened (ODS): maximum working temperature about 650°C.
4. Vanadium alloys: working temperature 700°C but with properties very sensitive to the degree of purity.
5. Silicon carbides: working temperature that is around 1000 ° C but the materials still to be developed from a technical point of view.

4 Superconductivity

4.1 Introduction to superconductivity

In 1911 the Dutch scholar and physicist Heike Kamerlingh Onnes managed to discover the phenomenon of superconductivity following various research on temperatures close to absolute zero.

These discoveries began first with the creation of liquid helium in the laboratory and then the physicist moved on to the study of certain metallic conductors, in particular mercury, in which he saw that resistivity ρ presented variations sensitive to high temperatures and tended to be zero near absolute zero thus transforming the metal into a superconductor.

The term that was initially used to describe the phenomenon was *supraleider* which, translated into English, became *superconductivity* and later *superconductivity* [14] .

It is now known how materials can be classified according to their ability to conduct electric charges, in particular metals are classified as good conductors while synthetic materials such as rubbers and plastics are instead good insulators; in the latter materials electrons are attracted to their respective molecules and can only move around their position.

Then there is a third category or that of semiconductors such as silicon that have intermediate characteristics between insulators and conductors; in particular, they can be doped with particular materials and they are used to build specific components such as transistors or electronic chips.

Once the phenomenon of superconductivity was discovered, it took about fifty years for physicists to theoretically explain this phenomenon and another fifty to be able to see practical and commercial applications.

To date, superconductors are used commercially for various purposes such as MRI⁶ and in natural levitation trains in Japan, but after a general introduction in this chapter there will be a focus on superconducting materials used for nuclear fusion applications.

⁶ Magnetic Resonance Imaging

To understand how much superconductivity is fundamentally different from the normal conductivity of a material, it is enough to think of a cable that carries electric current; after a certain interval of time, depending on the type of material and the current transported, an overheating will occur inside the material due to the Joule effect due to the resistance that the electrons encounter inside the metal during their passage; in the worst case⁷ the current could be so high that the metal could even melt or be irreparably damaged and this situation is called quench which has to be avoided at all costs in a superconductor (explained in details later).

A superconducting metal is ideally capable of carrying electric charges with zero resistance and therefore with zero Joule losses inside the cable.

To function as a superconductor, however, the material must be cooled to a very low temperature, and it is for this reason that the phenomenon of superconductivity was fully studied only after the techniques for cooling to extreme temperatures were refined.

The measurement of temperatures can take place using three scales mainly:

1. Fahrenheit scale: dates to 1724 and is commonly used in the United States.
2. Celsius scale: dates to 1744 and is instead commonly used in Europe.
3. Kelvin scale.

The Fahrenheit and Celsius measuring scales take as their reference temperature the freezing and boiling temperature of water.

During the 19th century, in-depth studies of the state of molecules showed a close correlation between the kinetic energy of molecules and the temperature of the system; leading scholars to the conclusion that the temperature of a system depends on the level of internal energy accumulated in the system itself.

In this regard, the so-called *absolute temperature* was identified: this temperature value corresponds to $-273.15\text{ }^{\circ}\text{C}$ and $-459.67\text{ }^{\circ}\text{F}$ and is the temperature at which all molecular vibrations cease⁸.

⁷ As in case of short circuit

⁸ This temperature is not experimentally achievable as the molecules would tend to no longer oscillate around their position resulting in a cancellation of the mass and in any case there would be the need to use infinite energy to reach this temperature.

The Kelvin scale is nothing more than the Celsius scale but shifted by -273.15 degrees and correspondingly the following fundamental values are found:

1. Absolute zero: 0 K.
2. Water freezing point: 273.15 K.

In this PhD thesis the Kelvin temperature scale will be used as it is more adherent to the scientific literature.

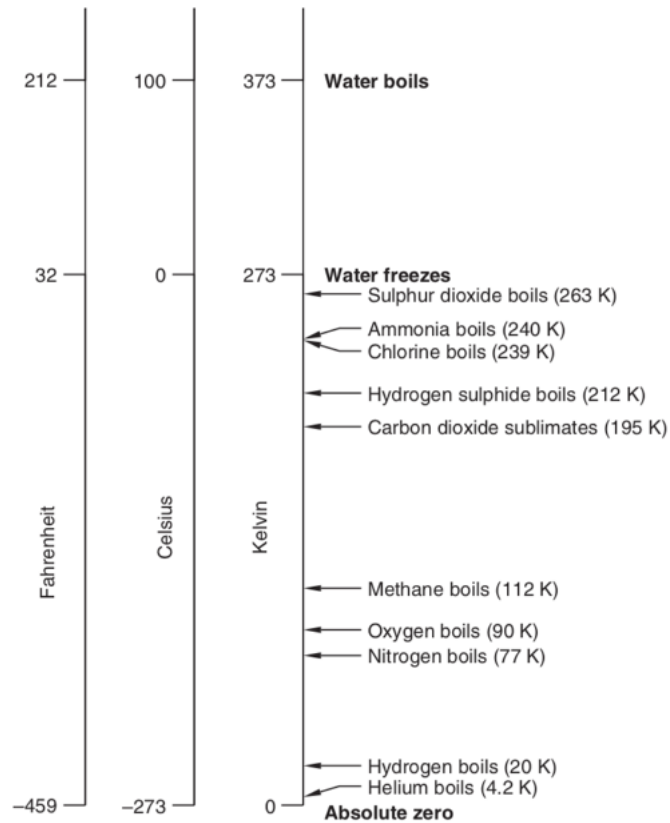


Figure 20: Temperature scales: Fahrenheit (left), Celsius (center), Kelvin (right) [14]

4.2 Superconductor materials' evolution

As explained above, the first experiments on superconducting materials were done by physicist Heike Kamerlingh Onnes; in particular, the physicist discovered for the first time in 1911 that mercury reached the *critical temperature*, or the temperature below which the metal entered a state of *superconduction*, below 4.2 K.

Liquid nitrogen, which boils at 77 K, is the most widespread and economical cryogenic fluid, which would pave the way for most of the hypothesized applications for superconductors. Usually, therefore, this is the temperature that is chosen as the dividing line between high temperature superconductors (called HTS, "High temperature superconductors") and low temperatures (LTS, "Low temperature superconductors") respectively. Most of the known superconductors unfortunately have temperatures far below this threshold.

The following table summarizes some characteristics of various superconducting materials [15]:

Table 1: General review of superconducting materials.

Material	Critic temperature [K]	Comments
Hg	4,2	<i>First discovered superconducting material in 1911.</i>
Nb	9,3	<i>Highest critical temperature between all the elements within atmospheric pressure.</i>
Nb ₃ Sn	18	<i>New type of superconductor that is expected to be used in future magnetic acceleration systems.</i>
Nb-Ti	9,2	<i>It is currently the most widely used alloy for magnetic acceleration systems.</i>
YBa ₂ Cu ₃ O ₇	92	<i>The first superconductor with a critical temperature greater than 77 K.</i>
MgB ₂	39	<i>Discovered in 2001.</i>
ReBCO	90	<i>It operates at temperatures greater than 77 K and can maintain magnetic fields of up to 50 T.</i>

4.3 Necessary conditions for superconductivity

For a specific superconducting material, three parameters can be defined:

1. Critical magnetic field B_{c0} corresponding to zero current and temperature.
2. Critical temperature T_{c0} corresponding to zero current and magnetic field.
3. Critical current density J_{c0} corresponding to zero temperature and magnetic field.

A superconducting material is in the *superconducting state* when the following three conditions are met:

1. The temperature T of the superconductor must be lower than the critical temperature of the material.
2. The magnetic field B of the superconductor must be less than the critical magnetic field.
3. The current density J of the superconductor shall be less than the critical current density.

The BJT surface can be obtained for each superconducting material, and it combines the trend of the three parameters as in Figure 21.

This surface is called a *critical surface* and determines the region of operation of the material as a superconductor; in particular, the material has almost no resistance if it is operating below the critical surface.

An observation that can be made about the figure is that as one of the three parameters increases, there is a decrease in the other two.

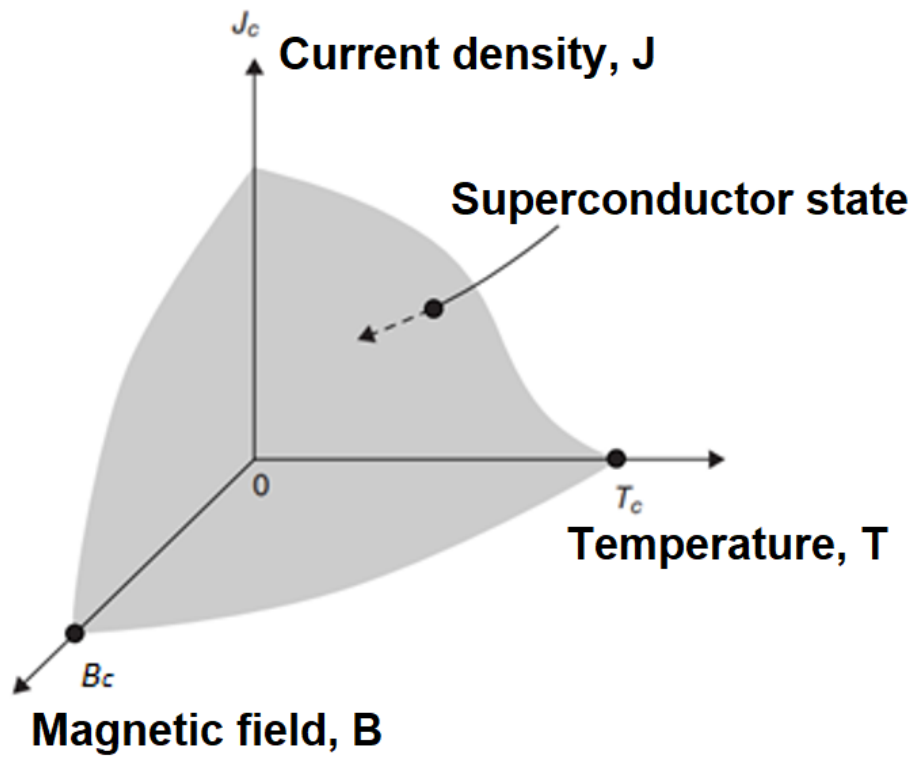


Figure 21: 3D illustration of the superconducting region, where the critical parameters are represented

[16]

4.4 High temperature superconducting materials

Until the 80s, researchers were convinced that superconductivity was a phenomenon related to very low temperatures and that there could be no further hint of application development under different operating conditions.

Following all the research on the new materials it was possible to have a transition from normal behavior to that of superconductor in 1973 with a new metal at a record temperature of 23.2K (Nb₃Ge).

It was later discovered that some minerals had special electrical characteristics such as Perovskite in Figure 22.

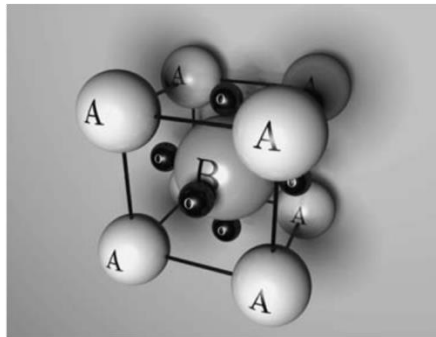


Figure 22: Perovskite structure

This mineral was studied by Karl Alexander Müller and the chemical formula is ABO₃ where A and B are two metals while O is oxygen. As a result of research, it was discovered that strontium titanate (SrTiO₃) if reduced becomes superconducting; in this way the property of superconductivity was also discovered in metal oxides.

Several studies were carried out in the field of oxides with various researchers who followed one another going to discover more and more combinations of elements that brought the transition of the superconducting phase to higher temperatures with possible changes in working pressures (greater than atmospheric ones); for example, an oxide was created with copper whose formula is (La,Ba)₂CuO₄ which had a structure called *layered perovskite*: this oxide could reach the superconducting phase even at 52.5K.

The research continued uninterrupted until the creation of increasingly efficient materials with higher critical temperatures until the record obtained by Mikhail Ermetz at the Max Planck Institute for Chemistry in Mainz (Germany): he, together

with his research group, managed to observe the superconductivity in the decahydrate of Lanthanum (LaH_{10}) with a critical temperature of 250K (-23°C) but at a pressure of 170GPa [17].

High-temperature superconductivity is therefore relative: the goal of the researchers to date is to create materials that can enter the state of superconductivity at increasingly higher temperatures up to the *so-called room-temperature*⁹, so as to be used in civil and industrial environments with very low energy dissipations.

Figure 23 shows the trend of the maximum critical temperatures of the materials over the years.

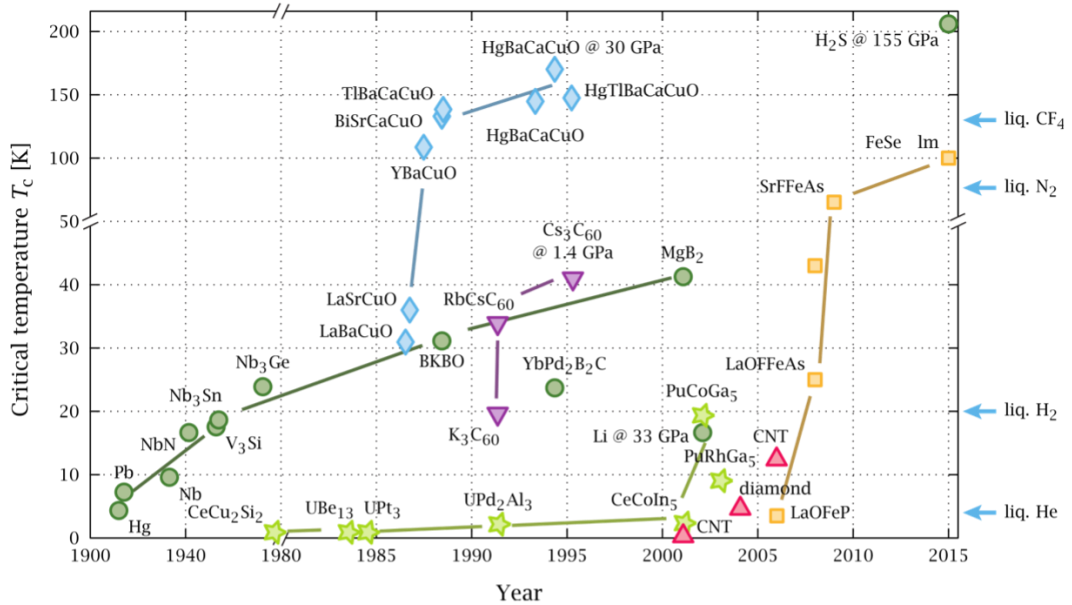


Figure 23: Critical temperature trend as a function of material and year [49]

⁹ Corresponding to the temperature of 300K

4.5 Quench

The quench of a superconducting magnet consists in the overheating of a part of its winding that leads to the loss of superconductivity: when this happens the circulating current is rapidly dissipated in the form of energy by Joule effect and the magnet ceases to work with catastrophic effects on the material itself (breakage and explosion due to the Lorentz forces generated in the transient) and with all the related economic consequences.

What happens then is a local transition from a *superconducting state to a normal state* that is very fast (dependent on the natural frequencies of the *RLC* circuit that is determined) and causes a complete transformation of the magnetic energy stored in the coils into heat. This process is called magnetic *quench*.

However, the superconducting magnet can pass from the superconducting state to the normal state also because of the forces of attraction and repulsion that are generated during normal operation, even small repetitive movements can lead to a temperature increase in the superconductor.

When two conductors are fed by current in fact, there is a mutual interaction of magnetic fields that leads to the attraction or repulsion of the conductors themselves; any movement of the superconductors can raise their temperature to such an extent that it generates, in the worst case, the *phenomenon of quench*.

When this phenomenon occurs there is a current pulse inside the conductor itself which therefore involves a very high heat dissipation, evaporation of the cryogenic fluid and increase in pressure with consequent explosion (in the worst case).

Now it will be described this phenomenon in more details as explained above and in accordance with *Ampere's Law* there is a certain current value that determines an induced magnetic field greater than the critical magnetic field.

The minimum amount of energy to create a *magnetic quench* is conventionally called **Minimum Quench Energy (MQE)** and, logically, the larger this energy is, the more stability the superconductor will be.

Another fundamental parameter for the study of quench is the so-called **Normal Zone Propagation Velocity (V_{nzp})**: this parameter allows to evaluate the speed of the displacement of the border zone between *the normal zone* and *the superconducting zone*.

to safeguard the integrity of the Tokamak and superconductors. In this case the so-called *FDU (fast discharge unit)* systems intervenes, which is basically made up of resistors to allow the discharge and rapid dissipation of energy; these systems covered by the doctorate research will be treated in more detail in the following chapters and their structure and the studies that have been conducted in 3 years will be explained extensively.

As mentioned above, the superconductor goes out from the superconducting zone when one of the three parameters (temperature, current density, or magnetic field) exceed the critical value.

In the case of quench, the zone that has returned to the normal conduction state must dissipate all the heat stored in the magnet in the form of magnetic energy in heat; this energy is calculated as $E = \frac{1}{2}LI^2$.

The possible causes of quench can therefore be summarized below:

1. Material degradation
2. Superconductor Training
3. Creation of hotspots

One of the fundamental parameters of the quench is the so-called *Normal Zone propagation Velocity*, it is to be considered as the propagation speed of the normal conduction zone inside a magnet in a superconducting state and is given by (assuming adiabatic conditions) [19]:

$$V_{nzp} = \frac{I_{op}}{C_0} \sqrt{\frac{\rho k}{(T_t - T_{op})}}$$

Where:

1. I_{op} is the operational current
2. C_0 is the heat capacity of the material expressed in $\left[\frac{J}{mK}\right]$
3. ρ is the electrical resistivity
4. k is the thermal conductivity of the material
5. T_t is the temperature at which the transition from the superconducting state to the normal state takes place
6. T_{op} is the operating temperature of the superconductor

The other fundamental parameter for the study of quench is the *Minimum Quench Energy* which can be estimated starting from the minimum propagation zone indicated by l_{mpz} and it is calculated as follows:

$$l_{mpz} = \sqrt{\frac{2k(T_t - T_{op})}{I_{op}^2 \rho}}$$

The Minimum Quench Energy (MQE) is therefore the minimum energy that must be accumulated inside the superconductor to increase its temperature above the transition temperature threshold in each section of the material corresponding to the minimum propagation zone. It is given by:

$$MQE = l_{mpz} \int_{T_o}^{T_t} C(T) dT$$

Where $C(T)$ is the heat capacity of the material dependent on the temperature of the conductor.

4.6 Use of superconductors

4.6.1 Magnetic Resonance Imaging

Superconducting magnets find their most important application in the field of medicine, in particular in the field of MRI.

The original name of this technique was *Nuclear Magnetic Resonance*, but it was later changed to *Magnetic Resonance Imaging* to arouse less fear in the public.

The basic principle of operation of this technique is precisely related to the interaction between the magnetic field generated and the water present in the body: in particular, the hydrogen atoms¹⁰ enter into resonance with the oscillating magnetic field produced by the source and produce energy that can subsequently be detected thus providing biological information.

An MRI scanner requires a magnet of modest size with a magnetic field as homogeneous as possible and in such a way that the patient or the area to be examined enters it completely; the magnets used are just superconducting magnets.

The patient is inserted inside the magnet that has been excited to produce a magnetic field of even 2T variable over time.

4.6.2 Particle accelerators

Since the 1970s, superconducting magnets have been used for the construction of particle accelerators.

The main purpose of such superconducting magnets is to divert the flow of particles accelerated at very high speeds precisely by making them interact with the magnetic field produced.

One of the most famous applications of these systems is the LHC system present at CERN in Geneva which, at the time of writing this paper, is being maintained for an enhancement in view of a future project or the so-called HL-LHC.¹¹

The tunnel for the particle accelerator in Geneva has a circumference of 27 km and is buried in the France-Switzerland border.

¹⁰ Which are nothing but protons.

¹¹ High-Luminosity Large Hadron Collider

To force the particles to curve inside this tunnel, 1,232 superconducting magnets were built each 15m long and weighing 35 tons.

Each magnet contains cables consisting of a Niobium-Titanium (NbTi) alloy cooled to a temperature of 1K.

About 100 tons of liquid helium are used for the cooling circuit, and superconducting magnets carry about 10,000A of current [14].

4.6.3 Energy Storage systems and transports

Today's society is extremely dependent on the continuous need for electricity.

Until a few decades ago, the production of electricity took place centrally in strategic points in the area and then transmitted through transmission and distribution networks to users; as is well known, in recent years the so-called *smart grid* configuration has been increasingly affirmed which implies the presence of many sensors distributed along the grid for a better distribution of electricity that is now also produced by small local generators.

A first possible application of superconducting materials could be in transmission and distribution cables but the continuous need for cooling (although with new materials there is no need to reach temperatures close to absolute zero) would require excessively high maintenance costs; a similar argument can be made about the use of superconducting cables inside the transformers: surely there would be less losses due to the Joule effect but the problem of cooling at extreme temperatures would always be present.

A possible application in the field of electricity is that of the so-called SMES: the principle of operation underlying these systems is relatively simple as it consists in accumulating energy in the form of magnetic energy within an inductance and then extracting it at the time of need; one of the advantages of these systems is the almost total absence of losses due to the Joule effect for the reasons mentioned in the previous paragraphs.

Other applications are those of the so-called *flywheels*: they are systems that rotate at very high-speed storing kinetic energy and not from the magnetic point of view as for SMES; to work correctly, these systems need frictionless bearings and this is where superconducting magnets come into play by exploiting the levitation principle due to the Meissner effect.

The Meissner effect is a phenomenon by which the superconducting material, when cooled to its critical temperature, begins to emit outside a magnetic field equal to that accumulated before entering a state of superconduction [20].

The principle of magnetic levitation is also used in levitation trains in Japan; these trains exploit this principle to eliminate the friction of the rails and with a particular wagon design to also reduce friction with the air. For these reasons these trains such as the *Japanese Maglev* can reach record speeds such as $600 \frac{km}{h}$ [21] .

4.6.4 Nuclear fusion

Another application of superconducting magnets certainly of great importance, especially in the last period, and which is also the purpose of this work is certainly that of nuclear fusion.

In this paragraph there will be simply a general information about a nuclear fusion reactor which is composed of several magnets, the number of which varies depending on the geometry considered and the type of operation that is envisaged and can be grouped into 3 main typologies: toroidal field coils (TF coil or TFCs), poloidal field coils (PF coil or PFCs), central solenoid (CS).

These types of magnets listed above are those that are used for a nuclear fusion reactor ITER-like and therefore should not be considered as a single structure for any type of reactor.

Construction characteristics, function, and type of operation of these superconducting magnets are already described in previous sections.

5 Existing Tokamaks

5.1 Introduction

In this section is not possible to report and describe all the *tokamaks* currently existing and in operation.

To avoid going too far on the description of nuclear fusion reactors that are significantly different from DTT or that in any case are little correlated from the point of view of design and technical choices, there will be a briefly description of JT-60SA (Japan), FTU (Italy), JET (UK), ITER (France), DEMO (TBD), DTT (Italy).

To have a more detail on the research activity carried out on DTT, ITER and DEMO during the PhD, please refer to the following chapters.

The reader should note that describing all those tokamaks in every single detail could be really complicated so in the next pages there is a general description of the component and its general scope.

5.2 JT-60SA

JT-60SA is an international nuclear fusion experimental reactor being built and operated by Japan and Europe in 那珂市 (Naka, Japan) using infrastructure of the previous JT-60 Upgrade experiment alongside new hardware. (“JT-60SA”)

JT-60SA stands for “JT-60 Super Advanced” since the experiment has superconducting coils to study advanced mode of plasma operations.

Main target of JT-60SA is to support ITER operation by following a complementary research and development program and to investigate how best to optimize the operation of fusion power plants that are built after ITER.

5.2.1 Research plan

When fully operational, JT-60SA will be able to sustain a plasma reaction temperature per 100 s (for a maximum current of 5.5 MA) with the following targets identified in Figure 25 where:

- $n_D(0)$ is the plasma central ion density.
- τ_E is the energy confinement time.

- $T_i(0)$ is the plasma central ion temperature.
- β_N is the normalized beta: the ratio of plasma kinetic pressure to magnetic pressure, multiplied by the product of minor plasma radius and toroidal magnetic field at the plasma center, and divided by the plasma current in MA [22].

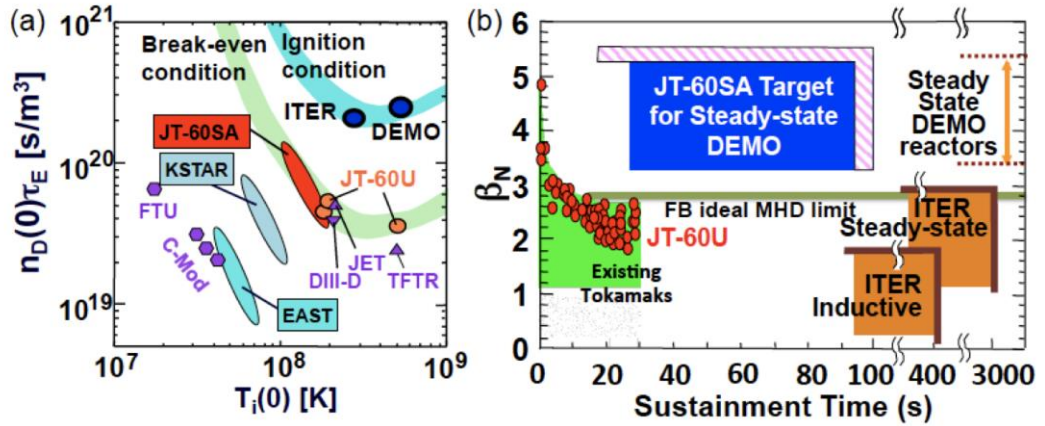


Figure 25: Target regimes of JT-60SA [23]

JT-60SA mission is to be first achieved with carbon components facing the plasma; once the integrated plasma control systems are sufficiently mature, the divertor target and the first wall will be replaced by tungsten-coated carbon.

In this environment, JT-60SA will support ITER by providing experimental data also suitable for the extraction for DEMO.

JT-60SA supports the exploitation of ITER and complements ITER in resolving key physics and engineering issues for DEMO reactors.

The main targets of JT-60SA are summarized as follow [23]:

1. Operation Regime Development

1.1 For ITER and DEMO

- 1.1.1 Identification of operational boundaries, control margins, plasma responses, suitable control logic and demonstration of the real-time control in long pulse discharges exceeding the longest time scale governing the plasma system.
- 1.1.2 Controllability of plasma equilibrium including recovery plasma events.
- 1.1.3 To carry out the previous studies at ITER and DEMO relevant parameter regions of low collisionality, small gyro radius, dominant electron heating, low external torque input and low central fueling.

1.2 For ITER

- 1.2.1 Demonstration of the required integrated performance of H-mode with the ITER-like plasma shape at high plasma current (4.6 MA, $q_{95} \approx 3$)¹² and high density ($1 \times 10^{20} m^{-3}$) by applying the plasma control techniques planned in ITER such as pellet injection, divertor pumping etc.
- 1.2.2 Demonstration of advanced inductive operation in improved H-mode at plasma current of 3.5 MA and $q_{95} \approx 4$ to contribute to the hybrid operation of ITER and provide the Q=10 alternative scenario.
- 1.2.3 Study of operational boundaries such as the stability limit and density limit and determination of control margins for the plasma.

1.3 For DEMO

- 1.3.1 Exploration and demonstration of integrated performance in steady state at high values of β_N
- 1.3.2 Determination of operational boundaries and control margins.
- 1.3.3 Study of the self-regulating combined system and development of a suitable control system for the plasma described in 1.3.1 with a minimum set of actuators and diagnostic.
- 1.3.4 Development of non-inductive current ramp-up schemes for minimization of required poloidal flux.
- 1.3.5 Validation of integrated modeling codes for prediction of Q>10 high beta high bootstrap fraction plasmas.

2. MHD Stability and Control Studies¹³

3. Confinement and Transport Studies

4. High Energy Particle Studies

5. Pedestal studies

6. SOL, Divertor and Plasma-Material Interaction Studies

¹² A magnetohydrodynamic safety factor describing the number of times field lines need to pass round the major circumference of the plasma before they close around the minor circumference:

$$q = \left(\frac{R}{a}\right) \left(\frac{B_T}{B_P}\right).$$

¹³ MHD=Magnetohydrodynamic

5.2.2 Magnet system

The superconducting coil system of JT-60SA consists of [24]:

- 18 $NbTi$ toroidal field coils TFC.
- 1 Nb_3Sn central solenoid CS made from 4 coil modules.
- 6 $NbTi$ equilibrium field coils EF.
- Other components as coil feeders and current leads.

In the next figures there are the TFC, EF and CS then all displayed in one picture [24]:

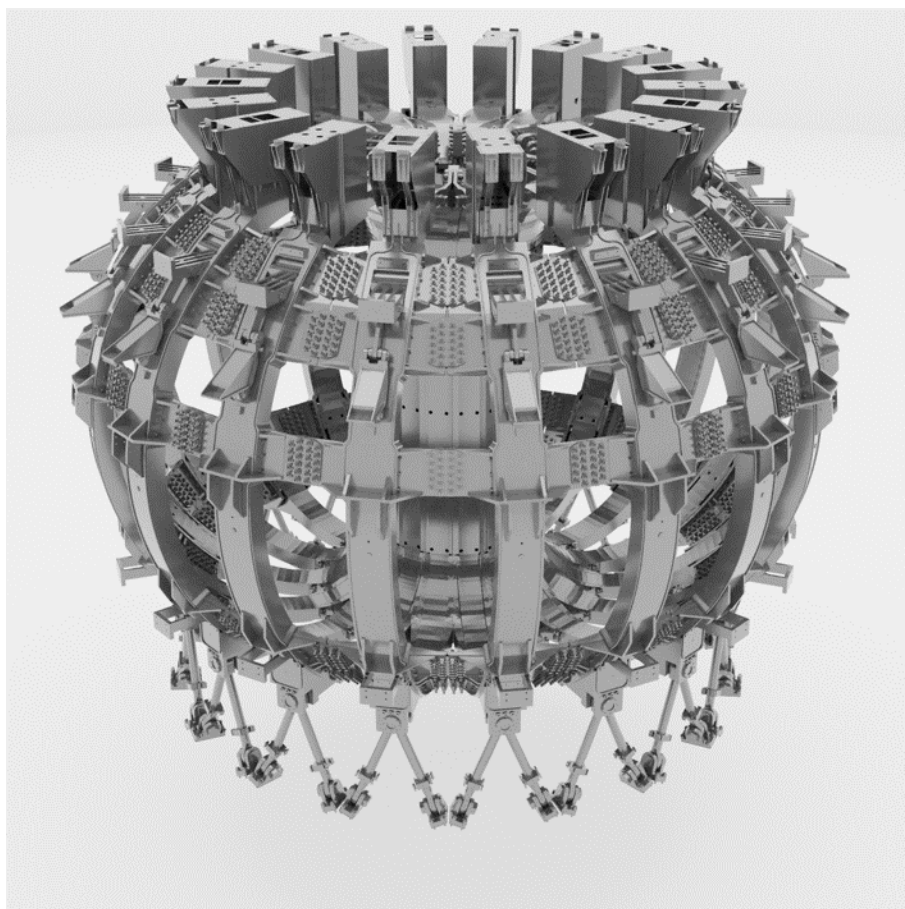


Figure 26: JT-60SA TFCs

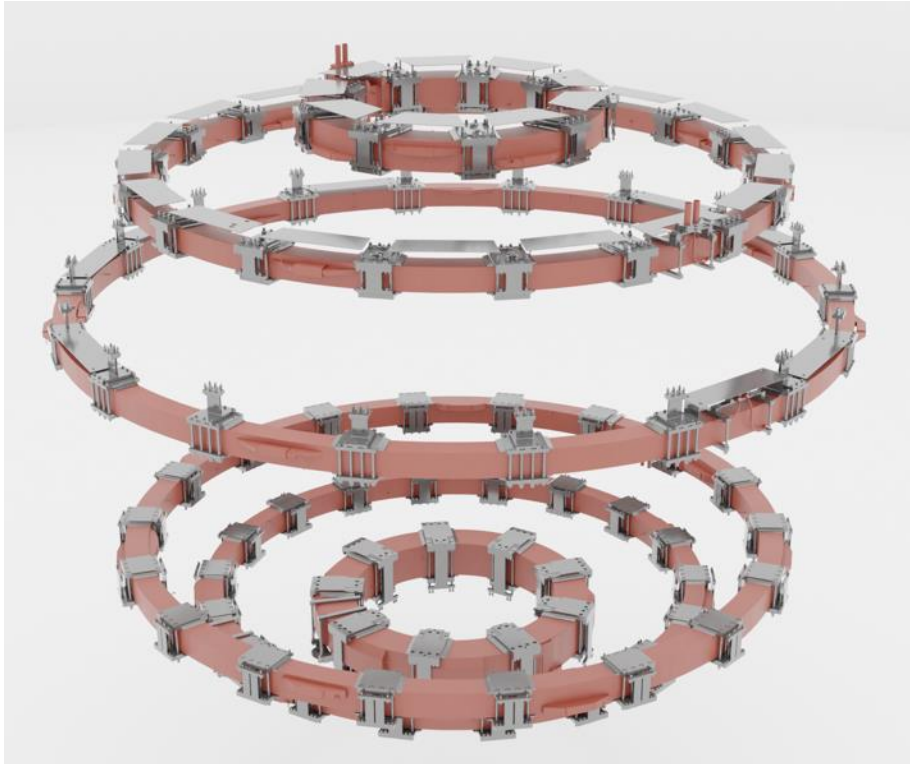


Figure 28: JT-60SA EFs

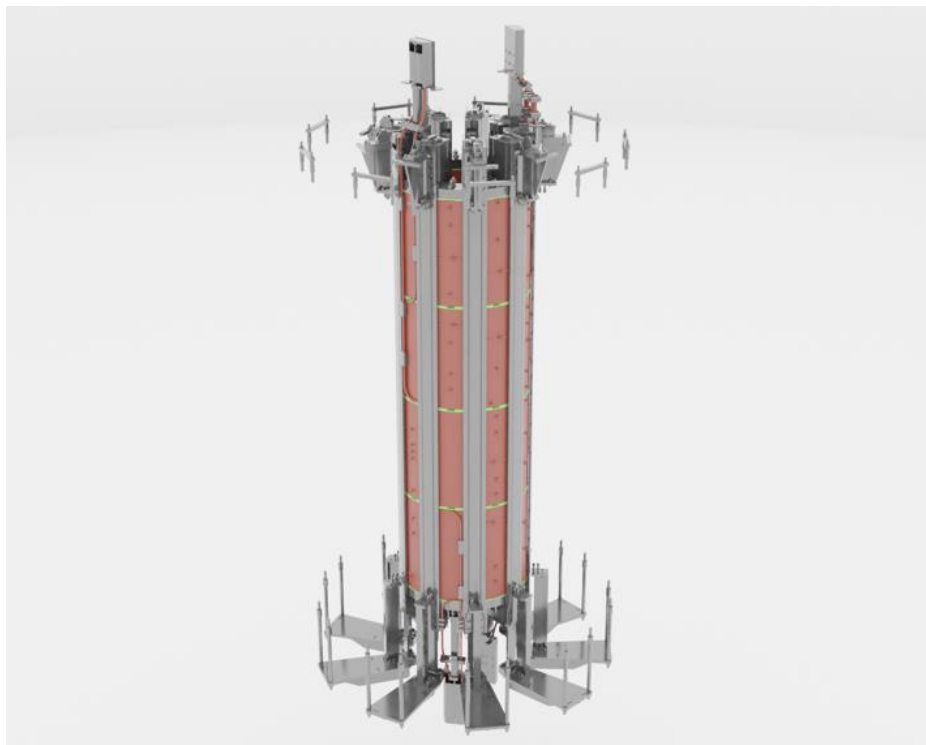


Figure 27: JT-60SA CS

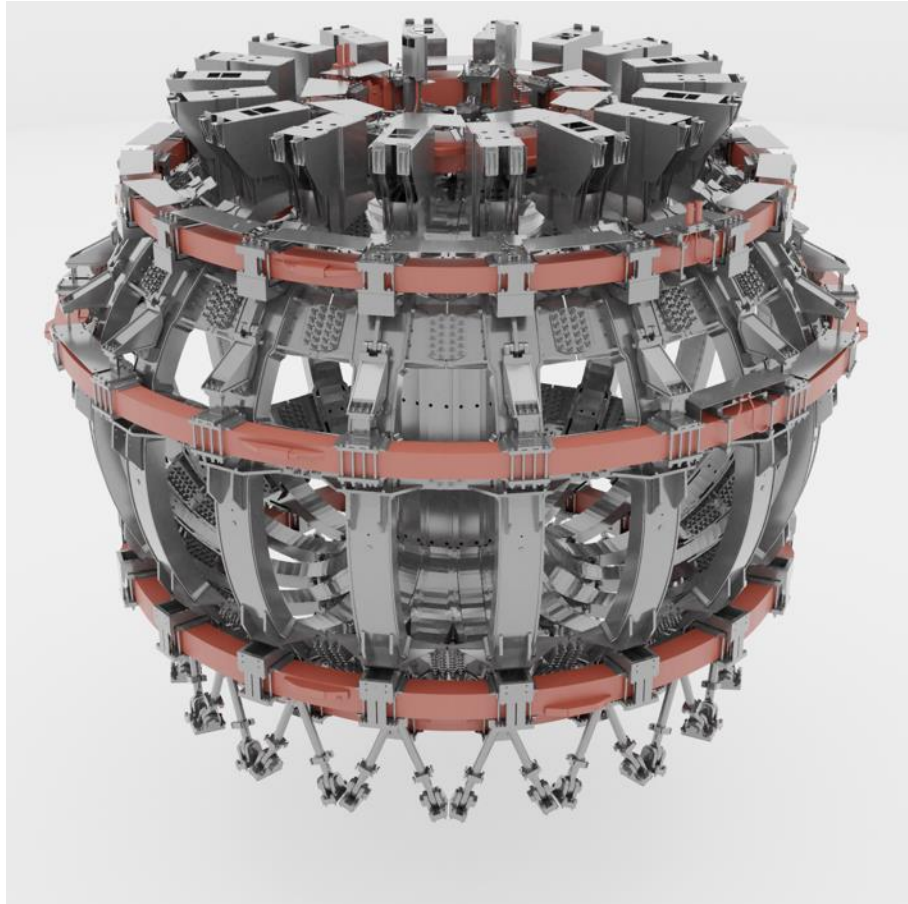


Figure 30: JT-60SA Total Magnet System

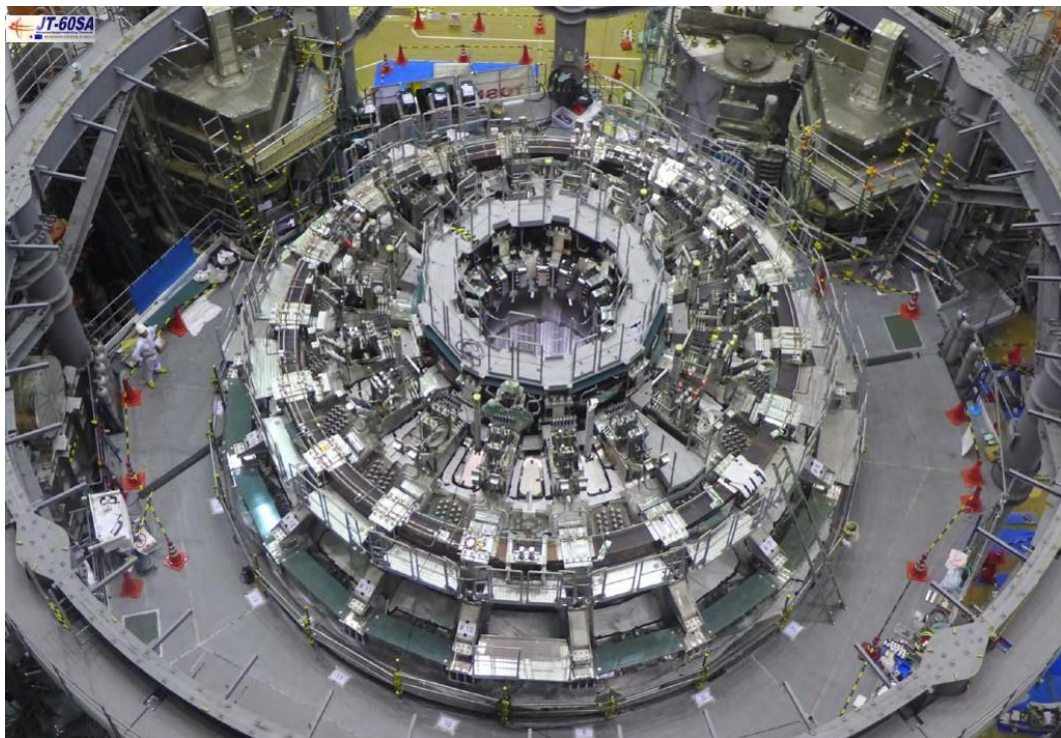


Figure 29: JT-60SA Magnets system top view

The D-Shaped TFCs were wound by ASG (Genoa, Italy) and Alstom (Belfort, France) from a square steel-jacketed NbTi cable-in-conduit conductor made by ICAS (Frascati, Italy) using strand made by Furukawa Electric of Nikko.

The winding pack is inserted in a stainless-steel casing, machined, and assembled by Walter Tosto (Chieti, Italy) with additional cooling channels to aid magnet cool-down.

The CS uses a conductor like that used for ITER and an identical strand for the ITER TF conductor. The conductor is a circular Nb_3Sn cable in square conduit cooled by supercritical helium. The EF coil conductor is a circular NbTi cable in square conduit cooled by supercritical helium. (“Magnets – JT-60SA”)

5.2.3 Vacuum Vessel

The main JT-60SA vacuum vessel is torus-shaped and double-walled. The space between the walls is filled with borated water during the operation to enhance neutron shielding of the vacuum vessel and the coolant will operate at 50°C approximately.

There is also the need to sustain the vessel and to protect it against electromagnetic forces and thermal expansion, for this reason every 40° is installed a gravity support with spring plates at the bottom of the vessel.

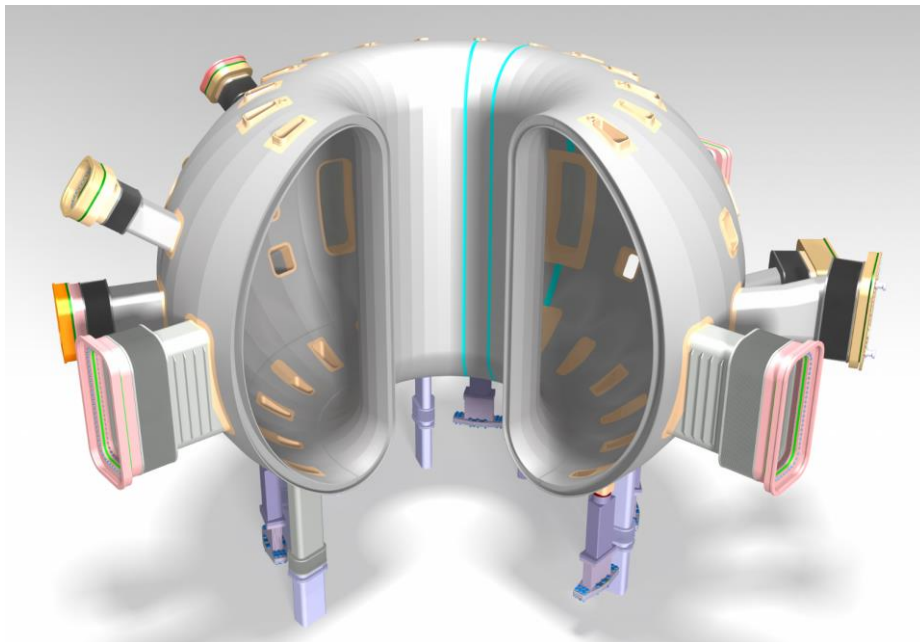


Figure 31: JT-60SA Vacuum Vessel [24]

5.2.4 Thermal Shield

The thermal shield is used to prevent the heating of the superconducting magnets due to radiation from the cryostat and from the vacuum vessel.

The thermal shield consists of 18 segments electrically insulated from each other to prevent excessive electromagnetic forces during disruptions.

The thermal shield is supported by TF coils, between EF coils 5 and 6 and at the top on alternate TF coil casings.

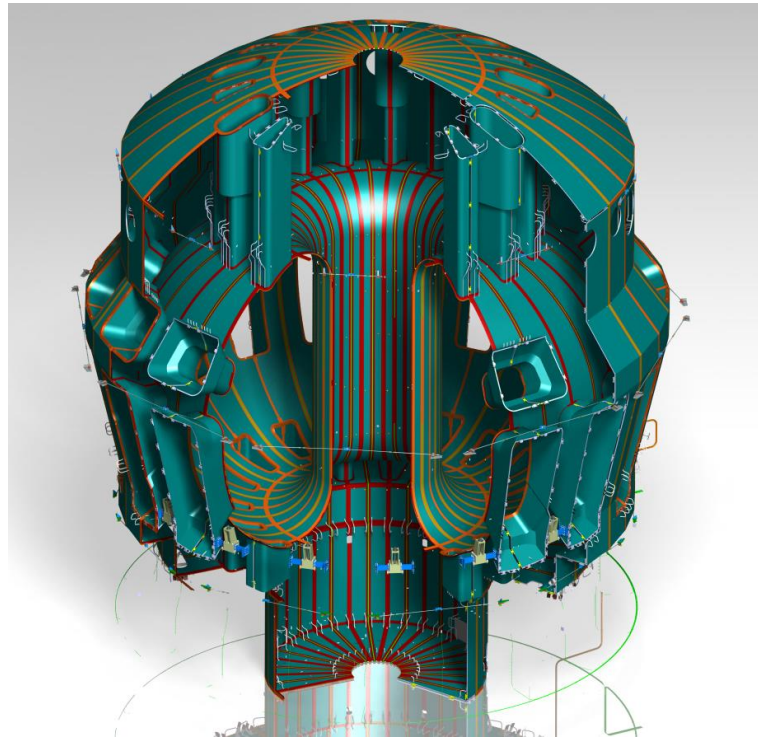


Figure 32: JT-60SA Thermal Shield [24]

5.2.5 In-Vessel components

The major in-vessel components can be described as follow:

- Divertor cassettes,
- Inboard first wall,
- Stabilizing baffle plate and outboard first wall,
- Fast plasma position control coils,
- Sector coils for resistive wall mode (RWM) control,
- Magnetic diagnostic coils,
- Error correction coils,

- Cryopanel for particle pumping.

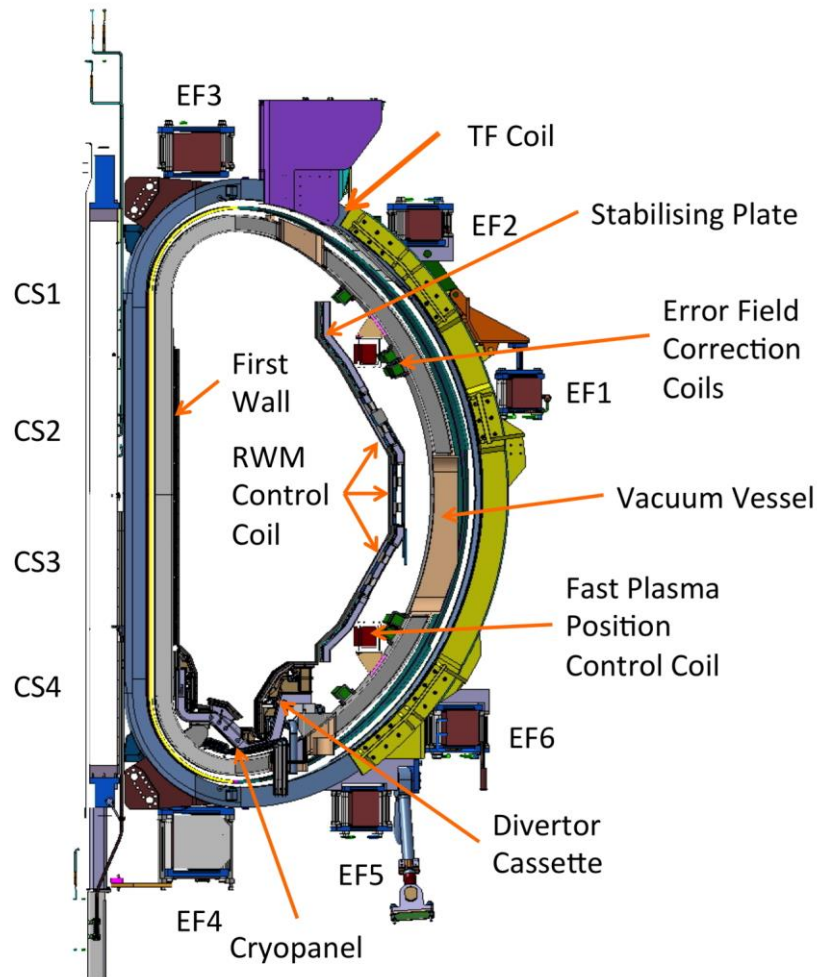


Figure 33: JT-60SA Section with in-vessel components [24]

For the first experimental phase only a lower divertor has been installed optimized for ITER-shape plasma and a second upper divertor will be installed at the extended research phase.

All the plasma facing components for the lower divertor are water-cooled for high-power and long-pulse heating and in the future some divertor cassettes with integrated coolant pipes for the plasma facing components will be introduced (they are designed as replaceable modules).

In the figure above are also represented the Cryopanel which focus is to improve pumping capability of the particles.

The stabilizing plate is used to enhance the ideal *beta limit* and to improve plasma positional stability (rather than protecting the first wall); those plates have a

thickness of 10 mm each and a rigid support with trusses to provide adequate strength against electromagnetic forces originating from eddy currents.

The Fast Plasma Position Control Coils consists of two circular normal-conducting coils (upper and lower) which can provide independent control of vertical and horizontal field. The maximum operating current is 5 kA for a period of 25 s [24].

The Error Field Correction coils are manufactured and assembled with finite tolerances, so those variations between the construction of one coil and another one can lead to asymmetric components of the magnetic field (so called error fields); to avoid destabilization of the plasma, Error field correction coils are installed on the vessel surface behind the stabilizing plate.

The Divertor Cryopumps, finally, are installed to evacuate neutralized hydrogen or deuterium fuel, seeding gases (N_2 , Ar). There are 9 cryopumps in total located in the volume underneath the divertor dome and each cryopump is made up by adsorption surfaces called Cryopanel cooled by 3.7 K supercritical helium and a thermal radiation shield surrounding the Cryopanel cooled at 80 K.

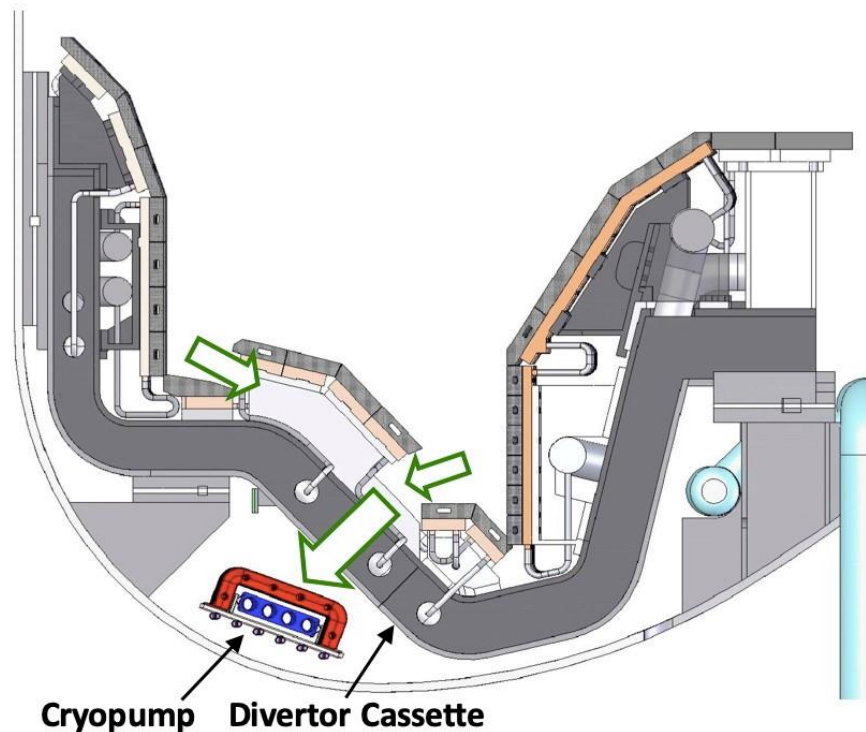


Figure 34: Cryopump under the Divertor Cassette in JT-60SA [24].

5.2.6 Cryostat

All the in-vessel components are kept under vacuum, this situation around the cold magnet components is kept by the cryostat to minimize the thermal load.

In JT-60SA the cryostat is a cylinder of about 14 m of diameter and 15.5 m high made up with 30 mm single walled stainless steel [24].

It is possible the access inside the cryostat to remove or reinstall the central solenoid, maintenance, and inspection purpose.

The cryostat is designed as a robust structure to support the whole weight of the superconducting magnets, thermal shield and vacuum vessel including in vessel components as well as thermal stress, standard operational conditions, accidental overpressure, and seismic loads.

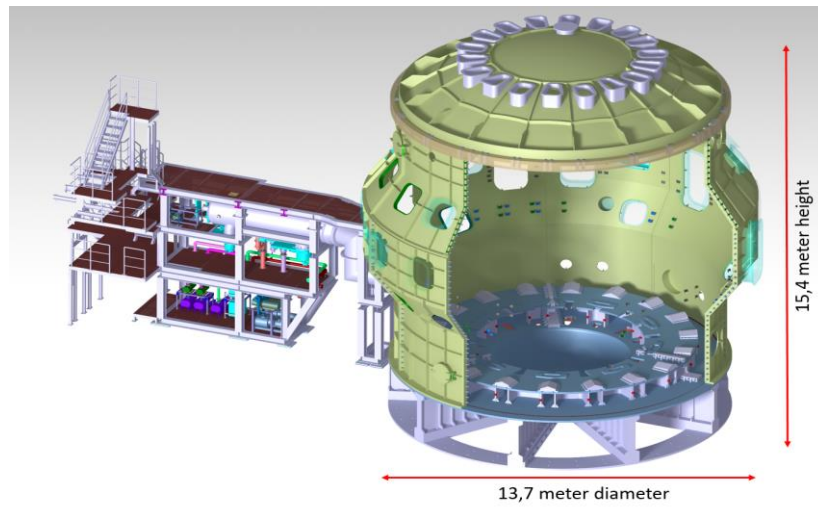


Figure 36: JT-60SA Cryostat [24].



Figure 35: JT-60SA Cryostat real view [24]

5.2.7 Magnet Shared Components

These components provide the interface between the magnets and their services (cooling, power, and instrumentation) and are often a common design for all the magnet systems. The magnet shared components can be listed as follow:

- Current feeder lines and structural support,
- Cryogenic supply lines including cryostat feedthroughs, servicing the conductors, magnet structure or feeders,
- Current leads connecting coil conductor and feeder lines,
- Coil terminal boxes and cryogenic valve boxes,
- Quench relief valve assemblies
- Instrumentation, cabling and control cubicles.

The TFCs use three separate power supplies, each one feeding six coils while the four CS and the six EF have one power supply each; all the coils use high temperature superconductor HTS at a rated temperature of 50 K to connect the power supplies.

5.2.8 Auxiliary Plant – Heating

JT-60SA uses a 34 MW neutral beam heating (NB) and up to 7 MW of electron cyclotron range of frequency heating system (ECFR).

The main purpose of the NBI is to heat up the central region of the plasma with high density with a dominant electro heating fraction, which is relevant to ITER and DEMO plasmas heated by alpha particles.

5.2.9 Auxiliary Plant – Power Supply

For JT-60SA most of the pre-existing equipment has been re-used where possible on a rearranged AC supply network.

5.2.9.1 Toroidal Field Coil Circuit

The TFC circuit is composed by 18 superconducting coils connected in series and supplied by a single unidirectional AC/DC converter called TF converter. The 18 coils are divided into three groups of six coils interleaved with 3 quench protection circuits to ensure the protection of the superconducting magnets in case

of faults or quenches by actuating a fast discharge of the coils; it should be seen that this type of configuration is also used for the design of DTT in Italy.

The operation of the TFC power supply is that the TF coils are energized every day in the morning before the start of the plasma experiments and discharged at the end of the day; the maximum time of ramp-up and ramp-down of the nominal current is 25 minutes and in case of quench there is the intervention of a component called Fast Discharge Unit (FDU) which is also the main studied component during the PhD Course in all its aspects which will be described more in detail in the dedicated chapter; for JT-60SA in case of quench the current is rapidly decreased to 0 A with the operation of the Fast Discharge Unit (which are called Quench Protection Circuit for JT-60SA) by dissipating the magnetic energy (more than 1 GJ) stored in the TFC with a maximum specific energy through of $4.6 \text{ GA}^2\text{s}$.

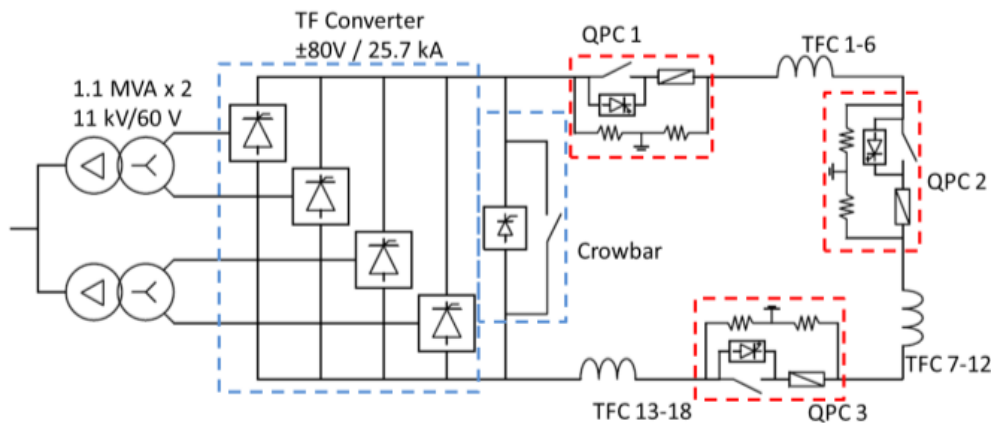


Figure 37: Toroidal Field Circuit with Power Supply [24]

5.2.9.2 Poloidal Field Coils Circuit

In JT-60SA, as described in previous sections, is composed by 4 CS (CS1-4) and 6 external Equilibrium Field Coils (EF1-6).

Regarding the power supply, the main components of each PF coil circuit are a *base converter*, *switching network unit (SNU)* or *booster converter* and a *poloidal QPC*.

The base converter has a rated current of $\pm 20 \text{ kA}$ with a duty cycle of 220 s / 1800 s and a nominal voltage of 1 kV.

The SNU can generate up to a maximum voltage of -5 kV by inserting a breakdown resistor in the circuit when a nominal current of 20 kA is flowing.

The booster converter has a rated voltage of $\pm 5 \text{ kV}$ with a current rating of $+4 \text{ kA} / -14.5 \text{ kA}$.

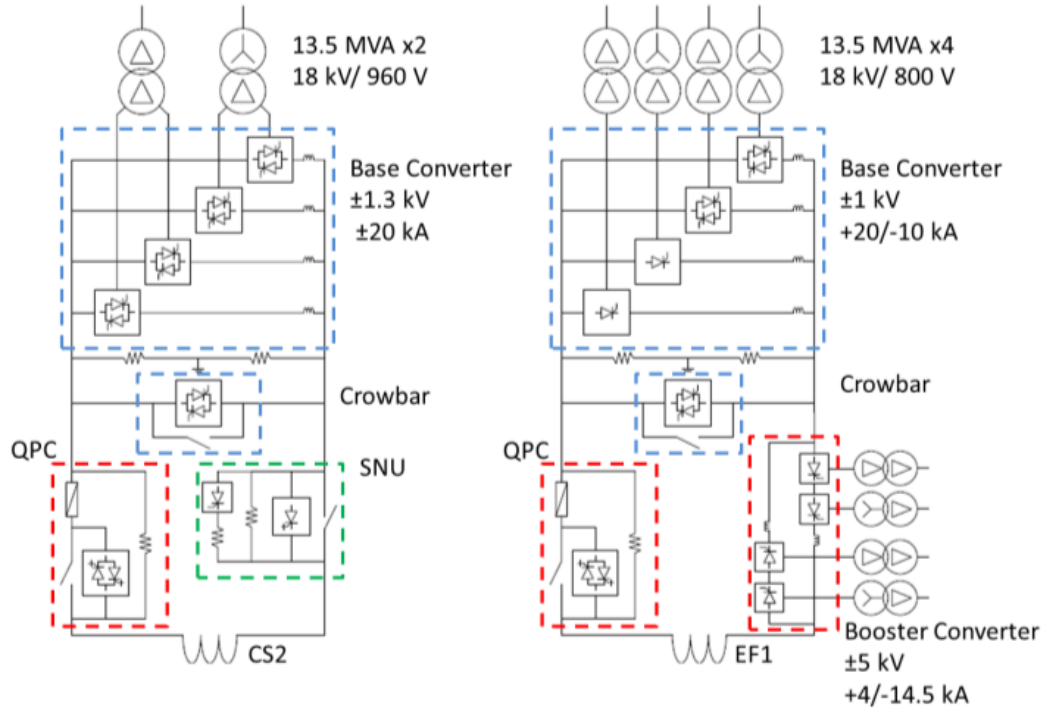


Figure 38: Poloidal Field Coil Circuits (CS2 and EF1) [24]

5.2.10 Auxiliary Plant – Cryogenics

The cryogenic systems supply the helium at different temperatures to cool down all the required components to their nominal steady state temperature, in particular the cryogenics supplies:

- The Thermal Shield (TS) is kept at a temperature between 80 K-100 K with a pressure of 15 bar.
- The HTS current leads (CL) which conduct the ambient temperature busbars to the low temperature superconducting coils are kept to a temperature of 50 K and a pressure of 4 bar.
- The superconducting magnet system composed by TFC, EF, CS are kept at 4.4 K and 5 bar of pressure.
- The divertor cryopumps are cooled at 3.7 K.

The main components of the Cryogenics system are listed as follow:

- A system of 8 parallel warm screw compressors with sound protection, a common oil and water removal system, pressure control and a gas management system.
- A refrigerator cold box with the main heat exchangers.
- An auxiliary cold box including a 7000 l liquid helium damper to absorb the pulsed heat loads during plasma operation.
- Gas storage and distribution system comprising six warm helium storage vessels with a total volume of 1500 m³, a liquid nitrogen storage, cryogenic transfer lines and a warm interconnecting pipework.
- Auxiliary equipment like cooling towers.

5.2.11 Auxiliary Plant – Cooling System

The in-vessel cooling system of JT-60SA is designed to handle the maximum plasma heating power of 41 MW for 100 s.

The cooling of the vessel is carried out by borated water coolant to have the maximum neutron shielding and the secondary water-cooling system serves all the primary cooling circuits throughout the plant including the vessel, magnets, heating, and diagnostic systems.

The system consists of a succession of heat exchangers and a pumped circulation system and at the end of the circuit wet cooling towers exchange heat with the atmosphere.

5.2.12 Auxiliary Plant – Control System

The supervisory control system and data acquisition system (SCSDAS) has the following functions:

- Plant monitoring,
- Discharge sequence management,
- Plasma real time control,
- Device protection,
- Discharge result data archive, storage, and database management.

Configuration of SCSDAS



SCSDAS have several types data and signal communication lines, such as **HMI-Network (TCP/IP)**, **CS-Network (TCP/IP)**, **reflective memory data communication for real-time, timing signals, and interlock signals.**

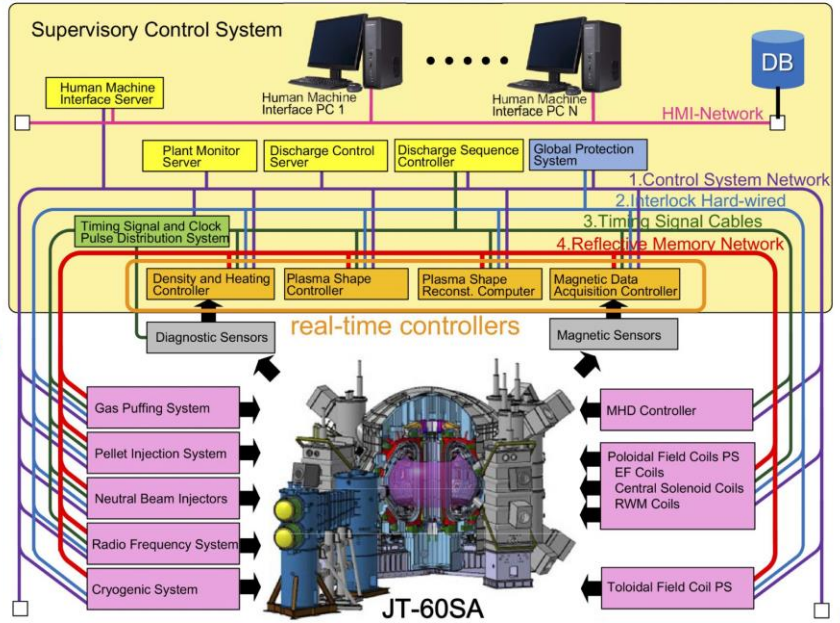


Figure 40: Configuration of SCSDAS for JT-60SA [24].

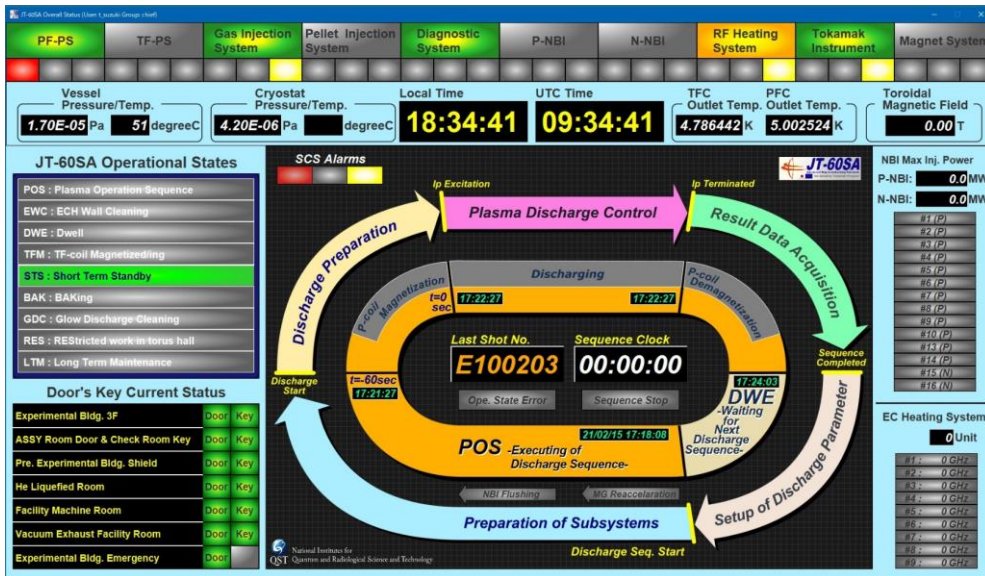


Figure 39: JT-60SA Overall Status Monitor [24].

5.3 JET

5.3.1 Research Plan

JET (Joint European Torus) is located at Culham Centre for Fusion Energy in Oxfordshire in UK and at the time of the construction it was the bigger tokamak in the world.

JET began operation in 1983 and it was built with the aim of reaching fusion energy gain factor $Q=1$.

The main features of JET can be listed as follow [25]:

- A flexible and powerful plasma auxiliary system consisting of Neutral Beam Injection (NBI) of 34 MW, Ion Cyclotron Resonance Heating of 10 MW and Lower Hybrid Current Drive of 7 MW.
- An extensive diagnostic suite of around 100 individual instruments capturing up to 18 gigabytes of raw data per plasma pulse.
- A high frequency pellet injector for plasma refueling and for ELM pacing studies.
- A massive gas injection valve for plasma disruption studies.
- Capabilities to operate with tritium fuel.
- Beryllium handling facilities, allowing use of beryllium plasma-facing components.
- Remote handling facilities that allow advanced engineering work to be performed inside the vacuum vessel without the need for manned access.

In the following list there are the main components of JET:

- Vacuum vessel made by stainless steel sections with a weight of 80 tons.
- 32 TFCs made of water-cooled copper conductors of 380 tons.
- PFCs made of water-cooled copper of 80 tons. It should be noted that in JET there are also the CS but they are called Internal PFCs.
- Power Supplies are a combination of power from the network and motor generator flywheels sets.

- The additional heating is provided by Neutral Injection, Radio Frequency Heating and Adiabatic Compression.
- The Control Circuit and Diagnostics is linked to computers for fast feedback control of the plasma.

5.3.2 Magnet System

On JET, the toroidal field is produced by 32 identical coils evenly distributed around the torus to have maximum uniformity on the field; the set of coils can maintain a magnetic field up to 3.4 T between 10 s and 20 s once every 10 minutes with a nominal current of 66 kA [26].

Each coil is made up of 24 turns of heavy copper bar insulated with glass tapes and vacuum impregnated with epoxy resin.

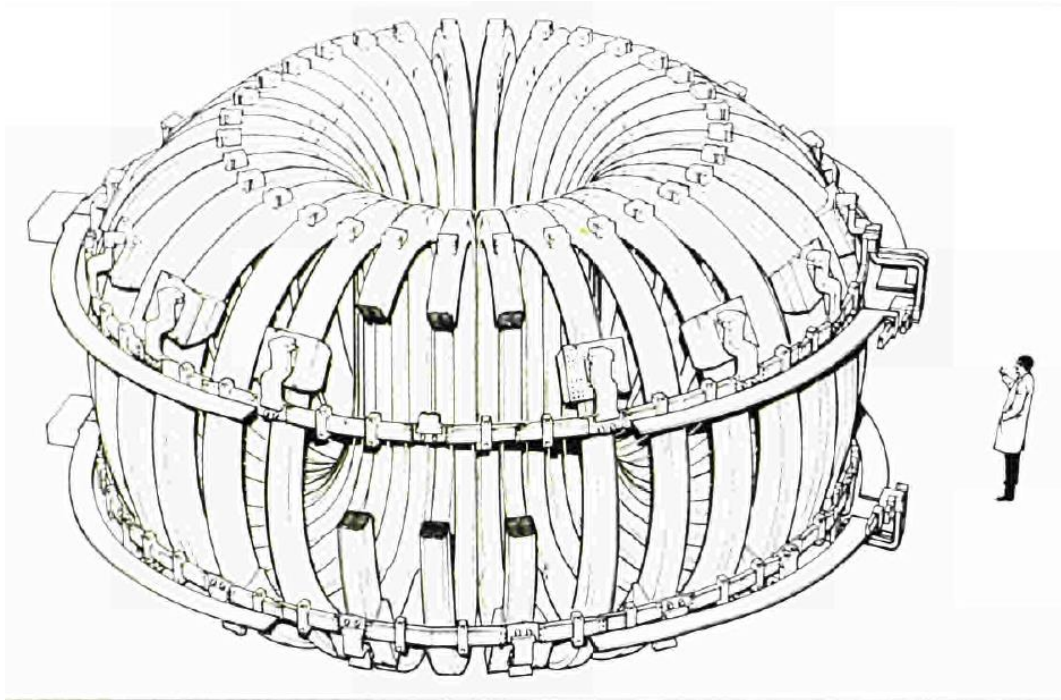


Figure 41: JET TFCs [26]

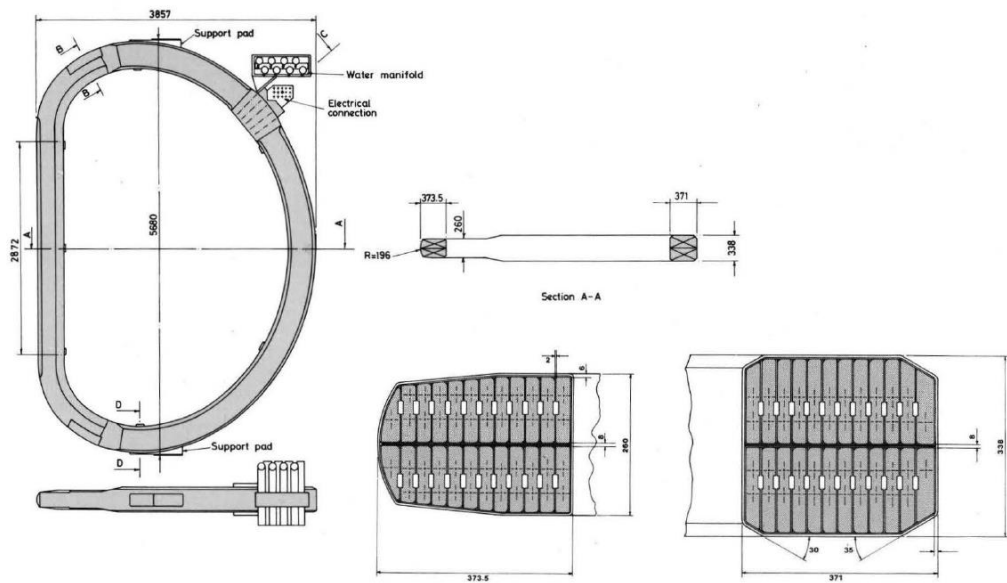


Figure 42: Detail on one TFC of JET [26]

The PFCs in JET are 6 with different nominal current between 40 kA and 45 kA and it contributes as described in the previous Sections to create the plasma inside the vacuum chamber between 2.6 MA and 4.8 MA [26].

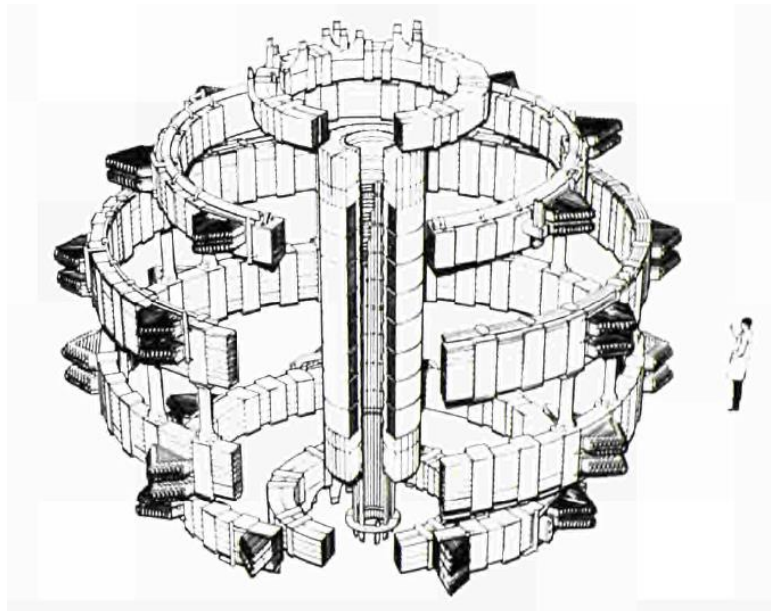


Figure 43: JET PFCs. [26].

5.3.3 Auxiliary Plant – Heating

The initial heating on JET is provided by the ohmic heating of the plasma due to the toroidal current but the main problem faced by JET is because the plasma resistance decreases as the temperature rises while the losses, for example due to radiation, increase.

For this reason, it's also used an additional heating system made by the following components [26]:

- Neutral Injection.
- Radio frequency heating: it's made by resonances at about 1000 MHz and in the region of the oscillatory frequency of the ions in the magnetic field which is from 5 to 50 MHz
- Adiabatic compression: the plasma starts circulating in the outer region of the torus and preheated by injection or radio frequency heating; then it will be moved rapidly to the inner part of the torus where the toroidal field is stronger. This resultant compression heats the plasma.

5.3.4 Auxiliary Plant – Power Supply

JET operation is based on pulse mode with a pulse length of up to 20 seconds every 5 to 15 minutes and during this pulse a very large electrical power peak input is required.

The required power pulse is provided by a combination of power from local network and from motor generator flywheel sets.

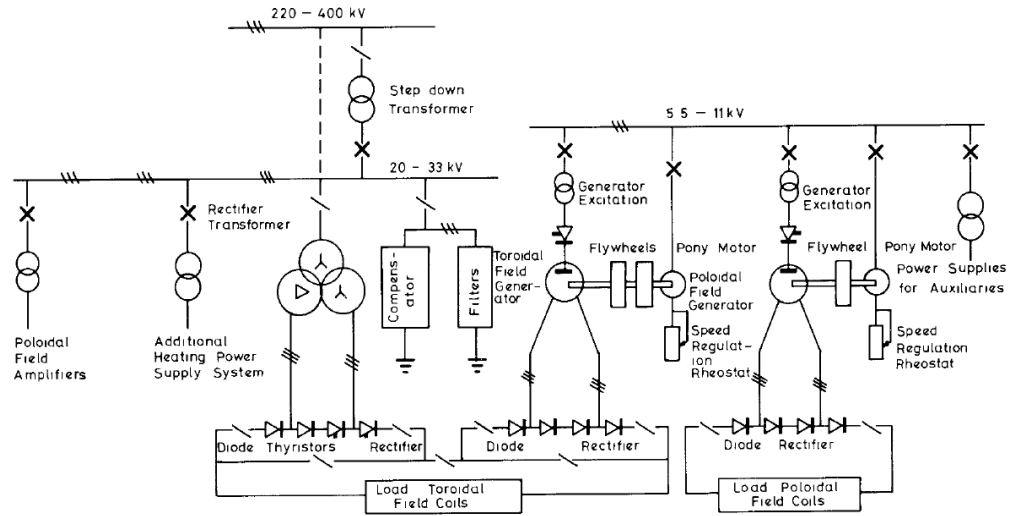


Figure 44: JET Main Power Supply Scheme [26].

5.3.5 Auxiliary Plant – Control System

The main control of the apparatus is made on preset basis, with some measure of self-adjustment in the circuit.

The fine control and the operation in the event of fault is directed from the analysis of measurements made on the apparatus and plasma.

On the apparatus the following measures are conducted: voltages, currents, hydrogen gas pressure, stresses and temperatures in the coils and vacuum vessel and the cooling water flow.

On the plasma there are the following measures: plasma position and shape, density, temperature, radiation, impurity level.

In the next figure all the measurement systems are reported.

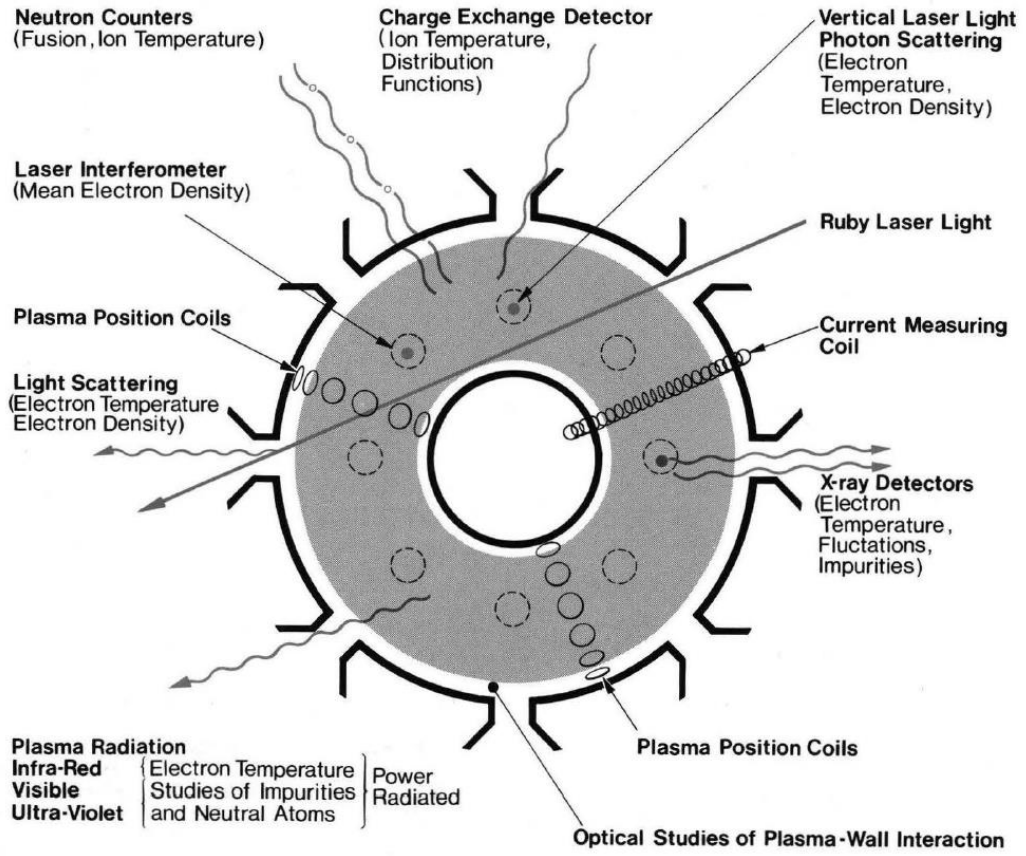


Figure 45: JET Diagnostics general view [26].

5.4 FTU

5.4.1 Research Plan

Frascati Tokamak Upgrade (FTU) was an experimental tokamak in Frascati at ENEA research center and today under dismantling in order to replace it with DTT (Divertor Tokamak Upgrade, see next chapters).

The most important issues addressed by FTU were the following:

- Test of heating and current drive schemes.
- Investigation of energy and particle transport.
- Test of first-wall materials.

5.4.2 Vacuum system

The system in FTU was mainly composed by [27]:

- 2 pumping groups for pre-void, each with Pirani instrument, with pumping capacity of 16 liters/s. The vacuum value reached with these groups is less than $5 \cdot 10^{-3} \text{ mbar}$;
- 6 pumping groups for high vacuum, each with ionisation measuring instruments, with pumping capacity of 2200 liters / s. The vacuum value reached by a pumping group closed on itself is in the order of $5 \cdot 10^{-9} \text{ mbar}$, while the six groups can maintain a vacuum value in the chamber of $2 \cdot 10^{-8} \text{ mbar}$.
- 1 pumping group for high vacuum dedicated to spectroscopic analyzes using a quadrupole instrument (mass spectrometer). The pumping capacity is 330 liters / s.

5.4.3 Cryogenics

The minimum temperature reached by the liquid nitrogen is -192°C and the whole cryogenic system was built by Rivoira; the main components are the following:

- 3 Rivoira storage tanks with a capacity of 30,000 liters each operating at a pressure of 2.5 bar.

- 2 cryogenic pumps built by the French company CRIOSTAR lubricated with the same liquid nitrogen and having a flow rate of about $30 \frac{m^3}{h}$ each.
- 2 evaporators operating alternately in order to avoid saturation during operations with high gaseous flows.
- tanks, valves, and accessories typical of a conventional hydraulic system.

5.4.4 Power Supply

The FTU Power Supply can be listed as follow:

- MFG1 for the generation of toroidal fields.
- MFG3 for the generation of poloidal fields.
- Converters AC/DC for PF coils.

5.4.4.1 MFG1 and MFG3

The MFG1 system consists of a motor-flywheel-generator unit and a diode bridge.

The 1200 kW motor at 1500 rpm drives the flywheel and alternator at 6000 rpm through a "speed multiplier".

The alternator is bipolar with a smooth rotor; the stator winding consists of two three-phase stars electrically out of phase by 30° , independent and isolated from each other.

The rectifier consists of two diode Graetz bridges, one for each star, connected in parallel on the DC side.

The MFG3 consists of 3 twelve-phase bridges with full thyristor control described in the next figure.

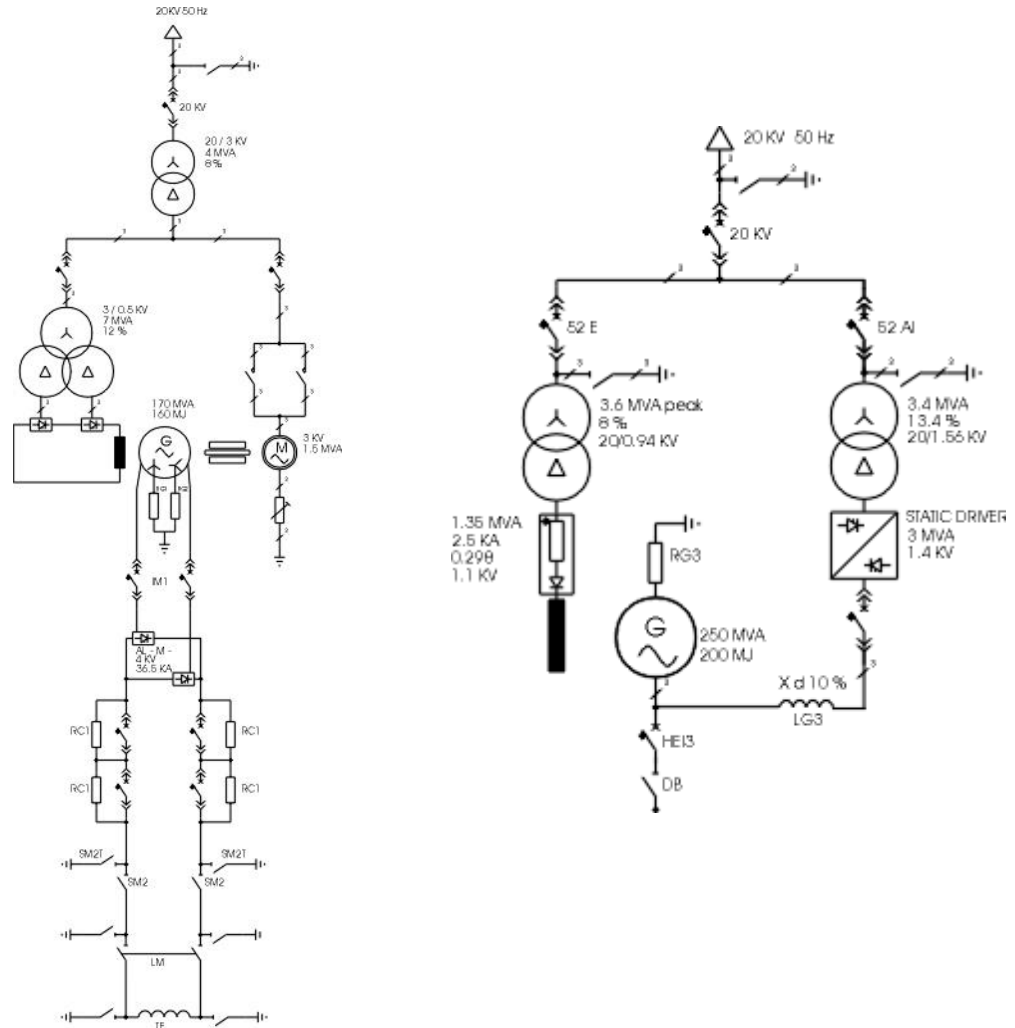


Figure 46: MFG1 (left) and MFG3 (right) electrical scheme [27].

5.4.4.2 AC/DC Converters

Thyristor converters transform input alternating voltage and current into direct voltage and current on the load with trends obtained from the regulation system.

Each converter has been designed according to the peak current and voltage values to be supplied to the load.

The regulation and control of the AL-T, AL-F and AL-V converters, powered by MFG3, was carried out by means of a digital programmable unit (PHSC), while the AL-H converter, powered by the ENEL network, was equipped with a of the Verimat series analog regulation.

Each converter was also equipped with a protection panel interfaced with the regulation panel and with the command-and-control system.

AL-T was powered at 15 kV by MFG3, it was a twelve-phase three-phase converter with sequence control operating on the four quadrants with the current circulation method without dead times.

The Switch is connected downstream of the power supply (gray rectangle in the figure on the right). The implant generates a voltage pulse which triggers the plasma current.

This converter feeds the winding T which has an inductance of 79 mH and a resistance (at 77 K) of 18.5 mΩ.

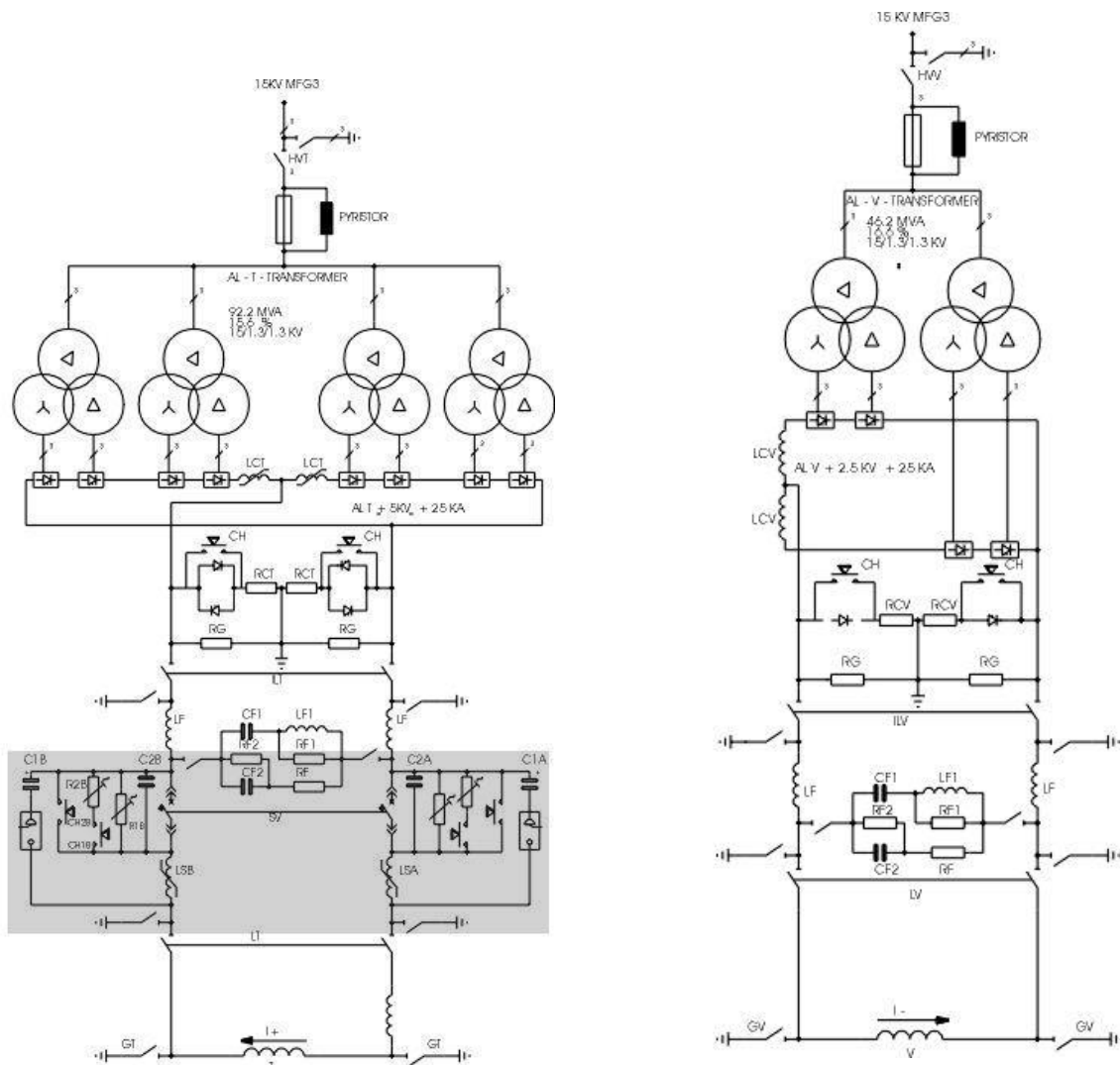


Figure 47: AL-T (left) and AL-V (right) Converters electrical scheme [27]

AL-V aim is to feed the Vertical Field Coils while Al-H feeds the Horizontal field coils.

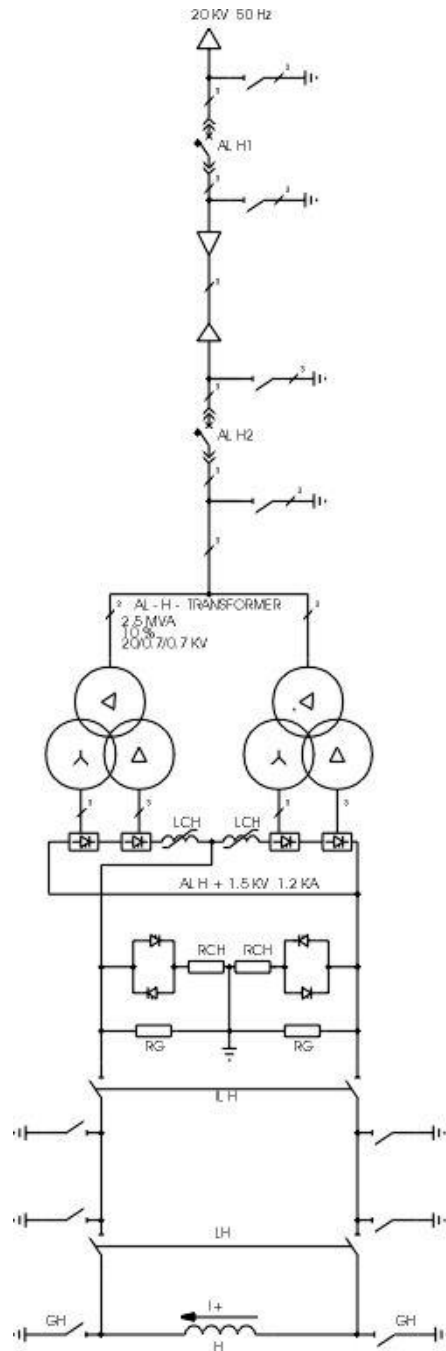


Figure 48: AL-H Converter Electrical Scheme [27].

Finally, AL-F is fed by MFG3 at 15 kV: it is a thyristor twelve-pulses converter with four quadrants control. AL-F feeds the feedback coil for horizontal position control of the plasma.

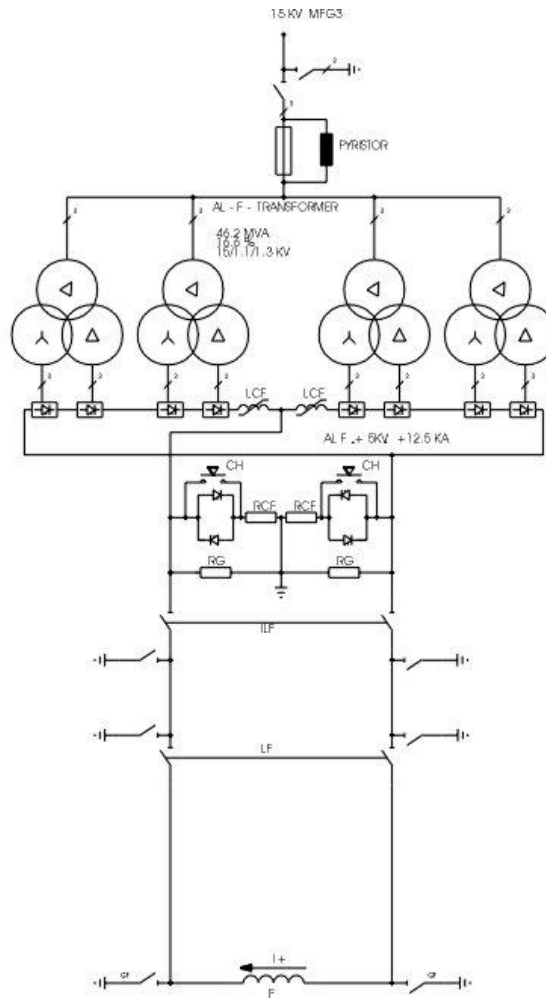


Figure 49: AL-F Converter Electrical Scheme [27].

5.5 DTT

5.5.1 Research Plan

The acronym DTT stands for Divertor Tokamak Test facility, this facility is currently in the design and planning phase at the research center in Frascati (Rome) and whose main objective is to study the use of conventional divertors that can subsequently be used for ITER and DEMO and bring the solutions adopted in theory to a sufficient level of maturity so that they can then be used in the projects mentioned above.

It should be noted that all the data referred to every single component of DTT used in this thesis are referenced to the PID (Plant Integration Document) version 3.2, August 2nd, 2022 [28].

The main objectives of DTT can be classified as follows [29]:

- Demonstrate that the heat removal system proposed for DEMO is capable of withstand the high thermal load that would occur if the radiated power would turn out to be higher than expected.
- To enrich the experimental knowledge in the field of heat dissipation and particles with those not obtainable with existing machines.
- Demonstrate that possible alternative or complementary solutions for the divertor will be adopted for the DEMO project.

It will be possible to evaluate whether:

- Alternative magnetic divertor configurations are acceptable in terms of heat removal.
- The magnetic configurations of the divertor are compatible with the current engineering limits for the generation of the poloidal magnetic field.
- The divertor configurations are compatible with DEMO's engineering constraints.

The DTT's objectives fills an important global lack of research capacity in the heat-exhaust scientific field, in fact:

- The current experiments operate in SOL conditions very different from the one in ITER or DEMO.

- The theoretical models, the extrapolations and the experiments and the related codes for the study of the SOL have a strong need for experimental confirmation.

5.5.2 Main Parameters

The toroidal field of DTT will be of $B_T = 6 T$ with a major radius of 2.19 m and a minor radius of 0.70 m. The plasma current is supposed to be of 5.5 MA [28].

DTT planning operations can be resumed as follow:

- The first phase will aim the realization of the machine.
- In a second phase the machine will reach the operative capability with a robust H-mode.
- The next phases will be reserved to test an alternative divertor solutions with different magnetic configurations and innovative technologies in the liquid metal.

5.5.3 ENEA Frascati Research Center

DTT new facility will be installed in the green area of the next figure inside the ENEA Research Center in Frascati (Rome).



Figure 50: ENEA Frascati Research Center [28].

5.5.4 Magnet System

The magnet system of the DTT machine consists of three types of magnets, whose name derives from their geometric shape and their position in space.

Since the magnetic confinement must be efficient and must allow the formation of different plasma scenarios, the proposal was made to build the machine with [29]:

- 18 superconducting toroidal magnets called TFCs (Toroidal Field Coils); these magnets are currently designed to conduct a maximum DC current of 42.5 kA.
- 6 superconducting magnets positioned in the center of the machine and stacked on top of each other called CS (Central solenoids) with a maximum DC current of 31.34 kA.
- 6 superconducting magnets positioned according to the poloidal axis of the toroid called PFCs (Poloidal Field Coils) and designed to conduct a maximum current of 28.6 kA.

The machine's magnetic superconductor system is designed to be symmetrical with respect to the equatorial plane with the PFCs designed to be equal in pairs.

The magnetic system of the machine can be appreciated in the following figure.

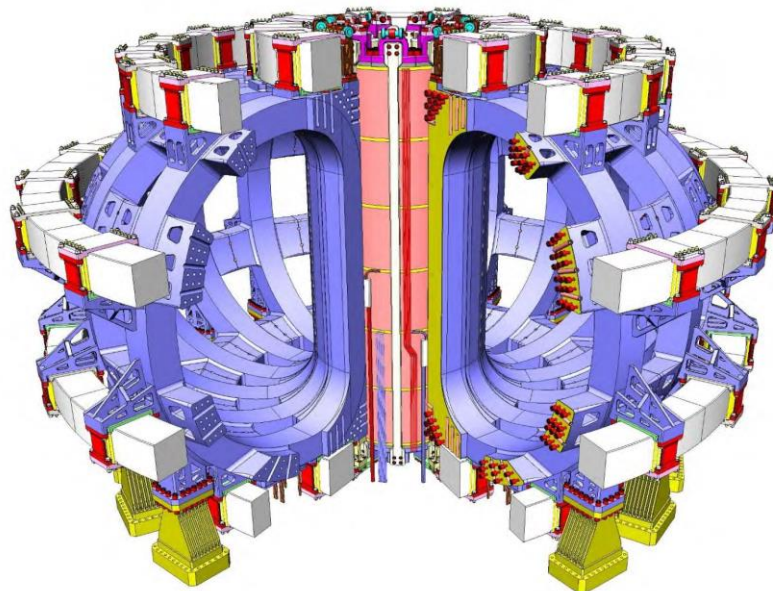


Figure 51: TFCs in blue, PFCs in white, CSs in pink [29].

5.5.4.1 Toroidal Field Coils

In the following figure is represented the cross section of the superconducting magnets in Toroidal Field configuration with $R_{plasma} = 2.19$, $B_{plasma} = 6 T$, $I_{plasma} 5.5 MA$:

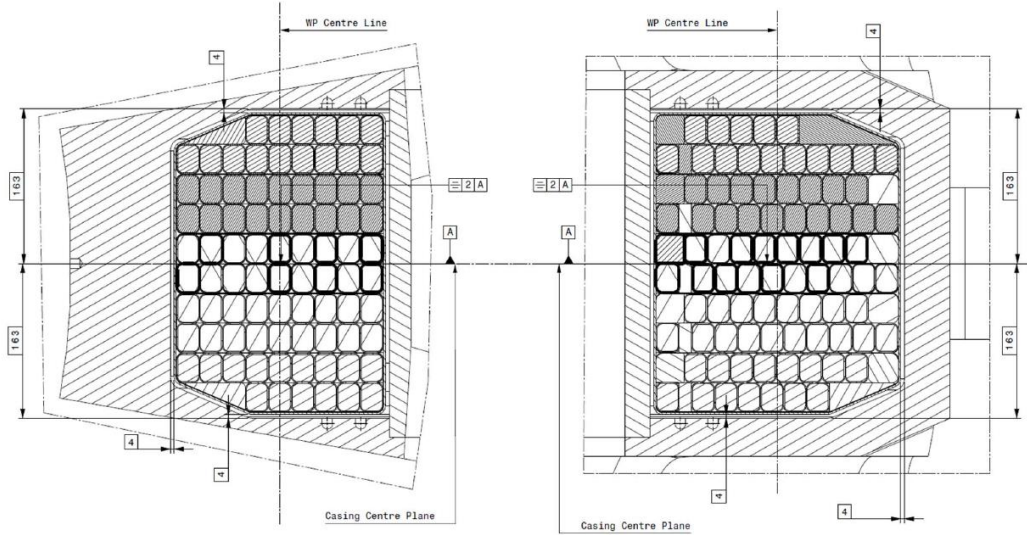


Figure 52: TFC cross section [30].

In the following table are reported the conductor parameters [30]:

	[Value]	[Unit]
Jacket thickness	1.9	mm
Inner corner radius	3.5	mm
Cu Area	203.1	mm^2
No-Cu Area	113.7	mm^2
Nb_3Sn strands	420	
Cu segregated strands	180	
Nb_3Sn strand	0.82	mm (diam.)
Cu segregated strand	0.82	mm (diam.)
Wrapping	0.05 mm	
Mass flow rate	4	g/s
B_{peak}	11.9	T
I_{op}	42.5	kA
ΔT	1.4	K

While in the following table are reported the main parameters of the winding pack [30]:

	[Value]	[Unit]
Inter-turn insulation (fiber glass)	1	mm
Vs ground insulation	2	mm
Insertion gap (fiber glass)	4	mm
Number of turns	84	
Double pancake insulation	0.5	mm

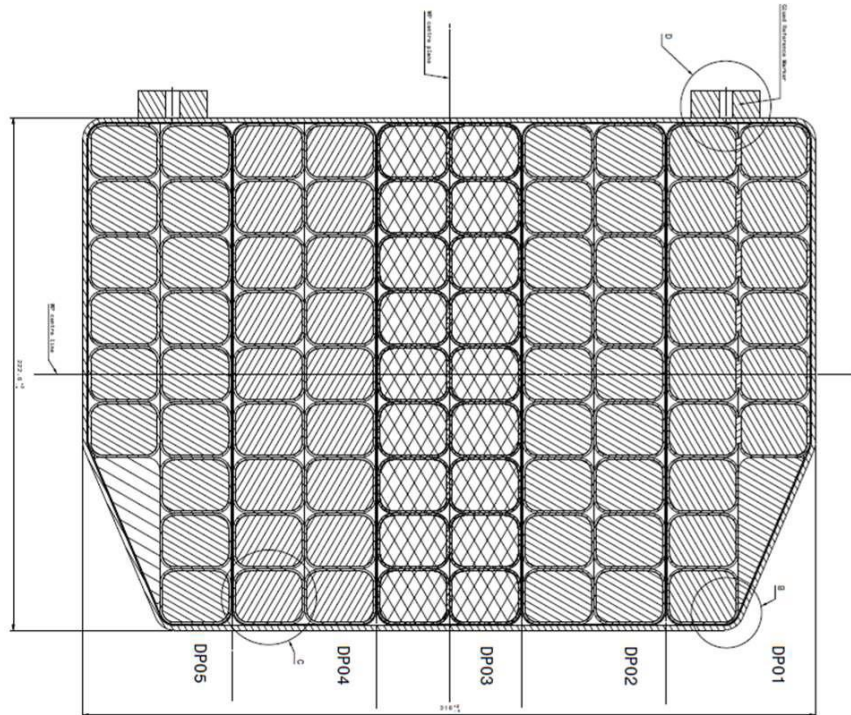


Figure 53: Cross section of TFC with details on the Double Pancakes [30]

5.5.4.2 Central Solenoid

The Central Solenoid assembly consists of a 5.2 m high stack of six identical solenoids with an axial precompression structure and a centering system. The weight of the CS system is loaded at the bottom through its support to the TF casing.

The CS allow not only to induce the current inside the plasma but also to shape it and each of the 6 coils is wound in layers in order to maximize the coil current density and thus to guarantee the required magnetic flux swing.

The layer-wound coil is made of three sections: High Field, Medium Field and Low Field grade and each section is connected to the adjacent one by a joint that will be manufactured in line, during winding, and embedded with the 66.3 mm space separating vertically two adjacent modules.

In the following table are reported the main parameters for CS [29]:

	High field	Medium field	Low field
Operating current	31342 A		
Peak field	13.6 T	10.7 T	8.8 T
SC wire features	0.82 mm diameter with Cu:nonCu=1		
Current per strand	260 A		
N. of SC wires	810	300	180
N. of Cu wires	0	159	216
Jacket material	316 LN Steel		
Jacket thickness	4.9 mm	3.9 mm	2 mm
Dimensions	44.35 x 28.29 mm ²	37.39 x 20,40 mm ²	30.83 x 15.25 mm ²
Turn insulation	1 mm (glass fiber + resin)		
Ground insulation	6 mm (glass fiber + resin + Kapton)		
N. of layers per turn	4 x 17	4 x 20	6 x 24
Total module current	2.13 MA	2.51 MA	4.51 MA
Length	210 m	300 m	630 m
CS module inductance	72 mH		
WP height	800 mm		
CS inner radius	423 mm		
CS outer radius	751.3 mm		

5.5.4.3 Poloidal Field Coils

Regarding the PFCs, they do not all have the same geometry, but they are grouped as follow: PF1-6, PF2-5 and PF3-4 following the symmetry along the equatorial plane of the tokamak. Each coil is separately and independently fed, and all the PF coils are designed to be wound with pancake technique.

In the following tables there are the main parameters of the PF coils [29]:

Conductor	PF1-6	PF2-5	PF3-4
SC material	<i>Nb3Sn</i>	<i>NbTi</i>	<i>NbTi</i>
Peak B Field	9.1 T	4.2 T	5.3 T
Pancake insulation	1 mm	1 mm	1 mm
R mm	1400	3079.5	4251.1
ΔR without insulation	510 mm	279 mm	389.8 mm
Z	± 2760 mm	± 2534 mm	± 1015 mm
ΔZ without insulation	582.4 mm	516.8 mm	452.2 mm
Ground insulation	5 mm	5 mm	5 mm
No. of radial turns	20	10	14
No. of vertical turns	18	16	14
Total number of turns	360	160	196
Max rated current	28.3 kA	27.1 kA	28.6 kA
L	0.454 H	0.298 H	0.690 H
			

5.5.5 Quench detection

The toroidal field coils, due to their physical steady state behavior, can be monitored for detecting possible quenches by measuring the voltage taps placed at the coil terminals and then comparing this signal with the one coming from other coils. The voltage threshold is currently set at 100 mV and the holding time is 1.0 s.

For the CS modules, the quench detection relies on co-wound sensors in order to subtract the inductive voltage signal and correctly identify the transition voltage.

Regarding the PFC at the end, the quench detection system is based on voltage quench detection and includes for redundancy two independent arrangements.

5.5.6 Vacuum Vessel

This system includes the following components [31]:

- Vacuum Vessel (VV) which is composed by 17 vacuum vessel sectors (VVS): 14 sectors with a toroidal extension of 20°; 2 sectors with an extension of 30° and a special sector of 20° without port ducts.
- Vessel ports.
- Expansion joints connecting the ports to the cryostat flanges.
- Gravity support for the vacuum vessel.
- Vacuum Vessel Instrumentation (VVI).

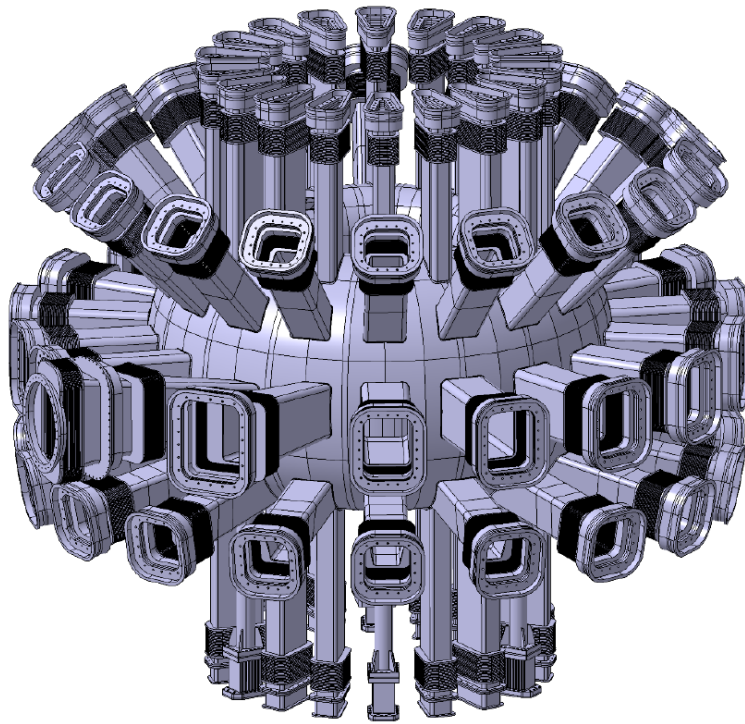


Figure 54: 3D CAD view of the vacuum vessel and ports [31].

It should be noted that the ports number are from 1 to 5 from the bottom to the top.

The Vacuum Vessel is designed to withstand all possible thermal and mechanical loads that are generated during the nuclear fusion reaction, also considering possible scenarios of failure and disruption of the plasma.

The DTT vacuum vessel is actively cooled through a fluid flowing into the interspace delimited by the double wall structure of the inner shell and the outer shell.

During normal operation the vessel double-wall cavity will be filled with water whereas the borated water will be used during high performance plasma operations as neutron streaming moderator to enhance the neutron shielding capability of the vacuum vessel thus reducing the nuclear heating density in the TF winding pack to acceptable limits.

5.5.7 Additional Heating

One of the main targets of DTT is to tackle the exhaust issue in a DEMO relevant context. In order to reach an additional power of 45 MW to the plasma, there are several heating systems [28]:

- Electron Cyclotron Resonance Heating (ECRH): cluster of 32 gyrotrons for a total power of 28.8 MW installed.
- Ion Cyclotron Resonance Heating (ICRH): pair of antennas that deliver 1.5 MW each with shared transmitters in the range of 60-90 MHz
- Negative Neutral Beam Injection (N-NBI): one 510 keV beam injector able to deliver approximately 10 MW to the plasma.

5.5.8 Divertor

In DTT there will be 56 divertor modules, 3 for each 20° sector plus 2 spares. Out of these, 4 divertor modules will be test modules where advanced configurations can be tested [28].

The layout for the divertor is based on proven technologies already qualified for ITER: 5000 cycles at $10 \frac{MW}{m^2}$ followed by 300 cycles at $20 \frac{MW}{m^2}$.

The following table represents the main parameters of the divertor:

Table 2: Thermohydraulic water conditions of standard DIV modules [28]

Parameter	Value
Inlet pressure [MPa]	5
Inlet temperature [°C]	30-130
Mass flow rate [kg/s]	577
Max, in-out temperature range [°C]	11
Max pressure drop [bar]	20
Standard divertor modules baking temperature [°C]	130

One of the main targets of DTT is to study different solutions of the power exhaust issues in view of DEMO future reactor. The test divertor modules will be also installed in order to simulate alternative solutions also considering various aspects like easy and fast installations, maintenance, and removal of test modules through port 4. In the following table are reported the main parameters of test module divertors:

Table 3: Thermohydraulic water conditions of DIV test modules [28]

Parameter	Value
Inlet pressure [MPa]	5-15
Inlet temperature [°C]	30-250
Mass flow rate [kg/s]	48
Max, in-out temperature range [°C]	11
Max pressure drop [bar]	20
Standard divertor modules baking temperature [°C]	130

5.5.9 First wall

The DTT First Wall consists of three main components:

- The inboard First wall (IFW).
- The Outboard First wall (OFW).
- The Top First wall (TFW).

The IFW has no poloidal segmentation with a length of 2300 mm and each module extends of 10° toroidally with 36 modules in total. The standard modules will be exposed to plasma radiation only with heat fluxes lower than $0.5 \frac{MW}{m^2}$. The IFW are actively cooled by water at 60°C and 4 MPa and with a maximum temperature increase of 18°C [28].

The OFW include the inter port and intra port modules and consists in actively cooled steel plates with a maximum plasma radiation of $0.5 \frac{MW}{m^2}$.

The TFW shares the same plasma facing components of the standard IFW modules based on coaxial steel pipes. The modules are actively cooled by water at 60°C and 4 MPa.

5.5.10 Cryostat

The Cryostat consists of three main sub-assemblies: Cryostat base, Cryostat cylindrical body and Cryostat Top lid.

The Cylindrical Body of the cryostat will be built by elements with cylindrical and truncated-conical shapes. The Top Lid will be built with a toro-spherical end that is shifted up by about 1 m to increase the rigidity generating compressive components of the circumferential stress and to maximize the inner space for the assembly and maintenance of cryogenic devices and of TF terminal joints. The Cryostat Base is much heavier in construction as it must bear the load of the entire machine, distribute the disruption and seismic loads, and transmit them to the lower pillars of the torus hall. The whole sub-assembly of CRS comprises one external ring, one internal ring, and 6 radial legs supported on both rings. Each sector is connected to the adjoining one through bolted flanges and dowels for alignment.

The Vacuum Vessel (VV) gravity supports rest on the 6 plates welded to the double ring. The Toroidal Field Coils gravity supports rest on 18 elements bolted to the double ring and fixed along the toroidal direction by means of shear keys to

increase the sliding resistance. The double ring is assembled onto the lower structure through bolts for fixing, dowels for alignment, and shear keys for preventing sliding. The CCB will be seated on an outer annulus of the lower plate where it is bolted. Vacuum tightness of the CCB is achieved performing sealing welds among the different double ring sectors at the lower plate.

The CCB is made of single-walled 304L(N) stainless steel ($\text{Co} < 0.05 \text{ wt\%}$) shell. ASME SA-240 specifications for cryogenic service apply to the material. The shell is connected through strength welds to a structure withstanding the external pressure load and supporting the weight of ports and port plugs. The different parts of the CCB, CBS, and CTL are connected by bolts at flanges and are sealed from the inner side by means sealing welds. The operational pressure is about $10^{-3} Pa$.

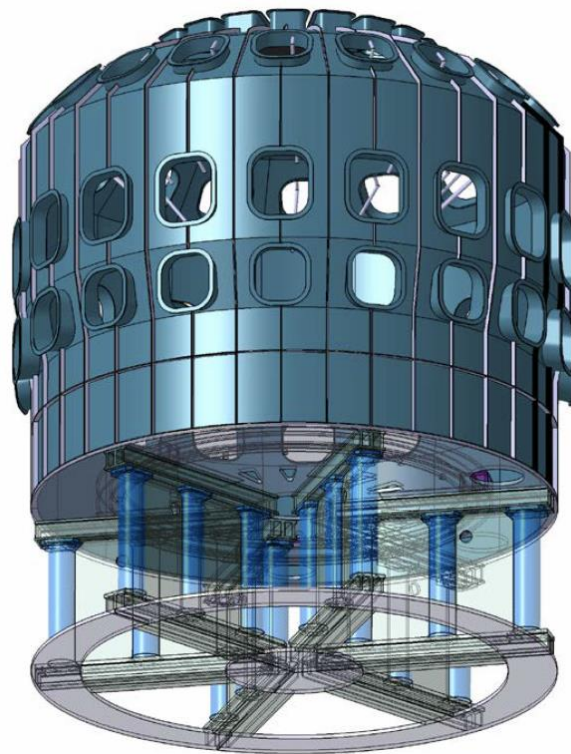


Figure 55: Overall view of the Cryostat [28]

5.5.11 Cryogenic System

The main purposes of the Cryogenic System (CRY) are [28]:

- To provide refrigeration to the following components:

- 18 TFCs, feeders at 4.5 K and 6 HTS current leads at 40-50 K.
- 6 CS, feeders and 12 resistive current leads at 4.5 K.
- 6 PFCs, feeders and 12 resistive current leads at 4.5 K.
- Thermal Shields at 80 K.
- Cryolines, valves, cold circulators.
- Cryogenic pumps.
- To provide Helium recovery in case of quench.
- To handle stationary heat loads, include thermal radiation, the conduction across the support structure, the current leads, the feeders and Joule heating in conductor joints and terminations during dwell periods.
- To handle nuclear thermal heating, eddy current losses in the massive support structure, and AC losses in the conductors, due to electromagnetic variations and all the loads above for the Plasma Operation State.

The DTT Cryogenic system will include:

- A warm storage system (WSS).
- Liquid nitrogen storage tanks.
- A warm compression station (WCS).
- A refrigeration cold box (RCB).
- An Auxiliary cold box (ACB) with thermal dampers, cold circulators, and cryogenic loops.
- The cryo-lines connecting the ACB to the RCB and the tokamak.

5.5.12 Thermal Shield

The Thermal Shield system is divided in three subsystems according to the warm regions to be shielded:

- Vacuum Vessel Thermal Shield – VVTS,
- Ports Thermal Shield – PTS,
- Cryostat Thermal Shield – CTS.

The VVTS, torus shaped, is arranged along the gap between the Vacuum Vessel and the TFC: it is electrically divided into 18 segments in toroidal direction and 2

segments in poloidal direction to avoid eddy currents during plasma transient scenarios, events, and disruptions.

The PTS is a port shaped shield mechanically connected to the VVTS and CTS.

The CTS follows the shape of the inner surfaces of the cryostat, and it's provided with multilayer insulator to reduce the radiation heat load on it.

The Thermal Shield is made of double wall stainless-steel panels 20 mm thick.

The two walls, 3 mm thick each, are spaced by 14 mm gap and joined together by means of stiffening frames placed at the panel edges. The panels are actively refrigerated by means of circular tubes welded to the panel walls. The cooling tubes are fed by pressurized helium gas.

Pressurized helium gas flows from the cold valve box (CVB) through parallel isolation valves into the Thermal Shield supply manifold. From the manifold, the helium is distributed into the cooling lines.

The Thermal Shield cooling system is subdivided into 36 parallel cooling lines that independently covers a complete 10-degree toroidal sector of THS. The cooling lines remove the heat load intercepted from the warm surfaces. The cold structures, operating at 4.5 K, face the THS surface only.

The THS cooling system is 100% redundant in case of a line failure, with the active line installed in parallel with the redundant line.

Thermal radiation to the superconducting magnets is minimized by operating the Thermal Shield in the temperature range of 80-120 K and providing surfaces with low emissivity. High vacuum in the cryostat chamber (10^{-3} Pa) minimizes free molecular gas conduction.

5.5.13 Electrical components – Power Supply

The Power Supply System (PSS) consists in the PSs for the superconducting and in-vessel coils and in some other systems which can be summarized as follow:

- TF, CS, PF Magnet power supply.
- TF Fast Discharge Units.
- Vertical stabilization coils power supply.
- Divertor coils power supplies.
- Not-axisymmetric coils power supplies.

- DC busbars.
- Other PS components.
- Control System Power supply.

5.5.13.1 TF magnet PS

The simplified circuit for the TFCs is shown in the next figure. The 18 coils are arranged in 3 sets, each composed of 6 coils in series.

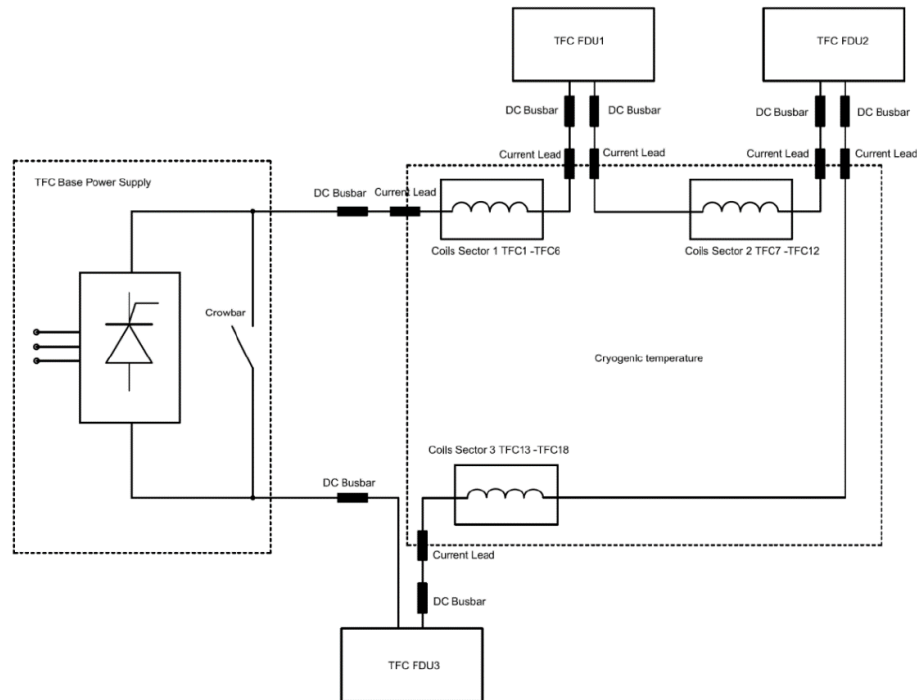


Figure 56: Simplified circuit for TFC PS [28]

The reference scheme for the TF PS is also shown in the next figure: it is based on 8 thyristor rectifier bridges 6-pulses (each operating at 6 pulses with a no-load DC current of 5.5 kA) connected in parallel.

Another main component of the Power Supply is the *Crowbar*: this is a protection device both for TFC PS and for superconducting TFCs and the main function is to allow, in case of fault or quench, the freewheeling circulation of the current in the TFCs.

The crowbar is composed by a hybrid making switch, composed by a static switch with a mechanical switch and a varistor in parallel.

The PS and the FDU protections are unidirectional and the direction of the current (and so the magnetic field) can be inverted before an experiment by exchanging the contacts at the coil terminals.

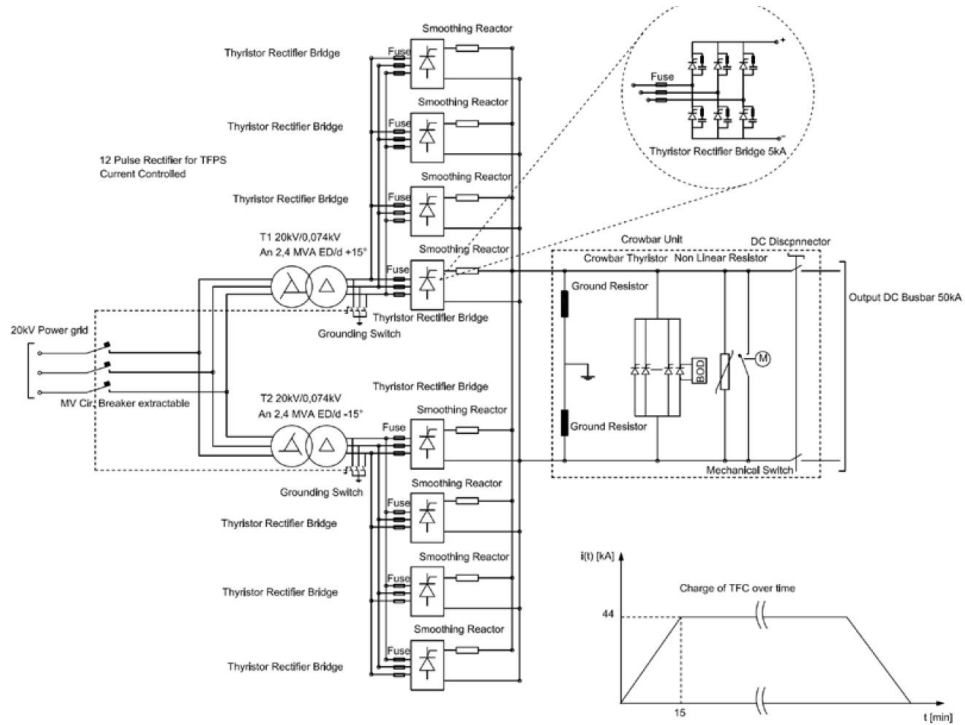


Figure 57: Reference scheme for the TFPS for DTT [28].

The plasma confinement and control require a low ripple in the magnetic field over the toroidal axis and if the TFCs are connected in series, only one Power Supply is required as reported in previous figure.

The high inductance resulting from the series of the 18 TFCs also reduces the ripple in the coil current [6].

5.5.14 Electrical components – Fast Discharge Units

The following scheme represents the simplified electrical circuit for the Fast Discharge Unit.

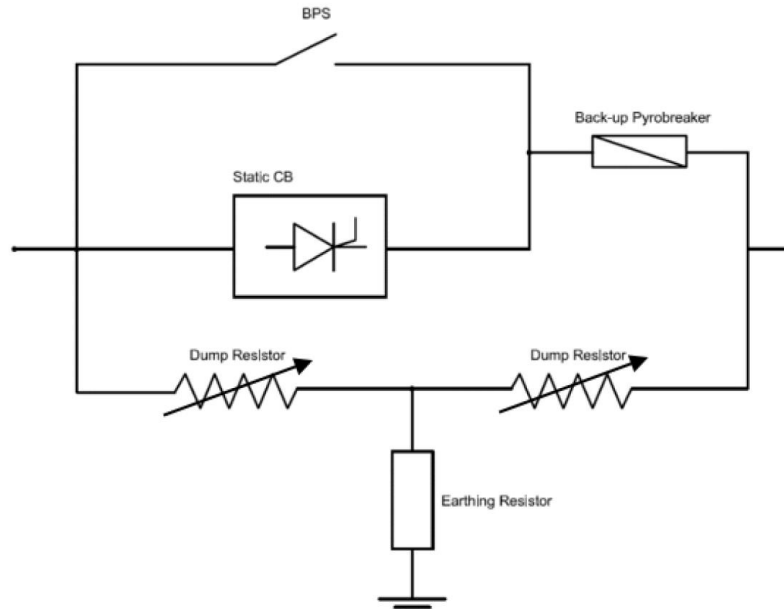


Figure 58: Reference scheme of the single FDU of DTT [28].

This scheme is based on a hybrid switch which is a combination of the following components:

- A mechanical bypass switch called BPS for current conduction during normal operation.
- A static circuit breaker called SCB for current interruption, based on parallel connected semiconductors controllable at turn-on and turn-off.
- A pyrobreaker in series to the hybrid CB as backup protection in case of fault of BPS and/or SCB.

In normal operating conditions the BPS is closed and the current flows through it. When the FDU intervention is required, the opening command (triggering signal) is given to the BPS and the turn-on command to the static breaker is generated.

After a delay due to mechanical inertia, the BPS contacts are open and the arc is formed; the arc voltage forces the current to commute from the BPS into the SCB and the SCB is maintained in the on-state until the current commutation is over and the BPS contacts are fully open.

The FDU scheme foresees to use of variable dump resistors to dissipate magnetic energy stored in the TF coils in order to have a more efficient linear discharge instead of an exponential discharge with fixed resistor. The variable dump resistor could be implemented both through an active method (as resistors switched by power electronic devices) or passive (nonlinear resistors or varistors) methods.

In the following table are reported the main parameters of the DTT FDU for TFCs:

Table 4: TF FDU's main parameters [28]

Characteristic	Single FDU parameter
Type	Unidirectional
Operating current	42.5 kA
Total energy	0.71 GJ
Specific energy through	7.23 GA^2s
Discharge τ	5 s
Maximum delay time from BPS to SCB opening	0.5 s
Maximum delay for the PB operation	0.5 s
Dump resistance for fixed resistor	0.151 Ω
Maximum voltage applied to coil sector at the discharge	6.44 kV
Insulation voltage to ground	7.2 kV rms
Dump resistor cooling	Air
Minimum time for a new operation after a FDU discharge	1 hour

From the coil point of view, the number of FDUs is theoretically marginal, as the rated voltage produced by a FDU across a single coil (about 1 kV) only depends on the energy to be extracted from it at the discharge [6].

A single FDU to discharge all the 18 coils would reduce the number of connections and penetrations into the vacuum vessel and the cryostat but in practice the coil overvoltage and the insulation level would be out of range according to the design project.

The final solution so to choose 3 FDUs in the circuit and to divide them into three groups as reported in the previous figure.

5.5.14.1 PF magnet PSs

The PF Power Supply is still under discussion and the preliminary hypothesis is reported in the following figure:

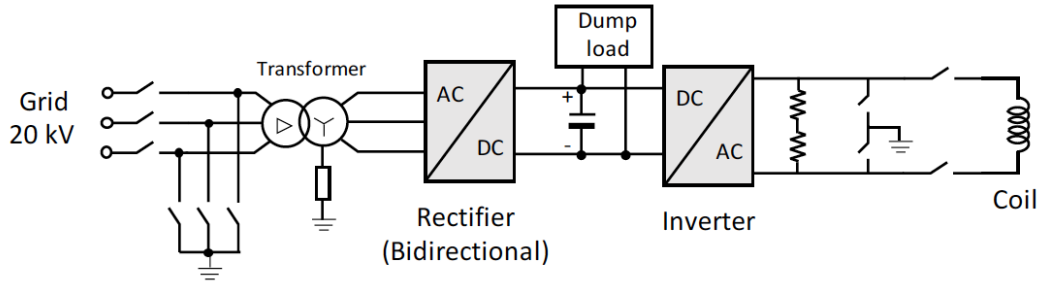


Figure 59: Reference scheme for each of the 6 PF PSs [28].

In the next table are reported the main preliminary specifications:

Table 5: Preliminary specifications of the PF PSs [28]

Characteristic	Value
Operation H-bridge and SNU	4 quadrants
Maximum pulse duration	200 s
Current ripple	$\leq 0.1\%$
Breakdown voltage rise time	$\leq 500 \mu\text{s}$
Maximum derivative of output voltage	100 MV/s
Breakdown duration (SNU resistor conduction time)	100 ms
Crowbar nominal current	Nominal current $\pm 10\%$

In the PF PS topology, a supercapacitor-based energy storage solution is employed [6].

The PF protection crowbar must be bidirectional, except for the PF3 and PF4 coils; the three-stage topology with an independent AC/DC front-end converter allows the control of the input harmonics and reactive power, together with the capability to invert the power flow towards the grid [6].

5.5.14.2 CS magnet PSs

The following figure reports a general electrical circuit for the 6 CSs and the related Power Supplies:

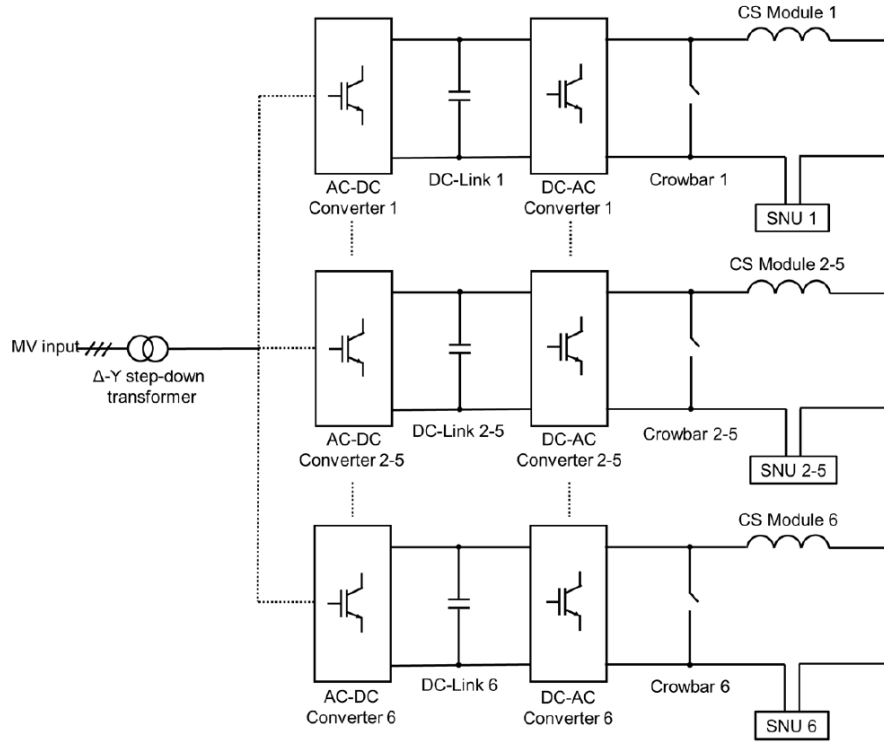


Figure 60: General electrical circuit for CS PSs [6]

In this case a single transformer can provide enough power for all the six circuits as the power demand is reduced by the energy storable in the DC-links based on supercapacitors [6].

The CS protection crowbar must be bidirectional like the coil current. Each CS circuit is supported by a switching network unit (SNU) able to generate an overvoltage of about 3 kV at the plasma breakdown and such SNU can be also operated as a FDU to protect the supplied superconducting module [6].

In the following table are reported the main parameters for the CS PSs:

Table 6: Main specifications of the CS PSs [28]

Characteristic	Value
Operation H-bridge and SNU	4 quadrants
Maximum pulse duration	200 s
Nominal current H-bridge and SNU	31.34 kA
Current ripple	$\leq 0.1\%$
Output voltage	$\geq 850 V$
Maximum output voltage, including SNU	$\leq 3000 V$
Nominal breakdown voltage	2800 V
Minimum current for full-voltage breakdown	$> 10 kA$
Nominal voltage of SNU	2300 V
Breakdown voltage rise time	$\leq 500 \mu s$
Maximum derivative of output voltage	100 MV/S
Breakdown duration	100 ms

Maximum energy dissipated in SNU resistors	40 MJ
Superconductors charge time	< 3600 s
Minimum energy to be delivered to the load	70 MJ
Maximum transformer load (for 6 chargers)	2500 kVA

5.5.14.3 DC Busbars

The DC busbars connect the output of the PS system to their load coils with transition current leads and feeders for the superconducting coils. In the following table are reported the main specifications of the DC busbars:

Table 7: Main specifications of the DC busbars [28]

Characteristic	CS+PF	VS+DIV	TF
Number of busbars	12+12	4+8	6x2 per pole
Operations	Pulsed	Pulsed	Steady State
Total length	60 m	On hold	40 m
Material	Al	Al	Cu
Width	40 mm	40 mm	50 mm
Height	250 mm	250 mm	500 mm
Cooling	Natural air	Natural air	Natural air
Distance between supports	3-4 m	On hold	On hold
Vertical distance between busbars	1 m	On hold	On hold
Horizontal distance between busbars	0.5 m	On hold	On hold

5.5.14.4 Electrical distribution system

DTT will be supplied by the national high voltage grid owned by Terna S.p.a. at 150 kV. The electrical distribution system includes an HV/MV substation at 150/20 kV/kV called SS0 dedicated to the DTT facilities.

The 20 kV distribution system will be divided into:

- SSEN, dedicated to supply the steady state loads.
- PPEN, dedicated to supply the pulsed loads.

At the moment of writing this document, the following substations have been identified based on available documents:

- 0608-0-ZD-001-Substation SS1, in building 176.
- 0608-0-ZD-002-Substation SS2, in building 88.
- 0608-0-ZD-003-Substation SS3, in building 58.
- 0608-0-ZD-004-Substation SS4, in building 72.
- 0608-0-ZD-005-Substation SS5, in building 173.



Figure 62: DTT substation foreseen position [28]

The substations are supplied by the 20 kV distribution power system of the HV/MV substation according to the following block diagram:

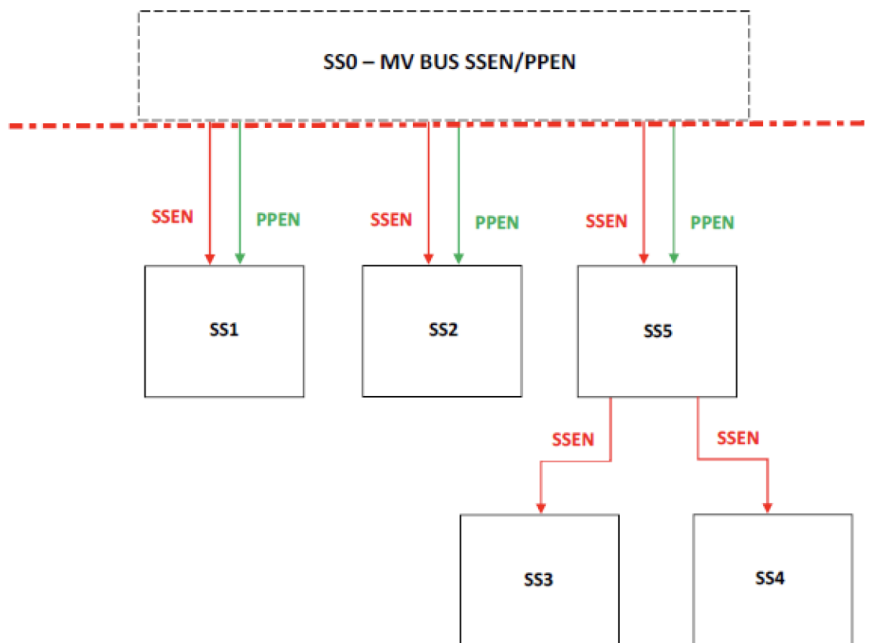


Figure 61: EDS block diagram of DTT [28]

The main power supply will be derived from the 20 kV SSEN section of the HV/MV substation and brought through not redundant 20 kV feeder to each substation where it's foreseen. Each couple of 20 kV feeders will be then connected to an air insulated type switchgear in single radial configuration.

In the substations where the pulsed behavior is also foreseen, power supply will be derived from the 20 kV PPEN section of the HV/MV substation and brought to each concerned substation through not redundant 20 kV feeder.

Downstream the 20 kV SSEN switchgears, the distribution system may be composed of:

- Single radial MV 6 kV distribution level obtained through 20/6.3 kV/kV power transformer.
- Single radial LV 400-230 V distribution level.
- At LV distribution level, emergency power supply will also be available (diesel generators).
- LV auxiliary service panels in each substation in order to feed the minor loads like lights, power sockets, auxiliary loads.

5.5.15 Electrical components – Grounding system

The grounding system will be developed according to the following standards:

- IEC 60364 for low voltage installations.
- IEC 61936-1 and EN 50522 for power installations exceeding 1 kV AC.

The grounding system will be also developed in order to protect against:

- Indirect contacts due to failure of the functional insulation of fed parts.
- Electrostatic discharges.
- Lightning.

5.5.16 Cooling system

DTT, as all tokamaks, must be actively cooled. In the next figure is reported a conceptual scheme of the cooling water system during plasma discharge:

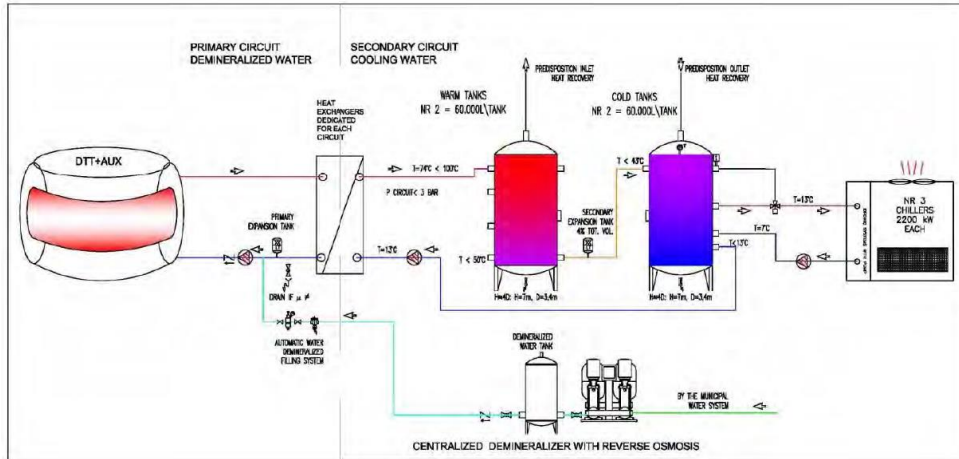


Figure 63: Conceptual scheme of Cooling Water System during plasma discharge [29].

The primary cooling circuit is filled with demineralized water while the cooling of the vacuum vessel is carried out by borated water to provide maximum neutron shielding.

The primary cooling circuit transfers the thermal load, produced during the plasma operation to the dedicated heat exchangers. All thermal loads are pumped in the secondary circuit using a classical cooling water equipped with filter and chemically processed to avoid any deposition and for removal of corrosion products. The loop is closed by two types of tanks for storage and by a set of chillers sized for this purpose.

5.5.17 CODAS

The Control and Data Acquisition System (CODAS) shall supervise the activity of all DTT, both pulses related and continuous.

CODAS will provide the following functions:

- Plant monitoring.
- Plant coordination via state Machine Management.
- Discharge sequence management.
- Data storage of discharge results.
- Experimental database management.
- Precise timing distribution.
- Real-time plasma control.

Those systems are integrated in the Machine Protection System (MPS) and in the Occupational Safety System (OSS).

The MPS shall provide the fast plant protection in case of off normal events that are not handled by CODAS failure while OSS shall provide personnel and environment protection action upon severe system failures that cannot be handles by the interlock systems.

5.6 ITER

5.6.1 Research Plan

One of the most known aims of ITER is to achieve the extended burn in inductively driven plasmas with the ratio of fusion power to auxiliary heating power, Q , of at least $Q > 10$ for a range of different operating scenarios and with a proper duration in terms of time in order to achieve steady state conditions on the timescale's characteristics of plasma processes.

By the technical point of view, ITER is the most complicated machine never built-in human history and another one main target is to develop technological basis for the design of future fusion power plants capable of generating electricity, in particular [32]:

- The device should demonstrate the availability and integration of technologies essential for a fusion reactor (such as superconducting magnets and remote maintenance).
- The device should test components for a future reactor (such as systems to exhaust power particles from the plasma).
- The device should test tritium breeding module concepts that would lead in a future reactor to tritium self-sufficiency, the extraction of high-grade heat and electricity production.



Figure 64: Schematic schedule for the first 10 years of ITER operations within the Staged Approach [32]

The first plasma will be achieved, according to the Staged Approach schedule, in 2025 with at least 100 kA of plasma current for at least 100 ms and during the subsequent Engineering Operation Phase for commissioning of the Magnet system to full current, it is expected to have a 1 MA plasma.

After the first plasma phase there will be a pre-fusion power operation 1 where it is expected to have diverted plasma operation in hydrogen/helium up to at least 7.5 MA/2.65 T, supported by a program of plasma control, diagnostics, ECRH and ICRF commissioning.

The pre-fusion power operation 2 will be addressed in order to have the commissioning of the Heating Neutral Beam, Diagnostic Neutral Beam and ICRF systems to full power together with the necessary plasma control capability.

The final and most important phase will be the Fusion Power Operation where the knowledge of the previous years will be used in order to start the experiments on Deuterium and Tritium; the goal of the first campaign would be to demonstrate fusion power production of several hundred MW for several tens of seconds at a Q value in range of 5 – 10. In subsequent experimental campaigns, the fusion gain would be optimized to achieve $Q > 10$ with a goal of 300 – 500 s.

5.6.2 Magnet System

The magnetic energy inside the superconducting magnets during operation in ITER will be about 51 GJ in order to initiate, confine, shape and control the ITER plasma [33].

The magnets are in *Nb3Sn and Nb – Ti* which will be held at a temperature of 4 K.

The TFCs are designed to produce a total magnetic energy of 41 GJ and a maximum magnetic field of 11.8 T with a weight of 360 tons each.

TFCs will be wound in double pancakes layers of spiraled conductor embedded in radial plates and encased in large stainless-steel structures.

The total weight of the TFCs system is of 3.400 tons and the following figure represents a general structure:

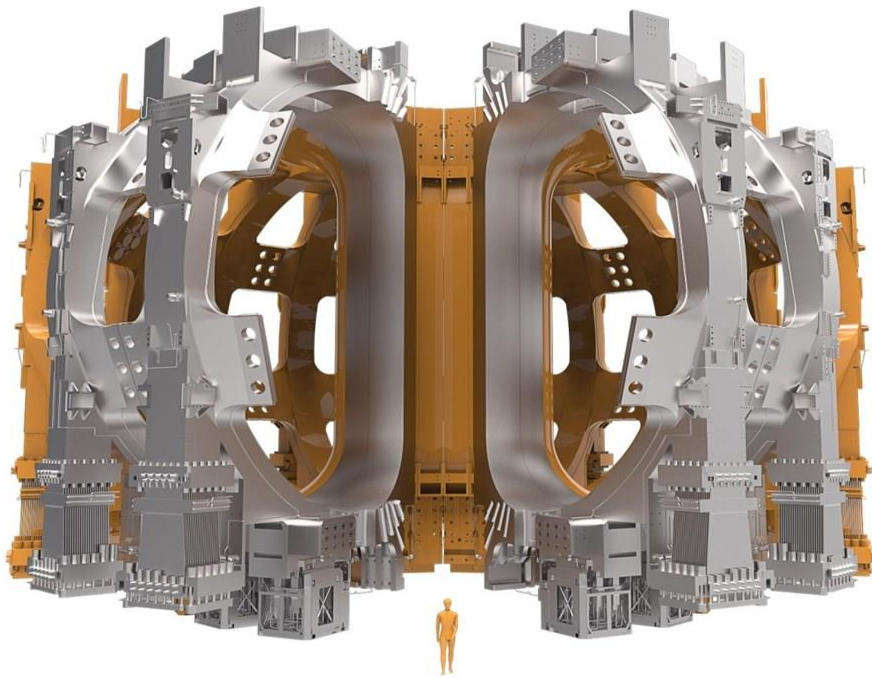


Figure 65: TFCs system in ITER [33]

The PFCs is composed of 6 ring-shaped poloidal field coils situated outside of the TFC structure to shape the plasma and ensure its stability.

The largest PFC has a diameter of 24 m while the heaviest will be 400 tons; they are also designed to have a total magnetic energy of 4 GJ and a maximum magnetic field of 6 T.

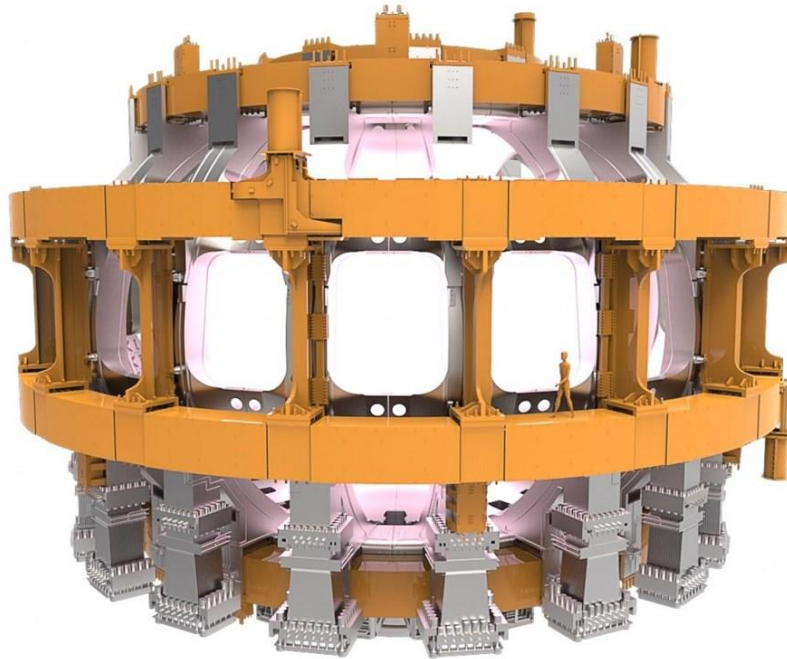


Figure 66: PFCs system in ITER [33]

The Central Solenoid is 13 m tall, 4 m wide and 100 tons in weight: the CS is made of six independent coil packs wound from niobium-tin superconducting cable.

The CS stored magnetic energy will be of 6.4 GJ which will sustain the plasma current of 15 MA for a duration of 300-500 s with a maximum magnetic field of 13 T by making the CS the most powerful magnet among all the superconducting magnets in ITER.

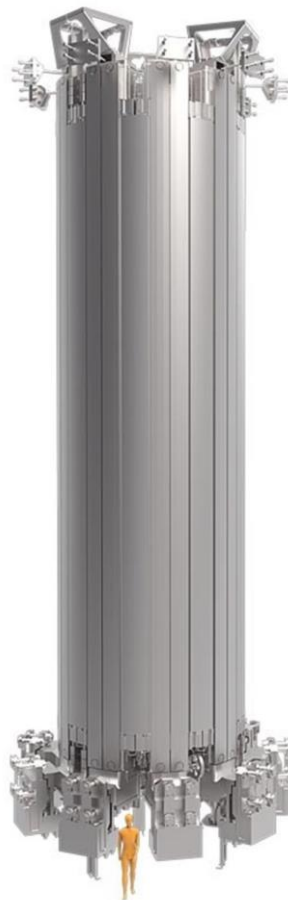


Figure 67: CS magnet system in ITER [33]

Among the main structure of the superconducting coils, there will be minor component but still necessary like correction coils whose main aim is to compensate field errors caused by geometrical deviations (manufacturing and assembly tolerances).

The magnet feeders are obviously vital for the operation of the Tokamak allowing the regulation of the temperature of the magnets and connecting the magnets to their power supplies.

5.6.3 Vacuum Vessel

The vacuum vessel, as widely expressed in the previous sections for other Tokamaks, provides a high-vacuum environment for the plasma, improves radiation shielding and plasma stability, acts as the primary confinement barrier for radioactivity and provides support for in-vessel components such as the blanket and the divertor.

In ITER vacuum vessel there will be 44 ports in order to provide access for remote handling operations, diagnostics, heating and vacuum systems.

The thermal shield will be composed of 2 layers interposed between the vacuum vessel and the cryostat to minimize heat loads transferred by thermal radiation and conduction from warm components.

The thermal shielding will be realized with stainless steel panels with a low emissivity surface (<0.05) actively cooled by helium gas flowing inside of a cooling tube welded on the panel surface [34].

5.6.4 Blanket

In the Tokamak there will be 440 blanket modules to completely cover the inner walls of the vacuum vessel.

Each blanket module measures 1 x 1.5 m and with a weight up to 4.6 tons for a full cover surface of $600 m^2$.

Due to the physical properties, beryllium has been chosen as the element to cover the first wall and depending on the position of the blanket module, two different kinds of panels have been the object of design: a normal heat flux panel designed

for heat fluxes up to $2 \frac{MW}{m^2}$ and an enhanced heat flux panel that can withstand heat fluxes of up to $4.7 \frac{MW}{m^2}$ [34].

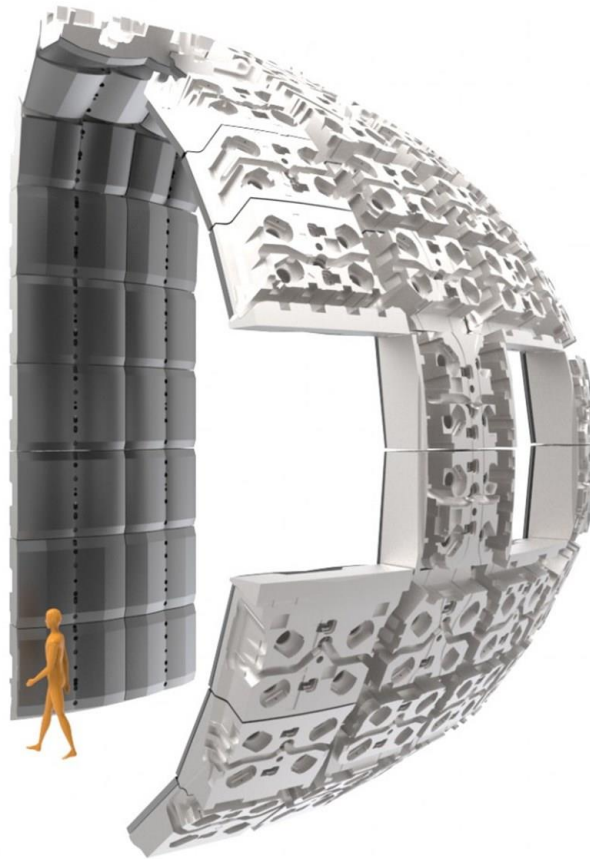


Figure 68: ITER Blanket design [34]

5.6.5 Divertor

As explained in previous chapters, the Divertor is needed to extract heat and ash produced by the fusion reaction, minimize plasma contamination, and protect the surrounding walls from thermal and neutronic loads.

At ITER there will be 54 *cassette assemblies* with a supporting structure in stainless steel and three plasma-facing components: the inner and the outer vertical targets and the dome.

The inner and outer vertical targets are positioned at the intersection of magnetic field lines where particle plasma will be very dense; the heat flux handled by the divertor vertical targets is estimated at $10 MWm^2$ in steady state.

The best metal to handle this kind of physical situations is tungsten with the highest melting point of all the metals.

It is foreseen to replace ITER divertors at least once during machine lifetime by remote handling.

5.6.6 Cryostat

The Cryostat is the largest stainless-steel high-vacuum pressure chamber ever built with 16.000 m^3 of volume providing high vacuum and ultra-cool environment for the vacuum vessel and the superconducting magnets.

The cryostat is composed by 23 penetrations to allow access for maintenance with over 200 penetrations for access of the cooling system, magnet feeders, diagnostics, auxiliary heating.

The cryostat is composed by four main sections which will be assembled on site before the transport to the tokamak assembly site as it can be seen in the next figure:



Figure 69: Cryostat in ITER [34]

5.6.7 Fast Discharge Units

Fast Discharge Units, as widely described in the document, are safety components in order to ensure the integrity of the magnets in case of quench by providing a fast discharge.

At ITER, the FDUs are fully passive components intended for dissipation of energy stored in the ITER magnetic system as a heat.

The modular approach for the design of the Discharge Resistor was chosen for TF, PF and CS FDU resistors: this is made by a resistive element with two current leads welded to its end and a steel casing, the resistive element is welded from mild steel cold-rolled 1 mm thick sheets in such a way as to form a tight zigzag pattern allowing for minimization of stray inductance of the resistive element.

The ITER FDUs are mainly composed by the following electrical components:

- BPS: Bypass Switch which is closed during normal operation, and it brings the full rated current of 68kA for TFCs. This is composed by a slow pneumatic drive.
- VCB: Vacuum Circuit Breaker which is used to bring the current while triggered during the opening sequence after the BPS (see 6.3 for more details). BPS and VCB are grouped in SWG (Switch Gear). VCB is composed by a fast-spring drive.
- CPC: Counter Pulse Circuit (bi-directional counter pulse unit) which main aim is to generate a counter pulse current in order to force the current flowing in the VCB to 0 A. This is composed by a thyristor bridge, a capacitance, and a charger of the capacitance.
- PB: Pyrobreaker, a backup component for the safety of the magnets as extreme ratio in case of failure of one of the components described above. The series of the SWG and PB is called MSU (Making Switch Unit), which includes also auxiliary components and parts like:
 - o Copper busbars for interconnection of the switches.
 - o Cable collector for connection of the switches with FDRs, CPC, and SC.
 - o Cooling water collector (CWC) which is a part of the switch and busbar cooling system.

- Firing Pulse Generator (FPG) for triggering the PB.
- SC: Snubber Circuit, optimized to reduce over voltages during transients.
- FDR: FDU Discharge Resistor, fixed resistor in order to discharge magnets as described above.

The simplified electrical circuit of ITER FDU can be seen in the next figure:

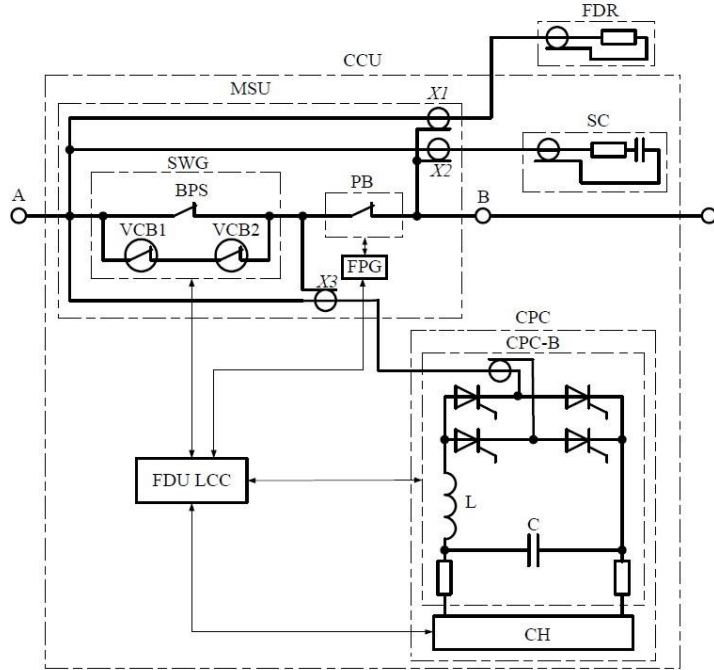


Figure 70: ITER FDU

The ITER TF FDUs are in series with the TFCs, each FDU is made for protection of 2 TFCs as described in the following figure:

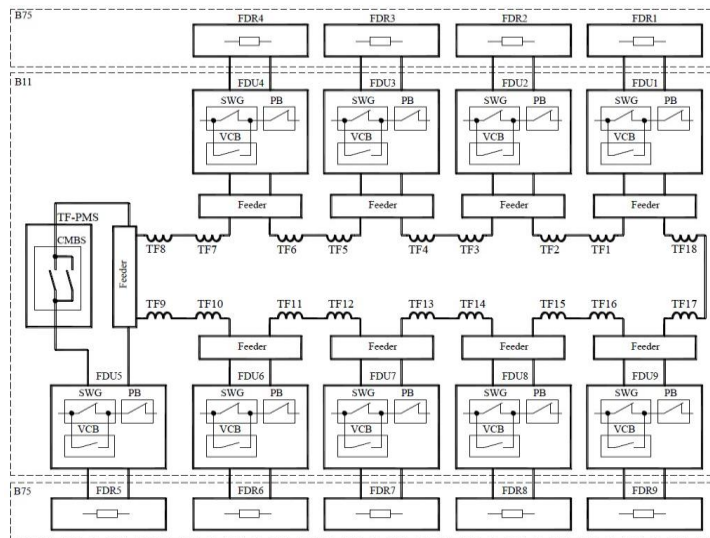


Figure 71: ITER TF FDUs simplified scheme

BPS normally carries the steady-state current during long-term operation of the TFCs.

When a signal initiating the fast discharge arrives from FDU LCC (Local Center Cubicle), the BPS contacts open, and current is transferred into the closed VCB contacts (which contains two vacuum bottles or interrupters connected in series to increase reliability).

Once the coil current has been fully transferred to VCB, the contacts in the VCB vacuum bottles open on the second command from LCC, and the electric arc appears between these contacts.

Current in SWG is finally interrupted by CPC and once the VCB contacts have been separated at a distance sufficient to withstand the high voltage that appears at current commutation from VCB to the discharge resistors, the pre-charged capacitor battery is discharged on third command from LCC via VCB in the direction opposite to the coil current, thus reducing the total current in VCB to zero.

The arc between the open VCB contacts is extinguished and the coil current is transferred into the discharge resistor called FDR.

In case of failure of SWG, the failure will be detected by zero current transducers (ZCD) forming part of PB and inserted in the circuit to be opened; the PB will be triggered providing protection of the coil.

6 Fast Discharge Units

This chapter will take into account the physical principle exploited for the extraction of the energy stored in magnets and which must be extracted in the event of failure of superconducting magnets.

In particular, all the research activities carried out during the three-year PhD and the related conclusions will be analyzed.

It should be noted that in some types of plants the terms QPC and FDU are used as synonyms, it should be remembered:

1. QPC stands for "Quench Protection Circuit"
2. FDU stands for "Fast Discharge Unit"

In some plants the term QPC is used (as for JT-60SA) while for others the term FDU (as for DTT, ITER and DEMO) but in both cases those are similar systems albeit with some differences at the design level, as seen in the related chapters.

In the case of quench, i.e., when the superconductor exits from the superconducting phase generating a local rise in temperature with consequent cascading of the entire magnet from the superconducting zone, this energy must be extracted as quickly as possible in such a way as to maintain the temperature at which the magnet is brought below its thermal limits (to analyze the phenomenon in detail refer to the section dedicated to the superconduction).

6.1 Fast Discharge Units on DTT

The DTT Superconducting Magnet System consists, as mentioned above, of [8]:

1. 18 TFCs divided into 3 groups of 6 (each group is protected by an FDU)
2. 6 PFCs equal in pairs (see Section 5.5.4)
3. 6 CS coils

In this paragraph the FDUs for TFCs are described with all the research tasks accomplished, which must dissipate a total stored magnetic energy of 2 GJ.

Figure 58: it can be seen how there are differences compared to the technical solutions adopted in ITER as there is no VCB (Vacuum Circuit Breaker) here and the interruption of the current and the subsequent deviation on the discharge resistors takes place through a mix of mechanical (BPS) and static (SCB) component.

It is noted that even in this case there is a backup protection provided by the Pyrobreaker (also present in ITER). The ground resistor instead is placed between the two Dump Resistors in order to halve the overvoltage that is generated on them at the time of discharge (as will be seen later).

This scheme was used as a starting point from which to then develop not only a more detailed model to simulate the discharge but also more efficient in terms of overtemperature reached, over voltages and discharge times.

With the model in Figure 58 there is an exponential discharge given by the time constant derived from the total inductance of the superconducting magnets and from the value of the Dump Resistor itself.

The limit value that was initially decided in order to have τ equal to 5 s as it allowed the establishment of a maximum temperature on the conductors equal to 312 K (simulating only the presence of the superconductor and not of all the coatings); having available the value of the total inductance of the TFC equal to $L = 2.272 \text{ H}$ ¹⁴ the following parameters were obtained:

1. $DR = 0,151 \Omega$
2. $V_d = 6,44 \text{ kV}$

¹⁴ It should be noted that some design values changed during the PhD Course and now are reported the values related to 2020 status.

3. $i^2t = 7,23 \text{ GA}^2s$

It is noted that in this case the overvoltage is the critical point and how it strongly depends on the value of τ chosen; in particular, a trade-off was found between all the operating parameters for the discharge of the FDU.

The principle of operation of the FDU is completely analogous to the FDU for JT-60SA, in particular the components present are the following:

1. Mechanical Bypass Switch (BPS) that conducts current during normal operating condition.
2. Static Circuit Breaker (SCB).
3. Dump Resistor (DR).
4. Pyrobreaker (PB).
5. Ground resistor.
6. Clamp circuit to limit surges.

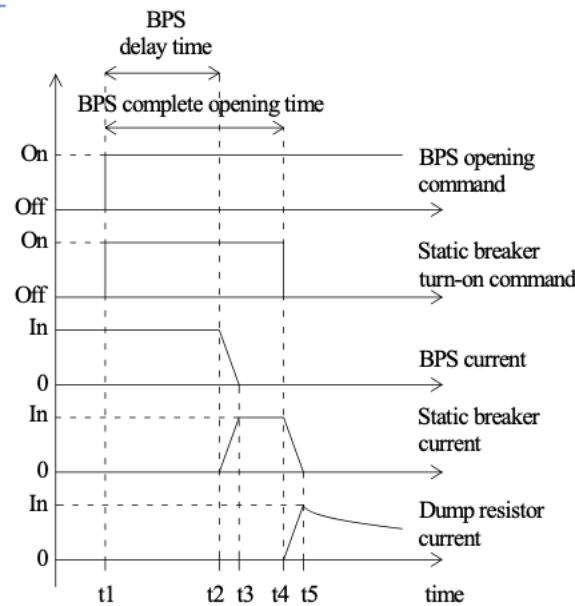


Figure 72: Opening sequence of TFC's FDU for DTT [4]

The BPS is closed during normal operation of the FDU, and it brings 44 kA¹⁵ to the superconducting coils; as stated before, the BPS is a mechanical breaker and when the opening sequence is triggered (t1) the arc occurs within the BPS.

¹⁵ This value was then updated to 42.5 kA according to design changes from superconducting team.

When the quench is detected, a delayed closing gate signal is given to the SCB (t2) and the current starts flowing in the SCB with a delay time due to the power electronic components (t3): the current on the BPS begins to decline until it reaches 0 A (t3). After a while, the opening sequence of the BPS can be considered concluded.

At t4 the opening gate signal is given to the SCB and all the current starts flowing in the Dump Resistor (t5): in this component the current (and hence the stored energy) is dissipated with an exponential trend since the total circuit can be considered as an R-L.

6.1.1 FDU Simulink model

In order to analyze two different configurations of DR, a Matlab-Simulink model was set up and in the following section all the schemes and results are reported.

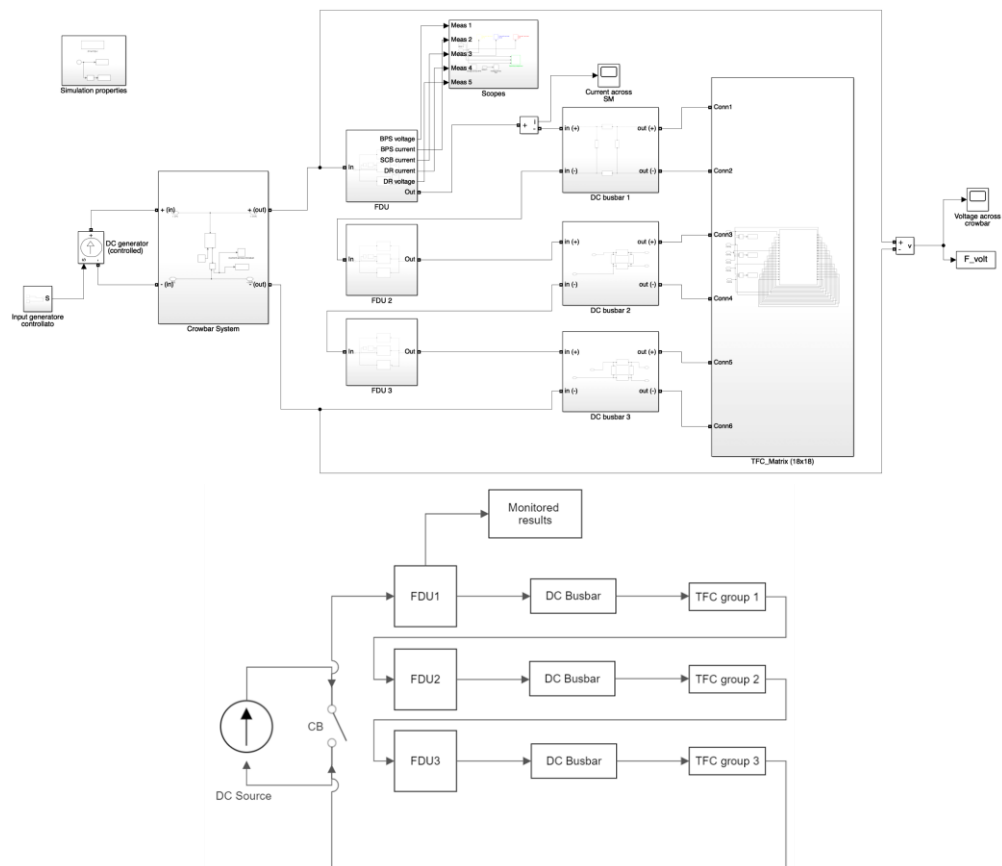


Figure 73: Complete electrical circuit on Matlab-Simulink for DTT [4] (up) and simplified block scheme for more legibility (down).

The previous figure shows the complete model (upgraded during the PhD) with all the related components, in particular:

- The DC controlled current generator is implemented in order to simulate DC current on the TFCs. The current is generated with a positive slope which is then added to an equal opposite slope to simulate the charge of TFCs up to 44 kA achieved in one second (just to speed up the simulation and to reduce time consuming).
- The Crowbar is simulated as an ideal switch controlled by a command signal that is given at the same time of the opening input of the BPS. The Crowbar creates a free-wheeling circulation of the current avoiding dangerous over voltages on the AC/DC converter power supply that feeds TF magnets, by closing the Crowbar there is a bypass on the power supply during the L-R discharge and the intervention of the FDUs.

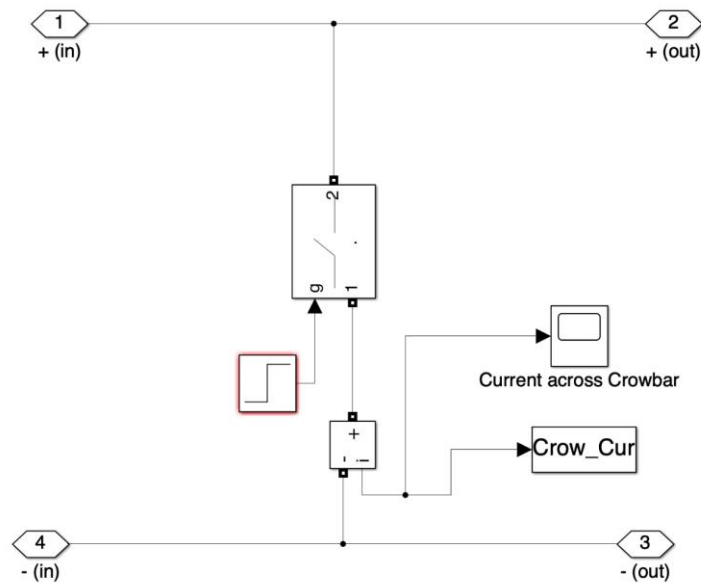


Figure 74: Crowbar circuit Simulink model [4]

- DC busbars are also simulated: those electrical components connect the FDUs, the TFCs with the TFC Power Supply.
- The load is represented as a self and mutual inductance matrix with all the 18 TFCs. The TFCs are fed in series at 44 kA and grouped in three sectors each composed by six TFCs in order to limit the maximum overvoltage at the coil terminals during safety discharge (that at the moment was about 1 kV).

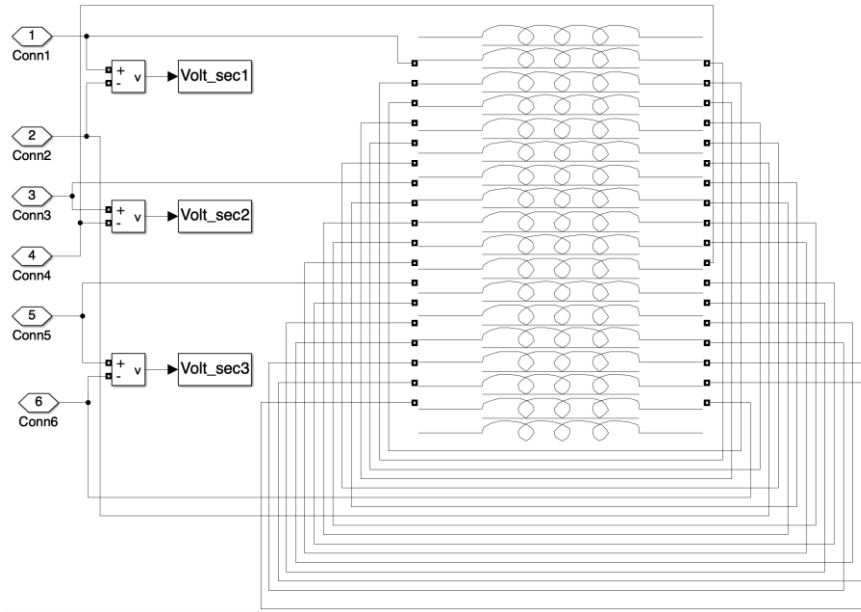


Figure 75: Self and mutual inductance matrix of Matlab-Simulink simulation [4]

The following tables show all the characteristics of the TFCs at the moment of the realization of the Simulink model and all the related characteristics of the FDU.

TFCS	Symbol	Value
Number of TFCs	N	18
Number of turns	N_t	80
Total inductance	L_t	2.067 H^{16}
Total energy	E_t	2.0007 GJ
Operating current	I_{op}	44 kA
Self-inductance	L	41.4 mH
Discharge time constant	τ	5 s
Delay time	t_d	1.5 s
Material	Nb_3Sn	

Figure 76: TFC characteristics (2020) [4].

TFC FDU	Symbol	Value
Number of FDUs	N	3
Dump Resistor for FDU	R	$0.138 \Omega^{17}$
Voltage applied to coil sector at the discharge	V_d	6.06 kV

Figure 77: FDU characteristics [4]

¹⁶ This value was later updated to 2.272 H, please refer to next section.

¹⁷ This value was later updated to 0.151 Ω due to changes in the TFC inductance parameter.

Two configurations of Dump Resistor have been simulated in order to evaluate time and speed of the discharge of the magnets and also the efficiency (taking also into account the specific energy through the Dump Resistors).

The first studied configuration is the one with fixed resistor with a value specified in the previous table while the second configuration is implemented with 15 identical branches and, in each branch, there are two DR in series with two Integrated Gate-Commutated Thyristors (IGCT) that control the insertion of a single DR branch like in the following figure.

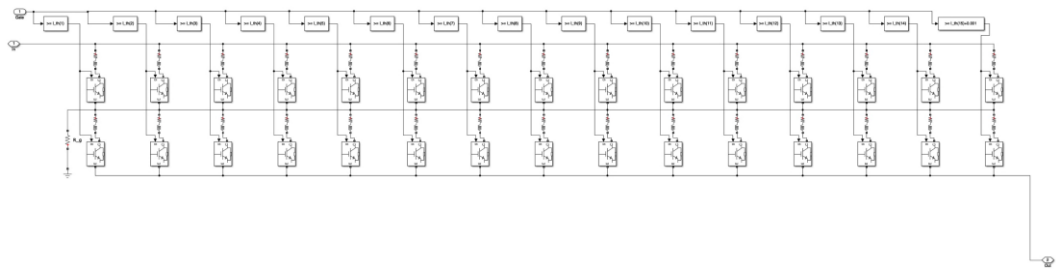


Figure 78: Dump Resistor simulated with IGCTs [4]

In the next figure it's just represented a zoom of the previous one on a couple of branches:

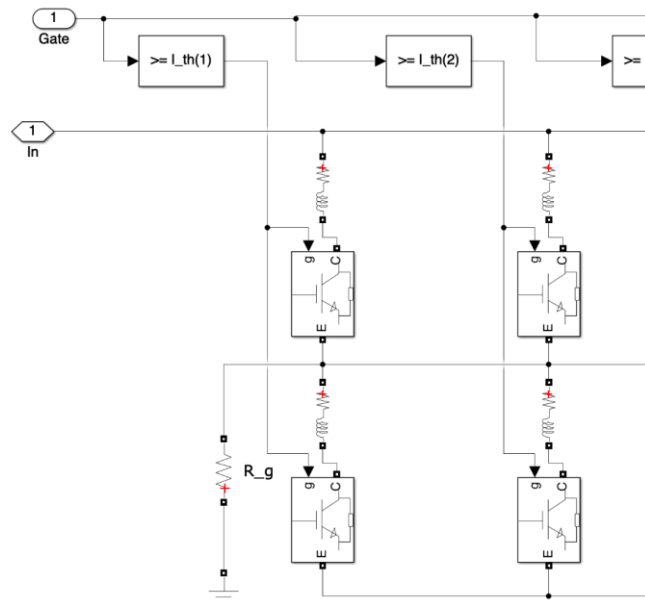


Figure 79: Zoom of the previous figure

In the next figure is represented the Matlab-Simulink block scheme for the FDU with the related BPS, SCB and DR:

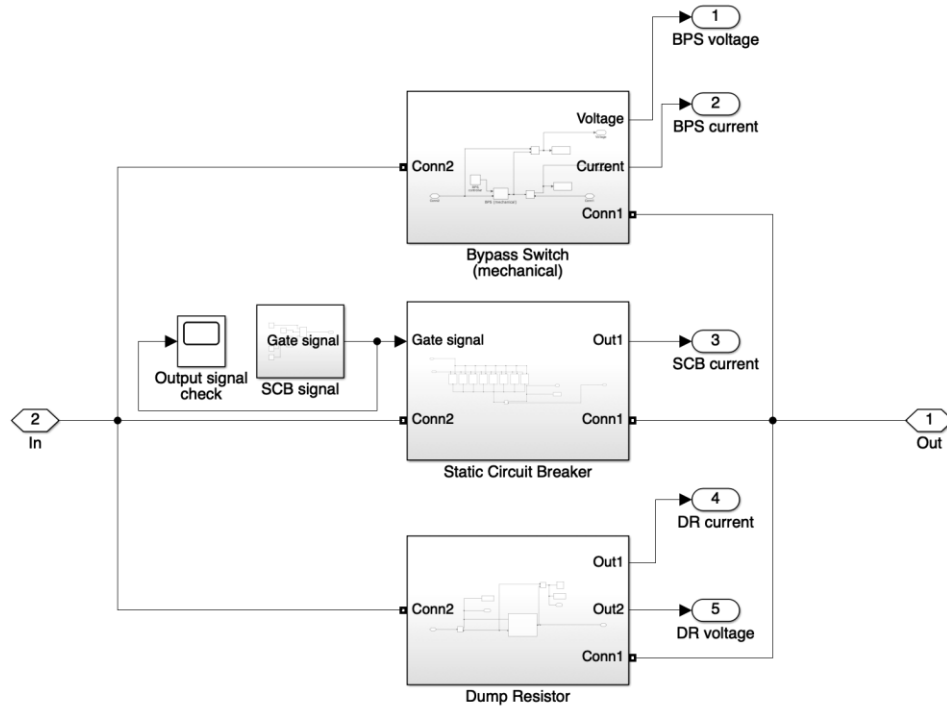


Figure 80: Matlab Simulink model of the FDU [4]

It should be noted that in this first PhD task the BPS was simulated with an ideal switch and later it was upgraded implementing the arc formation with the related transient at the opening allowing to simulate the natural current shift between BPS and SCB.

The SCB is demanded to bring the 44 kA when the quench is detected, and the opening sequence is realized with power electronics components (IGCTs).

6.1.2 Preliminary study with Fixed DR and Variable DR

The DR initially considered is fixed with a certain value depending on the desired time constant called τ .

The time constant is calculated as:

$$\tau = \frac{L}{R}$$

Where L is the equivalent inductance of the 18 TFCs equal to $L = 2.067 H$.

The time constant of about 5 s is the result of the trade-off between the need to have a discharge as fast as possible and to not stress the voltage insulation of the FDUs because it should be considered that the voltage at the beginning of the discharge is directly related to the DR value according to the DC law: $V_d = DR \cdot I_{op}$.

So, the first choice was to have a total resistance of $R = \frac{L}{3\tau} = 0.138 \Omega$ where at the denominator there is the total number of the FDUs which is equal to three.

In this way the global circuit is simpler but the final circuit during the quench is an R-L configuration with constant τ ; the 18 TFCs discharge in an approximate time of 20 s-25 s.

A new configuration was studied and implemented by replacing the fixed DR with multiple branches containing 2 IGCTs and 2 smaller DRs (in each branch) as reported in Figure 78, Figure 79 and generally simplified in the next figure.

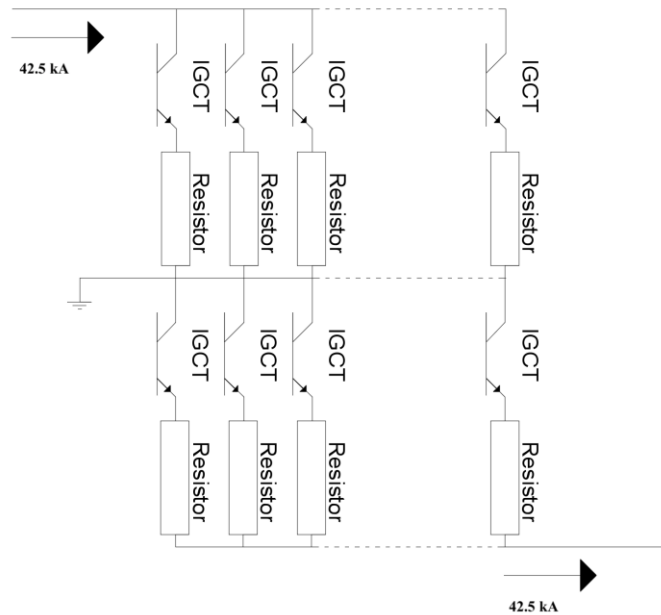


Figure 81: Variable DR electric simplified scheme [4]

The activation of each IGCT on a single branch is controlled by current thresholds in order to gradually open all the branches of the DR circuit by changing the τ value as a consequence and the voltage across the DR.

In this configuration the discharge is more efficient using the maximum available voltage across the DR for a longer period of time (see next figure).

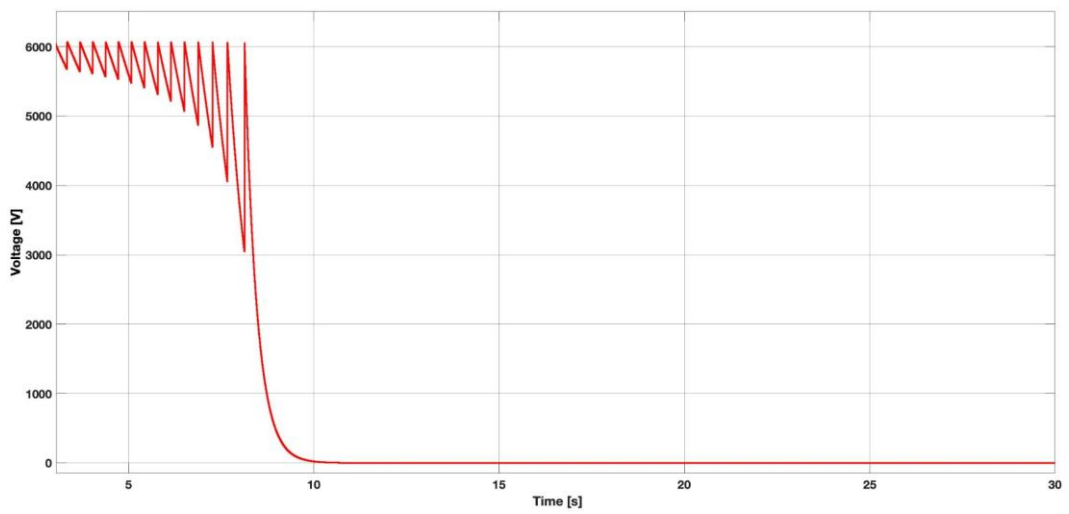
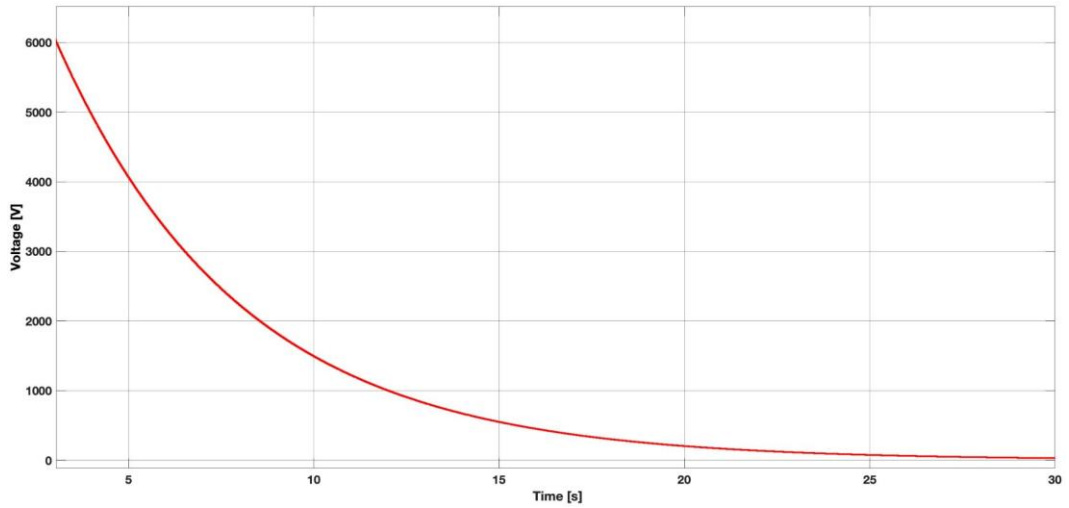


Figure 82: Voltage on fixed DR (up) and variable DR (down) [4]

In the following figures is also reported the opening sequence related to the current in the FDUs, in can be seen that the discharge with variable resistor is much faster than with fixed DR value (about 6 s).

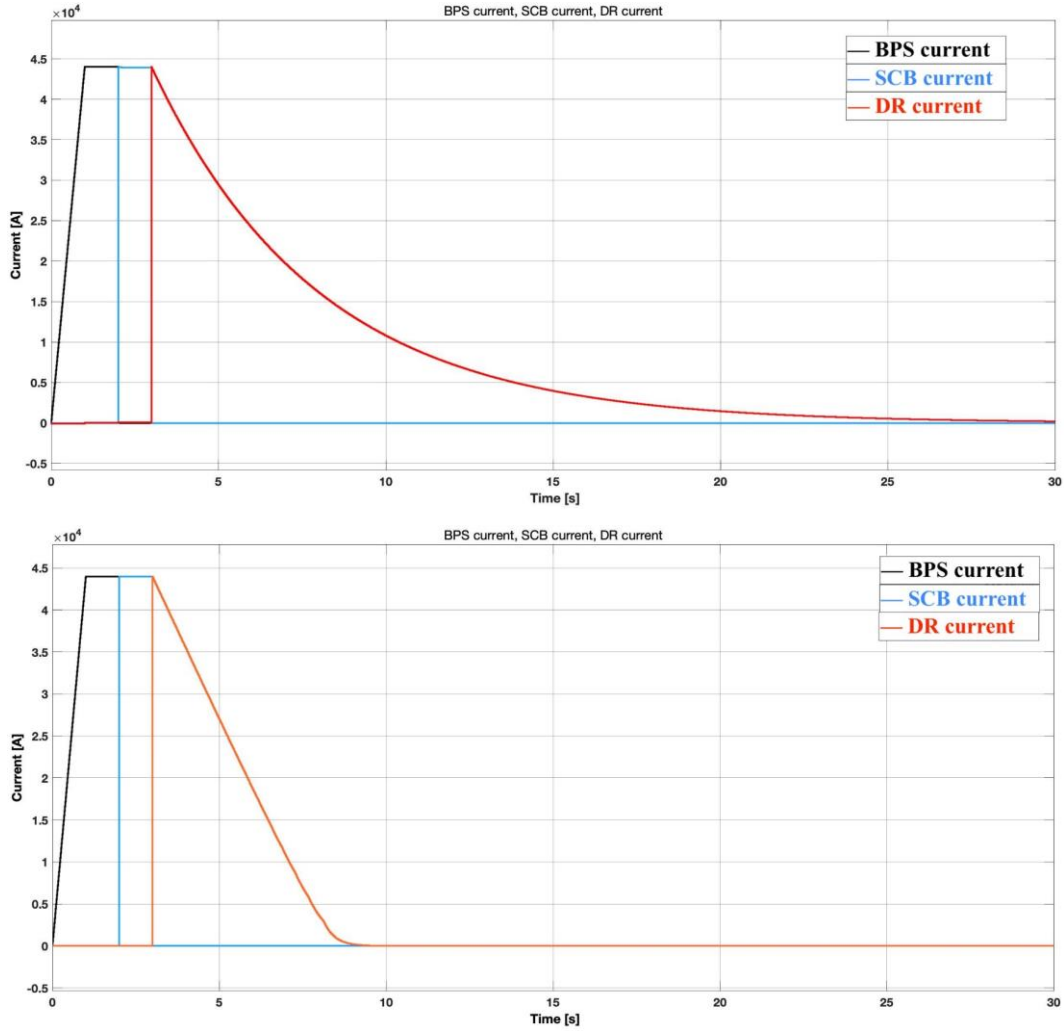


Figure 83: Opening sequence with fixed DR (up) and variable DR (down) [4]

In order to determine the correct value of the single branch resistance, it has been considered that the total value of the DR must be equal to the fixed DR:

$$R_{fixed} = 0.138 \Omega$$

$$R_{variable} = \frac{R_{fixed} \cdot 15}{2} = 1.035 \Omega$$

The value of $R_{variable}$ is for each resistor of each branch so the equivalent branch resistance is:

$$R_{branch} = 2 \cdot R_{variable}$$

The IGCTs must gradually open the circuit so the threshold values are calculated as follows [35]:

$$I_{th}(i) = \frac{n - i}{n} \cdot I$$

Where:

- $n = 15$ is the number of branches
- $i = 1, \dots, n$
- $I = 44 \text{ kA}$

The single branch current threshold is calculated as:

$$I_{th,b}(i) = \frac{I_{th}}{n - i + 1}$$

The equivalent resistance of the DR is calculated as:

$$R_{eq}(k) = \frac{n}{n - k} \cdot R_{fixed}$$

Where:

- $n = 15$ is the number of branches
- $k = 1, \dots, n$
- $R_{fixed} = 0.138 \Omega$

In both Figure 82 and Figure 83 the quench starts after three seconds of the beginning of the simulation and the current then flows from the BPS to the SCB (in this case as ideal switch so there is no transient) and, after 1 s, the SCB receives an opening gate signal and the current flows in the DR.

It should be noted that the discharge time for the fixed DR is 22 s and the discharge time for variable DR is 6 s with a reduction of the discharge time of 72%.

The specific energy through the DR is calculated by integrating the current and obtaining the following results:

- Fixed DR: $I^2t = 4.82 \text{ GA}^2\text{s}$.
- Variable DR: $I^2t = 3.37 \text{ GA}^2\text{s}$.

The total reduction of the specific energy through is of 30.08% and this reduces the thermal stress on the components [4].

It should be noted that in this case no delay time of the mechanical and static component was considered.

Figure 82 also shows the advantage by using a variable DR: in the first case the trend of the voltage is exponential, and it goes from 6 kV to 0 kV in 22 s. This is related to the exponential trend of the current which is also exponential.

In the second case the initial value is always the same (6 kV) and each time a single branch of the variable DR is opened, it is restored to the starting value allowing a faster discharge of all the coils.

6.1.3 Study with updated value of DR

After the preliminary study of the DR according to exponential and linear discharge, the value of the equivalent TFC matrix changed to 2.272 H due to design needs.

According to the new value, the DR value and other parameters changed as follow:

Parameter	Value	Unit
TFC equivalent inductance	2.272	H
Dump Resistor	0.151	Ω
Voltage T2T	6.5	kV

With the updated value of the DR, the discharge time with linear discharge is in 5.9 s (reduction of 75% of the time for the exponential discharge).

There are also some minor changes on the specific energy through which is now:

- $I^2t = 4.33 \text{ GA}^2\text{s}$ for fixed resistor.
- $I^2t = 3.02 \text{ GA}^2\text{s}$ for variable resistor.

The total reduction of the specific energy through is of 30%.

In the following figure are also reported the voltage trends for exponential and linear discharge: it can be seen how the initial value is always 6.4 kV but how, with each disinsertion of a single branch of resistors, it goes back to the initial value; as a result, there is an average value of voltage during the discharge greater than with fixed DR and this allows, as a consequence, a faster discharge.

It will be noticed later how the reduction of these parameters with variable DR (discharge time, specific energy through) can allow a change to the initial parameters of DR that also allow a reduction in the voltage applied to the FDU.

It has been seen how a linear discharge can be more efficient than an exponential one with important consequences also on the parameters just mentioned; it was therefore possible to carry out a feasibility study on the simulation with linear discharge starting from different values of the time constant τ (which, to be precise, will no longer have a constant value but will vary progressively during the discharge).

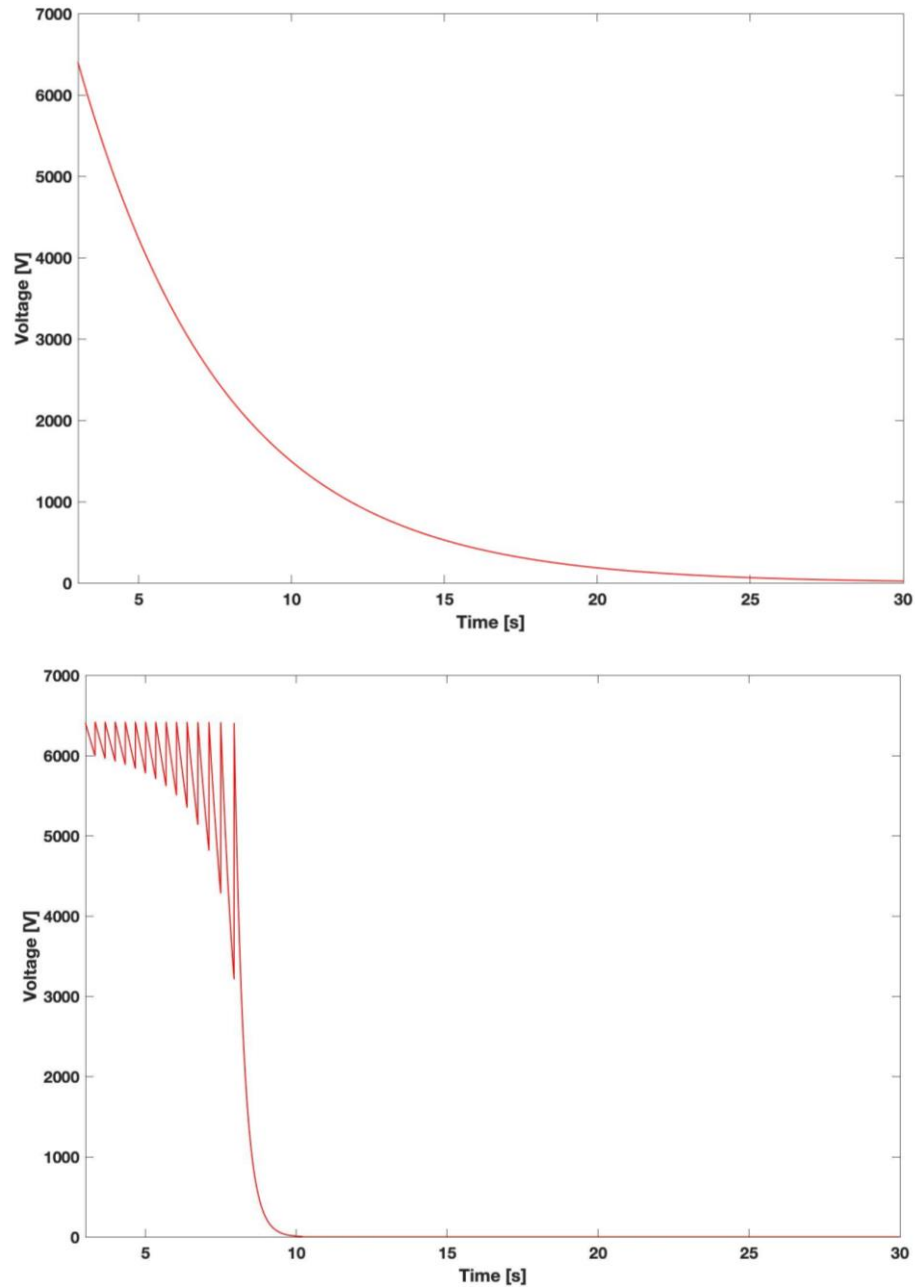


Figure 84: Voltage trend for exponential discharge (up) and linear discharge (down) with DR updated value.

It should be noted, in the context of recent statements, that from now on the value of the time constant and the linear discharge will be referred only to the initial value that the time constant assumes.

Simulations were then conducted in which the initial value of the time constant was varied with a cascading consequence on all the other parameters of the simulation (value of the DR and the voltage that is established, as well as the total discharge time).

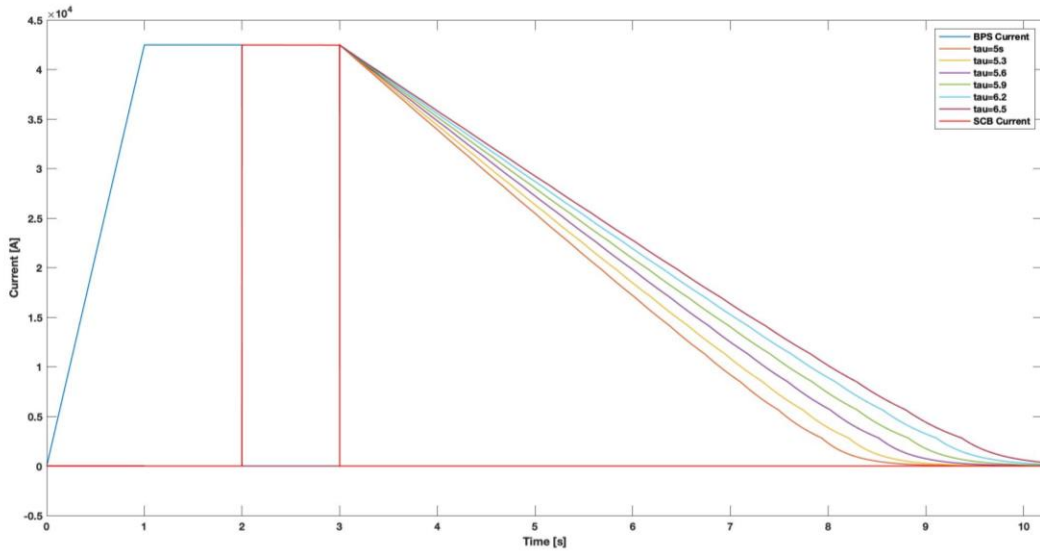


Figure 85: Different simulations with variable DR by changing the initial value of time constant [3]

It can also be noted that an increase in the time constant corresponds to a reduction in the voltage applied to the terminals of the FDU:

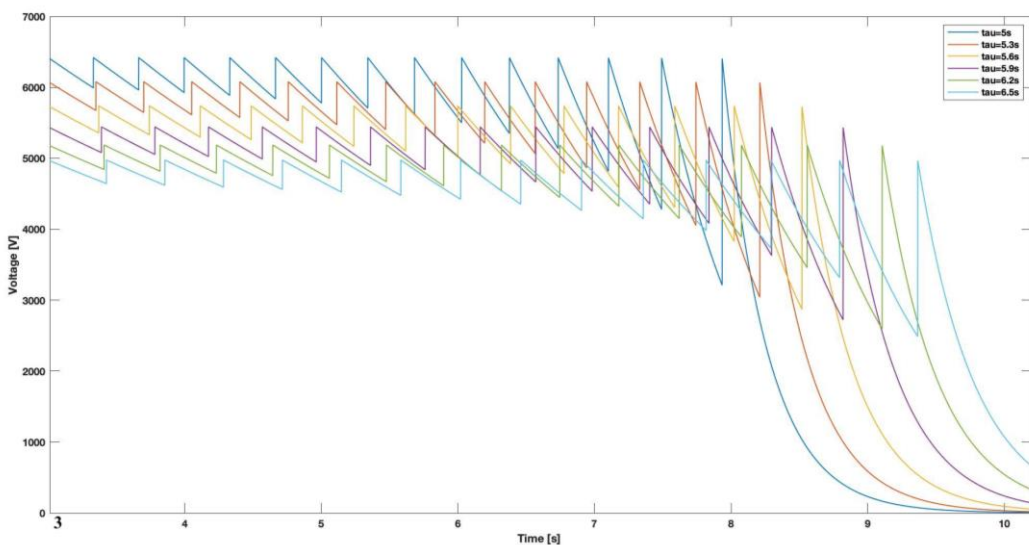


Figure 86: Voltage trends as a function of the time constant initial value [3]

The new simulations conducted with linear discharge considered the same value of the nominal current of 42.5 kA and equivalent inductance of 2.272 H; only the starting value of the time constant changed from 5 s to 6.5 s with an interval of 0.3 s, results can be seen later in this section.

These values of initial time constant were taken into account in such a way as to find an initial value of time constant that could allow to have acceptable values in terms of overvoltage and temperature to which the superconductors were brought.

The next summary table shows the values of discharge time, voltage, hotspot temperature on the superconductor, initial value of the DR, specific energy passing through in the case of exponential discharge and linear discharge.

Exponential discharge						
τ [s]	Discharge time [s]	Dvmax [V]	Hotspot temp. [K]	Fixed DR [Ohm]	$I^2 \cdot t$ [GA ² *s]	
5	23,5	6437,33	312	0,151	4,33	
Linear discharge						
τ [s]	Discharge time [s]	Dvmax [V]	Hotspot temp. [K]	Initial value of DR [Ohm]	$I^2 \cdot t$ [GA ² *s]	
5	5,9	6437,33	197	0,151	3,0262	
Related to exp.	%	-74,89	0,00	-36,86	0,00	-30,11
	5,3	6,3	6072,96	207	0,143	3,1953
Related to lin. $\tau=5$	%	6,78	-5,66	5,08	-5,30	5,59
Related to exp.	%	-73,19	-5,66	-33,65	-5,30	-26,21
	5,6	6,7	5747,62	220	0,135	3,3845
Related to lin. $\tau=5$	%	13,56	-10,71	11,68	-10,60	11,84
Related to exp.	%	-71,49	-10,71	-29,49	-10,60	-21,84
	5,9	7,2	5455,37	232	0,128	3,5694
Related to lin. $\tau=5$	%	22,03	-15,25	17,77	-15,23	17,95
Related to exp.	%	-69,36	-15,25	-25,64	-15,23	-17,57
	6,2	7,4	5191,40	245	0,122	3,7448
Related to lin. $\tau=5$	%	25,42	-19,35	24,37	-19,21	23,75
Related to exp.	%	-68,51	-19,35	-21,47	-19,21	-13,52
	6,5	7,5	4951,79	258	0,117	3,9046
Related to lin. $\tau=5$	%	27,12	-23,08	30,96	-22,52	29,03
Related to exp.	%	-68,09	-23,08	-17,31	-22,52	-9,82

Figure 87: Main results for changing time constant value with linear discharge [3]

The parts highlighted in yellow are those which needed to be focused for further feasibility studies and with regard to the possible distribution of IGCT failures because, being a more complex system, it was necessary to study the possible consequences regarding the malfunction of one or more static components.

With reference to the previous table, the initial term of $\tau = 6.5$ s was discarded because the superconductor was brought to a temperature above 250 K (considered the maximum value), therefore the focus was on the values of $\tau = 5.9$ s and $\tau = 6.2$ s.

The parameters of the FDU are resumed as follow:

1. $L = 2.272 H$ equivalent inductance of TFCs.
2. $\tau = 5 s$ time constant of exponential discharge.
3. $\tau = 6.2 s$ **initial** (fictitious) time constant of linear discharge.
4. $t = 7.4 s$ discharge time.
5. $V = 5191.40$ maximum voltage at the ends of the single FDU.
6. $T = 245 K$ Hotspot temperature reached by the magnet at the end of the discharge in t seconds calculated with a separate script starting from the discharge current as a function of time in adiabatic conditions (extremely conservative).
7. $R_{DR} = 0.122 \Omega$ equivalent value of the DR at the beginning of the discharge: this is given by the equivalent parallel resistance of all the resistors in Figure 81.
8. $n = 15$ number of IGCT branches in parallel.
9. $I^2t = 3.74 GA^2s$ specific energy passing through during discharge.

It should be noted that in order to be able to compare the exponential discharge and the linear discharge it is necessary to consider only and exclusively the initial value of the Dump Resistor as this value changes for $t > 0$ for the linear discharge (while it remains constant for the exponential discharge); for this reason the value of the time constant τ is merely for information and comparative purposes because, varying the value of the resistance, it varies during discharge.

The value of the time constant was taken into account since it is a fundamental parameter for the design of superconducting magnets.

Please note that, with the parameters considered above, it can be possible to have the following discharge performance:

1. Reduction of discharge time by 68.51%.
2. Maximum voltage reduced by 19.35%.
3. Hotspot temperature at the end of discharge reduced by 21.47%.
4. Specific through energy reduced by 13.52%.

The new configuration with IGCT has the advantages just specified and, in addition, allows to maintain three FDU instead of six resulting in a reduction in costs albeit with an increase in the complexity of the system.

Due to the presence of multiple components of power electronics, it was necessary to conduct a fault analysis in order to establish the maximum number of IGCTs faults simultaneously tolerable with the relative parameters in terms of discharge time, specific through energy and hotspot temperature; it should be specified that the fault analysis has also been extended in the event that the IGCT suffers a failure in conduction and therefore cannot be triggered for closure.

The only reason why the aforementioned case can occur is in the absence of the trigger signal inside the optical fiber (for example for the breakage of the same); in any case, before the magnets are powered, an automatic check is made of the integrity of all the control systems by the *Local Control System* through a self-diagnostic system, therefore this eventuality is avoided a priori (in any case the FDU is sufficiently tolerant in the presence of such failures, as will be seen later).

In-depth studies were then carried out on the possibility of failure of individual IGCTs following two criteria:

1. With the same number of IGCTs faults, the worst-case scenario is taken into account.
2. When a faulty IGCT has to be simulated, it is simulated among the first available in chronological order of opening as this corresponds to the most critical scenario (it is the one that determines a failure scenario that lasts for longer).

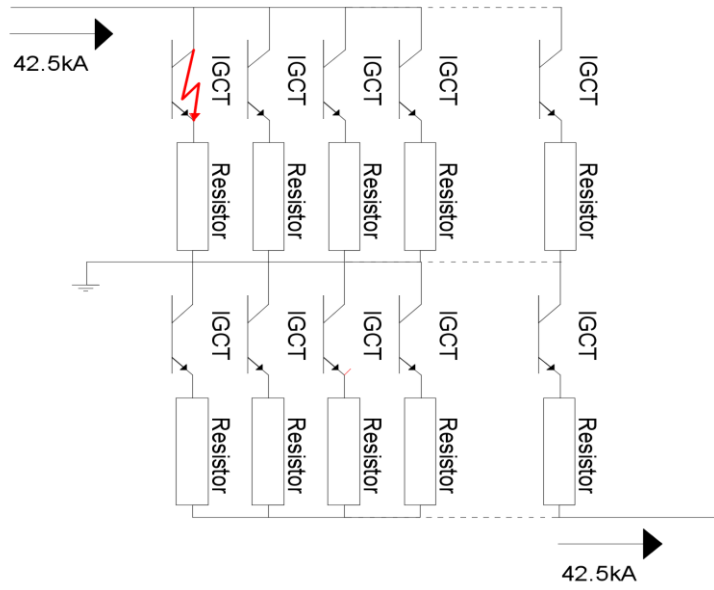


Figure 89: Example of Scenario 1 with single IGCT fault [3]

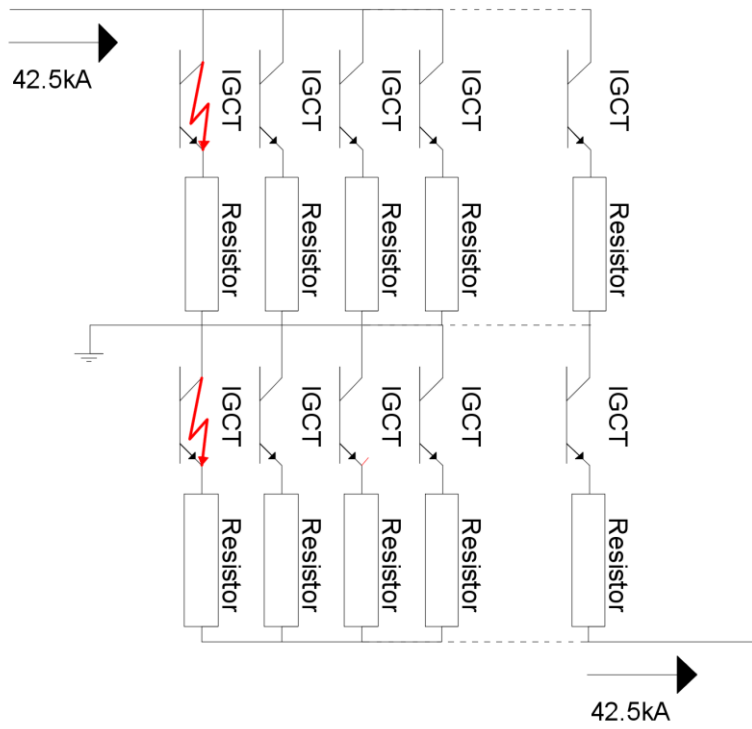


Figure 88: Example of Scenario 3 with 2 faults [3]

According to the results of the next table, when the considered time constant is $\tau = 6.2 \text{ s}$, 3 faults can be accepted:

Dump Resistor iniziale [Ohm]		Dvmax [V]			
0,122		5191,40			
τ [s]	Numero di IGCT guasti	Tempo di scarica [s]	$I^2 \cdot t$ [GA ² *s]	Temperatura HS [K]	
6,2	0	7,427	3,7448	245	
Scenario	1	1	7,690	249	
	2	2	7,835	252	
	3	2	7,987	253	
	4	3	7,931	253	
	5	3	8,148	256	

Figure 90: Fault scenarios for $\tau = 6.2$ s [3]

It can be noted that, in this case, the maximum allowed scenario is a scenario 5 corresponding to 3 failures:

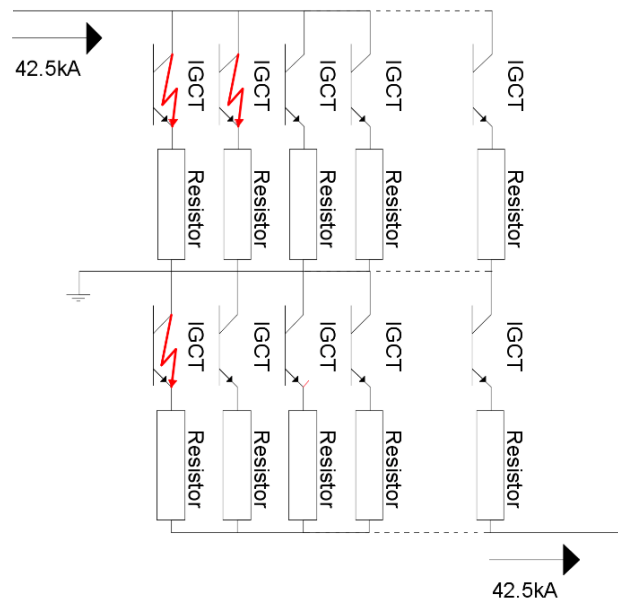


Figure 91: Scenario 5

However, it can be seen from the simulations carried out that with the same number of failures, the scenario in which the faulty IGCTs are located in the same branch is more serious than on individual different branches.

In the following table are reported the results with $\tau = 5.9$ s:

Dump Resistor iniziale [Ohm]		Dvmax [V]				
0,128		5455,37				
τ [s]	Numero di IGCT guasti	Tempo di scarica [s]	I^2*t [GA ² *s]	Temperatura HS [K]		
5,9	0	7,079	3,5694	232		
Scenario	1	1	7,330	3,6144	236	
	2	2	7,468	3,6465	238	
	3	2	7,613	3,6609	239	
	4	3	7,560	3,6690	240	
	5	3	7,766	3,6942	242	
	6	4	7,626	3,6846	241	
	7	4	7,868	3,7176	243	
	8	4	7,928	3,7283	244	
	9	5	8,035	3,7525	246	
	10	6	8,145	3,7772	248	
	11	7	8,224	3,7944	249	
	12	8	8,304	3,8119	250	

Figure 92: Fault scenarios with $\tau = 5.9$ s [3]

It can be seen that in this case it is allowed up to a scenario 12, corresponding to 8 IGCT failures (i.e., the first 4 branches of the DR completely broken and therefore remained closed).

The following conclusions can therefore be reached:

1. With the same IGCT failures, a scenario corresponding to two IGCTs failing on different branches is better than a scenario with the two IGCTs failing on the same branch.
2. With a constant of time $\tau = 6.2$ s it is possible to have up to 3 IGCT failures exactly as in scenario 3 described above.
3. With a constant of time $\tau = 5.9$ s it is possible to have up to 8 IGCT failures exactly as described above or with the first four branches of the DR completely failed.

Considering these results, the proposal made regarding the design of the FDU corresponds to a variable DR based on IGCT to have a linear discharge; it allows to have the following advantages:

1. Reduction of the maximum temperature reached by the magnet up to 250K and no longer 312K.
2. Reduction of the overvoltage established at the heads of the FDU from 6.4 kV to 5.45 kV.
3. I^2t reduced by 30% compared to the exponential discharge with consequent lower thermal stress for the components.

4. The lowering of the maximum voltage allows the maintenance of 3 FDUs to protect each of a group of 6 TFC.

6.1.4 Guided User Interface for IGCT MTTF study

Finally, a study was conducted on the MTTF values of both the variable DR and the BPS based on IGCT referring to ABB's data sheets and considering a junction temperature of 125 ° C, voltage reported above and height above sea level equal to 300 m (altitude of the construction site at the Research Centre of Frascati).

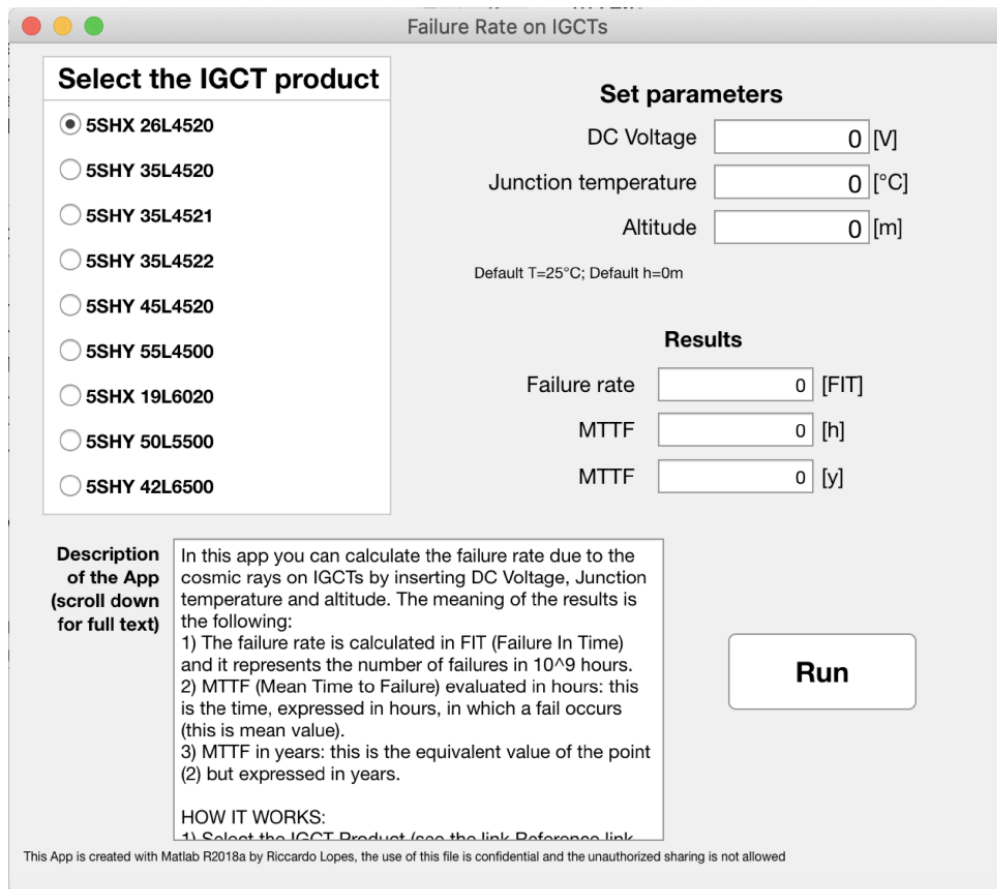


Figure 93: IGCT MTTF calculation GUI.

The app allows to calculate the failure rate due to the cosmic rays on IGCTs by inserting DC Voltage, Junction temperature and altitude.

The meaning of the results is the following:

- The failure rate is calculated in FIT (Failure in Time), and it represents the number of failures in 10^9 hours.
- The MTTF (Mean Time to Failure) evaluated in hours: this is the time in which a failure occurs (mean value).

- MTTF in years: equivalent value of previous point but expressed in years.

The chosen IGCTs can be seen in the next figure:

	IGCT	Vmax/Vdc perm.[kV]	MTTF ¹ [Year]
Switched DR	5SHY 35L4522	2,8 kV/2,8kV	∞
BPS	5SHY 42L6500	5,5 kV/4kV	10

Figure 94: MTTF values for proposed Switched DR and BPS [3]

6.1.5 Arc voltage and current transient modelling

Following the simulations carried out on the Dump Resistor, it was necessary, in order to obtain a simulation as complete as possible, to model the arc that is formed at the terminals of the Bypass-Switch following the opening command by the FDU control.

Arc resistance is a function variable over time and dependent on different parameters that will be analyzed in detail in the following paragraphs.

The scientific literature has introduced in the past several empirical formulas for the modeling of the arc resistance that is formed when opening a switch, taking into account, however, that the arc phenomenon is a stochastic phenomenon that does not always occur with the exact same magnitudes of voltage and current even in the presence of the identical laboratory conditions and, therefore, the relationships that are identified are necessarily empirical and with a particularly accentuated error threshold.

In the literature there are the Stokes-Oppenlander relations that present an average deviation of *the steady state arc voltage* equal to 27.3% and up to a maximum deviation of 45% (with a consequent lower ability to predict the results from the laboratory and less reliability of the model [1]).

One of the most present models in the literature is that of Mayr-Cassie; it consists of two differential equations that allow to derive the function of arc conductance as a function of time [1].

Over the years, several models have always been developed based on empirical relationships and confirmed by laboratory tests such as models based on *Multiple Linear Regression*, models based on the Stokes-Oppenlander equations but

readapted with new coefficients, models based on the maximum power transfer of the arc by convection and radiation, but also Ayrton equations, Steinmetz, Nottingham, Vand and Warrington and many more [1].

The model used was developed on Matlab/Simulink taking into account the following hypotheses [1]:

1. The model takes into account different hypotheses based on different models that will be deepened in the appropriate sections.
 2. The model is based on the Mayr-Cassie equations regarding the implementation of arc conductance as a function of time.
 3. The model also takes into account Paukert's hypotheses for low voltage arcs for the calculation of *steady state arc voltage*.
- I. Time constants were extrapolated from JT-60SA's BPS tests.

6.1.5.1 Resume on different arc voltage calculation approaches

There are different methods in order to evaluate the arc parameters, which can be resumed as follow:

Ayrton formulated the first equation in 1902 for the modelling of the arc voltage in steady state, it was obtained from an arc in the air on two separate electrodes of a few millimeters [36]:

$$V_{arc} = A + BL + \frac{C + DL}{I_{arc}}$$

Where:

- A is the electrode voltage drop.
- B is the voltage gradient.
- L is the arc length.
- C and D are constants related to the nonlinear characteristic of the arc.

In 1906 Steinmetz derived a semiempirical V-I relation based on carbon and magnetic arc experiments [37]:

$$V_{arc} = A + \frac{C(L + D)}{I_{arc}^{0.5}}$$

Where:

- A, C and D are constants.
- L is the arc length

Nottingham studied the arc behavior in 1920 bringing to this equation [37]:

$$V_{arc} = A + \frac{B}{I_{arc}^n}$$

The constants A and B are related to arc length and electrode material and n varies as a function of the electrode material.

In 1931, Van and Warrington founded a V-I characteristic of a stable arc for arcing currents between 100 A and 1000 A [37]:

$$V_{arc} = \frac{8750L}{I_{arc}^{0.4}}$$

Where L is the arc length in feet.

Stokes and Oppenlander conducted the most exhaustive study of free burning vertical and horizontal arcs between series electrode in open air [37].

The model of the arc voltage calculated is above a transition point defined as $I_t = 10 + 0.2 z_g$ where z_g is expressed in mm and is the length of the gap.

Above the transition point, voltage and resistance are defined as follow:

$$\begin{cases} V_{arc} = (20 + 0.534z_g)I_{arc}^{0.12} \\ R_{arc} = \frac{20 + 0.534z_g}{I_{arc}^{0.88}} \end{cases}$$

The starting equations are the known Mayr-Cassie ones, they serve to simulate the arc conductance at the terminals of the BPS. The equations are as follows:

$$\begin{cases} \frac{dg_m(t)}{dt} = \frac{1}{\tau_m} \left(\frac{i^2(t)}{P_0} - g_m(t) \right) \\ \frac{dg_c(t)}{dt} = \frac{1}{\tau_c} \left(\frac{i^2(t)}{u_c g_c} - g_c(t) \right) \end{cases}$$

From which the total arc strength is derived:

$$R_{arc} = \frac{1}{g} = \frac{1}{g_m} + \frac{1}{g_c}$$

Where:

1. g_m is Mayr's conductance.
2. g_c is Cassie's conductance.
3. τ_m is Mayr's time constant.
4. τ_c is Cassie's time constant.
5. $i(t)$ is the arc current as a function of time.

6. P_0 are the power losses in *steady state* by convection and radiation.
7. u_c is the arc voltage in *steady state*.

Experimental studies have shown how the Mayr component of the equations just described allows to simulate the behavior of the arc at the end of the transient while the Cassie component in the very first moments [38].

As mentioned above, the phenomenon to be described is characterized by a high degree of uncertainty and therefore the choice of the correct parameters must be considered as a general choice that can be different from those that will then be the final values obtained experimentally.

For the calculation of u_c and P_0 refers to Paukert's studies on DC and AC arcs in different geometric configurations and with current range from 0.3 A to 100 kA [37], in particular:

$$u_c = 13.04 \cdot I_{arc}^{0.098} = 37.05 V$$

The arc current was considered equal to the nominal current of the BPS and therefore $I_{arc} = 42.5 kA$ not assumed as a short-circuit current since in this case the intervention of a FDU does not occur in the presence of a short circuit but in the presence of quench of a superconductor that does not determine a significant increase in the nominal current.

From *the steady state arc voltage*, it is possible to derive the loss of power in *steady state* by convection and radiation:

$$P_0 = u_c \cdot I_{arc} = 1.575 MW$$

The time constants were instead derived from the experimental BPS data of JT-60SA. Starting from those data and readapting them according to the different values of nominal current, it is possible to obtain [39]:

$$\begin{cases} \tau_m = 7 ms \\ \tau_c = 1.5 ms \end{cases}$$

6.1.5.2 Arc simulation Matlab/Simulink model

In this section, the model implemented on MATLAB/Simscape Electrical (Simulink) with the fundamental BPS models are implemented.

The arc conductance is calculated starting from the two inductances calculated individually according to the equations of the model just described and then make the sum at each moment and then derive the arc resistance.

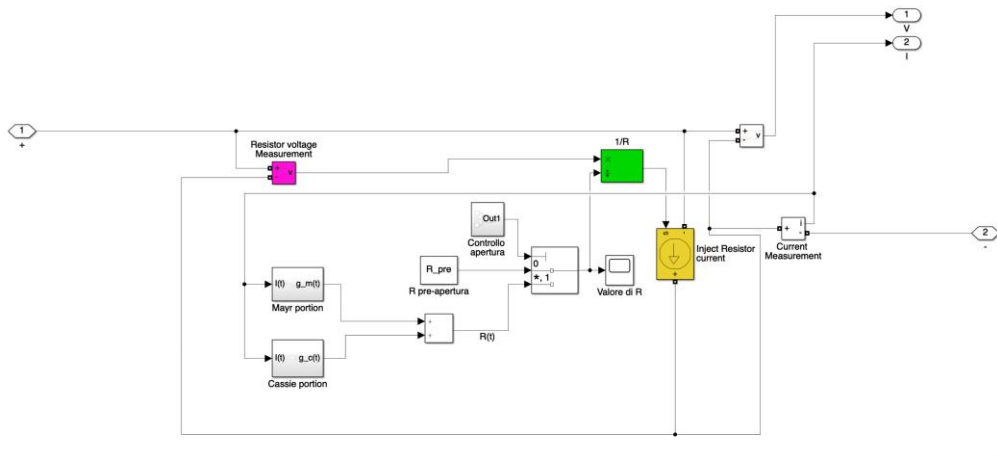


Figure 95: Matlab-Simulink block for implementation of Mayr-Cassie model [1]

On Simscape Electrical it is not possible to insert a variable resistor whose value is controlled by a time function therefore it is modeled as a voltage at the ends of the variable resistance block on the value of the resistance itself (obtained from the Mayr-Cassie equations calculated in real time); subsequently the output is used as an input by a controlled current generator, it determines the circulating current on the variable resistance (which corresponds, therefore, to the arc current).

6.1.5.3 Arc voltage simulation results

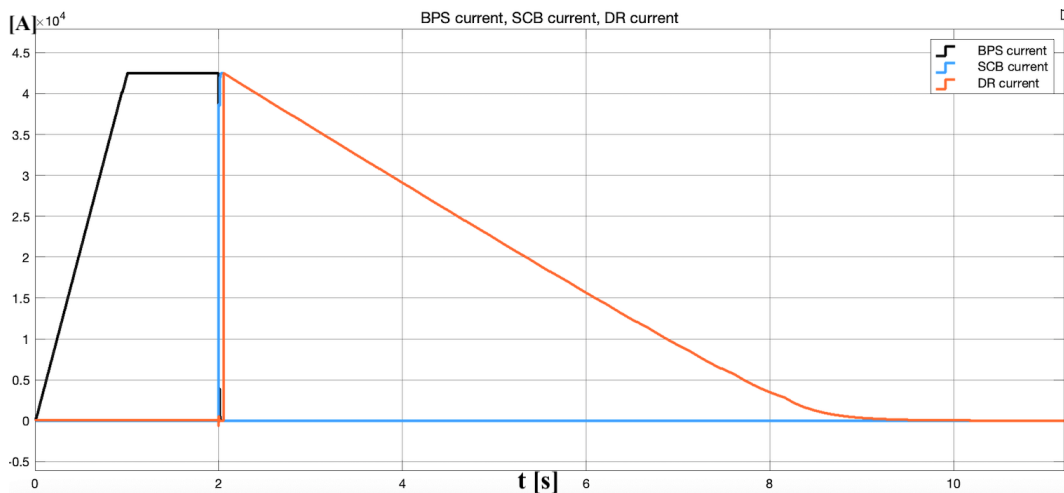


Figure 96: FDU Opening sequence (SCB opening at t=2 s) [1]

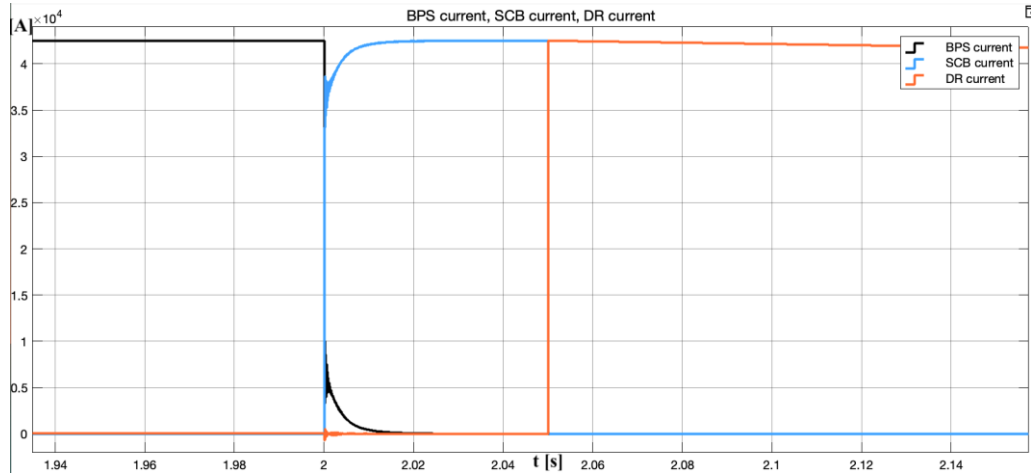


Figure 97: Zoom on opening sequence at $t=2$ s [1]

Previous figures show the opening sequence where:

- In 1 s the current reaches the rated value of 42.5 kA.
- At $t=2$ s the opening signal is given to the FDU, and the current starts to flow from the BPS to the SCB (and after that, on the DR).

Figure 97 shows a zoom on the opening transient where the current starts flowing from the BPS to the SCB; the arc is extinguished after 25-30 ms (not taking into account the mechanical delay of the BPS).

6.1.5.4 Ansys Simplorer implementation

The model just describe was subsequently used for the study of the electrical transient of the TFCs during a fast discharge in order to evaluate the voltage and the current trend in the first instants of opening the circuit and thus be able to best size the insulation levels.

When the FDU intervenes, there is an overvoltage at the terminals of the TFCs; the model including the FDUs, the arc model and the superconducting magnets allow to investigate the distribution of voltage at the terminals of the magnets but also at the terminals of each single Double Pancake (DB).

The simulation was implemented in two different operating conditions: the first is in the absence of faults and the second is in the presence of an earth fault [5].

The model will be described in detail in next Sections in which the three TF blocks and the three FDUs are modeled.

Each TFC model includes the input and the output ports for each DB and the ground connection.

The 18 sub-circuits are divided into three groups: each group is connected in series, and they are all connected in series to the TFPS (Toroidal Field Power Supply) with the Crowbar in parallel. The busbars were modeled with a resistance of $R_{busbar} = 116 \mu\Omega$ and an inductance of $L_{busbar} = 460 \mu\Omega$.

The TFPS has been modeled as a DC current source while the Crowbar has been modeled as an ideal switch connected in parallel to two earth resistors (whose central point is connected to earth) with value $R_{ER} = 1 k\Omega$.

Thanks to this simulation it was possible to evaluate the trend of over voltages at the terminals of each superconductor group but also at the terminals of each DP inside the model allowing a correct evaluation of the level of insulation to be used for the individual components: for further details on the simulation refer to the Ansys-Simplorer Model section.

6.1.6 Ansys-Simplorer Model for electric transient during a Fast Discharge

The simulations presented in the previous section were subsequently implemented in a simulation model in an Ansys-Simplorer environment going to simulate, in addition to the FDUs in the latest version (complete FDU of DR with linear discharge through IGCT and arc simulation) also the TF magnets of DTT to be able to study their behavior in terms of electrical parameters during a rapid discharge and in the presence of a fault condition; in particular, the parameters analyzed are mainly over voltages and voltage distribution on TF magnets and on each *double pancake* inside the magnet itself.

The simulation was carried out to study the voltage level to which the toroidal magnet is brought and then verify that the degree of insulation is adequate both in the absence and in the presence of failure (two different types of failure have been studied).

The objective of the simulation is to carry out an electromagnetic analysis during the transient that occurs inside the TFC following the intervention of the FDU and in the simultaneous presence of a failure condition.

Studying the behavior of TFCs in these conditions allows to predict the distribution of voltage waveforms on each Double Pancake (DP) of the TF and then

verify the correct sizing of the electrical insulation and *the case to ground* resistance inserted in each TF coil.

The simulation consists of three main parts:

1. Finite element simulation (FEM).
2. Implementation of the circuit model.
3. Analysis in the time domain.

The TF circuit model was implemented using a matrix of inductances calculated individually for each TF and modeled as a sub-circuit (as well as for FDUs).

Calculations were made for two different scenarios:

1. Reference scenario: the synchronous intervention of the three FDUs.
2. Failure scenario: delayed intervention of a FDU and additional failure towards the ground.

In both scenarios, the following were calculated:

1. Voltage *terminal-to-terminal*.
2. Voltage *terminal-to-ground*.
3. Voltage between adjacent Double Pancakes.
4. Overvoltage to the terminals of each TFC.

6.1.6.1 FEM model description

The FEM model presented in this section was useful to derive the inductance value of each individual TFC; this model was implemented using Ansys Maxwell 3D.

Each TF magnet was modeled as a solid conductor and, due to the presence of 18 TFC, the result of the analysis carried out formed an 18x18 matrix in which there are auto ($L_{TF} = 45.71 \text{ mH}$) and mutual inductances between each possible magnet.

The Winding Pack (WP) of each TFC consists of 84 turns grouped into 5 *Double Pancakes*: the three central *DPs* each consist of 18 turns while the two outermost ones consist of 15 turns.

The superconducting cable is contained within a rectangular steel section around which there is a fiberglass tape wound so as to form an insulator of 2 mm between adjacent conductors while there is an additional insulating fiber of 0.5 mm between each DP; Finally, there is an additional layer of polyamide insulation around the

entire Winding Pack and a layer of conductive paint in such a way as to have an equipotential surface for the electric field.

The Winding Pack is then placed in a special stainless-steel container and grounded by resistance.

Following all these operations all the magnets are filled with epoxy resin in order to obtain the final insulation.

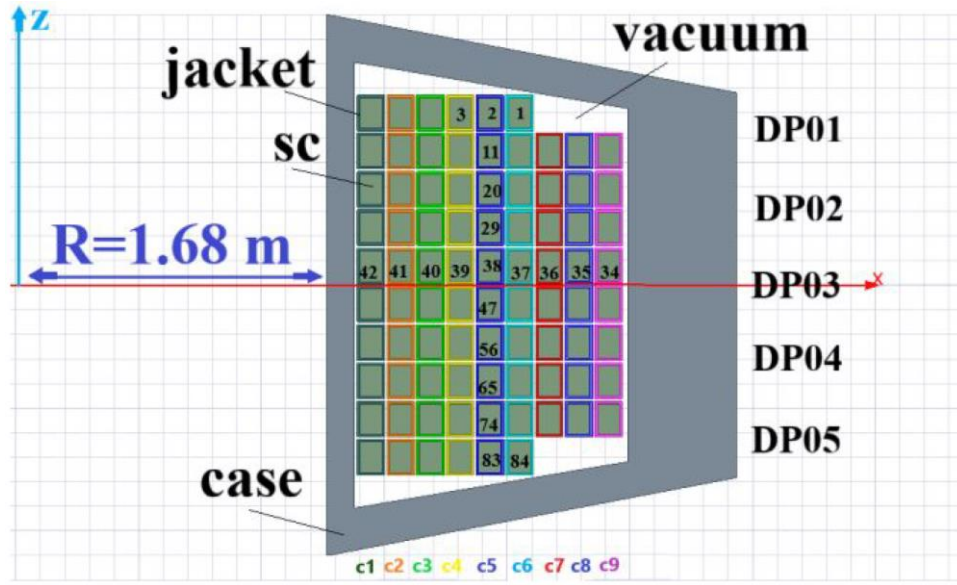


Figure 98: 2D axialsymmetric model of the Winding Pack (WP) in Ansys Maxwell [5]

Particular attention is given to simulations to ground resistance which is considered with two values: 1 $m\Omega$ and 100 $m\Omega$.

The FEM analysis was first simplified by introducing the *circular shape coil* or the coil with the classic D-shape and then it was converted into a circular coil with equivalent inductance; this circular coil has an equivalent diameter of 1.68 m, allowing to simplify the model but maintaining the same dimensions of the *case* and *the cross section* of the WP. Introducing the circular coil brings a difference on self-inductance of 2% therefore it is considered acceptable (see next table).

Table 8: Auto and mutual inductance value for D-shaped and circular coil [5]

Symbol	Geometry	Value
L_D	D-shape	45.71 mH
L_C	Round shape	46.6 mH

Subsequently, the 2D axialsymmetric model of the WP was set by associating each element with the appropriate material from the Ansys Maxwell library and the

values of auto and mutual inductance were obtained for all the individual conductors, obtaining the results in Figure 99.

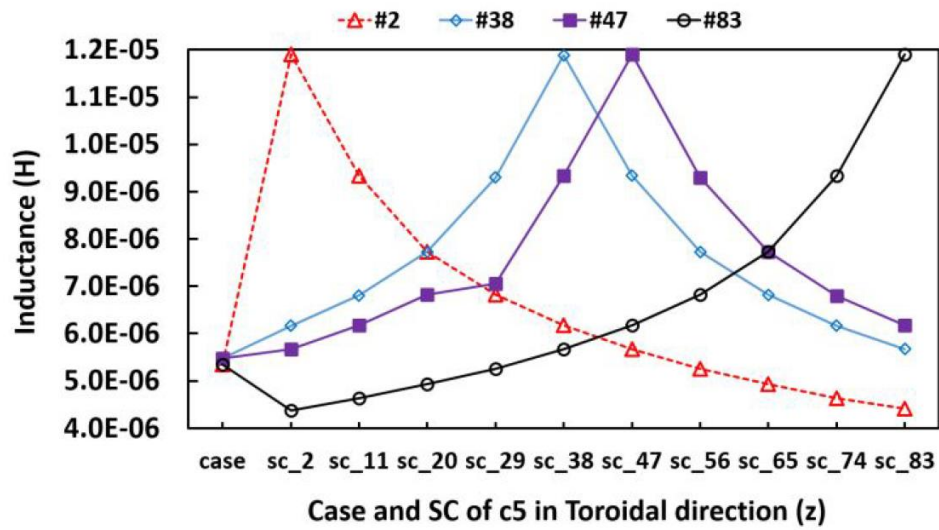


Figure 99: Mutual inductance coefficients comparison for some WP [5]

It should be noted that the mutual inductance coefficient is higher for Coils sc_38 and sc_47 which are those ones in the middle of the WP.

6.1.6.2 Ansys-Simplorer TFCs electrical model

The matrix of auto and mutual inductances obtained in Maxwell 3D was later imported into Ansys Simplorer by modeling each of the 84 superconductors as follows:

1. *SC branch*: it constitutes the 84 superconductors each consisting of 5 turns modeled as an inductance obtained from the matrix.
2. *Jacket branch*: model the *jacket* of the superconducting cable.

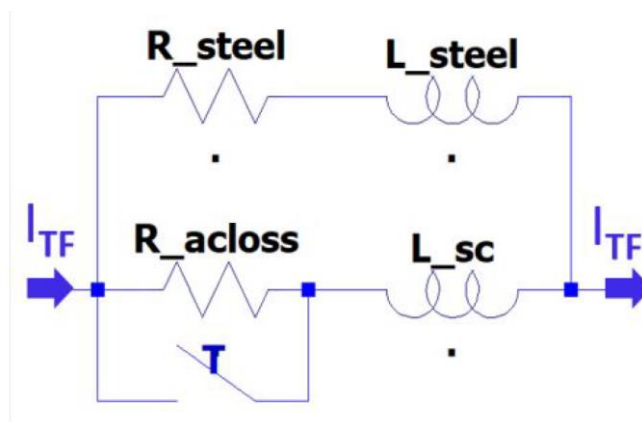


Figure 100: Electrical circuit of one coil [5]

The L_{SC}, L_{steel} parameters were derived from magnetostatic analysis while R_{steel} was derived analytically. The parameter $R_{aclosses}$ is the resistance associated with joule losses in the superconductor during transient; these losses can be considered as contributing to hysteresis and coupling losses, and the parallel switch serves to exclude them from the circuit at the end of the transient.

Ultimately, each model of the individual TFC includes:

1. The matrix of inductances.
2. The resistances R_{acloss} and R_{steel} every breath.
3. The resistance of the joints between adjacent *Double Pancakes* $R_{joint} = 1n\Omega$.
4. The strength of conductive paint described above $R_{paint} = 210\Omega$.
5. The capabilities between the coils.
6. Electrical parameters of the *case*.

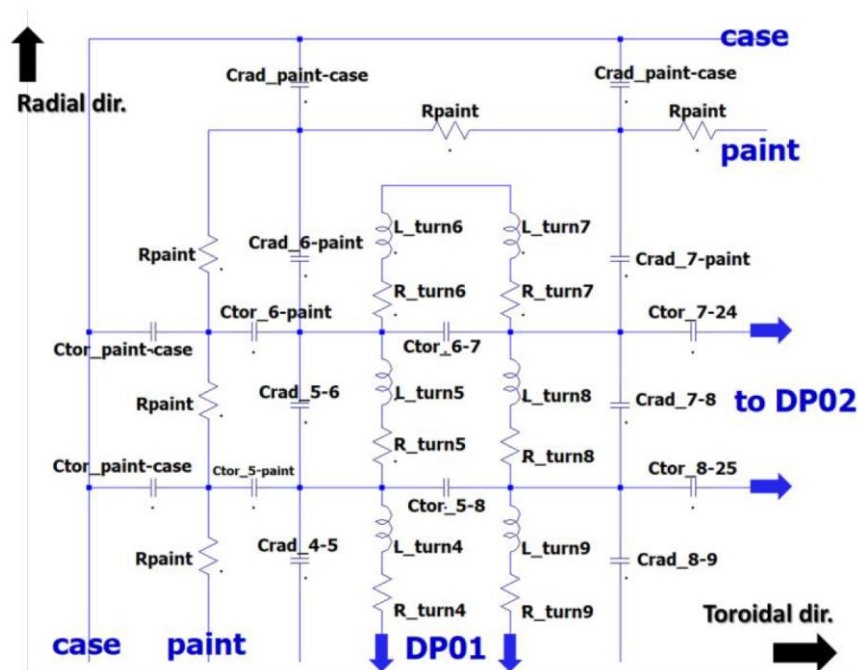


Figure 101: Simplified scheme of TF coil [5]

6.1.6.3 Ansys Symplorer Fast Discharge Unit

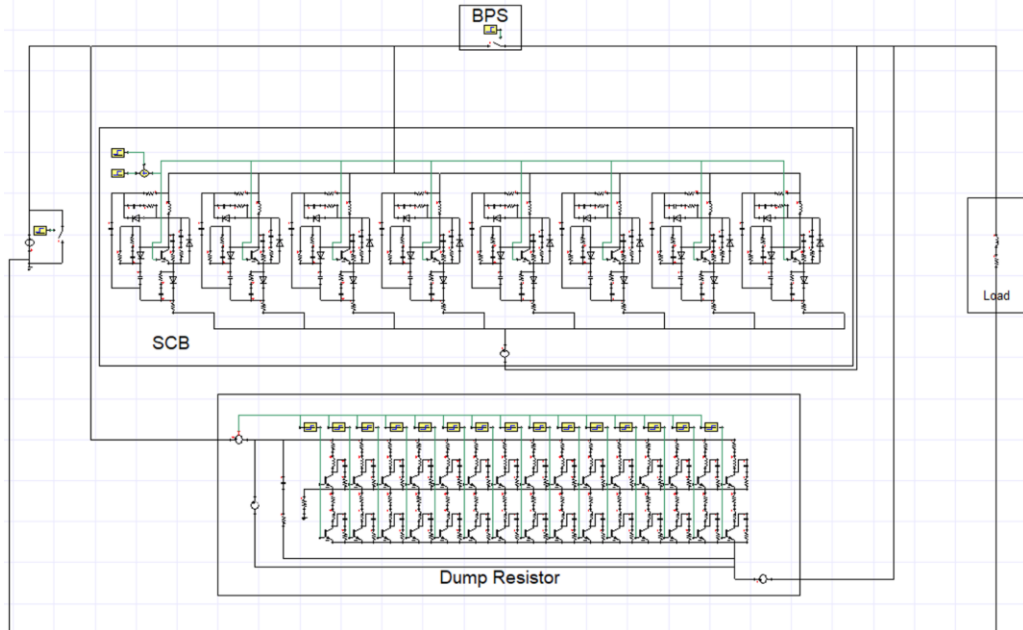


Figure 102: FDU model in Ansys Simplorer [5], this model is coherent with the one reported in Figure 80.

This paragraph describes in detail the implementation of the FDU model in an Ansys Simplorer environment so that it can be interfaced with the TFCs described in the previous section (for a detailed description of the operation of the various components see the previous chapters).

The model consists of:

- 1) Generator that delivers a current of 42.5 kA in DC (constant value).
- 2) Crowbar simulated with an ideal switch that short-circuits the generator when the opening command is given to the Bypass Switch (variable name: T_ap).
- 3) Simulated BPS with switch that opens when the opening command is given: the resistance of this component is not linear and is controlled by an Excel table whose values follow the arc resistance obtained with the Mayr-Cassie equations.
- 4) SCB (Static Circuit Breaker) that leads from the moment the opening command is given to the BPS (T_ap) until the SCB opening command is given (T_ap_SCB defined as T_ap+Deltat).
- 5) Dump Resistor consisting of 15 branches of resistors in parallel appropriately controlled by the current threshold.

- 6) Load consisting of an inductance equal to 1/3 of the equivalent of superconducting magnets as there is only one FDU of three here (later the load was replaced with superconducting magnets).

Table 9: FDU parameters

Variable name	Value	Unit
I_nom	42500	A
T_ap	1	s
R1scb	0.6	Ohm
L1scb	1e-10	H
C1scb	1e-9	F
R2scb	4.7	Ohm
C2scb	1e-10	F
R3scb	5e-5	Ohm
Deltat	1	s
T_ap_SCB	T_ap+Deltat	s
L_load	0.723	H
R_load	1e-5	Ohm
Rb	0.915	Ohm
Lb	1e-5	H
Rg	160	Ohm
C_clamp	0.001	F
A1	0	
A2	1	
For_vol	0.8	V
Bulk_res	0.001	Ohm
R_igbt	0.001	Ohm
C_snub	2.5e-7	F
R_snub	500	Ohm
C_igbt_snub	1	F
R_igbt_snub	100.000	Ohm
C_igbt_snub_DR	1	F
R_igbt_snub_DR	100.000	Ohm
R_clamp_DR	0.05	Ohm

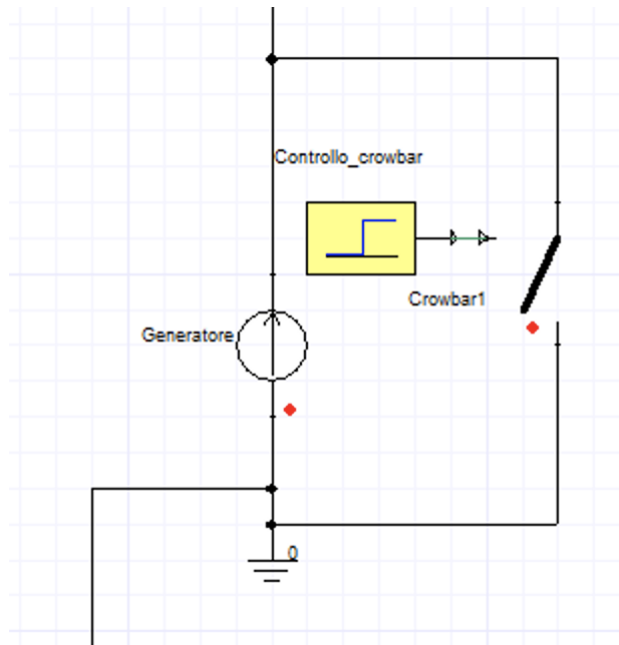


Figure 103: FDU generator detail

The power supply consists of a current generator controlled by the variable $I_{nom}=42500$ A in fixed DC. In parallel there is an ideal switch that simulates the Crowbar; this switch is controlled by a step that varies from 0 to 1 in a time T_{ap} so that it can short-circuit the generator when the intervention command is given to the FDU (the crowbar closes simultaneously with the opening of the BPS).

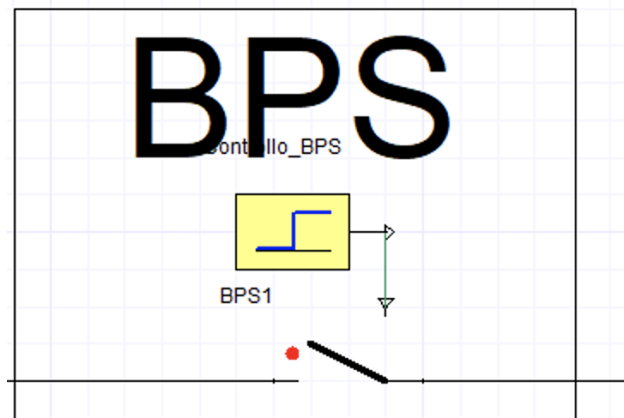


Figure 104: BPS detail

The BPS consists of a switch whose resistance is variable and dependent on an Excel file imported from Matlab/Simulink that allows the simulation of arc resistance (widely described in the previous Section).

The SCB is composed by 8 parallel branches simultaneously controlled but it is not possible to show it on this document due to company policy.

The control of the SCB is done through two steps to carry out a trapezoidal control. The logic followed is that the conduction command should be given to the 8 branches of the SCB only for a certain Delta T. To give a trapezoidal command, the sum of the inputs of two steps out of phase in time and controlled by the variable "Deltat" (on which the dependent variable "T_ap_SCB" depends).

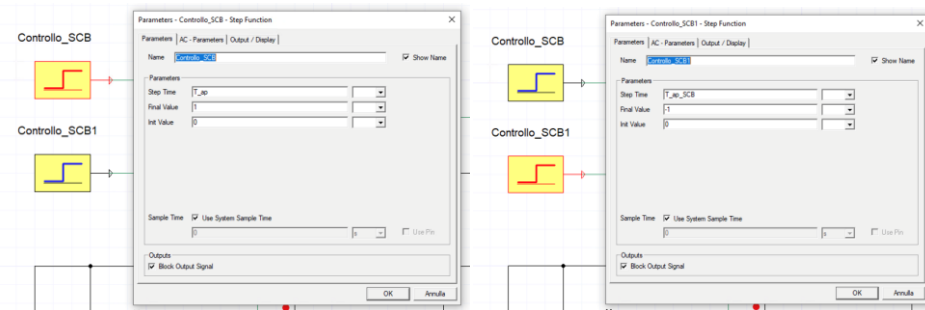


Figure 106: SCB control: closing command (left) and opening command (right)

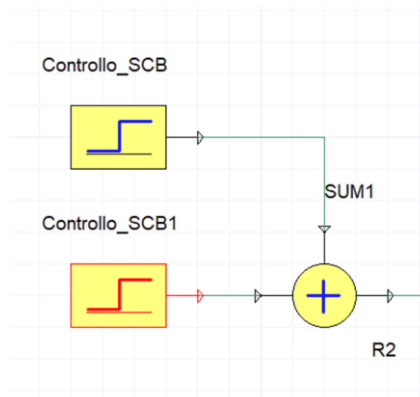


Figure 105: Command logic of SCB.

The Dump Resistor consists of 15 branches in parallel, in each branch there are two resistances dependent on the variable "Rb" and two inductances dependent on the variable "Lb" arranged as in the figure. The central point is grounded and dependent on the variable "Rg".

The command to the IGBTs is given by a "Comparator" block that evaluates the current circulating on the DR and progressively deactivates the various branches of the DR.

The "comparator" block has a threshold that varies progressively as $\frac{i}{15} * I_{nom}$; con $i = 14, \dots, 1$.

The A1 and A2 values are the output variables output from the comparator (0 or 1) that then send the conduction or aperture command to the IGBT.

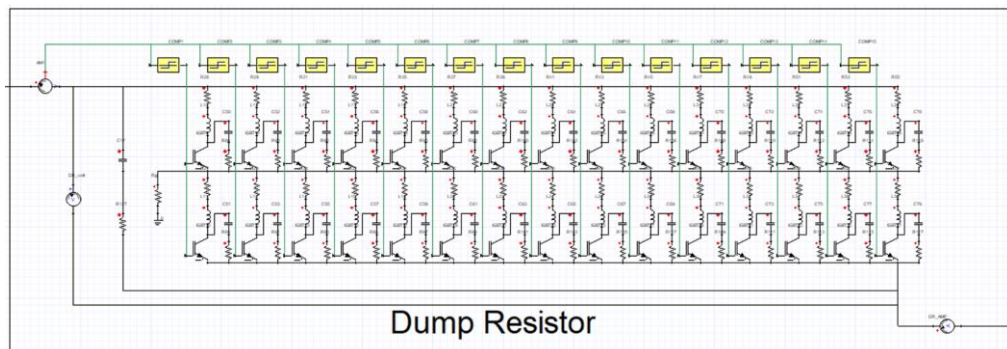


Figure 108: Dump Resistor detail.

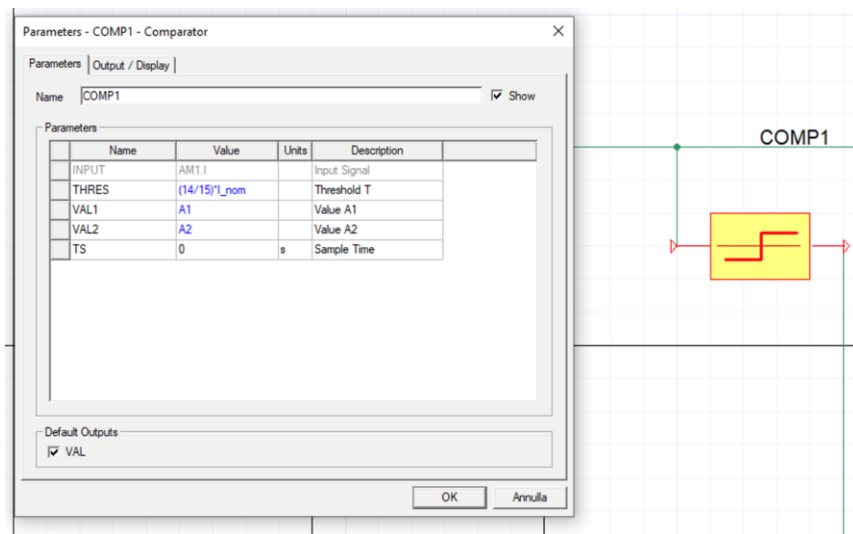


Figure 107: Control detail of DR.

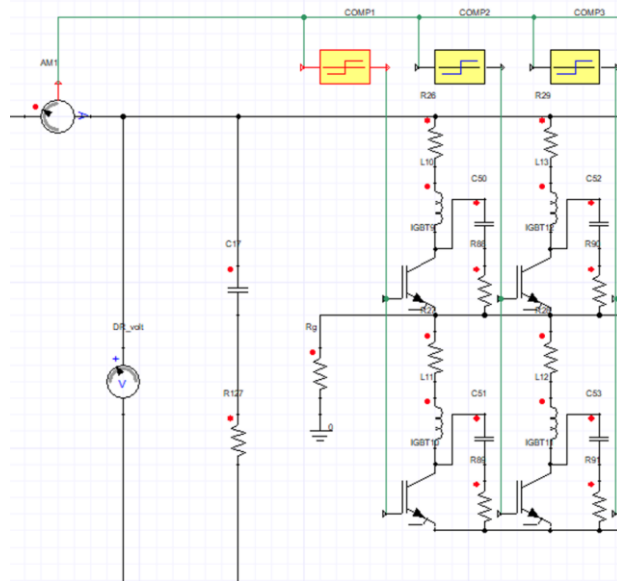


Figure 110: Detail on the control of the DR.

6.1.6.4 Final Model

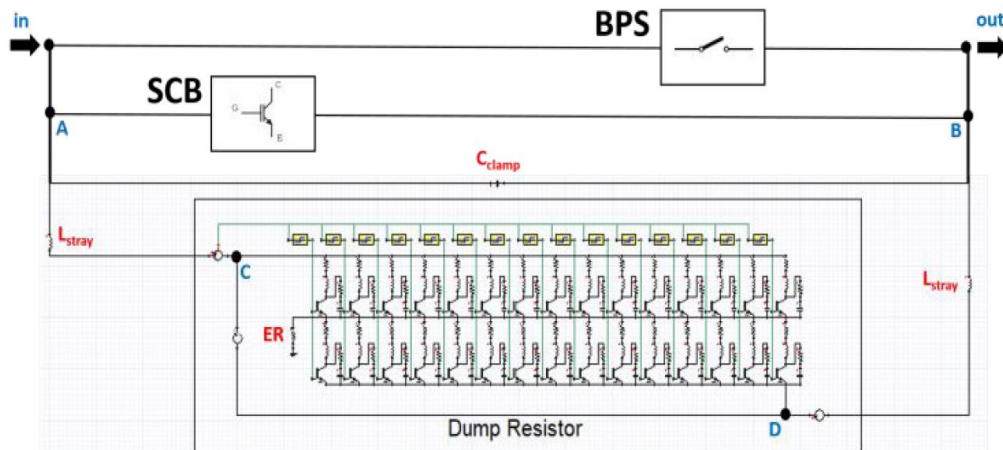


Figure 109: Final Ansys Simplorer FDU model.

The final model includes, in addition to the components described above, also the capacity of Clamp $C_{clamp} = 3mF$ and eddy inductances $L_{stray} = 10\mu H$.

Eddy inductances were inserted since they play an important role in the final waveforms of the voltage while the clamp capacities serve to reduce the peak in the voltage transient (together with the snubber circuits inserted in both the SCB and the DR).

In the final model the equivalent load has been replaced with the complex of magnets described above; the magnets, however, are considered as magnetically decoupled in the frequency range from 1kHz to 100kHz since the skin effect

determines a penetration of the magnetic field on the *case* of about 1cm up to 1kHz and can be considered null for higher frequencies.

The 18 subcircuits made up of magnets are divided into 3 groups of 6 sub-circuits: all groups, their busbars ($R_{busbar} = 116 \mu\Omega$; $L_{busbar} = 460 \mu H$) and the 3 FDUs are connected in series.

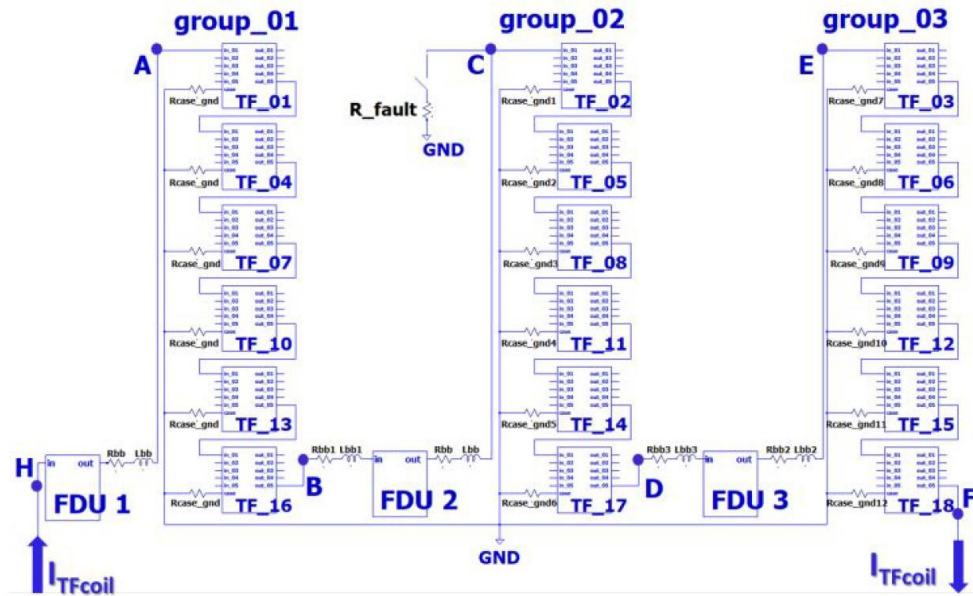


Figure 111: Simplified electrical scheme with TFCs and FDUs [5]

6.1.6.5 Results analysis

The simulation was conducted on Ansys Simplorer with a minimum *time step* of $1 \mu s$ and a maximum *time step* of $100 \mu s$ and a simulation time of 200 ms. The rated current is 42.5 kA, and the crowbar closes after 1.5 ms from the beginning of the simulation and the opening command to the FDU is sent after 2 ms with the actual start of the discharge after 50 ms.

6.1.6.5.1 Reference Scenario

The reference scenario is related to the synchronous intervention of all the FDUs after 0.5 ms of the closure of the Crowbar.

The waveform of the voltage at the heads of each group of superconductors was calculated by setting a resistance from *the case* to the ground

$$\text{of } R_{\text{case-to-gnd}} = 100\text{m}\Omega.$$

The three waveforms are superimposed due to the symmetrical arrangement of the circuit in relation to power supply and grounding.

It is noted that there is an initial voltage spike of up to 5.33 kV followed by an oscillation around 5 kV which corresponds to the moment when the first pair of IGCTs is controlled in the opening.

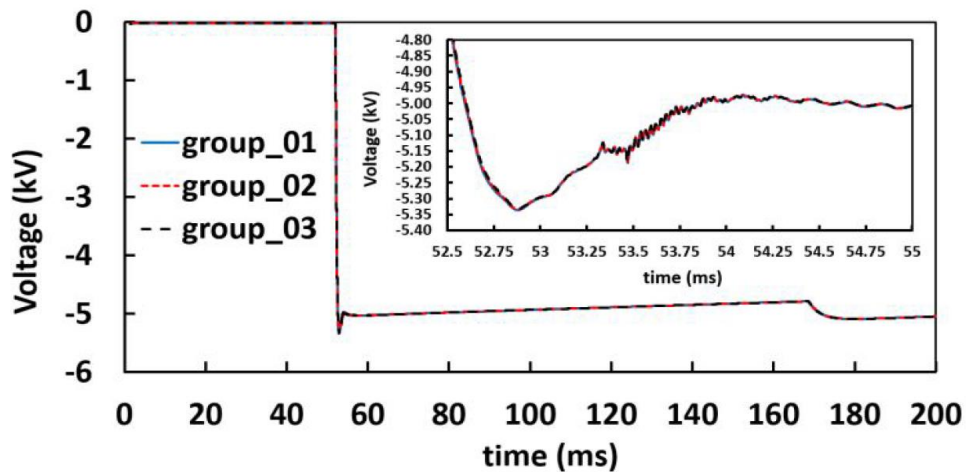


Figure 112: Terminal voltage on the 3 groups with $R_{\text{case-to-ground}} = 100\text{ m}\Omega$ [5]

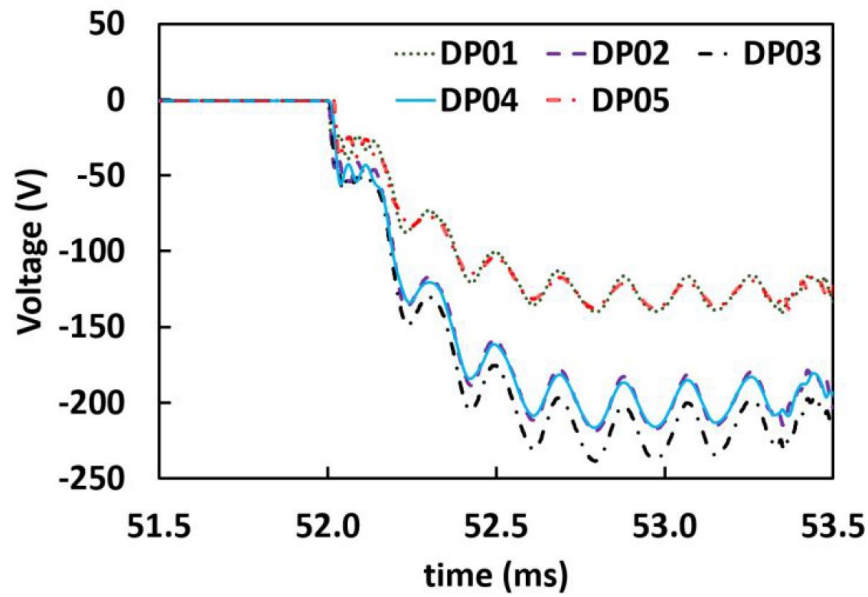


Figure 114: Voltage at the terminals of the DP of coil 1 with resistance case to ground of 100 mOhm [5]

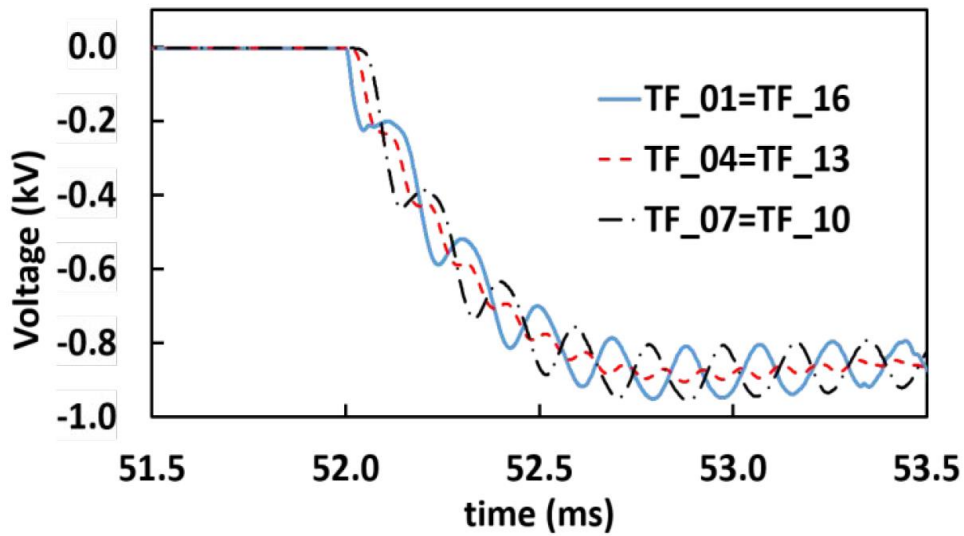


Figure 113: Terminal voltage on group 1 with resistance of 100 mOhm [5]

Figure 113 shows the trend of the *terminal-to-terminal* voltage of the 6 coils of group 1 (arranged in series): it is noted that the voltage distribution is not uniform and in particular the coils 01-16 and 07-10 have greater oscillations with a value of up to 950 V; this is due to the greater proximity to the FDU.

Figure 114 is instead represented the trend of the voltage inside the coil 01 and relative to the individual *Double Pancakes*; also, in this case the distribution is not uniform both because of the different number of turns and for their different position inside the case. It is noted that the DP that reaches the maximum voltage

value is the DP03 of about 250 V. The oscillations are due to the capacities present between the coils and the electrically close elements connected to the ground.

The *terminal-to-ground* voltage of each group of coils has also been calculated in order to correctly size the insulation of each individual component; there is a maximum value of 2.64 kV in absolute value at 52.88 ms and it is noted that there is a higher voltage in the outer coils.

In the Figure 115 there is the trend of the *terminal-to-ground* voltage for the Double Pancakes inside the TF01 coil.

The switching of the current inside the components is seen in the next figure: initially there is the switching of the current from the BPS to the SCB and then from the SCB to the DR within a few microseconds; this second transient is more critical as it involves the presence of a voltage spike, limited by the *clamp* circuit of the DR components.

Subsequently, the resistance $R_{case-to-ground}$ was modified 100 mΩ and it was found that this new condition does not affect the trend of tensions.

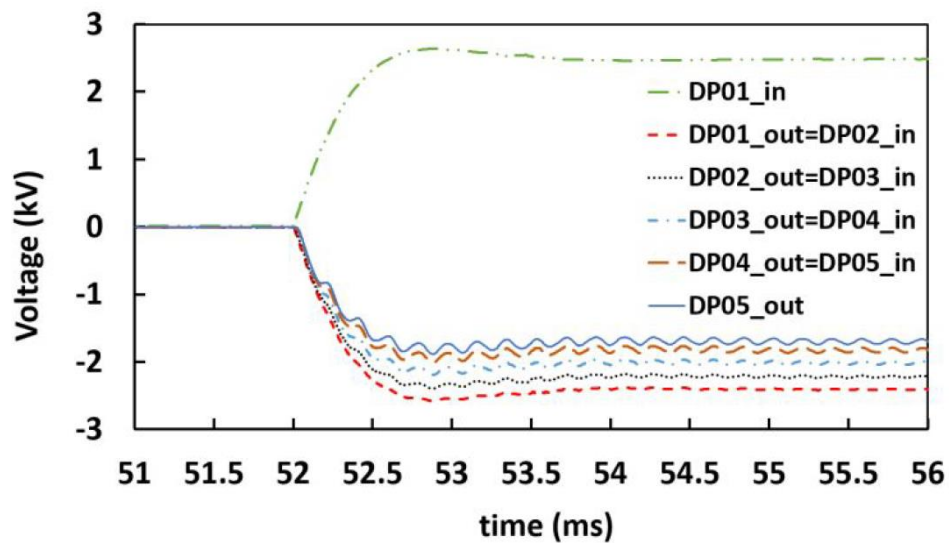


Figure 115: Terminal to ground voltage for all the DPs of TF01 coil [5]

6.1.6.5.2 Fault scenario

The failure scenario has been studied in order to evaluate the trend of the over voltages at the ends of the terminals of the TFC, in particular a double fault condition has been studied: the FDU2 intervenes with 5 ms of delay compared to the other two and, after 10 μ s, there is a failure on the ground with a resistance $R_{fault-to-gnd} = 1 \Omega$ (Figure 111).

The non-synchronous intervention of the FDU's and the failure on the ground result in a transient with a higher voltage on the TFC2 group as in the following figures:

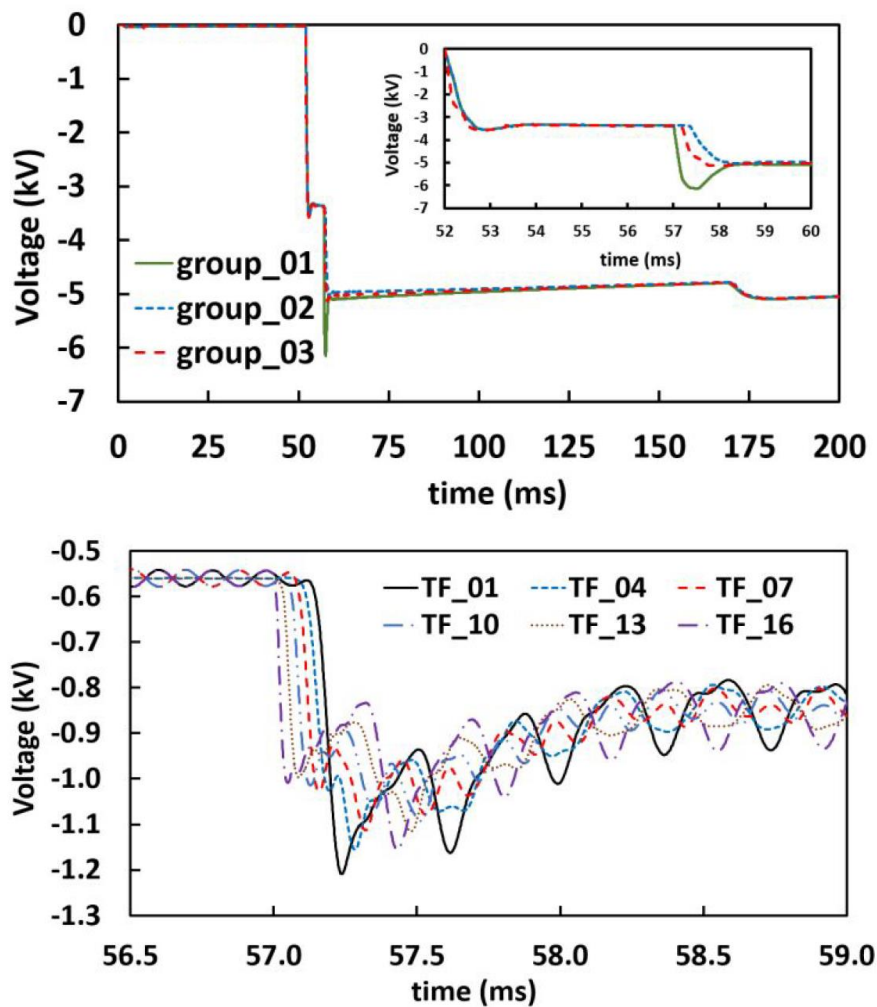


Figure 116: Terminal voltage on TFC groups (up) and terminal voltage of coils inside group 1 (down). Both with fault resistance of 1 Ohm [5]

It should be noted that Figure 116 there are two peak values, one of 3.57 kV at the time 52.7 ms when the FDU1 and FDU3 intervene and of 5.1 kV at 57.5 ms;

the heads of group 2 of the coils there is instead an overvoltage of up to 6.15 kV due to the late intervention of the FDU2 and the failure condition.

In the next figure the detail of the voltages at the ends of the individual coils of group 1 with the relative oscillations are shown.

Figure 117).

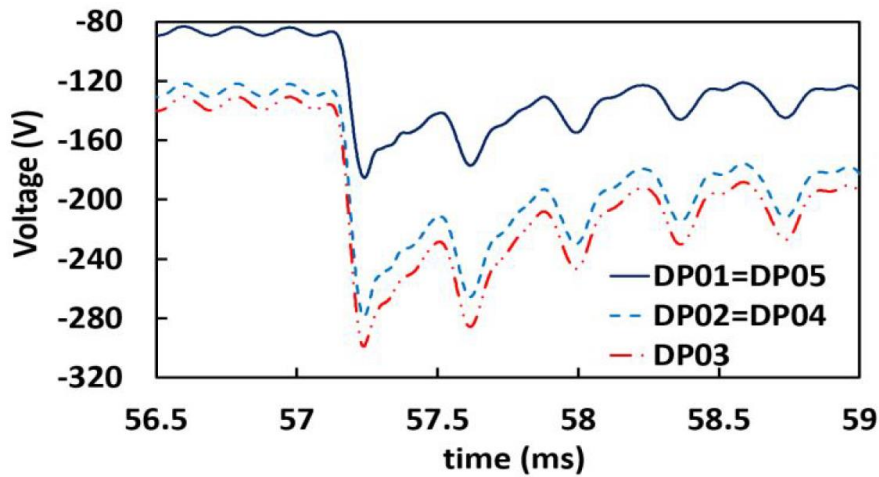


Figure 117: Terminal voltage on DPs of TF01 with fault resistance of 1 Ohm [5]

The fault resistance also has an impact on the *terminal-to-ground* voltage Figure 111 there are the following voltages.

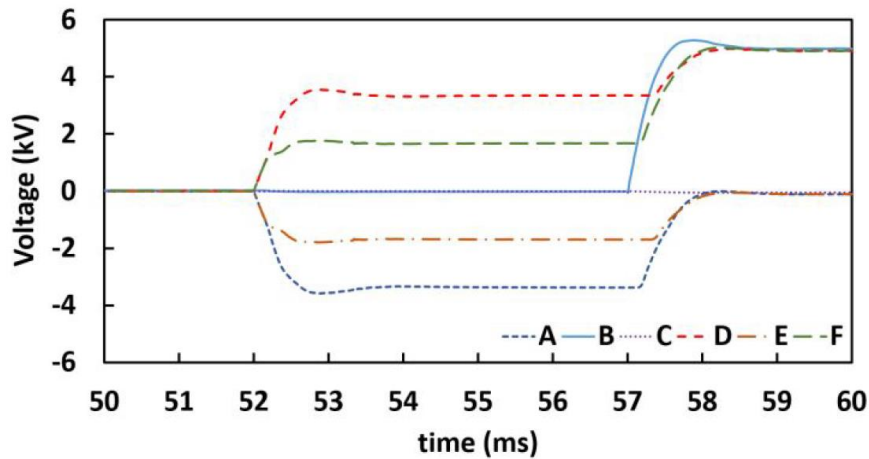


Figure 118: Terminal to ground voltage of each group for fault resistance of 1 Ohm [5]

The different behavior of the voltage just shown can be described as follows:

1. From 52 ms to 57 ms: the FDU2 has not intervened yet.
2. From 57 ms to 62 ms: the FDU2 intervenes and there is a fault on the ground.

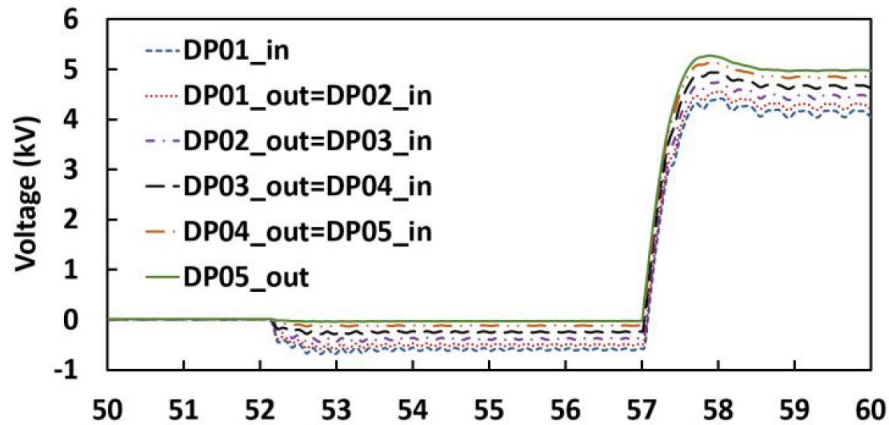


Figure 119: Terminal to ground voltage for all the DPs in TF16 coil for fault scenario [5]

Terminal C is short-circuited while terminal D goes to 3.3 kV and up to 5 kV when FDU2 intervenes; the terminals E and F associated with group 3 are brought to a voltage of 2 kV equal and opposite up to 57 ms when they are brought respectively to a few tens of Volts and 5 kV.

Terminals A and B associated with group 1 also have asymmetric behavior: terminal A has a voltage value equal to and opposite to that of terminal D but increases up to a few tens of Volts when the FDU2 intervenes; Terminal B has the same voltage as terminal C up to 57 ms when it then reaches its peak value of 5.27 kV to reach 5 kV.

Figure 119 the voltage of the DP of the TF16 coil is shown which is the most stressed together with the TF01); the maximum permissible voltage for the WP insulator is 10 kV / mm and, by design, the insulation has a thickness of 2 mm; with these results the WP (Winding Pack) insulator resists the overvoltage that is generated in this scenario of double failure.

The transient analysis was repeated with two other failure resistance values, in particular:

1. $R_{\text{fault-to-ground}} = 10 \text{ m}\Omega$.
2. $R_{\text{fault-to-ground}} = 100 \Omega$.

The voltage at the ends of group 1 undergoes a variation in the second case just described and leads to a value of 5.40 kV as shown in Figure 120.

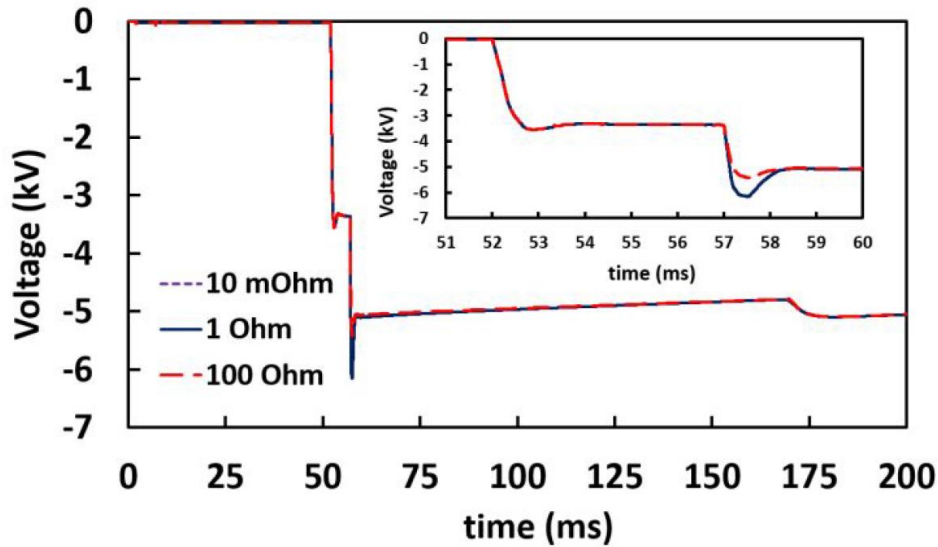


Figure 120: Terminal voltage on group 1 for different fault resistances [5]

6.1.6.6 Conclusions

It is very important to be able to predict with sufficient precision the trend of transient voltages in the presence of failures so as to be able to better size the protections and insulation of the magnets [5].

The model initially developed is that of TFCs and subsequently it was implemented on an Ansys-Simplorer environment with the modeling of FDUs implementing all the aspects that have been studied and described in the previous paragraphs.

The results report a maximum voltage of 5.33 kV in the event of a fault-free scenario and at the ends of each coil group with a *terminal-to-terminal* voltage of 950 V and a maximum voltage of 250 V at the heads of the DP03.

The absolute worst condition is that identified by the double fault with a maximum peak voltage of 6.15 kV at the heads of group 1, a *terminal-to-terminal* voltage of 1.21 kV and a maximum voltage of 300 V at the heads of the DP03.

The insulation of the Winding Pack of the outermost coil of group 1 is the one most stressed by the voltage that is going to be established in transient (5.26 kV terminal to ground).

However, it should be noted that during the design phase an insulator was chosen that can withstand 10 kV/mm so in case of failure it is able to resist (if properly manufactured).

6.2 Conceptual design of the Grounding System of DTT

At the time of writing the guidelines for the ground system of DTT there was not much information in the literature about it.

The main reason for the lack of such information is to be found in the fact that this type of facility currently under construction is experimental and non-commercial and therefore specific precautions are required that must be taken taking into account that the operating conditions of DTT are significantly different from a conventional plant.

The DTT grounding system must meet the conditions of safety, reliability and continuity of service required by the power supply system.

Equipment grounding insulation must be designed to prevent problems due to electromagnetic forces, heating, plasma control, electrical noise and faults caused by induced current during interruption or ramp-up of the plasma current.

The main target of the grounding system is:

- Protection of personnel from contact and step voltages.
- Protection of the installation from lightning (CEI EN 62305).
- Screening of diagnostic equipment.

In case of buildings without an external structural seal, the grounding shall be achieved using the reinforcement steel rods of the foundations.

Underground connections in foundations and walls, additional mesh should be laid underneath the grid intersections and those must be securely fastened so that they are electrically connected.

Mesh intersections must be securely clamped so that the conductive connection cross-sections are at least equal to the mesh cross-sections [40].

In case of buildings with external structural seal (insulated foundation), the ground network mesh must be made with a spacing of 10 m; if the ground mesh is made of reinforced steel, the diameter of each bar must be at least 10 mm and shall be embedded in a concrete layer of a thickness no smaller than 10 m and consisting of at least a grade B15 concrete.

The grounding system of DTT is related to the grounding of different components, in particular:

- **Grounding of the cryostat:** a grounding wire for the cryostat shall be connected to a ground reference terminal to assure the grounding. The Cryostat is one of the most important systems from the point of view of grounding. The main aspect that has to be considered is that, unlike magnets (superconducting or not), diagnostics and additional power systems, almost all Out Vessel Component parts (exception done for in-vessel coils) are not electrically powered, but currents can be induced on them during operation by inductive effect or short-circuits. Currently, the plan is to separate electrically the vacuum chamber from the cryostat. All the other internal components will either be insulated (in which case they will have to be grounded to avoid variable potentials) or electrically connected to the cryostat by means of, for example, flanges (this is the case with the in-vessel components which are cooled by water flowing through the flanges). The in-vessel coils themselves will be electrically insulated from the vessel and the power cables will pass through the flanges by insulating loops. The vessel containing the in-vessel coils (as well as the ex-vessel superconducting coils) will be grounded to reduce the risk of variable potential but taking care not to create loops.
- **Grounding of the vacuum vessel:** Since the vacuum vessel is a large structure placed in a high magnetic field during the operation, large eddy currents can be induced in the vacuum vessel by disruptions. For those reasons, the Vacuum Vessel shall be electrically isolated from other equipment and grounded with a wire outside the cryostat.
- **Grounding of the superconducting magnets:** The CS structure and the TFC case shall be grounded via a resistance outside the cryostat.
- **Grounding of the thermal shield:** The thermal shield for each magnet section shall be grounded via a resistance outside the cryostat.
- **Current feeders:** the current leads for TF, CS and PS superconducting coils shall be grounded via a resistance outside the cryostat.
- **Grounding of the cooling pipes:** since the cooling pipes generate loops, their arrangement will have to take into account the

considerations on the eddy currents induced during Tokamak operations.

- **Grounding of the equipment outside the cryostat:** the principle to be followed is the single-point grounding: each piece of equipment should be isolated from others and grounded with its own grounding wire. Equipment near the tokamak may need countermeasures against problems caused by induced currents.

Built in the early 1980s, it was oriented towards continuity of operation and the separation between the LV power supply of the plasma monitoring, diagnostic and control systems. No automatic ground current interruption system was installed to protect the personnel operating the tokamak plant, but there was a ground loop detection system that prevented the correct acquisition of monitoring data.

The DTT TN system provides for the creation of an electrical system compliant with the technical standard with the aim of guaranteeing high levels of safety for the personnel who work in the Tokamak systems for diagnostics, monitoring and plasma control. In many cases, modern monitoring and diagnostic devices for plasma control make it possible to limit the electrical separation between them and the power supply system, thanks to the advent of fiber in particular.

DTT will be built in the area of the pre-existent system of Frascati Tokamak Upgrade (FTU), which started operating in 1990 and which is currently under dismantling. Hence, DTT will partially exploit the FTU's grounding system (Figure 122), which will be characterized following specific investigations. The DTT project requires dedicated studies which must include information on the subsoil of the new buildings (Figure 121) to correctly size the Ground System.

Moreover, not only the special needs of DTT major components listed in Section II-B, but also the several minor devices requirements must be taken into account. Consequently, Table I groups them depending on the Work Package (WP) to which they belong and it clarifies their type, quantity, and building.

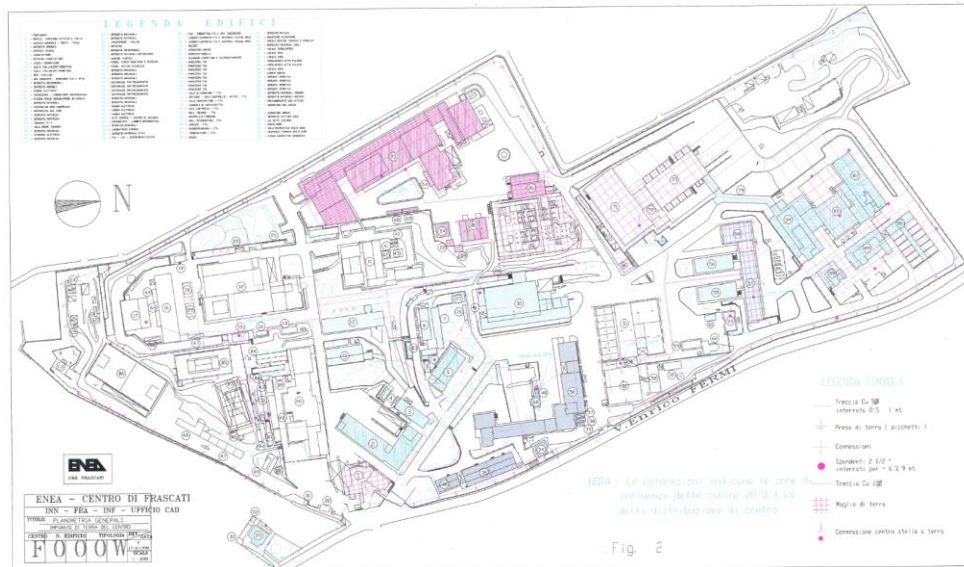


Figure 122: ENEA research center grounding system [2]

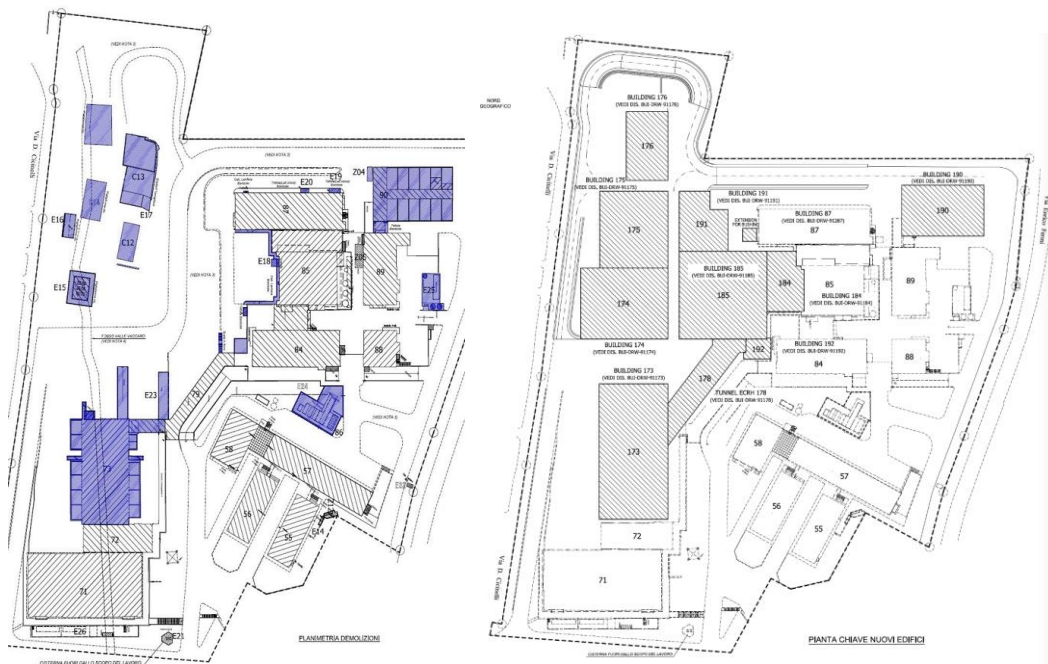


Figure 121: Buildings in ENEA to be demolished (left) and to be built (right) [2]

Moreover, not only the special needs of DTT major components listed previously, but also the several minor devices requirements must be taken into account. Consequently, next table groups them depending on the Work Package (WPck) to which they belong and it clarifies their type, quantity, and building.

Table 10: Minor DTT Devices, main components for Grounding system [2]

WPck	Type	Quantity	Buildings
PSS	Transformers (cases, star central points)	1+6+1+2+4+1	TF: 184 PF: 175 CS: 175 DIS: 191 NAS: 191
	Converters (cubicles, crowbars)	13+72+72+12+8+33	
	SNU cubicles	0+0+12+0+0	
	FDU (cubicles, DREP)	6+12+0+0+0	
	Busbars supports	(12+12+12+4+8) *number of supports	-
DIA	Measurement systems' racks	53+35+23	84, 192, 184
ECRH	Power supplies	16*32+16*32+2*16+2*16+16+16+32+16+32+16	173
	Compressors	32	173
	Gyrotrons	32	173
	Control System cubicles	32+16+12+8+2	72, 173
	Pumping units	4+4	173,178
ICRH	Switch & soft start cabinets	3	89, 190
	Power Cabinets	4	
	Amplifier and control cabinets	5+1+2	
	Transmitters	4+4	
	Pumps	4	85, 89, 190, 191
	Antennas	4	185
	Racks for CODAS and signal conversion	15+14	84, 85, 191
WPck	Type	Quantity	Buildings
NBI	Transformers	2+2+1+1	87
	Converters	1+1+1+1+1+1	87
	High Voltage Deck	1	87
	Transmission Line, bushings, damping resistor, filters	TBD	87, 190
	Control System cubicles	1+1+1+1+1	PS Local Control Room
	Pumps	3	190

AUX	LV pumps	TBD	71, 173, 174, 190, 191, external area
	MV pumps	3+1+1	174, 191, 71
	LV packages	TBD	71, 173, 174, 190, 191, external area
	MV packages	1	External area
	MV compressors	2	External area
BUI	Panels	3*14 buildings = 42	71, 72, 84, 85, 87, 173, 174, 175, 176, 178, 184, 185, 191, 192
	Bridge Crane	1	185
EDS	Substations	9	58, 72, 88, 173, 176
AUT	I/O cabinet and data analysis	4	57, 72, 84, 89
	LV panels	4	

The reference standard for ground fault protection is IEC 61936-1, the latter specifically refers to protection against electric shock.

As regards nuclear plants, reference is made to the IEEE standards in the table to identify those of greatest interest:

Table 11: IEEE Standards used as reference for DTT Grounding system [2]

Standard number	Standard title
IEEE 80-2013	IEEE Guide for safety in AC substation grounding
IEEE 81-1983	IEEE Guide for measuring ground resistivity, ground impedance and ground surface potentials of a ground system.
IEEE 81.2-1991	IEEE Guide for measurement of impedance and safety characteristics of large, extended, or interconnected grounding systems
IEEE 142-1991	IEEE recommended practice for grounding of industrial and commercial power systems
IEEE 367-1996	IEEE recommended practice for determining the electric power station ground potential rise and induced voltage from a power fault

IEEE 487-2000	IEEE recommended practice for the protection of wire-line communication facilities serving electric power stations
IEEE 666-2007	IEEE design guide for electrical power service systems for generating stations
IEEE 1050-2004	IEEE guide for instrumentation and control equipment grounding in generating stations
IEEE 1100-1999	IEEE recommended practice for powering and grounding sensitive electronic equipment
IEEE C37.101-1993	IEEE guide for generator ground protection
IEEE C57.13.3-1983 (reaff. 1990)	IEEE guide for the grounding of instrument transformer secondary circuits and cases
IEEE C62.23-2017	IEEE guide for surge protection practices applicable to power generating stations
IEEE C62.92.1-2000	IEEE guide for the application of neutral grounding in electrical utility systems, part I
IEEE C62.92.2-1989 (reaff. 2001)	IEEE guide for the application of neutral grounding in electrical utility systems, part II
IEEE C62.91.3-1993 (reaff. 2000)	IEEE guide for the application of neutral grounding in electrical utility systems, part III
IEEE C62.41-2002	IEEE recommended practice on surge voltages in low voltage AC power circuits
IEEE C62.45-2002	IEEE guide on surge testing for equipment connected to low voltage AC power circuits

In the table there are four standards indicated in bold: these standards are those to be considered as the main reference while the others are recalled later.

Special reference should therefore be made to IEEE 62.23-1995 as it was specifically developed for overvoltage protection in nuclear plants.

Similarly, IEEE 666-1991 (reaffirmed 1996) describes the methods for grounding of auxiliary systems in medium voltage systems; this standard applies to all types of power plants and in particular to those that need to work continuously.

The standards listed contain numerous references to secondary standards that contain additional information.

It should also be noted that these standards have been developed for “electric generating stations” and this, unless otherwise indicated, also includes nuclear power plants [41].

As regards the IEC standards, see the next table:

Table 12: IEC Standards used as reference for Grounding system of DTT [2]

Standard number	Standard title
IEC 62003: 2020	Instrumentation, control, and electrical power systems – Requirements for electromagnetic compatibility testing
IEC 61000 series	Electromagnetic compatibility
IEC 61508-2010	Functional safety of electrical/electronic/programmable electronic safety-related systems
IEC 61513-2011	Instrumentation and control important to safety – General requirements for systems
IEC 60780-323: 2016	Electrical equipment important to safety - qualification
IEC 63046: 2020	Electrical power systems – General requirements
IEC 62855: 2016	Electrical power systems analysis
IEC 61225: 2019	Static uninterruptible DC and AC power supply systems
IEC 63272	AC interruptible power supply systems
IEC 60772: 2018	Electrical penetration assemblies in containment structures

IEC 62582	Electrical equipment condition monitoring methods
-----------	---

The main standard which must be taken in consideration for the grounding system is the IEC 61000 series which is equivalent to the IEEE C62.41-1991, IEEE C62.45-2002, IEEE 1050-2004, IEEE 473-1985, IEEE 665-1995.

The IEC 63046 it's also of primary importance as it takes in consideration the overall electrical power system with the electrical disturbances.

6.3 Fast Discharge Units on ITER

For a full description of electrical scheme and details on ITER FDUs please check Section 0.

In this paragraph all the results of the internship at ITER Organization will be reported according to the simulations on Matlab-Simulink environment.

The following section will be focused on the FDU circuit model with full details on used parameters and logic control both in TFC and DL configuration.

After that, a report on fault analysis in DL configuration will be described.

The developed model describes all the main electrical components which can be resumed as follow:

- Bypass Switch (BPS)
- Vacuum Circuit Breaker (VCB)
- Counter Pulse Circuit (CPC)
- Pyrobreaker (PB)
- Discharge Resistor (DR)
- Dummy Load (DL)
- TFCs equivalent circuit
- DC busbars
- FDU logic control for BPS, VCB, CPC, PB

6.3.1 Matlab-Simulink electrical model

6.3.1.1 General model in DL configuration

In the following figure is represented the general model with all the components for the simulation of the electrical circuit in Dummy Load configuration.

The whole switching sequence is modelled, and all the switches are triggered in a sequential way by the control blocks (see related Section for Logic Control).

This model reproduces normal operation and does not consider any fault recovery sequence.

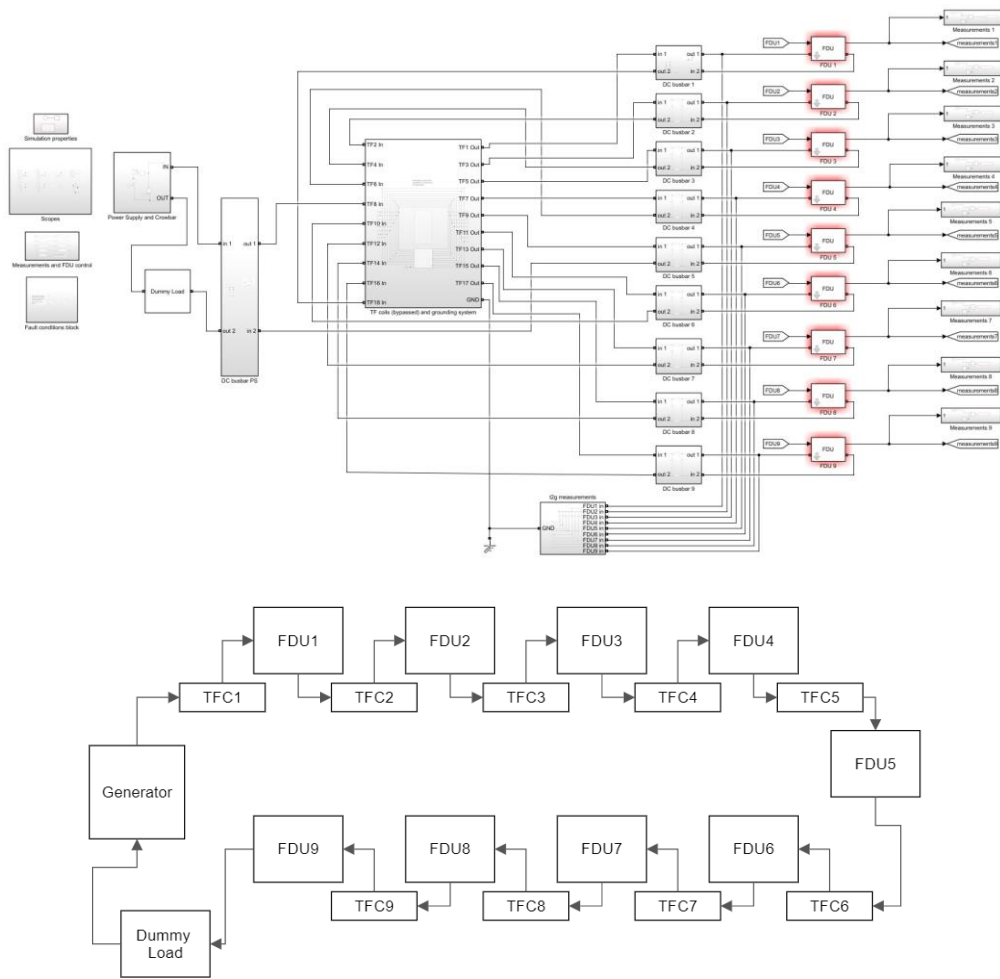


Figure 123: General model with DL configuration (up) and simplified diagram block for more legibility (down).

The referenced electrical scheme is the following:

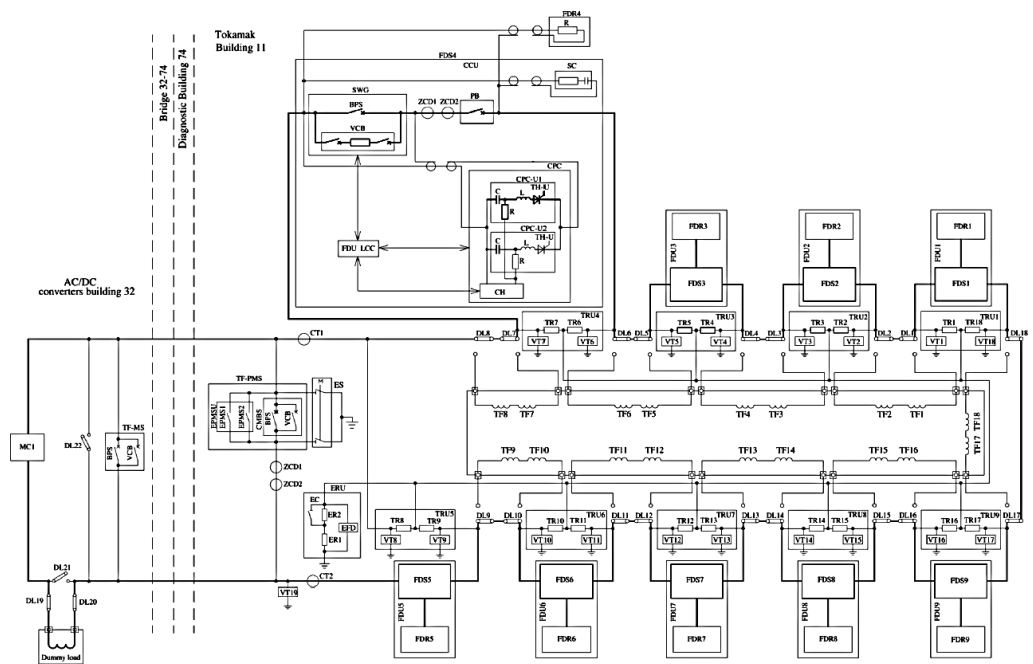


Figure 124: General electrical scheme with DL configuration

6.3.1.2 General model with TFCs configuration

In the following figure is represented the general model with all the components for the simulation of the electrical circuit with TFCs configuration.

This model reproduces normal operation and does not consider any fault recovery sequence.

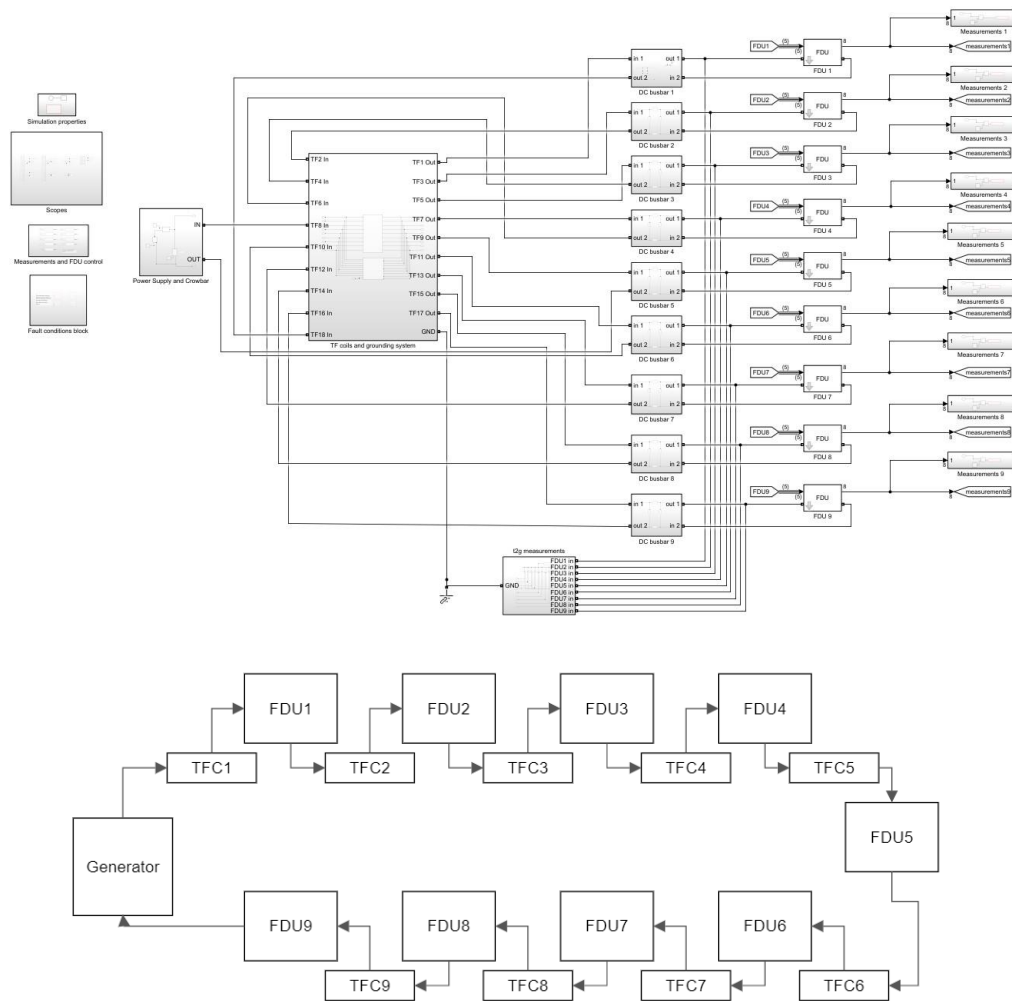


Figure 125: General model with TFCs configuration

6.3.2 TFCs model detailed configuration

The following figure represents the TFCs self and mutual inductances matrix with the related connections to the grounding system.

The matrix value is not accessible in this document due to Company policy.

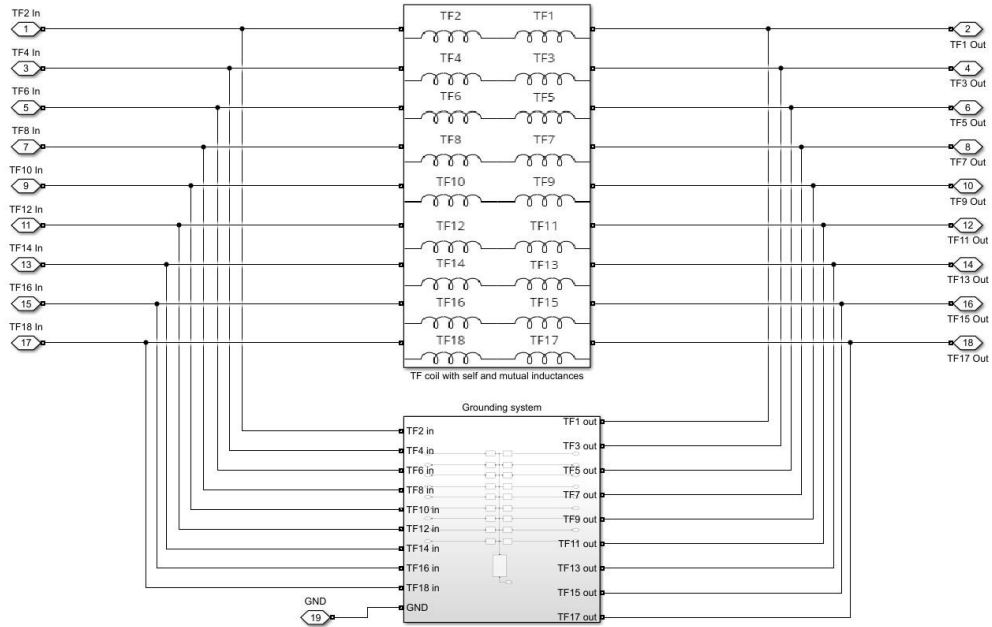


Figure 127: TFCs connections with grounding system

The grounding system block is shown in detail in the next figure: the grounding system is mainly composed by Terminal Resistors (TR) and Earth Resistor Unit (ERU).

The logic control of the ERU is to insert in series to the ground resistance of 990Ω a resistor with a value of 9840Ω (reference: internal document).

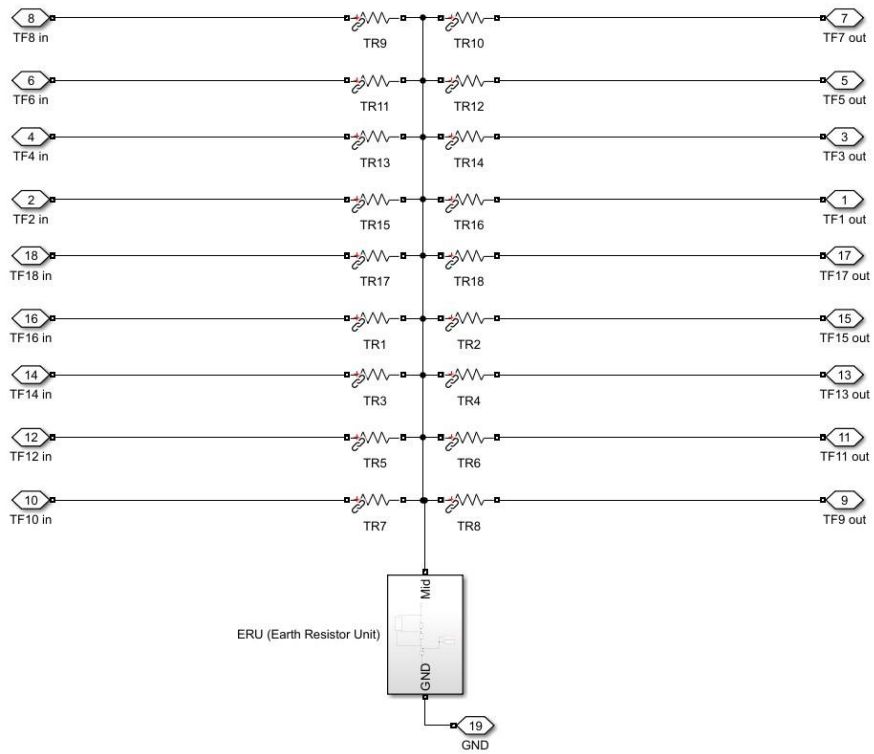


Figure 129: Grounding system details

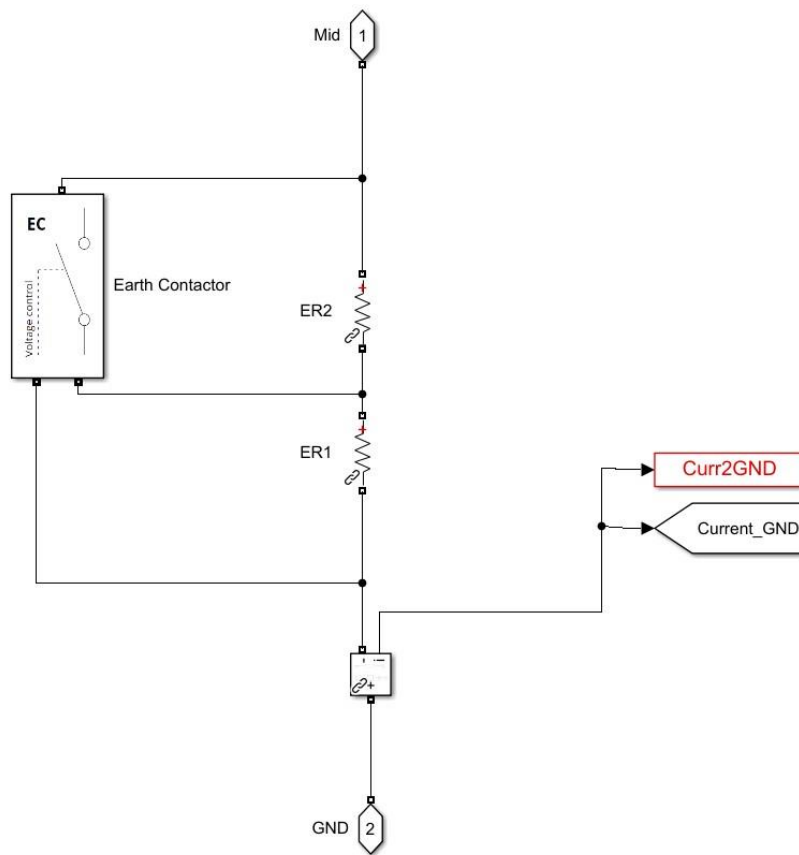


Figure 128: ERU details with ER1, ER2 and EC

6.3.2.1 Scopes

Following figure represents the signals coming from the model and that are sent to the scopes and to the “To Workspace” blocks in order to save all the variables.

The signals sent to the workspace are listed as follow:

- Voltages T2G for each FDU.
- Voltages T2T for each FDU.
- DR resistance value for each FDU.
- DR temperature value for each FDU.
- I^2t for each FDU.
- PB activation log for each FDU.
- Dummy Load current.
- Dummy Load current leakage to GND.
- Dummy Load voltage T2T
- Fault current (if the block is used).
- BPS current for each FDU.
- VCB current for each FDU.
- CPC current for each FDU.
- PB current for each FDU.
- DR current for each FDU.
- SC current for each FDU.

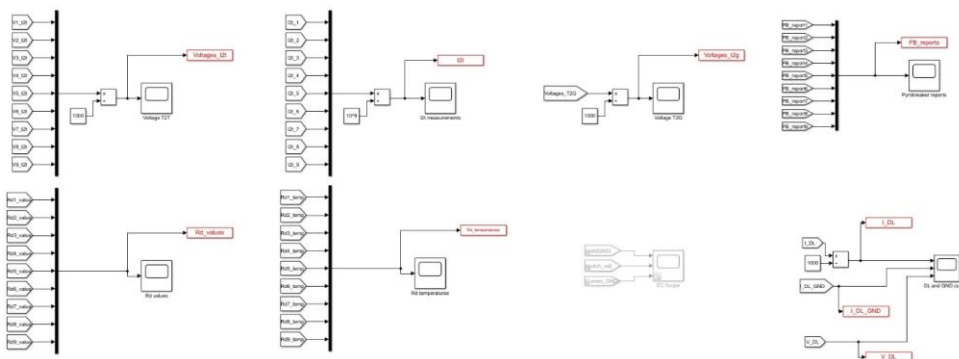


Figure 130: Scopes signals of the model

6.3.2.2 Measurements and FDU control

Next figure represents the FDUs control blocks with a Step block controlling the activation of each single FDU and connected to the measurement blocks in order to activate the control logic algorithm. The step block is activated at $t=0.11$ s. The control of the FDU can be adapted if needed.

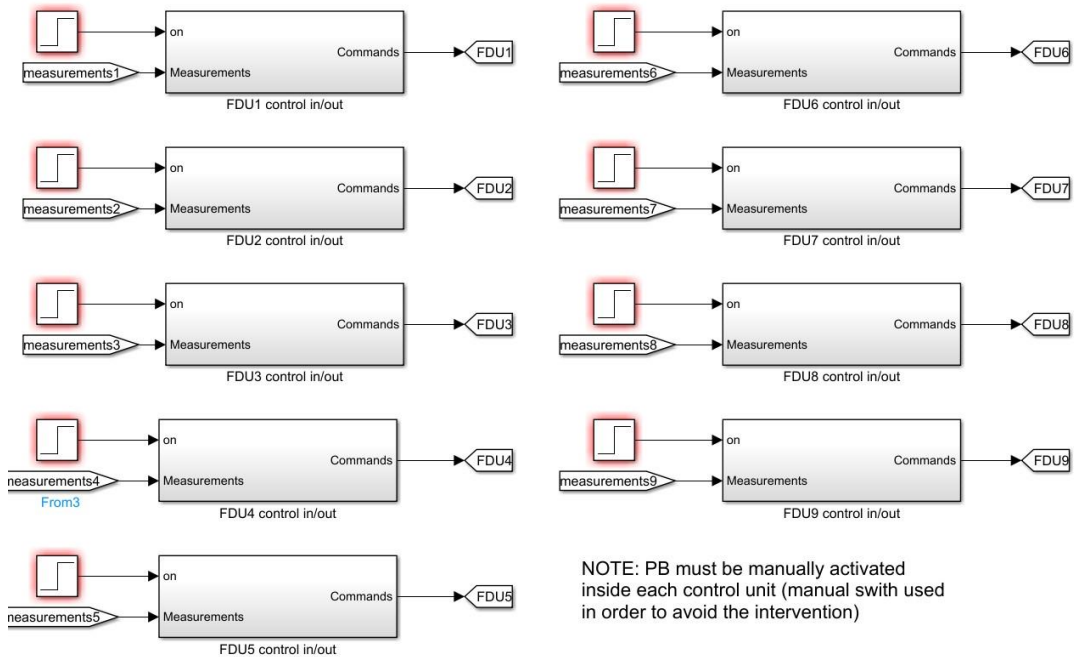


Figure 131: FDUs controls

The “measurements” signals are the following:

- Current of the BPS
- Current of the VCB
- Arc voltage measurement
- Current of the Thyristor
- Current of the PB
- Current of the DR
- Current of the SC
- DR resistance value
- DR temperature

While the output “FDU” signal includes the following signals (sent to the FDU block):

- Activation signal of BPS
- Activation signal of VCB
- Activation signal of CPC
- Activation signal of PB

6.3.2.3 Control Logic of FDUs

The control logic for each FDU for both TFC and DL configuration is implemented according to an internal document which schemes are reported in the following figures:

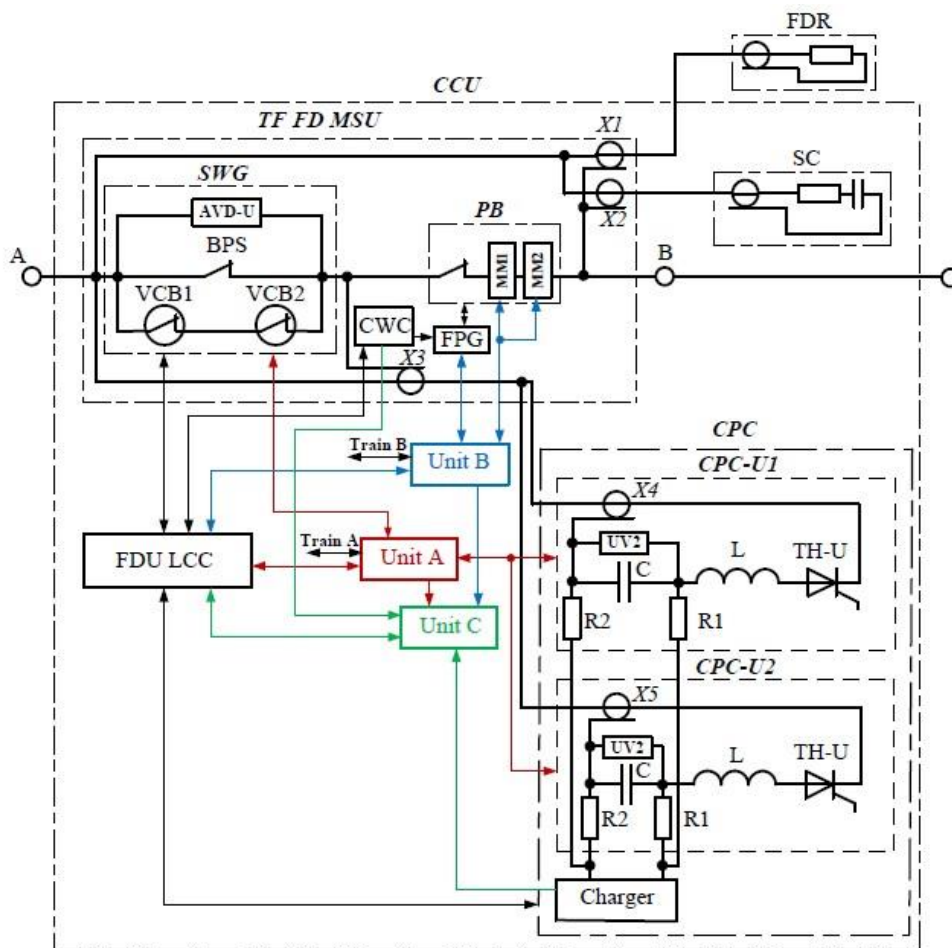


Figure 132: FDU logic control electrical scheme

- TF FDU consist of two major parts:
 - TF FDU Current Commutation Unit (CCU)
 - Fast Discharge Resistor (FDR).
- CCU consists of the following main components:

- High-current circuit breaker, hereinafter called switchgear (SWG), equipped with the
 - Unipolar arc detector (AVD-U).
 - Pyrobreaker (PB) equipped with the Firing Pulse Generator (FPG).
 - Cooling Water Collector (CWC).
 - TF Counter Pulse Circuit (CPC) consisting of:
 - Two CPC Unidirectional Units (CPC-U), and
 - Charger (CH).
 - Snubber circuit (SC).
 - TF FDU Local Control Cubicle (FDU LCC).
 - Units A, B and C.
 - Unit A realizes the information exchange and electric connections between SWG and the channels of the safety (Train A) control, interlock control of SWG and generation of the control signals for SWG and CPC-U's initiation.
 - Unit B realizes the information exchange and electric connections between FPG (PB) and the channels of the safety (Train B) control, interlock control of FPG and generation of the control signal for PB initiation.
 - Unit C realizes monitoring of the Units A and B and transmission of the check-back signals to conventional controllers of FDU LCC.

The logic diagram for the FDU control is reported as follow:

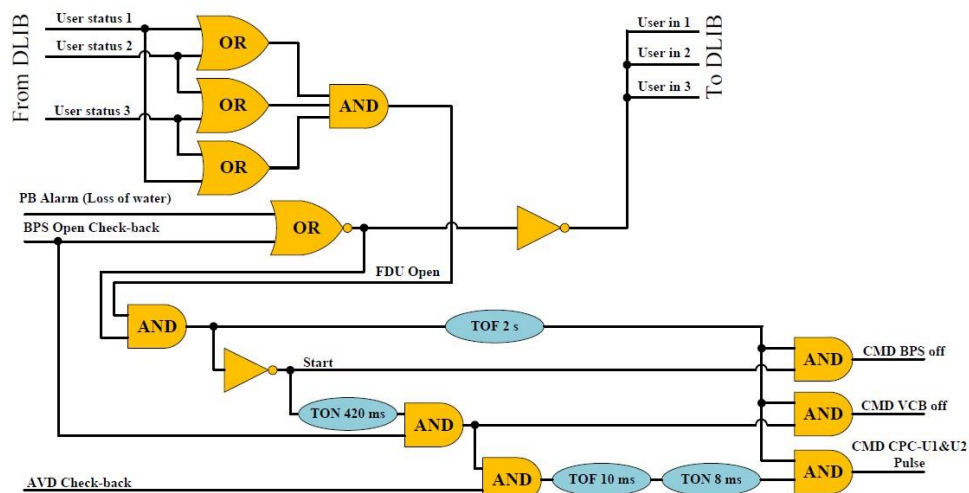


Figure 133: Logic control for BPS, VCB, and CPC

figures; the PB will intervene in case of failure of one of the components between BPS, VCB or CPC.

The following figures represent the previous figures reported in Matlab-Simulink model:

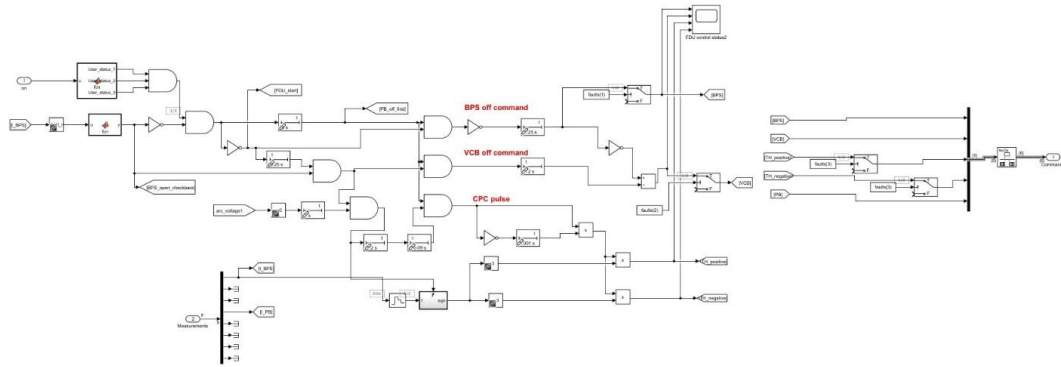


Figure 135: Logic control for BPS, VCB, CPC

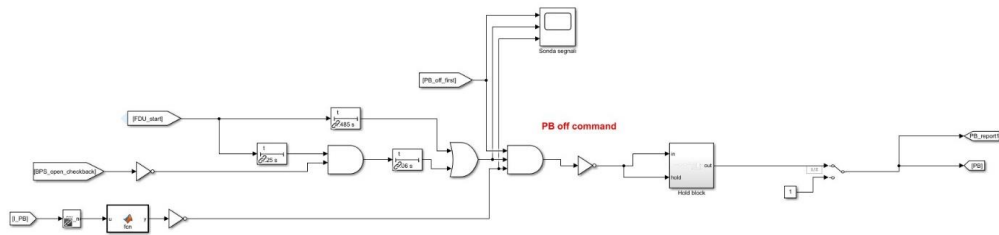


Figure 136: Logic control for PB

6.4 Fault blocks

Next figure represents the parameters of the Fault to Ground block. The control of the fault blocks can be adapted if needed.

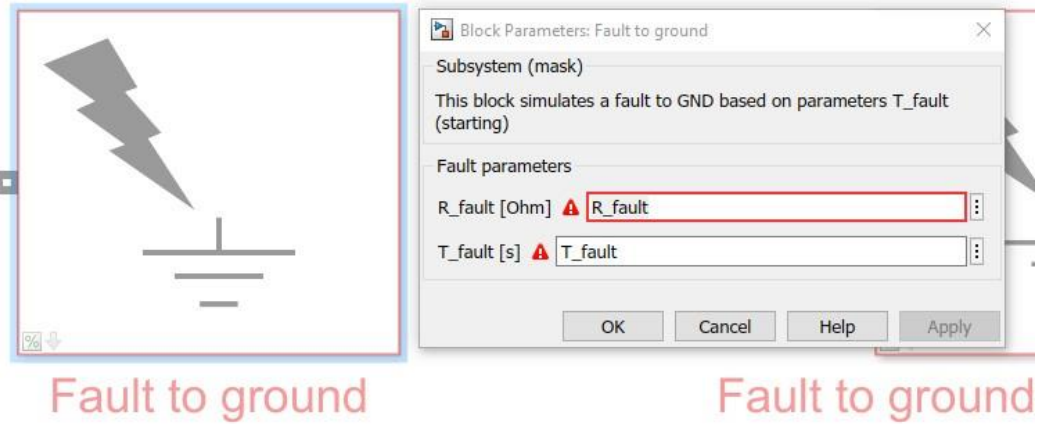


Figure 137: Fault to GND block

In the next figure are represented the fault blocks used as library block model.

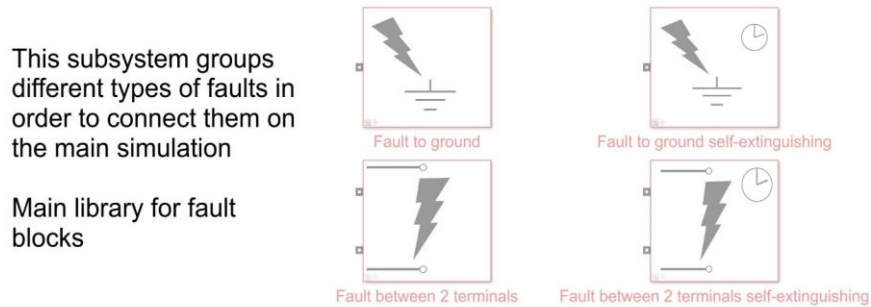


Figure 138: Fault blocks

Parameter	Value	Unit	Description	Reference
R_fault	1e-9	Ω	Fault resistance	-
T_fault	0.115	s	Time of fault to GND appearing	-

6.4.1.1 Power Supply and Crowbar

The Power Supply in this model is represented with an ideal current generator while the Crowbar is simulated with an ideal Switch since the study of the behaviour of both components is out of scope.

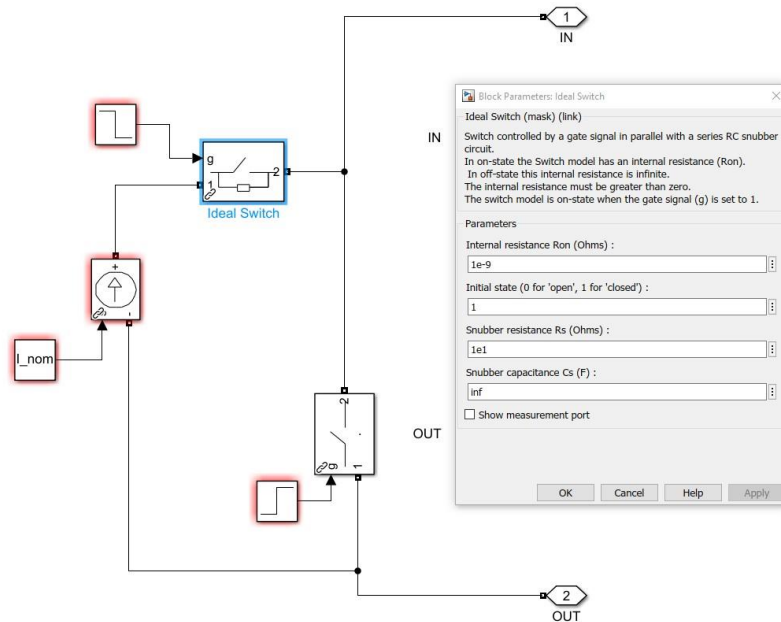


Figure 139: Ideal Switch for opening the PS circuit branch

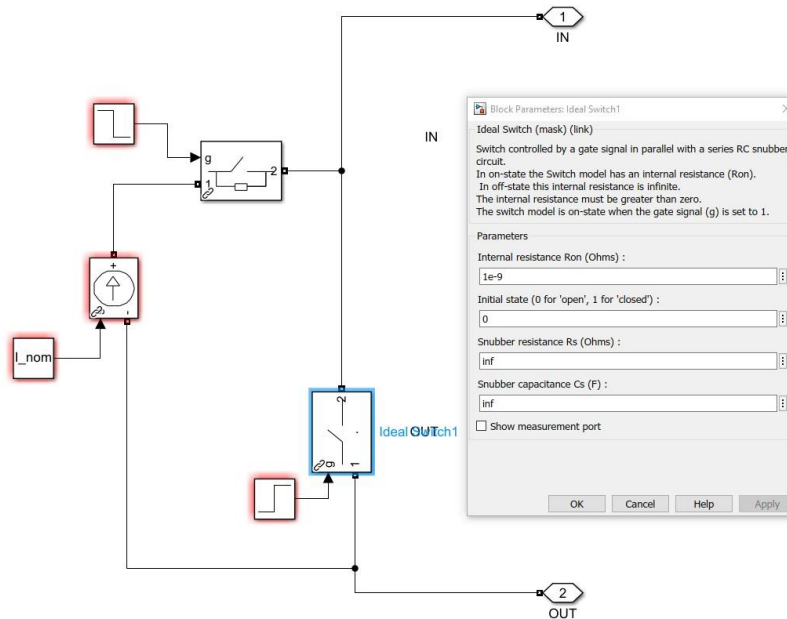


Figure 140: Ideal circuit for simulation of Crowbar

6.4.1.2 Dummy Load

The Dummy Load is present in the simulation only for the Model related to General model in DL configuration.

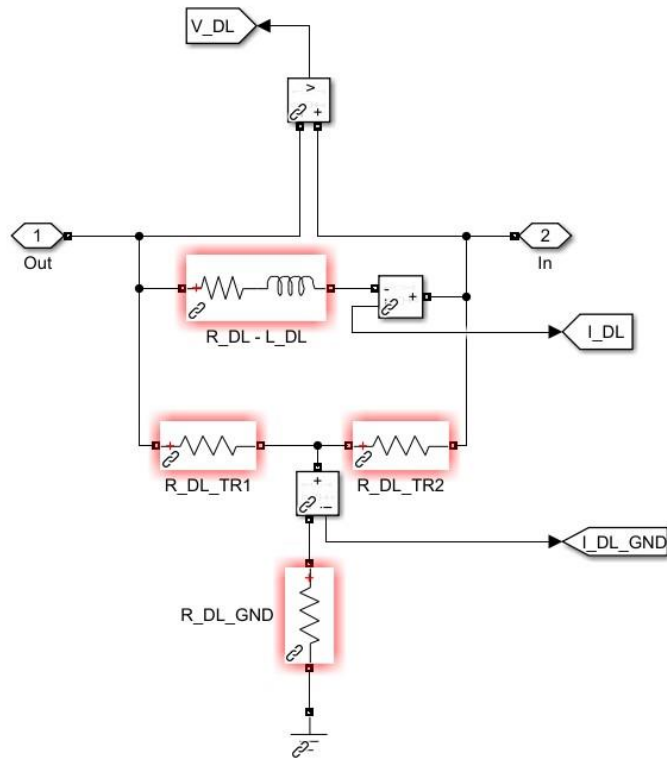


Figure 141: Dummy Load circuit

6.4.1.3 DC busbar for Power Supply

DC busbars for both FDUs and Power Supply are simulated as follow:

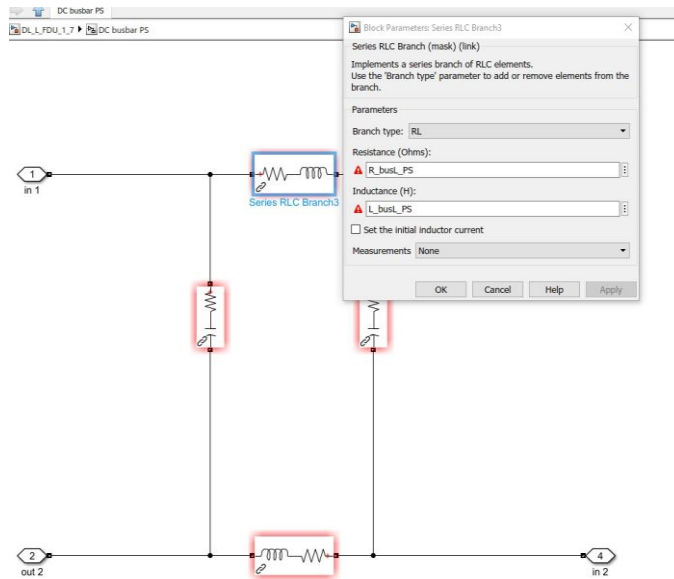


Figure 143: DC busbar for PS - Line resistance and inductance

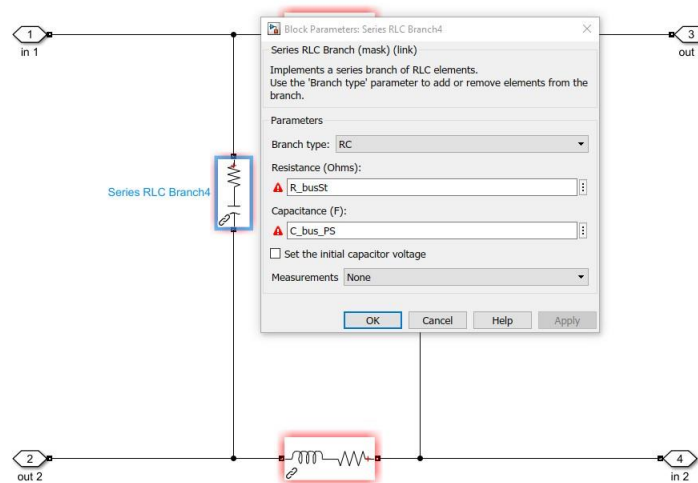


Figure 142: DC busbar for PS - Stray resistance and capacitance

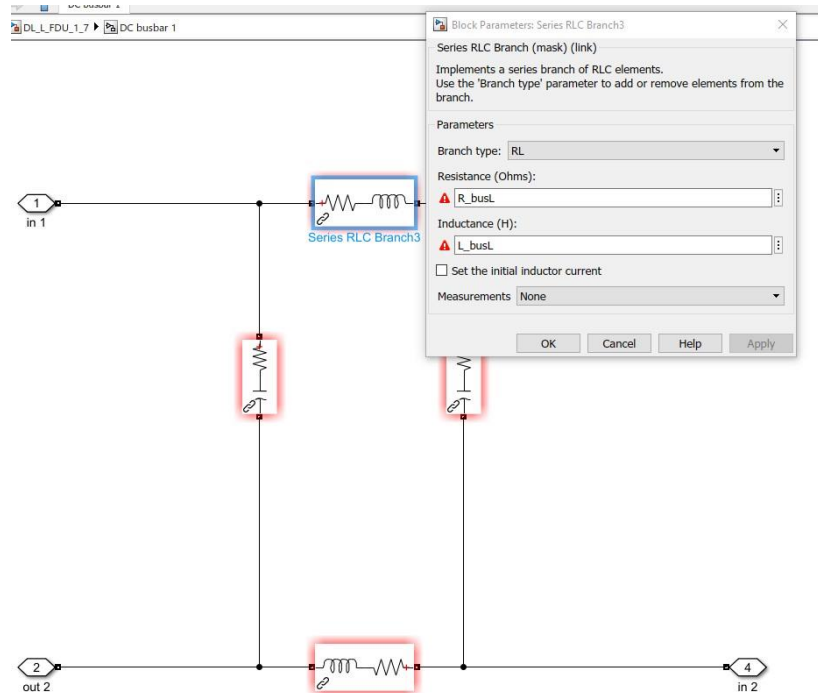


Figure 145: DC busbar for FDU - Line resistance and inductance

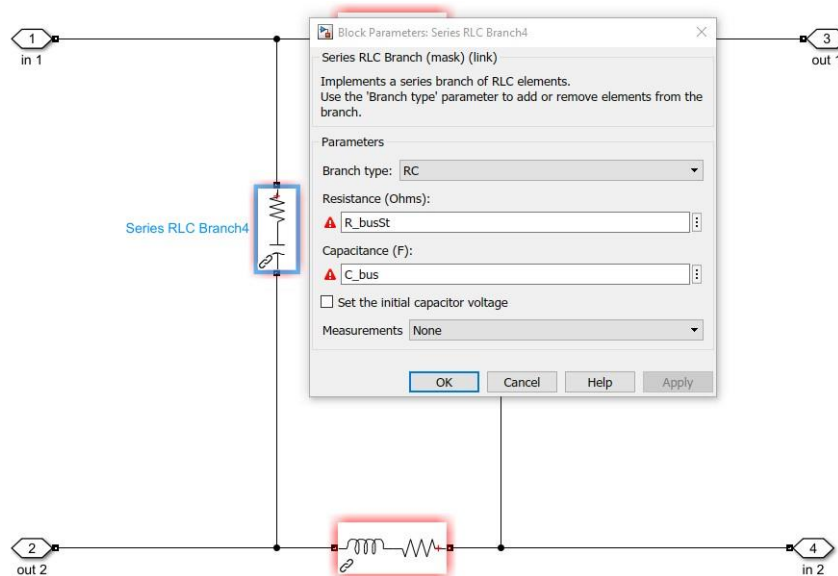


Figure 144: DC busbar for FDU - Stray resistance and capacitance

6.4.1.4 FDU

The FDU models are created by using switches and resistors (FDR).

Each switch has three possible states: open, open with current inside (arc) and closed and it's simulated with a Controlled Voltage Source component.

The arc voltage is set in the parameters list, excepted for the Pyrobreaker for which it is fixed inside the model according to more complex calculations.

For the resistors, they are modelled with a current source as their resistance vary depending on the temperature.

The BPS, the VCB and the PB are modelled as Controlled voltage sources according to the control logic shown in the previous section.

The electrical Matlab-Simulink model cannot be shown according to Company policy; however, the electrical scheme can be found in Figure 132.

6.4.2 Results for TFC configuration model

Below are presented the waveforms obtained for TFC configuration circuit FDU at 68 kA for a time simulation of 0.7 s without faults.

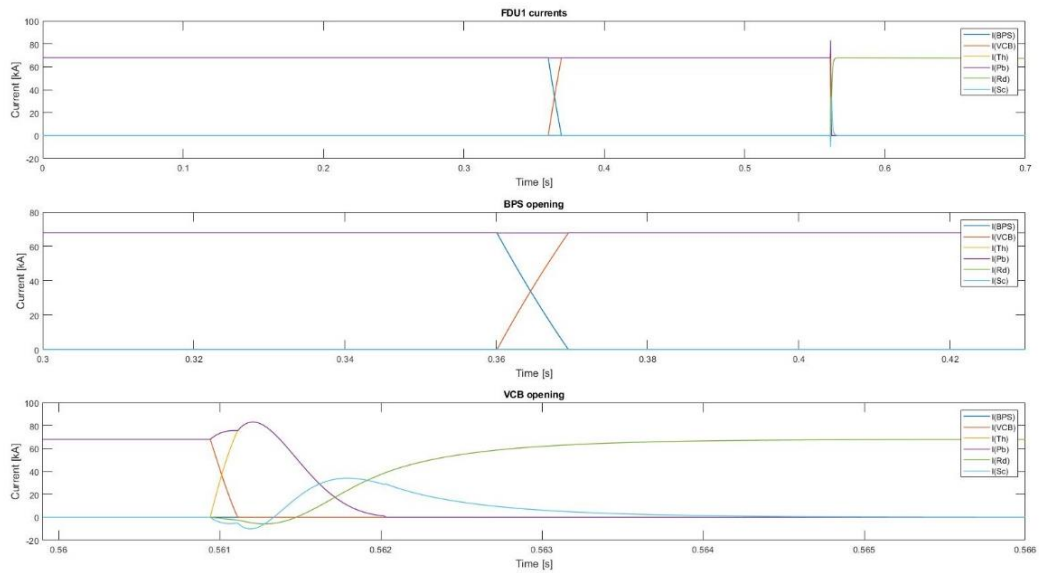


Figure 146: FDU1 opening sequence

The opening sequence starts at 0.11s but the BPS opening starts at 0.36s due to mechanical delay.

The current switches in less than 20 ms to the VCB with the formation of the arc on the BPS.

After 20 ms the opening signal is sent to the CPC in order to send a pulse with opposite sign to the VCB and bring the current to 0 A; the current then flows in the Discharge Resistor.

In the following figures are represented the voltages terminal to terminal and terminal to ground on the FDU1:

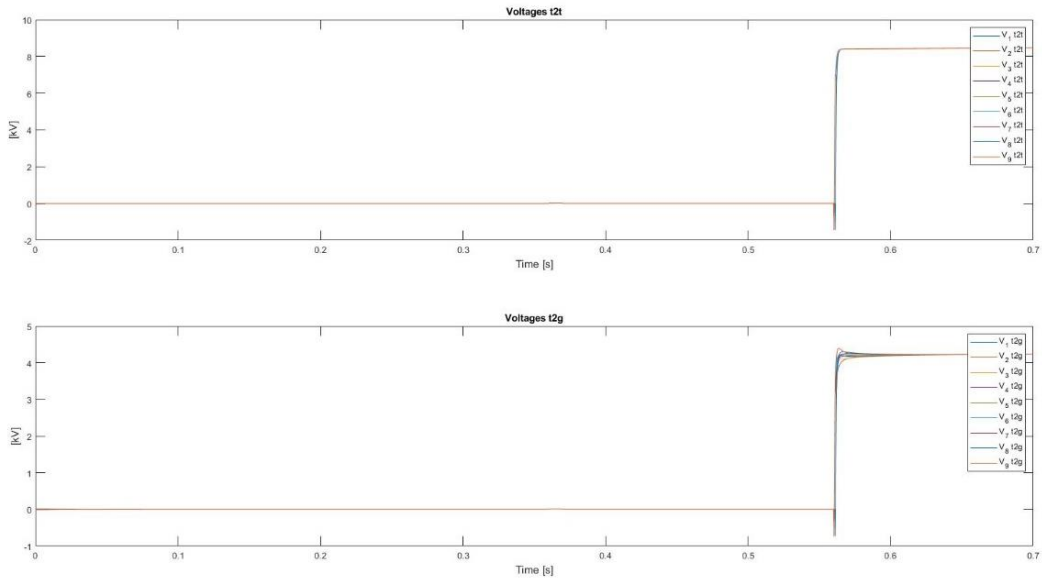


Figure 147: FDU1 voltages T2T and T2G

6.4.3 Results for DL configuration Model

Below are presented the waveforms obtained for an operation of DL configuration circuit FDU at 68 kA for a time simulation of 1 s without faults. The opening FDU is the FDU2 (chosen arbitrarily). For the logic control, please check the previous section as it is the same for both models.

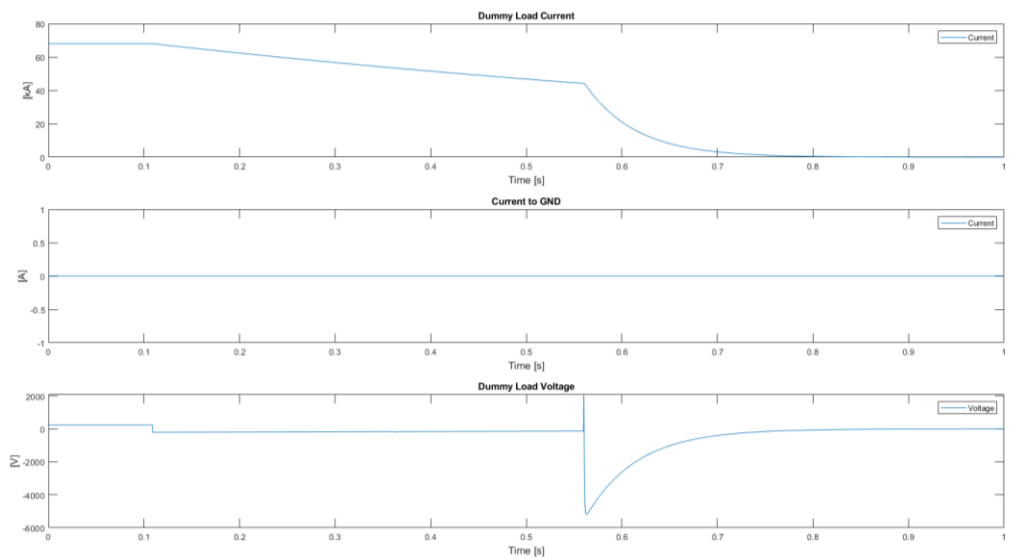


Figure 148: Dummy Load signals

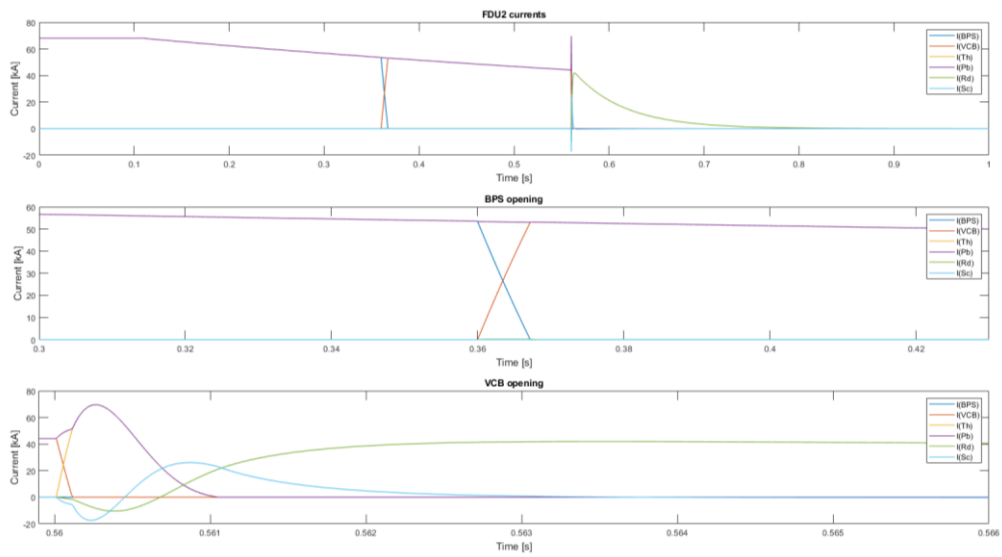


Figure 149: FDU2 opening sequence

The opening sequence is very similar to the previous case with the FDUs in TFCs configuration however it can be noted in this case that from the beginning of the triggering command of the FDU to the opening of the BPS the current is not kept at nominal value of 68 kA.

Since the Dummy Load has a very small inductance value (in terms of mH), the current cannot be kept stored in the DL as form of magnetic energy as the previous case.

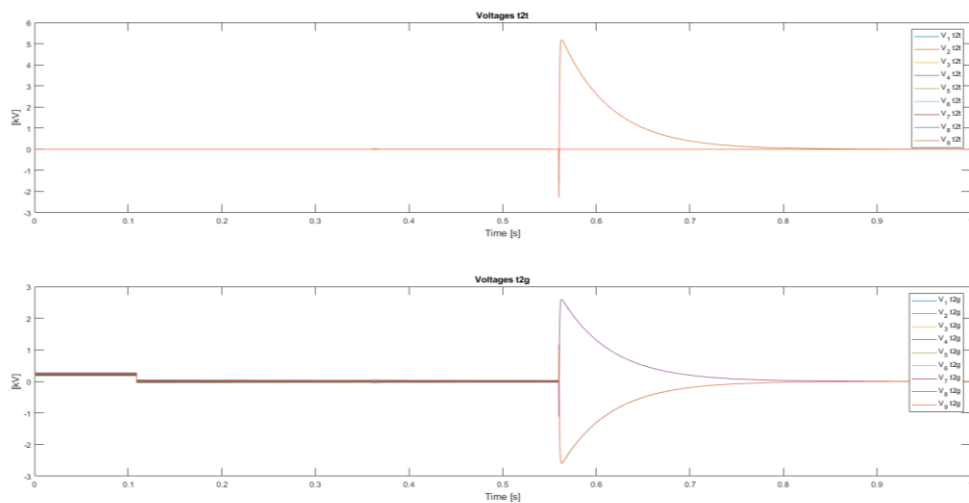


Figure 150: FDU2 voltages T2T and T2G

The voltages are now related to the opening of only one FDU and so it is configured now an asymmetric configuration.

6.4.4 Fault analysis of FDU in DL configuration

A deep analysis related to the worst possible fault conditions has been conducted with the Matlab-Simulink model described in the previous section.

The analysis is performed in order to evaluate the possible stressing conditions depending on the type of fault appearing before the triggering command of the FDU in order to evaluate overvoltage and transients during FDU opening sequence; some other scenarios also consider misfiring on single FDU components.

Accordingly to the test for Dummy Load configuration, there is only one FDU operating at each time; in this case the triggering command is given only to FDU number 2 (arbitrarily chosen).

All the faults described in Section 6.4.4.1 are related to a fault appearing at 0.015 s; during normal discharge operation (so at the beginning of each simulation) the current is flowing in the BPS of each FDU and at the above specified time the fault appears in the circuit and the location depends on the type of the Scenario.

The time of 0.015 s was chosen in order to have the fault at the beginning of the simulation but keeping a little margin (15 ms) after the beginning of the simulation in order to simulate the fault condition since the beginning of the discharge sequence of the FDU.

It should be noted that for Scenario 5-6 they are been taken into account the faults closest to FDU2 and the farthest (so FDU6) in order to evaluate the electrical quantities in opposite conditions.

The faults considered in the following scenario are grouped as Terminal-to-Terminal fault, Terminal to Ground fault and Double Terminal to Ground fault in order to evaluate all the possible situations.

The fault location changes for each Scenario and all of them are considered in order to evaluate all the fault locations; it should also be taken into account that the fault does not appear on other FDUs rather than FDU2 in the Dummy Load configuration since during the discharge with DL configuration all the FDU are bypassed by the BPS (no evaluable differences with faults in other FDUs).

It should be noted that the Scenario on fault location on the Power Supply is out of scope of the study: the fault locations considered here are in the discharge path and they appear after the bypassing of the Power Supply.

In next sections are reported the electrical schemes and a brief description of the fault Scenario; results and comments are reported at the end of the Section 6.4.4.

It should also be noted that the Pyrobreaker command circuit is not activated for all the simulations, according to the internal test procedure.

6.4.4.1 Fault list for Dummy Load Scenario

For DL configuration and only related to the T2T faults, they are only taken into account considering the fault between input and output terminal of FDU2 for the reason specified above: all the other terminals of other FDUs are short-circuited with a very low internal resistance so the only evaluable scenario is the one with T2T fault appearing on FDU2 (the only one triggered for discharge).

About the T2G faults for DL configuration: both simulations on input and output terminal of FDU2, FDU2's busbar and Dummy Load are considered, the results are the same but with opposite sign as expected (results of Scenario 1,2,4).

In the following list all the considered faults are reported with the related number of simulations included, it should be noted that the first simulation is normal operation without fault. According to the typology of considered Scenario, there will be different simulations (fault studies) among the same scenario in order to evaluate different locations of fault in the electrical circuit:

- Scenario 0-1: Dummy Load discharge operation without faults (**1 simulation**)
- Scenario 1: Fault to GND on input (and output) terminal of FDU2 (**2 simulations**)
- Scenario 2: Fault to GND on input (and output) terminal of FDU2's busbar (**2 simulation**)
- Scenario 3: Fault to GND of output terminal of power supply (**1 simulation**)
- Scenario 4: Fault to GND on the input (and output) terminal of Dummy Load (**2 simulation**)
- Scenario 5: Double fault to GND on input and output terminals of FDU2; Double fault to GND on input terminal of FDU2 and input terminal of FDU6 (**2 simulations**)
- Scenario 6: Double fault to GND on input and output terminals of FDU2's busbar; Double fault to GND on input terminal of FDU2's busbar and input terminal of FDU6's busbar; (**2 simulations**)
- Scenario 7: Short-circuit on FDU2's input-output terminals. (**1 simulation**)
- Scenario 8: Short-circuit between same terminals of DC busbar's of FDU2 (**1 simulation**)

- Scenario 9: Short-circuit on input-output terminals of Dummy Load (1 simulation)
- Scenario 10: Fault on triggering command of BPS (1 simulation)
- Scenario 11: Fault on triggering command of CPC (1 simulation)

Total simulations: 17

In the next Sections there are the fault scheme for each Scenario and all the results are reported in a Table at the end of this Section (with the max value for each electrical parameter).

6.4.4.2 Normal operation

6.4.4.2.1 Scenario 0-1

In this Scenario there are no faults. The following image is related to the electrical scheme with Dummy Load configuration without faults:

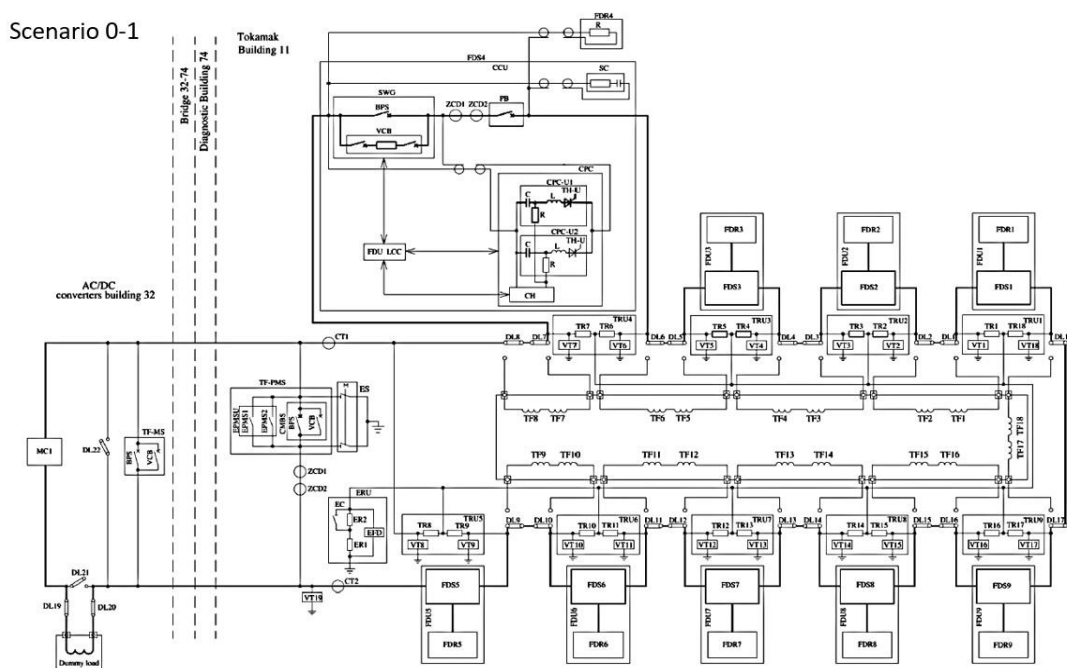


Figure 151: Electrical scheme with DL config. without faults

According to the discharge procedure, the following figure represents the current path before the triggering of the FDU2:

Scenario 0-1

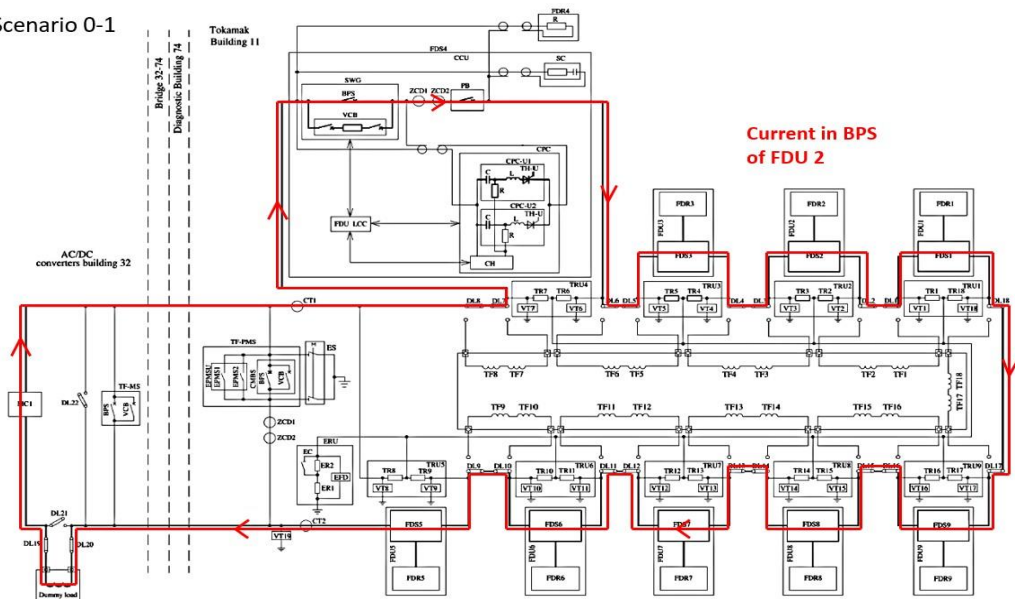


Figure 152: Current path before triggering

With a zoom inside electrical scheme of FDU2:

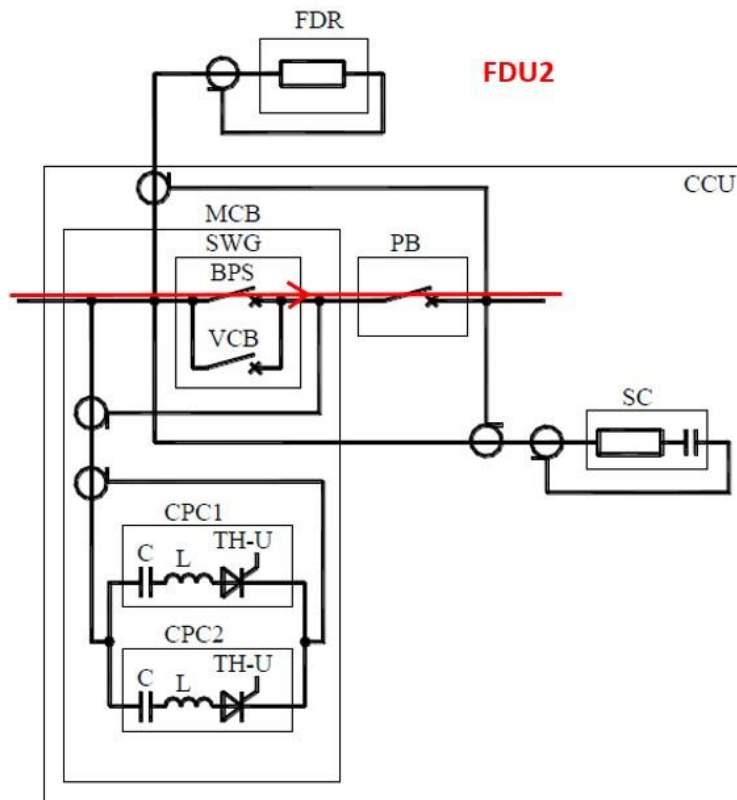


Figure 153: Zoom on electrical scheme of FDU2 (current flowing in BPS)

After the triggering of the FDU2, the current flows in the VCB ($t=0.36s$), in the next figure are represented both moments of current flowing in the VCB and then the transient while the CPC sends a counter pulse current in order to force the current to reach 0 A in the VCB ($t=0.56s$). It should be noted that the current path in the next figure is the same as the previous one, the only change is the current path inside FDU2 which is flowing in the VCB:

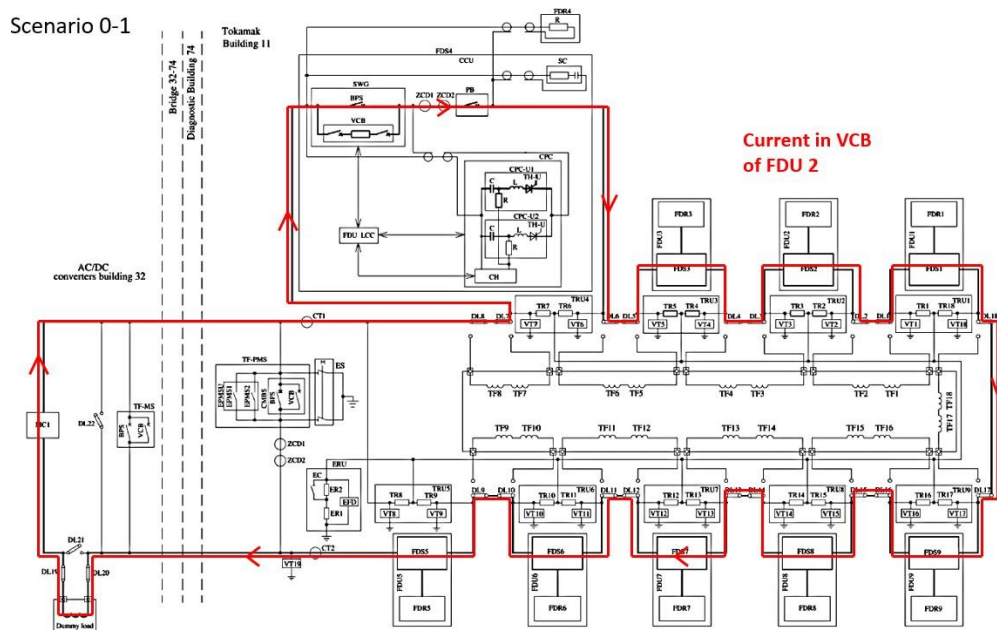


Figure 155: Electrical path of current flowing in the VCB of FDU2

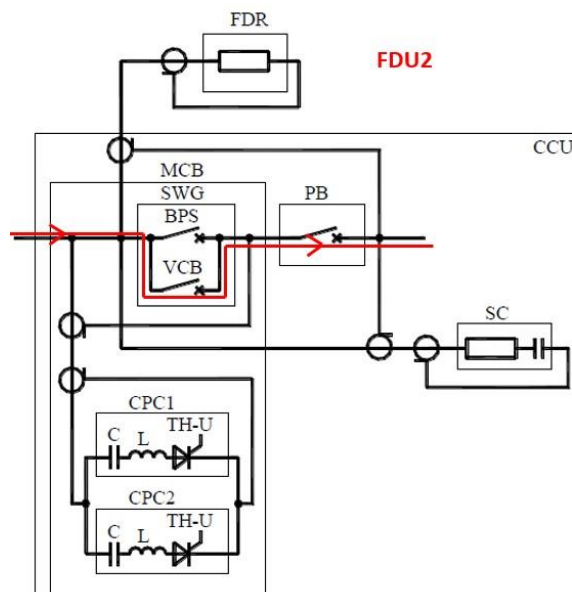


Figure 154: Current flowing in the VCB of FDU2 ($t=0.36 s$)

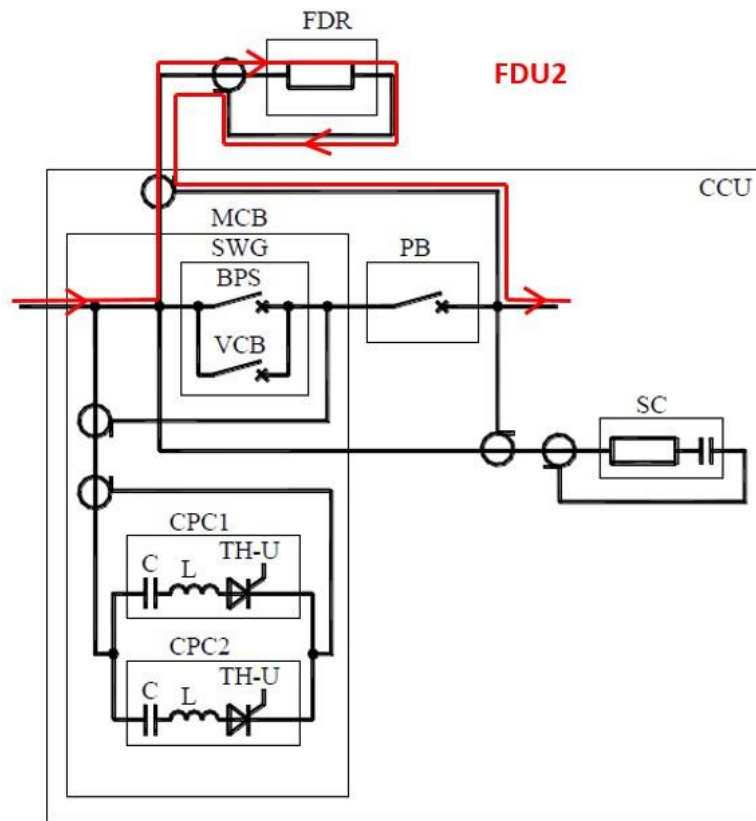


Figure 158: Electrical path of the current in FDU2 ($t > 0.56$ s)

The graphs seen in Figure 149 represent the trend of the electrical parameters during the discharge: it should be noted that at $t > 0.56$ s the current has a negative transient; this is due to the fact that the current coming from CPC1 and CPC2 (which path is described in Figure 157) goes also in the Snubber Circuit and in the Discharge Resistor. Only for a short transient so the current is negative.

6.4.4.3 Faults to GND

6.4.4.3.1 Scenario 1

Fault to GND on input (and output) terminal of FDU2 (2 simulation)

Scenario 1
(sim. 1)

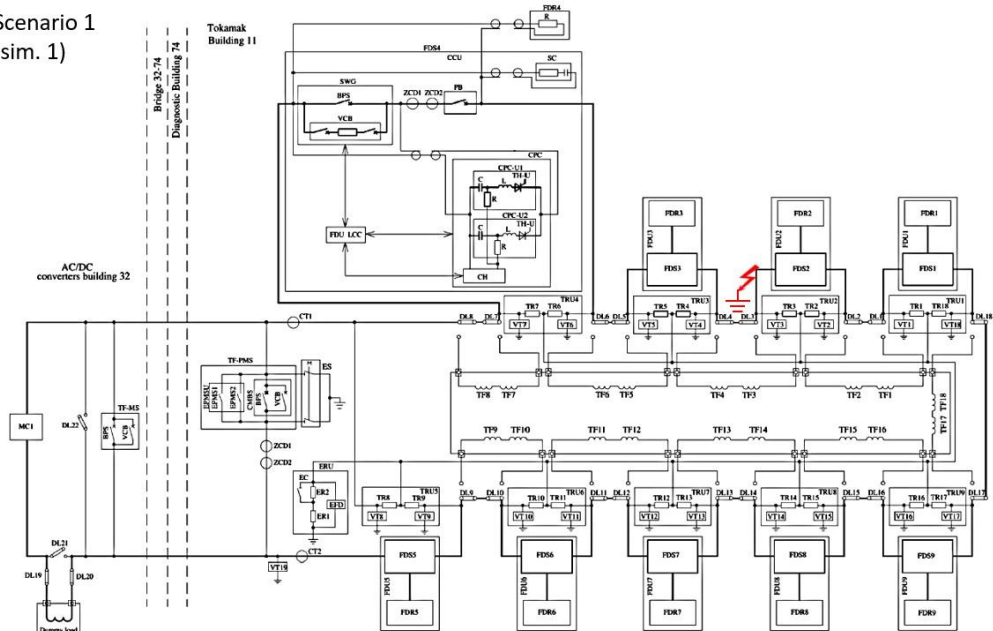


Figure 160: Scenario 1, Simulation 1.

Scenario 1
(sim. 2)

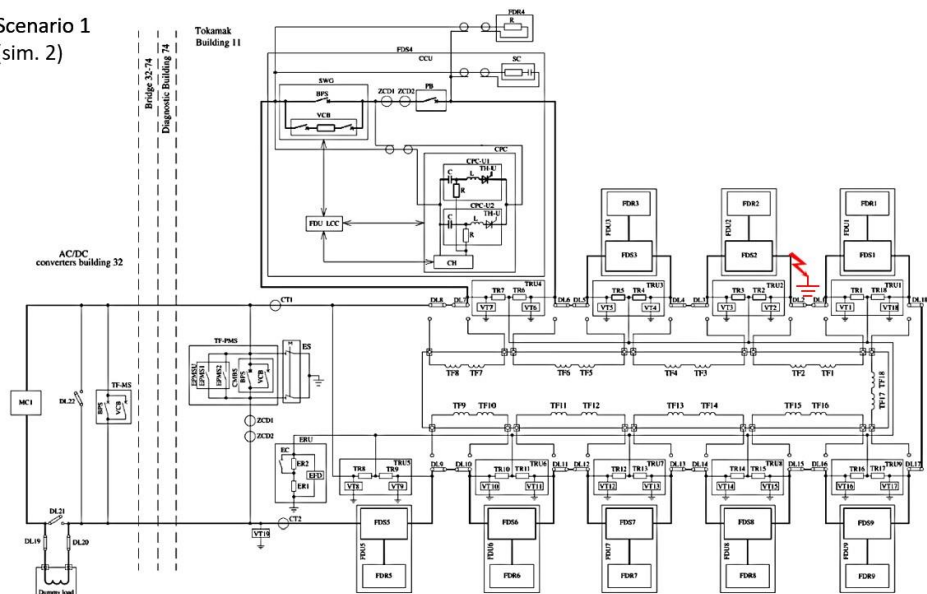


Figure 159: Scenario 1, Simulation 2.

6.4.4.3.2 Scenario 2

Fault to GND on input (and output) terminal of FDU2's busbar (2 simulation)

Scenario 2
(sim.1)

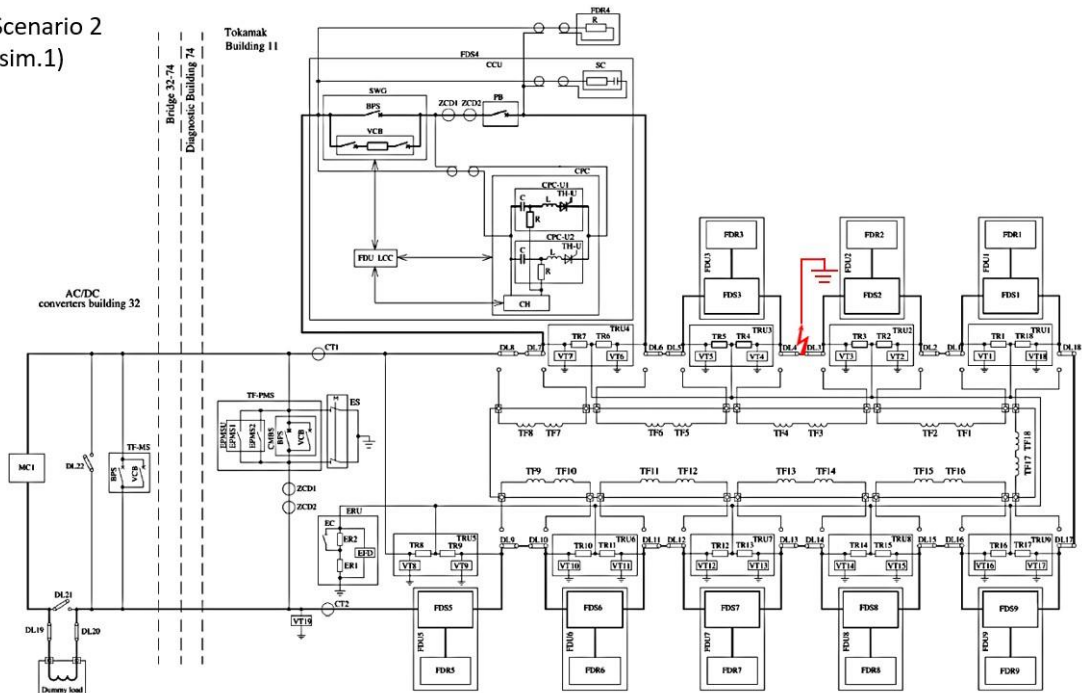


Figure 162: Scenario 2, Simulation 1

Scenario 2
(sim.2)

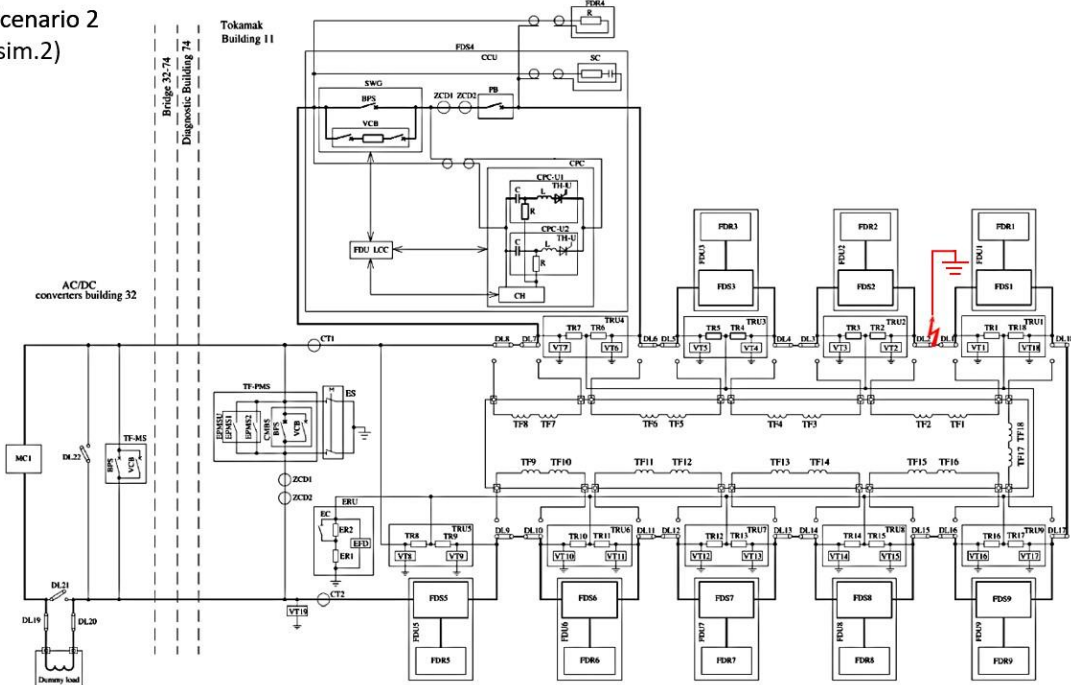


Figure 161: Scenario 2, Simulation 2

6.4.4.3.4 Scenario 4

Fault to GND on the input (and output) terminal of Dummy Load (2 simulation)

Scenario 4
(sim. 1)

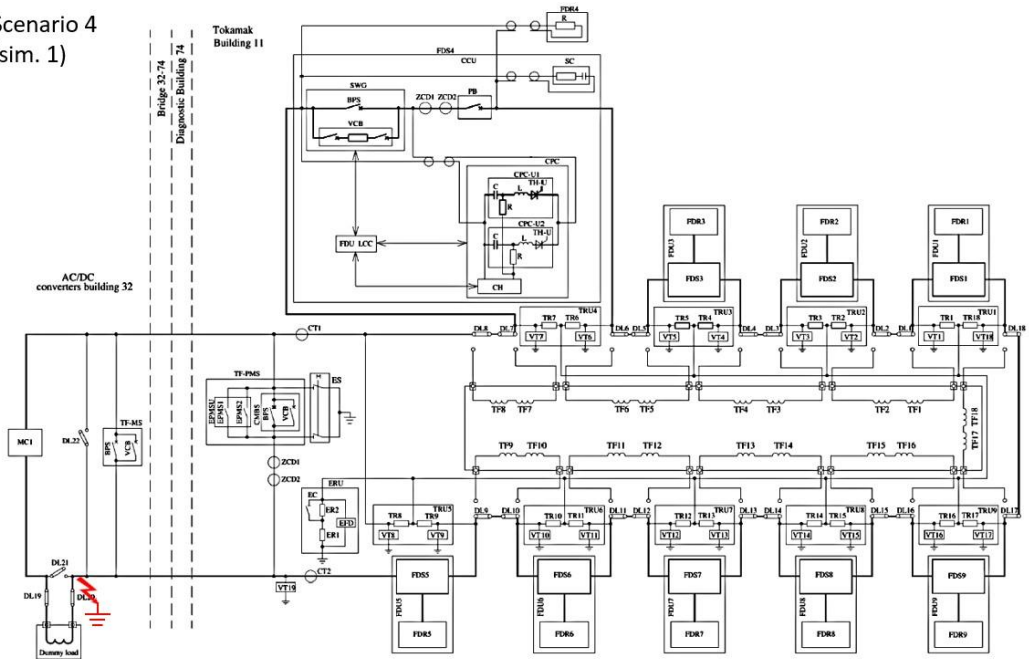


Figure 165: Scenario 4, Simulation 1

Scenario 4
(sim. 2)

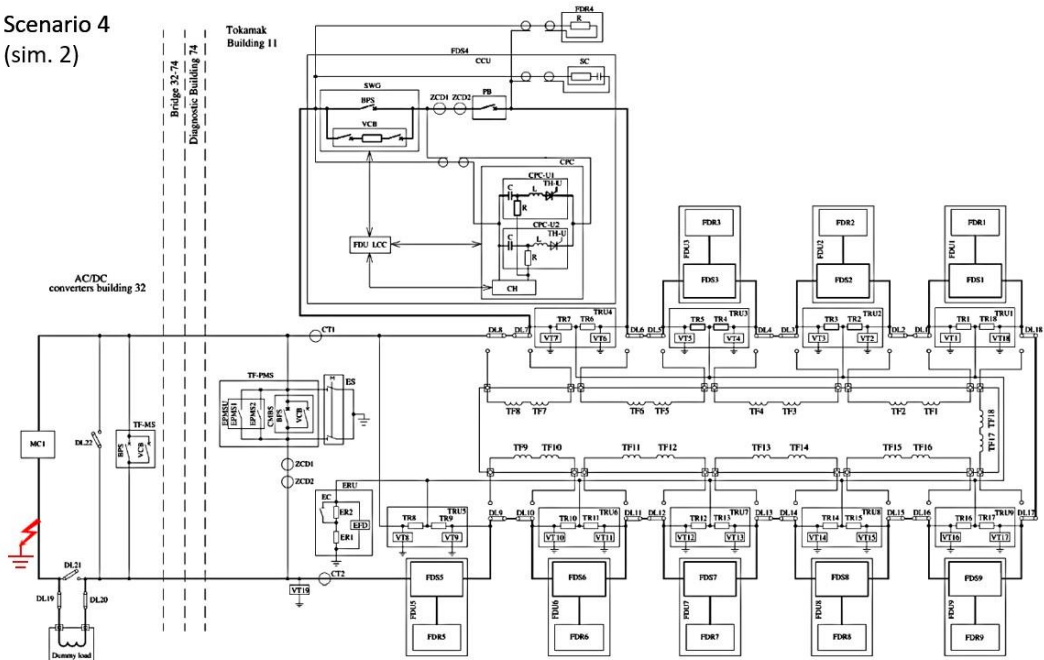


Figure 164: Scenario 4, Simulation 2

6.4.4.3.5 Scenario 5

Double fault to GND on input and output terminals of FDU2; Double fault to GND on input terminal of FDU2 and input terminal of FDU6 (2 simulations)

Scenario 5
(sim. 1)

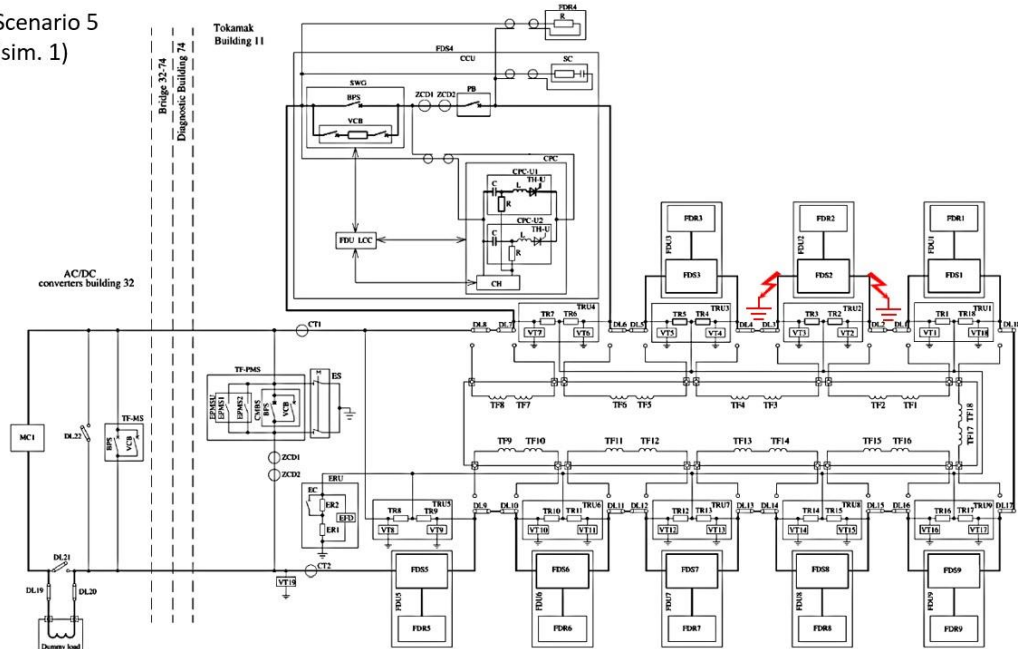


Figure 167: Scenario 5, Simulation 1

Scenario 5
(sim. 2)

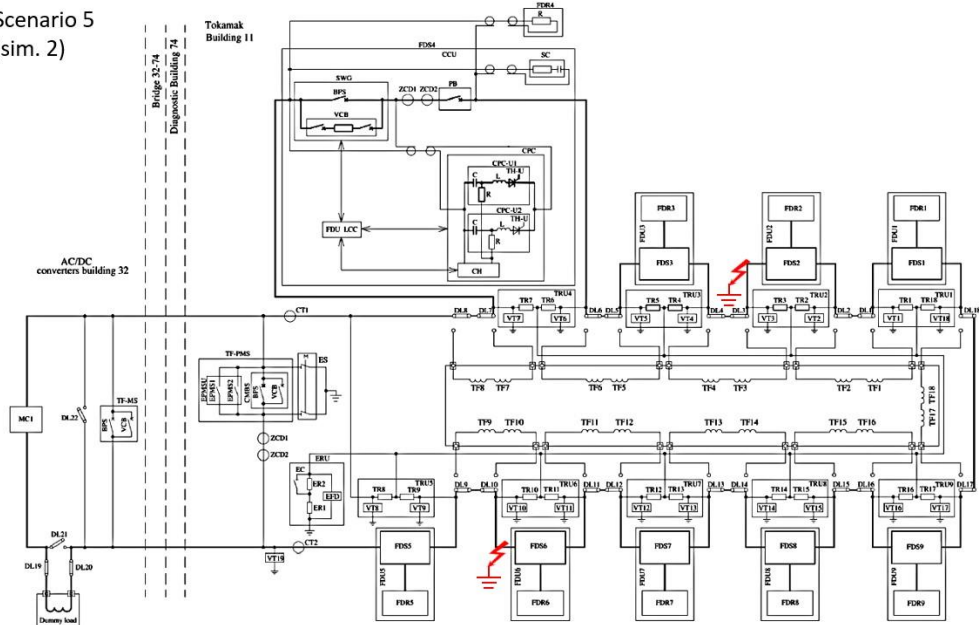


Figure 166: Scenario 5, Simulation 2

6.4.4.3.6 Scenario 6

Double fault to GND on input and output terminals of FDU2's busbar; Double fault to GND on input terminal of FDU2's busbar and input terminal of FDU6's busbar; **(2 simulations)**

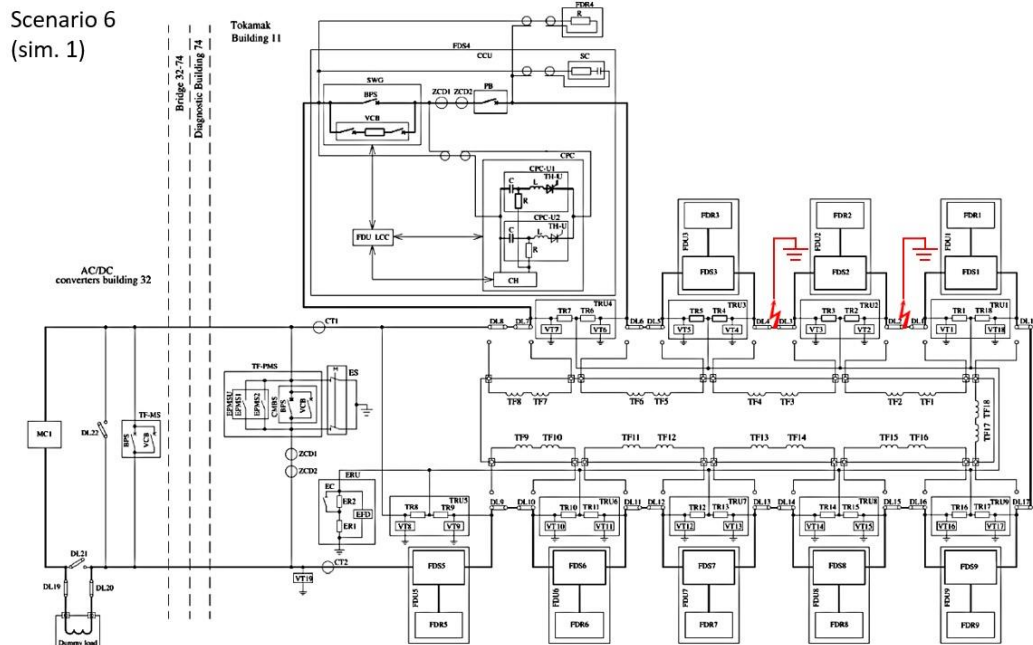


Figure 169: Scenario 6, Simulation 1

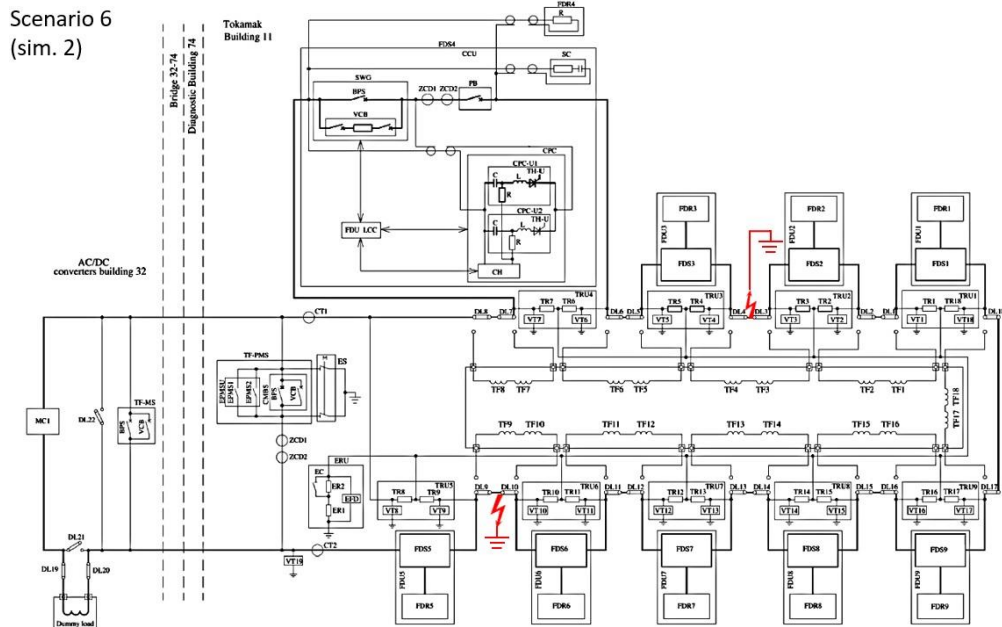


Figure 168: Scenario 6, Simulation 2

6.4.4.4 Fault between terminals

6.4.4.4.1 Scenario 7

Short-circuit on FDU2's input-output terminals. (1 simulation)

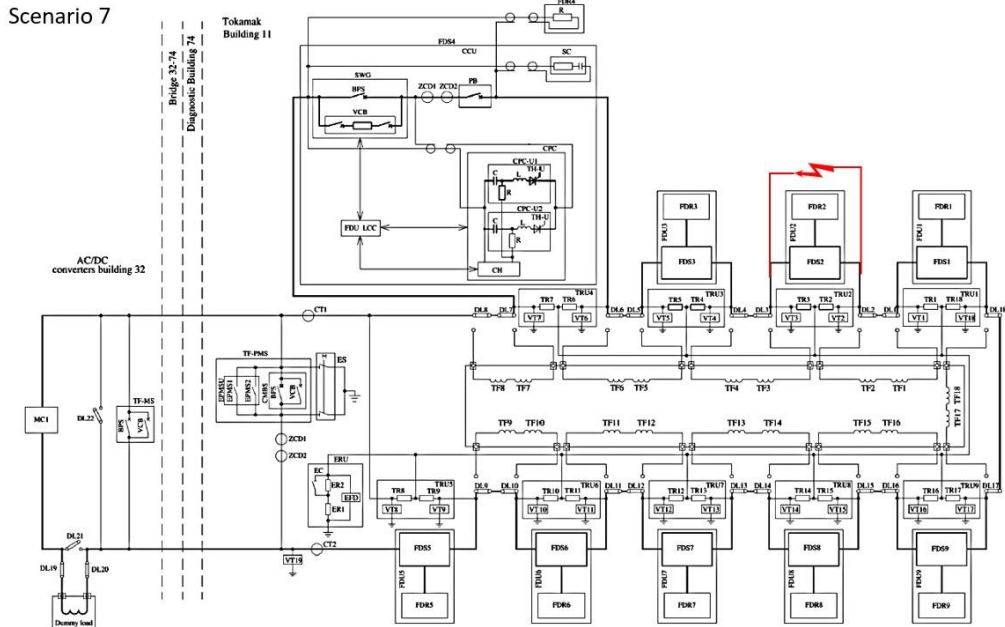


Figure 170: Scenario 7

6.4.4.4.2 Scenario 8

Short-circuit between same terminals of DC busbar's of FDU2 (1 simulation)

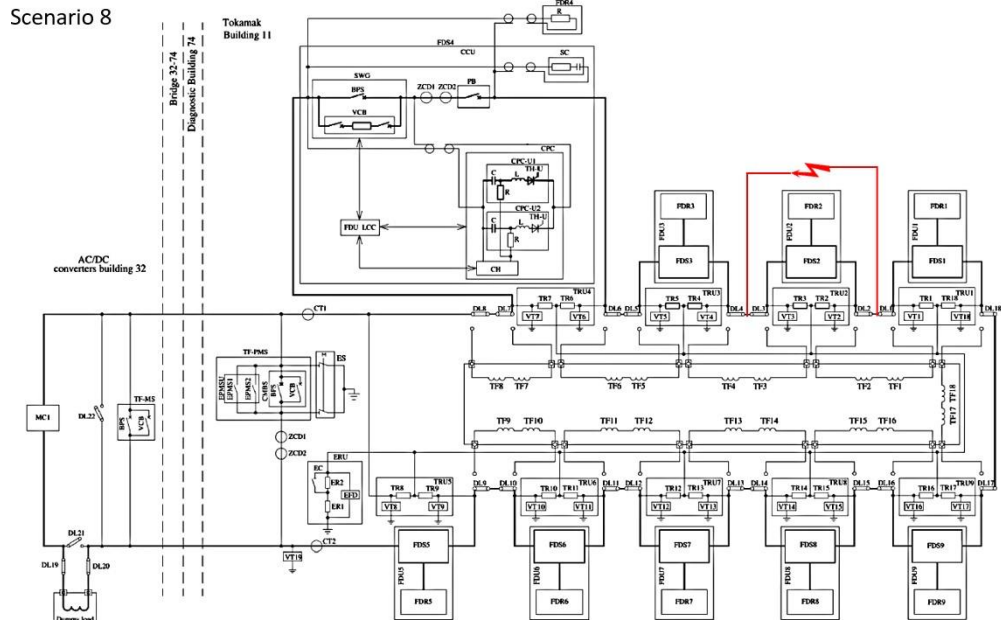


Figure 171: Scenario 8

6.4.4.4.3 Scenario 9

Short-circuit on input-output terminals of Dummy Load (1 simulation)

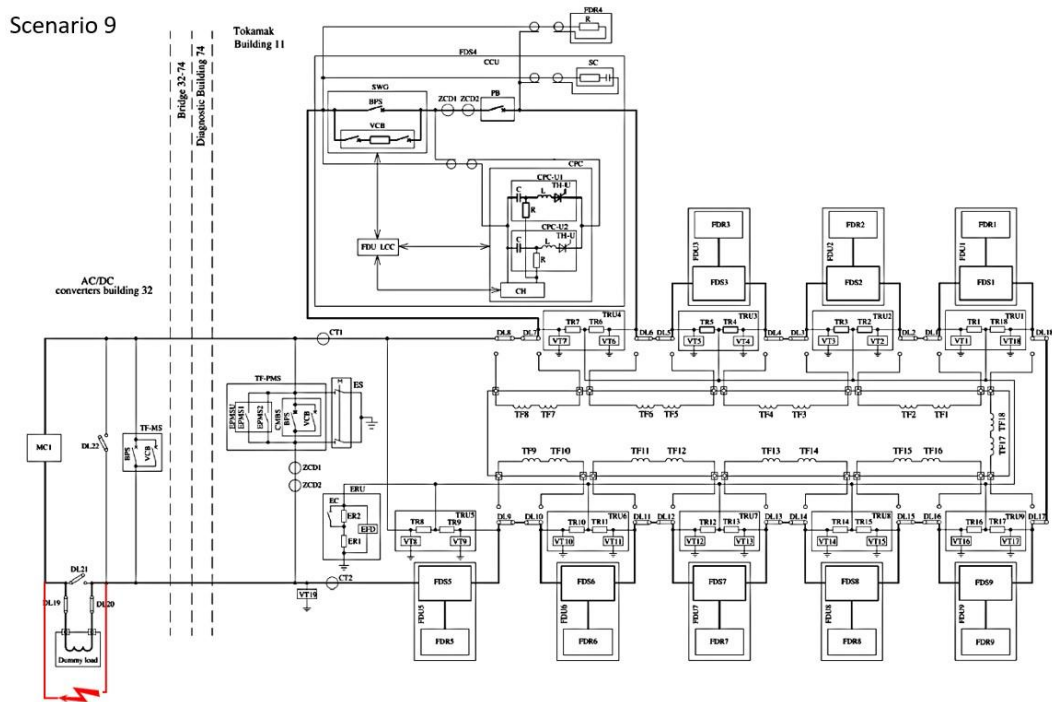


Figure 172: Scenario 9

6.4.4.5 Fault on triggering commands

6.4.4.5.1 Scenario 10

Failure of BPS opening (1 simulation)

In the following figure is reported the simplified electrical scheme for the FDU, in this simulation the fault is related to the BPS which is still closed after the triggering open command (triggering command not received).

6.4.4.5.2 Scenario 11

Failure of CPC (1 simulation)

In the previous figure is reported the simplified electrical scheme for the FDU, in this simulation the fault is related to the CPC which doesn't send the counter pulse current after the triggering open command on the VCB (triggering command not received).

6.4.4.6 Results

The following table reports the maximum absolute value of the related electrical parameter for Scenario with Dummy Load configuration (with activation only of FDU2) for the Scenarios 1-11:

Table 13: FDU fault analysis in DL config. results

Scenario name	Leakage Current to GND (max.) [A]	Dummy Load Voltage (max.) [V]	Fault current (max.) [A]	T2T max. FDU Voltage [kV]	T2G max. FDU Voltage [kV]
0-1	0	5189.52	0	5.18	2.59
1 (sim.1)	1.29	5189.55	1.29	5.18	5.18
1 (sim.2)	1.29	5189.55	1.29	5.18	5.18
2 (sim.1)	1.29	5189.55	1.29	5.18	5.19
2 (sim.2)	1.29	5189.55	1.29	5.18	5.18
3	1.29	5189.55	1.29	5.18	5.19
4 (sim.1)	1.29	5189.55	1.29	5.18	5.18
4 (sim.2)	1.29	5189.55	1.29	5.18	5.19
5 (sim.1)	0.011	237.99	0.011	0.001	0.270
5 (sim.2)	0.005	238.00	0.005	3.22	2.74
6 (sim.1)	0.011	237.99	0.011	1.66	0.83
6 (sim.2)	0.002	237.99	0.002	3.22	2.51
7	0.0002	237.99	46754.11	0.002	0.271
8	0.0002	237.99	53590.03	1.663	0.816
9	0.004	237.99	59270.53	3.68	2.14
10	0	5198.89	0	5.19	2.60
11	0	237.99	0	0.024	0.271

It can be seen that Scenarios 1-4 do not deviate too much from the normal no-fault discharge parameters and the only differences are in the maximum voltage to ground which is obviously twice as high in this case, this is to be justified to the type of fault being simulated (i.e., a ground fault).

There is also a current to ground of 1.29 A for each Scenario. It can be assumed that under such fault conditions there are no critical overvoltage and overcurrent conditions outside the design limits.

Scenario 5 and 6, on the other hand, are related to a double ground fault, there are no electrical parameters out of standard with respect to the design parameters and the leakage current to ground remains minimal.

The most severe conditions are definitely those related to Scenarios 7,8,9 which simulate a fault between two terminals that does not include ground (short circuit between two terminals of the same component, e.g., for Scenario 7 there is a short circuit between input and output terminal of FDU2).

Such scenarios do not result in the emergence of an overvoltage as much as a particularly high fault current that, in the worst case, reaches 59.3 kA (Scenario 9).

Scenario 10 involves the failure of the BPS trip command: this does not affect the FDU's ability to complete the circuit discharge.

Scenario 11 is similar to the previous one as that involves the failure of the activation command but of the CPC: in this case there is no complete discharge by the FDU and current continues to flow in the VCB without flowing into the Discharge Resistor.

In conclusion, the scenarios that should be given the most attention are definitely Scenarios 7,8,9 and 11: in particular, Scenarios 7,8,9 report an abnormal sequence of discharge by the FDU with particularly high values of fault current while Scenario 11 reports a fault condition in which proper discharge by the FDU cannot be completed as, reported on the introduction, the PB does not intervene.

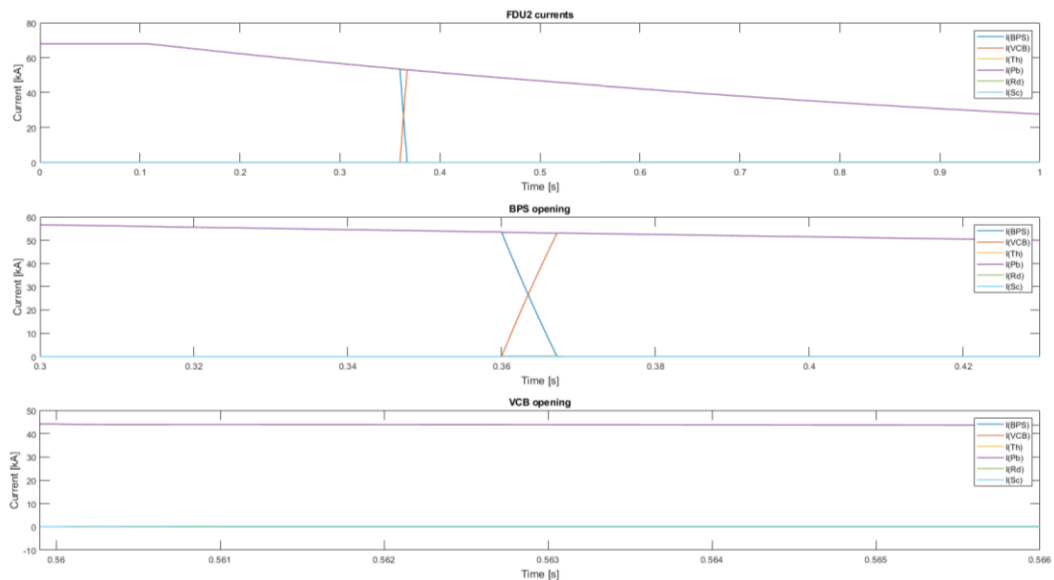


Figure 173: Scenario 11 opening sequence not completed

The results related to the other scenarios are available in the Appendix.

6.4.5 FDU control logic description

In this section the control logic of the FDU is reported with the implementation on the Matlab-Simulink model and with the related results.

The basic logic diagram for BPS, VCB, CPC and PB is reported in Figure 133 and Figure 134 with the full description of how the logic works.

The following results are related to the missed opening of BPS, VCB and missed counter pulse command from CPC in TFC configuration circuit with FDUs.

In the next sections there will be reported:

- The FDU1 control status with the signal on BPS, VCB and CPC
- PB control status
- PB control status zoom
- PB report

The FDU control status is a diagram with the signals sent to all the FDU components specified above in order to check if the opening sequence is properly followed.

The PB control status is a diagram with the signals sent to the PB in order to control its activation with signals coming from BPS and VCB failure blocks and Zero Current detectors block.

The PB control status zoom is just a zoom of the previous diagram to the time range of when the PB is activated.

PB report is a diagram which reports if the PB was activated or not.

6.4.5.1 No faults

In the following figures are reported again the FDU opening sequence with the related currents:

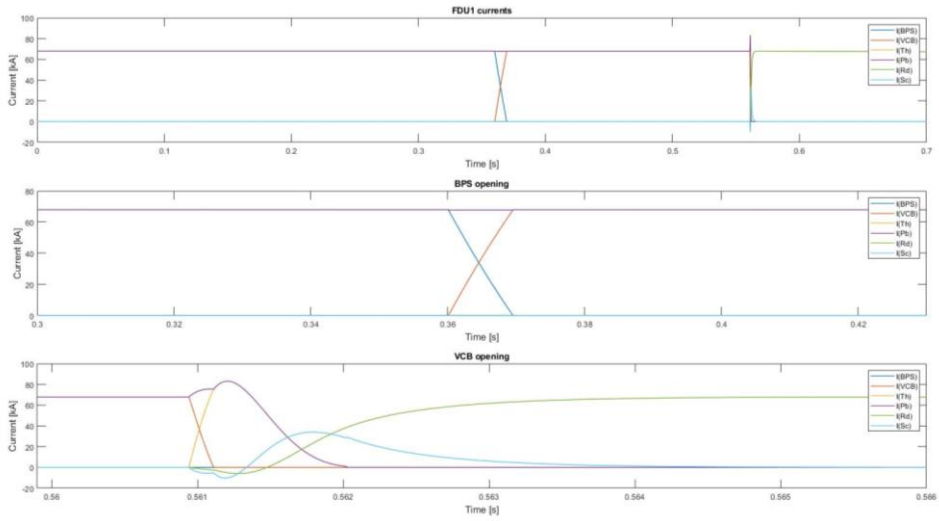


Figure 175: FDU normal opening sequence

The FDU control status related to a normal opening sequence is the follow:

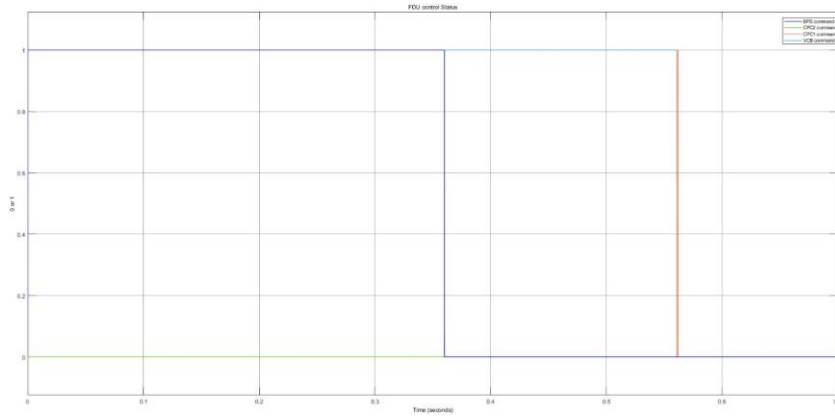


Figure 174: FDU1 Control Status

The PB control status and the PB report are the following figures:

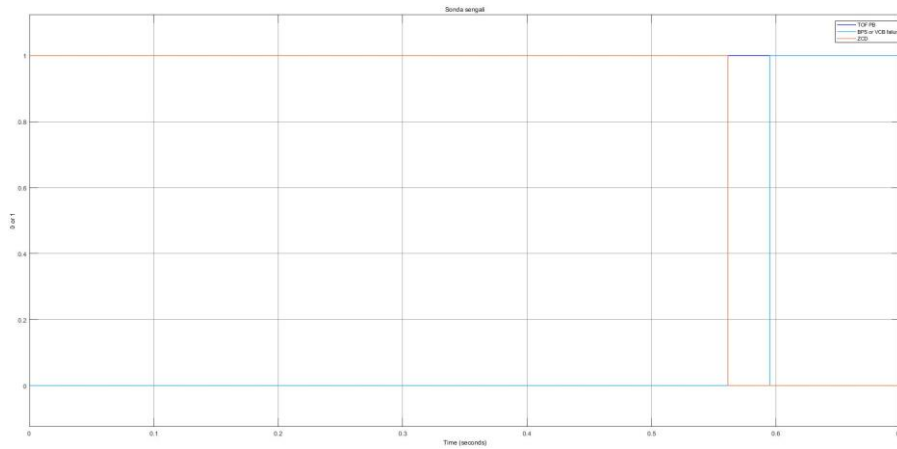


Figure 176: PB control status

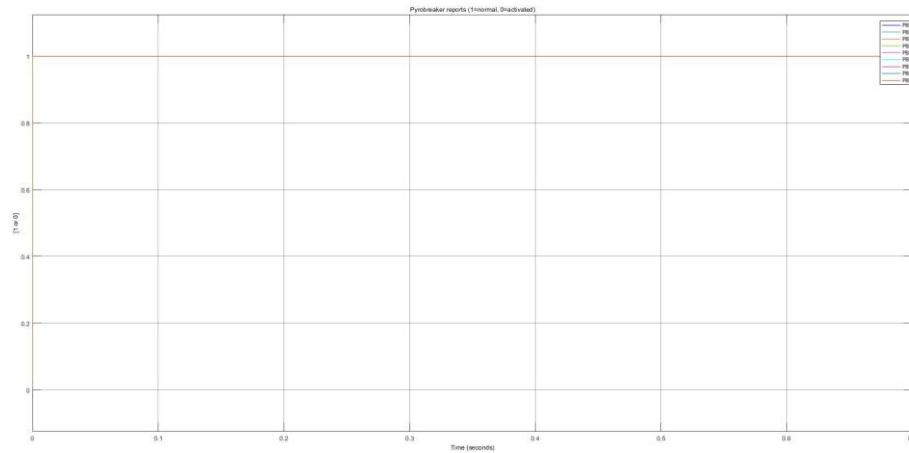


Figure 177: PB activation report

In this study, there are no faults related to the triggering command of the FDU components, so the PB control status never has all the 3 signals equal to 1 which determines the activation of the PB.

The previous diagram is confirmed by the PB activation report which is always 1 so there is no activation of the PB for all the simulation (PB activation = 0 at the moment of the activation of the PB).

6.4.5.2 Fault on BPS

The FDU1 opening sequence is represented in next figure:

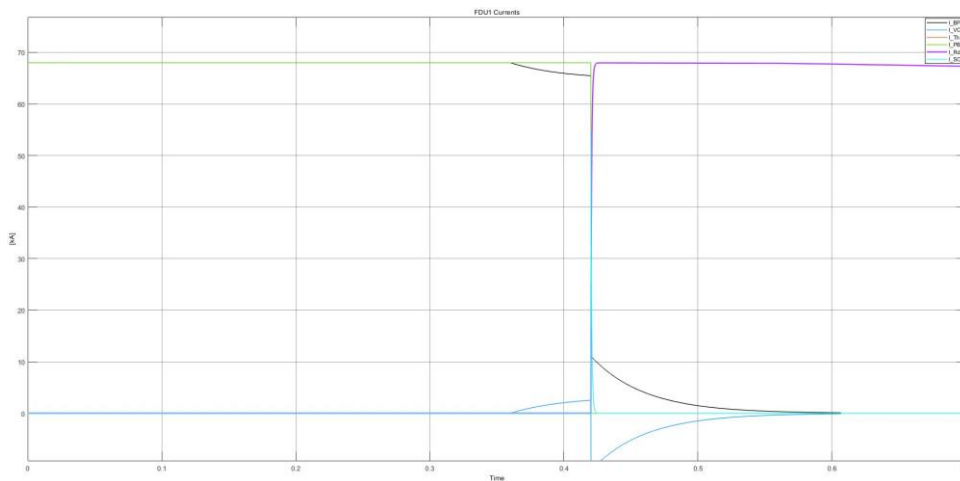


Figure 178: Opening sequence with BPS fault and PB activation

The BPS does not receive the activation command and as can be seen from the previous figure, the PB proceeds to the current interruption.

More details are provided in the next figures:

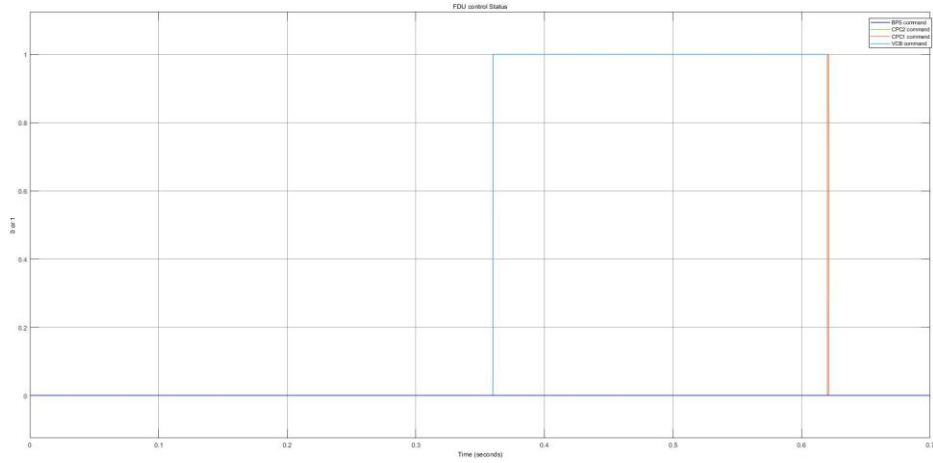


Figure 180: FDU1 control status with BPS fault

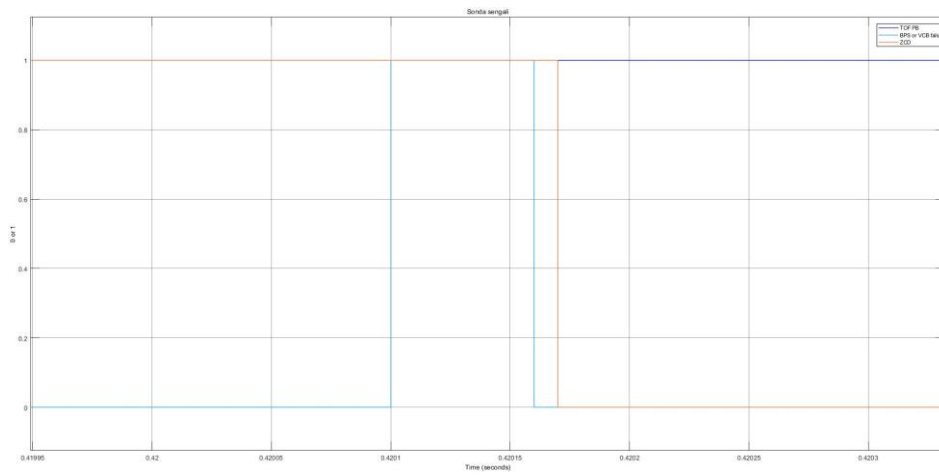


Figure 179: PB control status zoom on PB activation

6.4.5.3 Fault on VCB

The FDU1 opening sequence is represented in next figure:

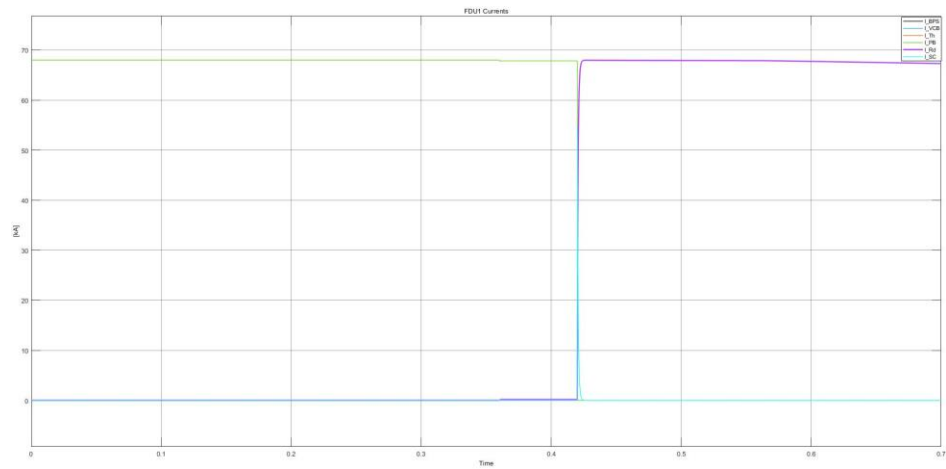


Figure 181: Opening sequence with VCB fault and PB activation

The VCB does not receive the opening triggering command with a consequent activation of the Pyrobreaker at 0.4201 s:

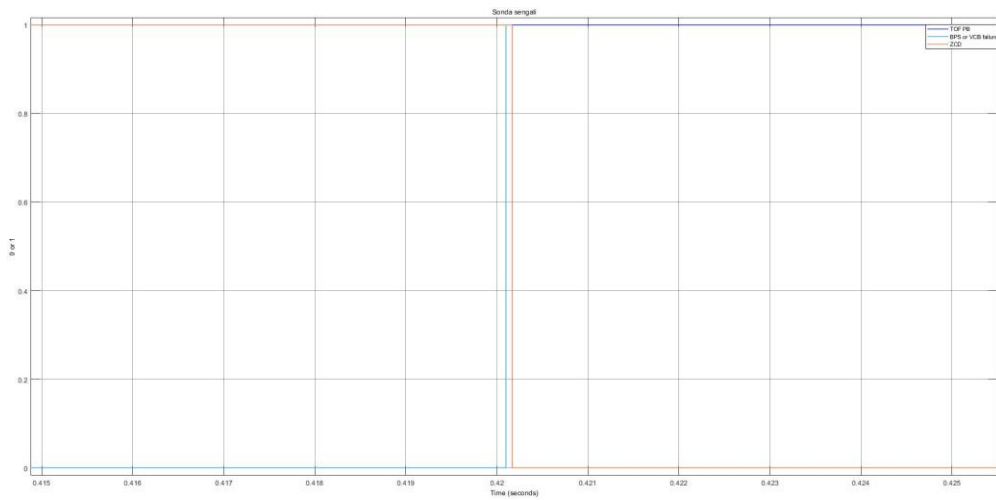


Figure 182: PB control status zoom on PB activation

6.4.5.4 Fault on CPC

The CPC does not receive the activation command and as can be seen from the previous figure, the PB proceeds to the current interruption.

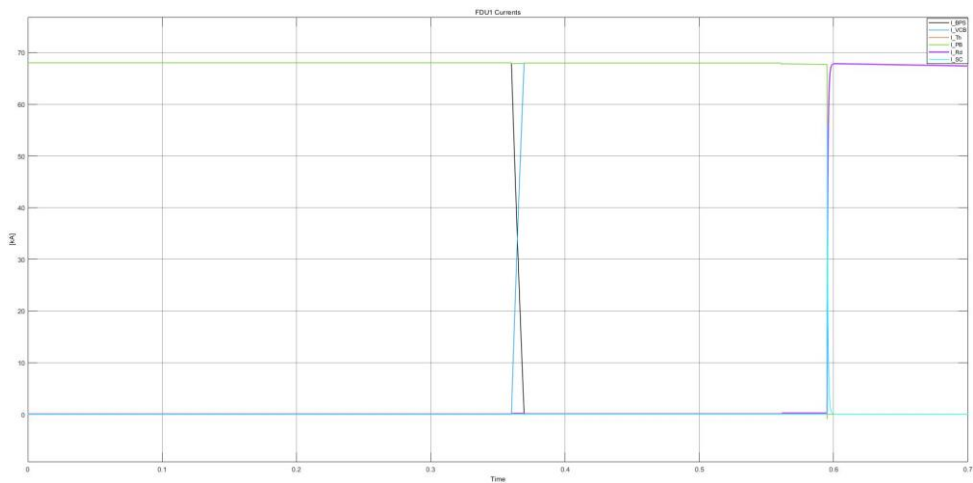


Figure 183: Opening sequence with CPC fault activation and PB activation

The PB control status diagram is the same as the previous case but shifted at 0.5951 s.

6.5 Fast Discharge Units on DEMO

The main purpose of the study related to DEMO was to validate the applicability of the ITER-like technology for DC Circuit Breakers for the FDUs of TFCs in the whole range of current and voltage values under consideration for the TFCs.

It should be noted that all the information reported in this chapter are referenced to an internal document, [42] .

In the next table are reported the main characteristics of the TFCs for DEMO [42]:

Table 14: Main characteristics of DEMO TFCs (updated to 2021)

TFCs	Symb.	Value
Number of TFCs	N	16
Number of turns per coil	N_t	142
Total Inductance	L_T	22.56 H
Total Energy	E_T	124.36 GJ
Operating Current	I_{op}	104.95 \cong 105 kA
Equivalent coil inductance	L	1.41 H
Discharge Time Constant	τ	35 s
Delay Time	t_d	1.1 s

Whereas the voltage stresses of DEMO superconducting TFCs are reported in the next Table:

Max terminal-to-terminal voltage at current dump in normal operation [kV]	Max terminal to ground voltage at current dump in normal operation [kV]	Max terminal to ground voltage at current dump in case of fault [kV]
6	3	Value to be quantified

Since all TF coils are operated with the same DC current, they can be connected in series and supplied by a single Base Power Supply. The protection of the TFCs from quench is delegated to the FDUs, which insert resistors in the circuit in order to safely discharge the TFC energy, satisfying the coil operative limits in terms of maximum applied voltage and Joule integral.

Concerning the FDU topology, to reduce the voltage at FDU intervention, the number of FDUs must be increased up to the number of TF coils and to balance the voltage to ground, the FDU units have to be interleaved with the coils. Four different topologies (called A, B, C and D) have been identified as possible candidate for the DEMO TF circuit, differing for the earthing topology: one ITER-like and one JT-60SA-like, and for the connection of the discharge resistors (DR), either in parallel to the FDU circuit breakers or to the coils. These topologies are shown in Figure 184.

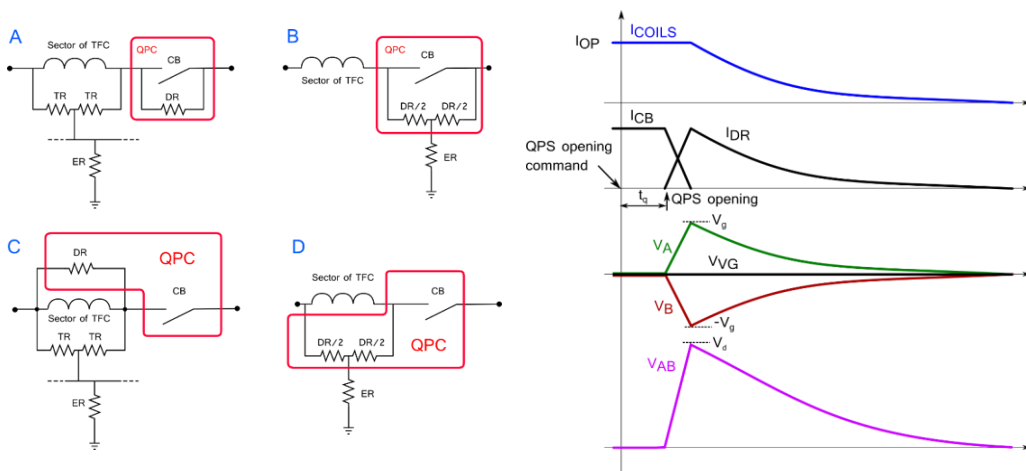


Figure 184: Circuit topologies: A is ITER-like, B, C and D (left). Conceptual waveforms of main currents and voltages in TFC circuit in case of FDU intervention in normal conditions (right) [42]

The earthing circuits derive from those adopted in ITER and JT-60SA: the first consists in a couple of terminal resistors connected at one side to the terminals of each coil and at the other side to a common earthing resistor grounded (ER) (Fig. A); the second is implemented connecting the central point of each discharge resistor to ground through an earthing resistor grounded (Fig. B). In all the topologies analysed the earthing system is such that the voltage to ground at the coil terminals (v_A and v_B) is half the voltage across the coil (v_{AB}), at the FDU intervention and in normal conditions, thanks to this wise earthing circuit topologies.

However, the analysis of a specific fault conditions led to discard C and D topologies: in case of untimely intervention of one FDU only, the voltage which would appear across the CB of that FDU would be the sum of the voltages across

all the TF coils, causing the destruction of the CB. Thus, it is considered the ITER-like connection (Fig. A) as reference case [42].

Therefore, the TF coils are all connected in series and fed by one thyristor converter (TC). The ITER-like topology for the DEMO TF circuit has been studied both for 16 FDUs configuration and 8 FDUs configuration. The ITER-like design of DEMO is composed by 16 FDUs one for each TFC.

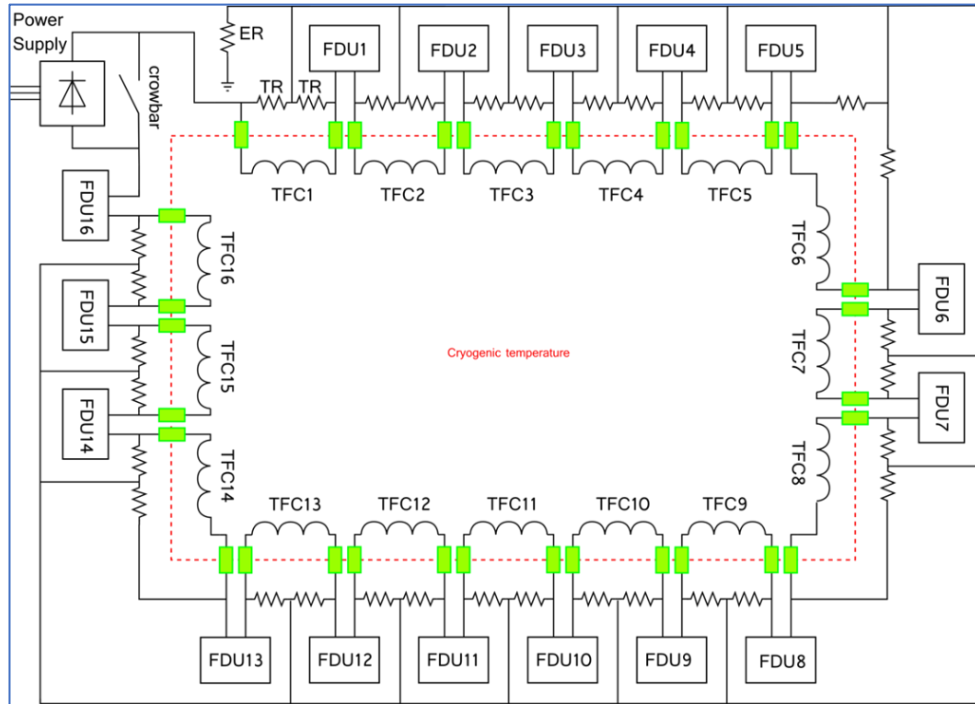


Figure 185: ITER-like circuit configuration with 16 FDUs [42]

From input data of the table at the beginning of the chapter, some characteristics parameters of the FDUs can be achieved, in particular: the Discharge Resistor value (DR), the peak voltage in operation for one FDU (V_d) and the specific energy through i^2t .

$$\left\{ \begin{array}{l} DR = \frac{L_T}{16\tau} = 0.040 \Omega \\ V_d = I_{op} \cdot DR = 4.23 \text{ kV} \\ \int i^2t \approx I_{op}^2 \cdot t_d + I_{op}^2 \cdot \frac{\tau}{2} = 205.07 \text{ GA}^2\text{s} \end{array} \right.$$

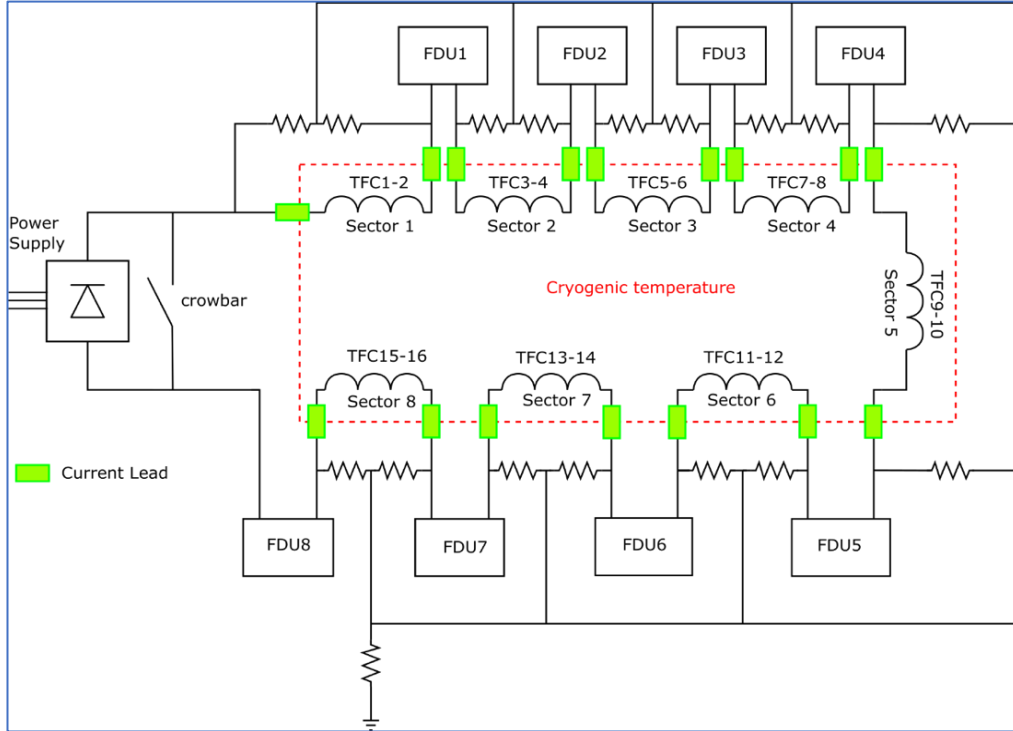


Figure 186: ITER-like circuit configuration with 8 FDUs [42]

Instead considering 8 FDUs it can be achieved:

$$DR = \frac{L_T}{8\tau} = 0.081 \Omega$$

$$V_d = I_{op} \cdot DR = 8.46 \text{ kV}$$

$$\int i^2 t \approx I_{op}^2 \cdot t_d + I_{op}^2 \cdot \frac{\tau}{2} = 205.07 \text{ GA}^2\text{s}$$

The choice of 8 sectors instead of 16 implies halving the number of feeders and FDUs, a reduction of power losses and recirculating power and a great simplification of the layout, considering for example the reduction of the number of penetrations through the tokamak building.

The result is also a reduction of the investment cost for the plant for such components. On the other hand, 8 sectors imply a doubling of the voltage applied to the coil terminals referred to ground.

It has been demonstrated in that the use of the temperature-dependent resistors can help in reducing the voltage applied to coil terminals with respect to constant resistors. However, the analyses with the updated values of nominal current (105 kA), I^2t (205.07 GA²s) and coil inductance (L = 1.41 H) show that with 8 sectors and temperature-dependent resistors the voltage to ground limit could be exceeded. So far in the analysis the energy dissipated in the surrounding passive structures

was neglected (since not yet known), thus overestimating the energy going into the discharge resistors and the consequent peak voltage at the coil fast discharge.

Table 15: Comparison between 16 FDUs and 8 FDUs configuration with constant resistances [42]

16 FDUs		
Parameter	Value	Symbol
Dump Resistor	0.040 [Ω]	DR
Max. Voltage during the discharge	4.23 [kV]	V_d
Specific energy	205.07 [GA^2s]	$\int i^2 t$
8 FDUs		
Parameter	Value	Symbol
Dump Resistor	0.081 [Ω]	DR
Max. Voltage	8.46 [kV]	V_d
Specific energy	205.07 [GA^2s]	$\int i^2 t$

6.5.1 TF FDU Dump Resistors study

The design studies reported in this section are referred to the DR associated to two configuration of TF circuits with 16 or 8 sectors, the scheme impacting only on the connections between DR and the rest of the circuit. The main design data for the design of the DR are shown in Table 16, comparing the DEMO requirements for 16 and 8 FDUs. As for the DEMO discharge resistor, the minimum constant resistance value required to satisfy the maximum I^2t limit is reported in the table.

In ITER a modular approach has been adopted in the design of FDU resistors. They are based on a unified resistor section, consisting of a resistive element with two current leads welded to its ends, enclosed in a metallic box. The resistive element is made of a mild-steel tape (1 mm width) in a tight zig-zag pattern. The dimension of the resistor section in ITER (L×W×H) are: 0.75 m x 0.75 m x 0.58 m. The number of sheets composing the zig-zag tape is 150, by dividing the length L by the distance between the sheets (5 mm).

Table 16: Discharge Resistor parameters for one TF coil [42].

Data for one TF sector	DEMO 16 FDU	DEMO 8 FDU
Rated energy	7.75 GJ	15.5 GJ
Nominal current peak	105 kA	105 kA
Resistance at 20°C	0.040 Ω (constant)	0.081 Ω (constant)
Peak terminal to terminal voltage on the TF coil	4.23 kV	8.26 kV

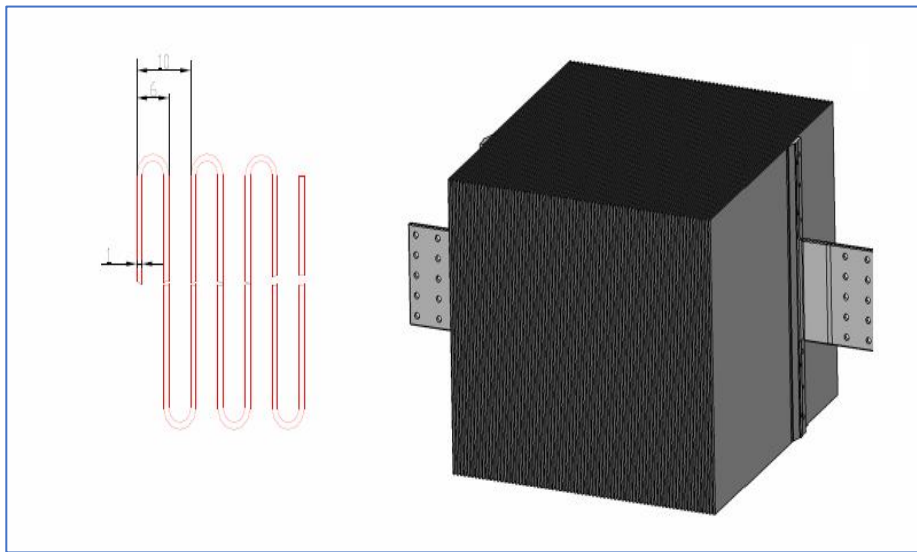


Figure 187: Unified resistor section of ITER FDU resistors [42]

The resistor is made out of mild steel, a material with a resistive temperature coefficient higher than that of stainless steel, to exploit the increment of the resistance during the coil discharge. Therefore, for the same I^2t , the value of the resistance at 20°C can be reduced with respect to the constant-resistance case, and consequently the voltage peak applied to the coil at the beginning of the FDU intervention is lower. The thermal coefficient for the mild steel used in ITER is $\beta \approx 4.6 \cdot 10^{-3} \text{ K}^{-1}$.

The same modular approach has been adopted for a first tentative design of the DEMO DRs. The ITER solution has been adapted to DEMO requirements and a first estimation of the initial value of resistance of a temperature dependent resistor has been outlined. It is assumed to adopt the same ITER unified resistor section,

arranged with proper parallel/series connections to achieve the required resistance value. The nominal current peak for the resistor section of 17 kA implies that in DEMO at least 7 sections shall be placed in parallel to satisfy the nominal current peak of 105 kA.

Table 17: Parameters of the module

	Value	Unit
Rated energy	220	MJ
Nominal current peak	17	kA
Resistance at 20°C	0.025	Ω
Mass of conductor (m)	517	kg
Total mass	1000	kg
Dimensions (L×W×H)	0.75 x 0.75 x 0.58	m
Max temperature	300	°C

In order to find an optimal solution, a first model with fixed resistance was created and after that the number of series and parallel connections were reached according to an optimization model.

The maximum temperature of the resistor is 300°C with a maximum initial temperature of 40°C. The circuit model used to simulate a discharge with temperature-dependent resistor is shown in Figure 188.

The temperature dependent resistor is simulated as a voltage generator controlled through the Ohm's law with feedback on the instantaneous values of current and resistance, the latter being dependent on the temperature of the material (β is thermal coefficient). The temperature variation is function of the dissipated power, the thermal capacitance, and the thermal resistance of the overall discharge resistor, and it is summed to the initial resistor temperature (40°C in the worst case).

The thermal capacitance is determined by mass of the material and its heat capacity as follows:

$$C_{th} = N \cdot m \cdot c = N \cdot 517 \text{ kg} \cdot 620 \text{ J}/(\text{kg} \cdot \text{K}) = N \cdot 320540 \text{ J}/\text{K}$$

where N is the number of unified resistor sections and $c = 620 \text{ J}/(\text{kg} \cdot \text{K})$ is the specific heat capacity of mild steel, as found in literature.

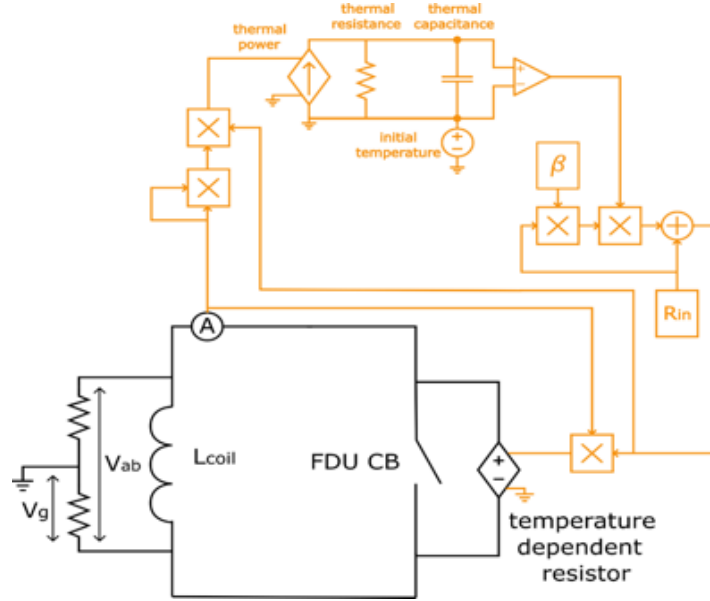


Figure 188: Model of the FDU with temperature-dependent discharge resistor [42]

The thermal resistance takes into account the effect of the convection of the air cooling and it is determined by the surface of the resistor sheets:

$$R_{th} = \frac{1}{\alpha A \cdot N} = \left[\frac{1}{\left(\frac{W}{m^2 K} \right) * m^2} \right] = \frac{1}{\alpha \cdot W \cdot H \cdot \left(\frac{L}{0.005} \right) \cdot 2 \cdot N}$$

$$= \frac{1}{20 \cdot 0.75 \cdot 0.58 \cdot 150 \cdot 2 \cdot N} = \frac{3.83 \cdot 10^{-4}}{N} K/W$$

where $\alpha = 20 \text{ W/m}^2\text{K}$ is the heat transfer coefficient for a laminar sheet with air natural convection, and A is the total area cooled by air convection, which is the area of the sheets composing the zigzag pattern of the resistor section, in both the sides.

In the present design, the ITER FDU are cooled only by natural convection; the same approach is considered also in this analysis, as worst case.

The thermal time constant of one resistor section, equal to the thermal time constant of more resistor sections, is:

$$\tau_{th} = R_{th} C_{th} = 123 \text{ s}$$

The thermal time constant is higher than the discharge time constant of the coils (35 s) by one order of magnitude. Then the heat dissipation in the resistors by air convection is not negligible and the thermal transient cannot be assumed adiabatic.

6.5.2 Dump Resistor optimization model

In order to find the proper value for n_s and n_p which are the single resistor module in Figure 187 described in the previous section in series and in parallel respectively, a Matlab-Simulink model was created and then implemented with an optimization tool.

In the next table are reported the resistor module and magnet parameters:

Table 18: Resistor module and magnet parameters for design optimization [42]

Parameter	Description	Value	Unit
R_m	Module resistance	0.025	Ω (At 20°C)
I_m	Rated current of the module	17	kA
T_{\max}	Maximum temperature of the module	300	°C
E_m	Maximum energy of the module	220	MJ
E_{FDU}	Maximum energy of the FDU	7750	MJ
$I^2 t$ (max)	Maximum specific energy through the module	205	GA^2s
L_T	Total equivalent inductance of TFCs	22.56	H
L	Equivalent inductance of one TFC	1.41	H
t_d	Tau delay	1.1	s
β	Thermal coefficient	$4.6e - 3$	K^{-1}
Δt	Variation of initial temperature of DR (reported to 40°C)	20	°C
I_{op}	Rated current of TFC	105	kA

In the following table are reported the limits related to the specified quantities:

Table 19: Parameters limits for design optimization [42]

Parameter	Description	Value	Unit
$n_p \cdot I_m \geq I_{op}$	Current limit for each module	-	-
$n_s \cdot n_p \geq \frac{E_{FDU}}{E_m}$	Energy limit for each module	35	-
T_{\max}	Maximum temperature for each module	300	°C
T_{\min}	Minimum temperature for each module (for optimization purposes)	280	°C
$I^2 t_{\max}$	Maximum specific energy through	205	GA^2s

In the next figures are reported some screenshots of the model:

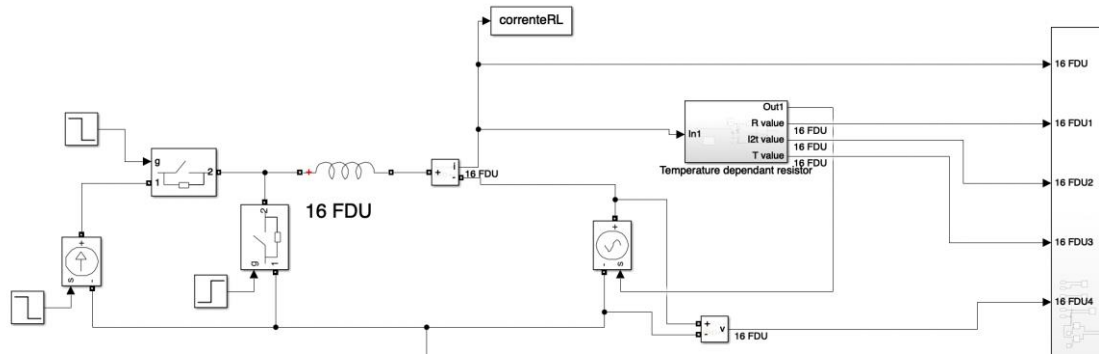


Figure 190: Model with single inductance and single FDU (equivalent to 16FDUs)

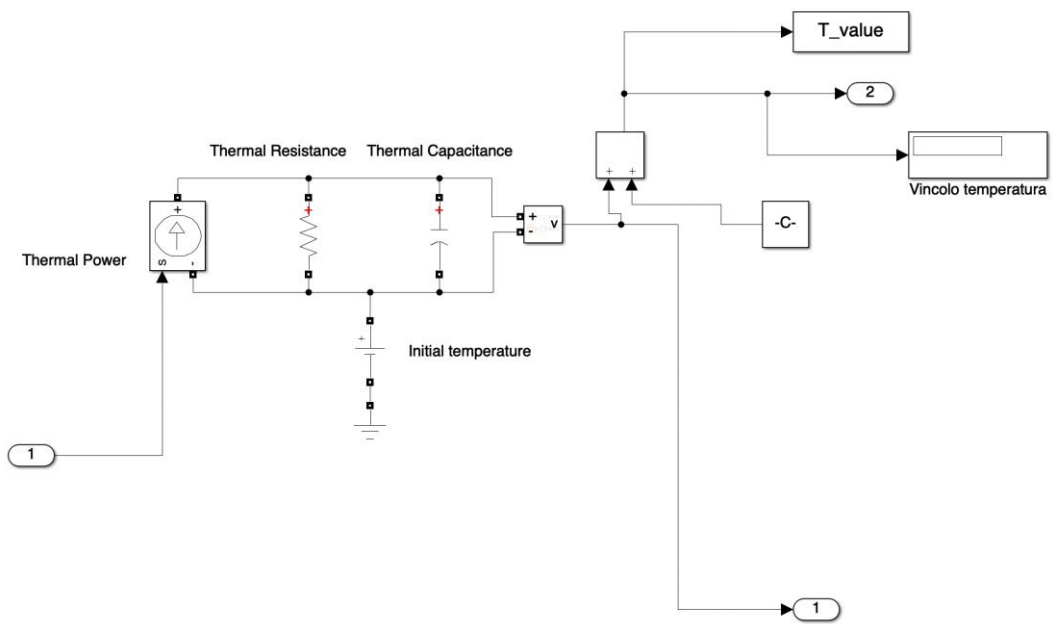


Figure 189: Temperature-dependant resistor and temperature limit

▼ Data	
Name ▲	Value
Corrente_modulo	1x1 Signal
Energia_modulo	1x1 Signal
I2t	1x1 Signal
ReqValues	5x1 struct
T	1x1 Signal
T_max	1x1 SignalBound
T_min	1x1 SignalBound
Vincolo_I2t	1x1 SignalBound
Vincolo_corrent...	1x1 SignalBound
Vincolo_energia...	1x1 SignalBound
np_ns	2x1 Continuous

Figure 191: Imported signals on Simulink Design Optimization tool

After the optimization, the proposed results according to the Matlab Simulink Design Optimization tool are $n_p = 7$ and $n_s = 10.2$ which means $n_p = 7$ and $n_s = 11$.

In the next figures the results of the optimization are reported.

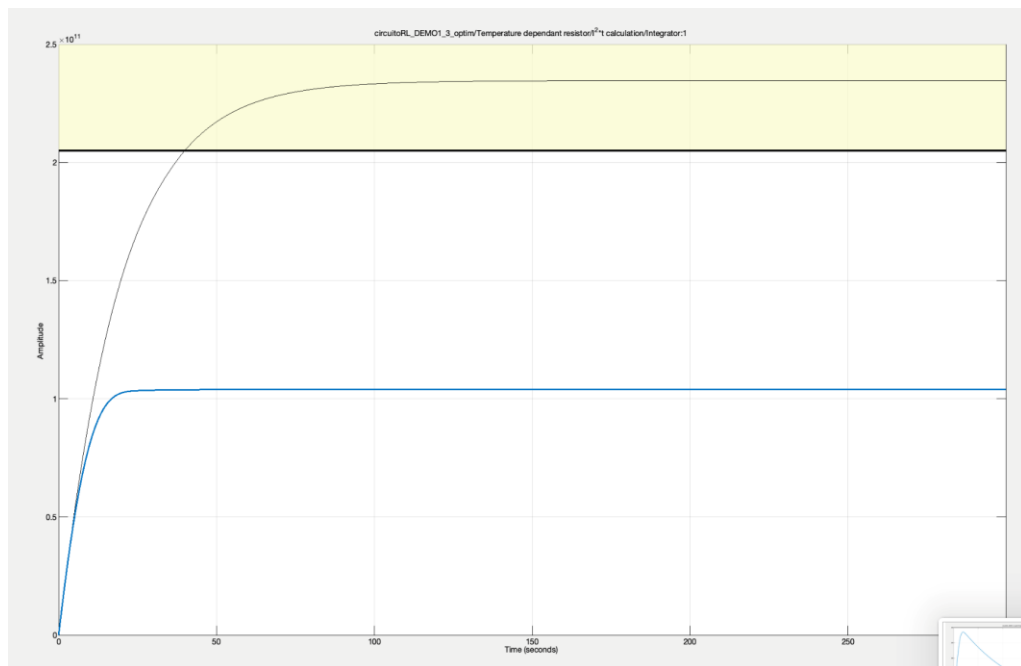


Figure 192: Specific energy through limit (blue line after optimization)

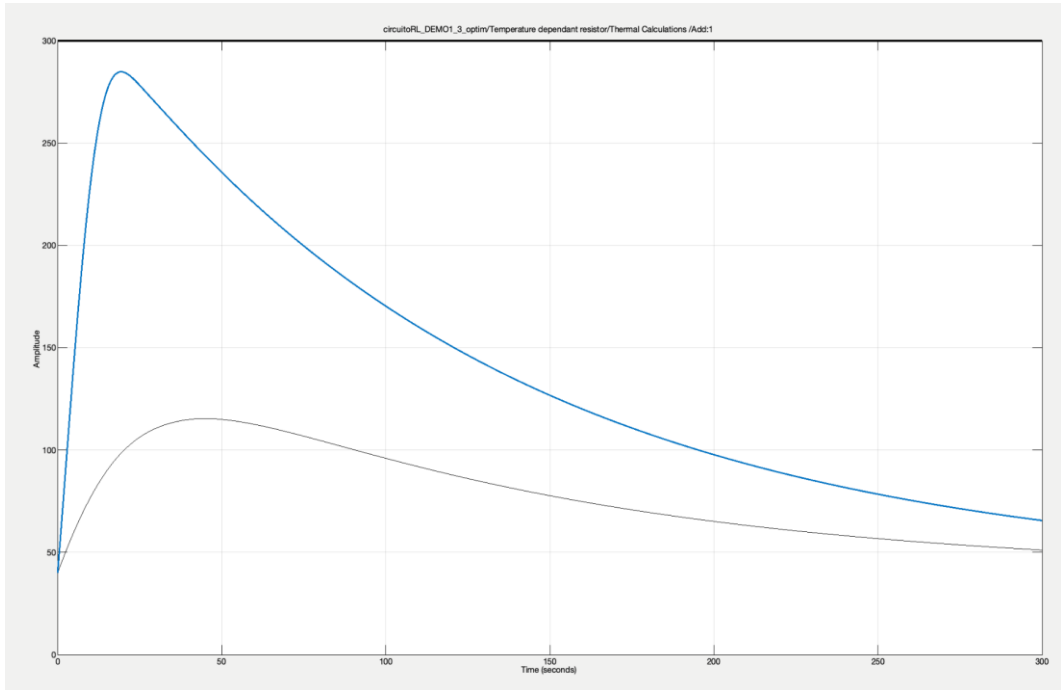


Figure 194: Maximum temperature limit (blue line after optimization)

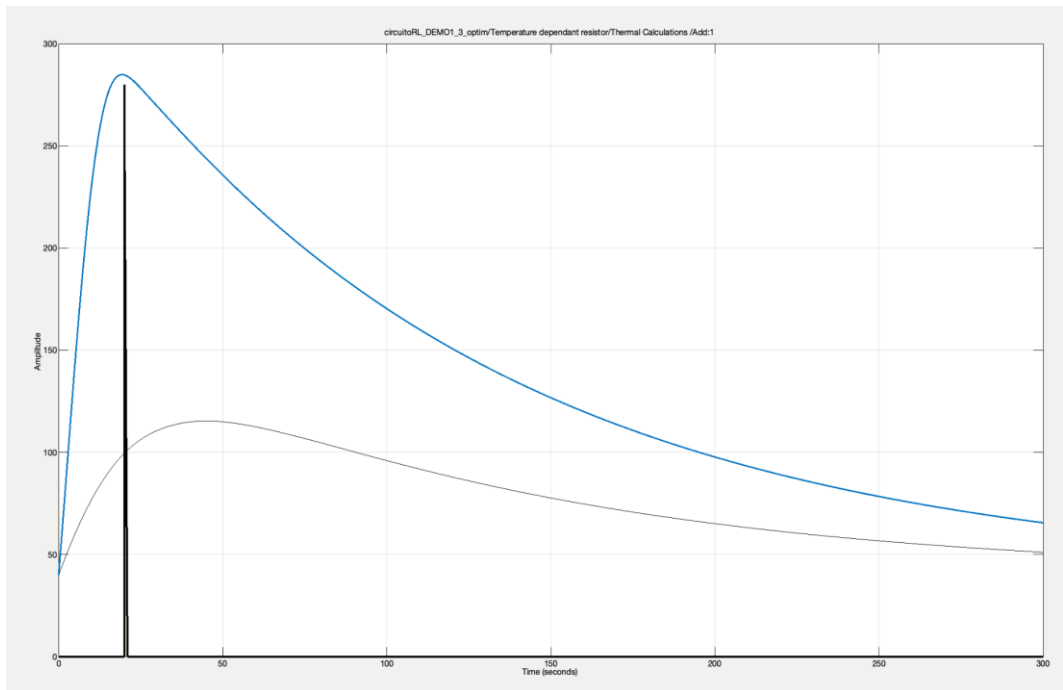


Figure 193: Minimum temperature limit (blue line after optimization)

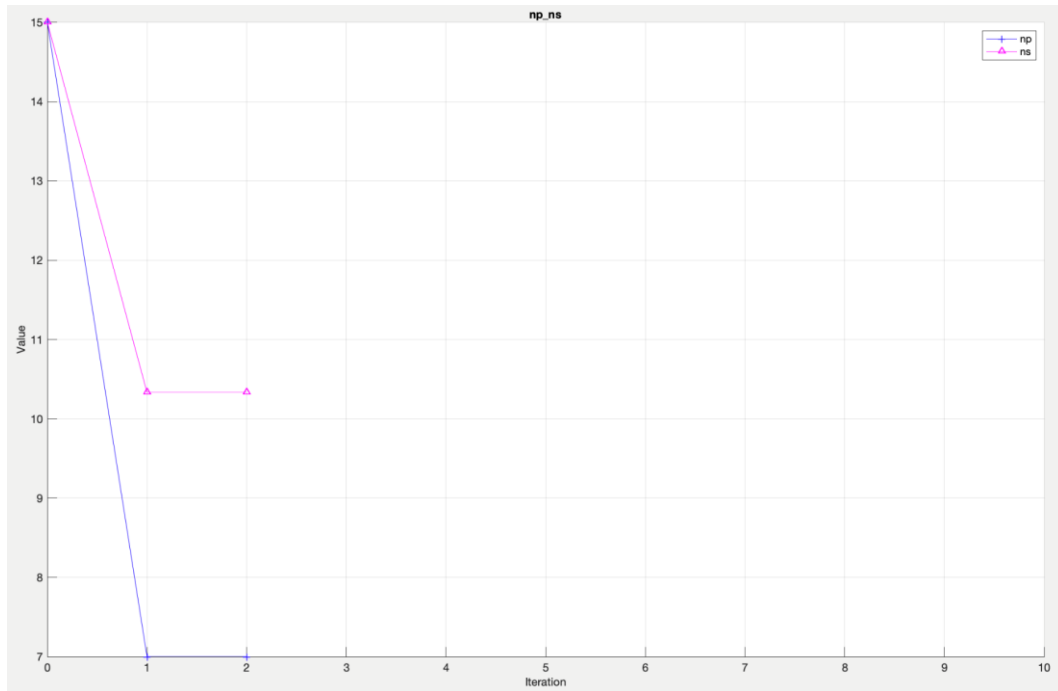


Figure 195: Optimization results

6.5.3 Final Matlab-Simulink model

The model was then upgraded introducing the self and mutual inductance matrix and keeping the results of the previous section as default parameters for the FDU, so:

$$\begin{cases} n_p = 7 \text{ and } n_s = 11 \text{ for 16 FDU configuration} \\ n_p = 7 \text{ and } n_s = 22 \text{ for 8 FDU configuration} \end{cases}$$

The following figure represents the whole model with 16 and 8 FDUs configuration with the related results.

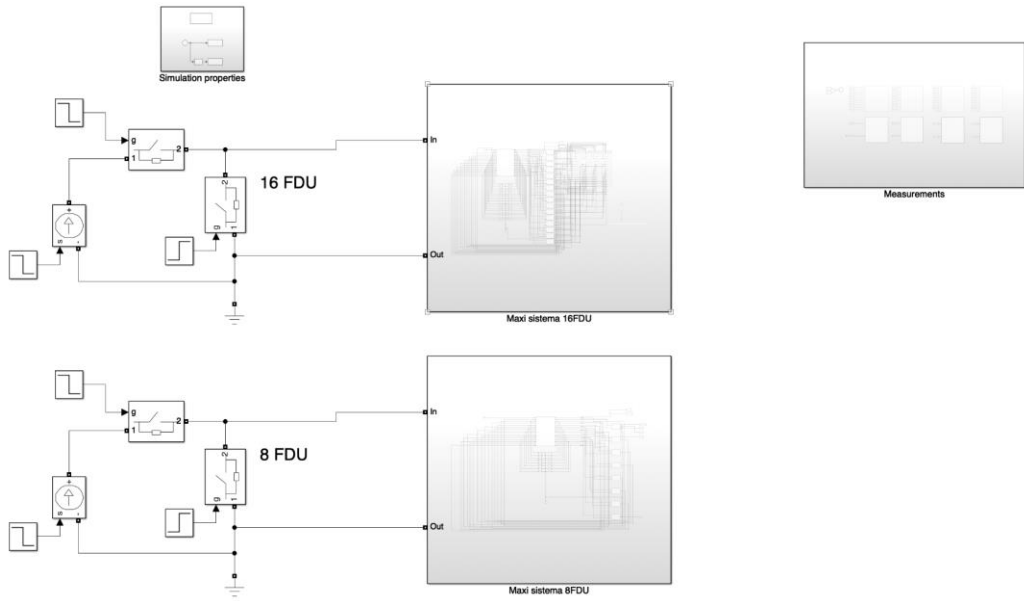


Figure 197: General model

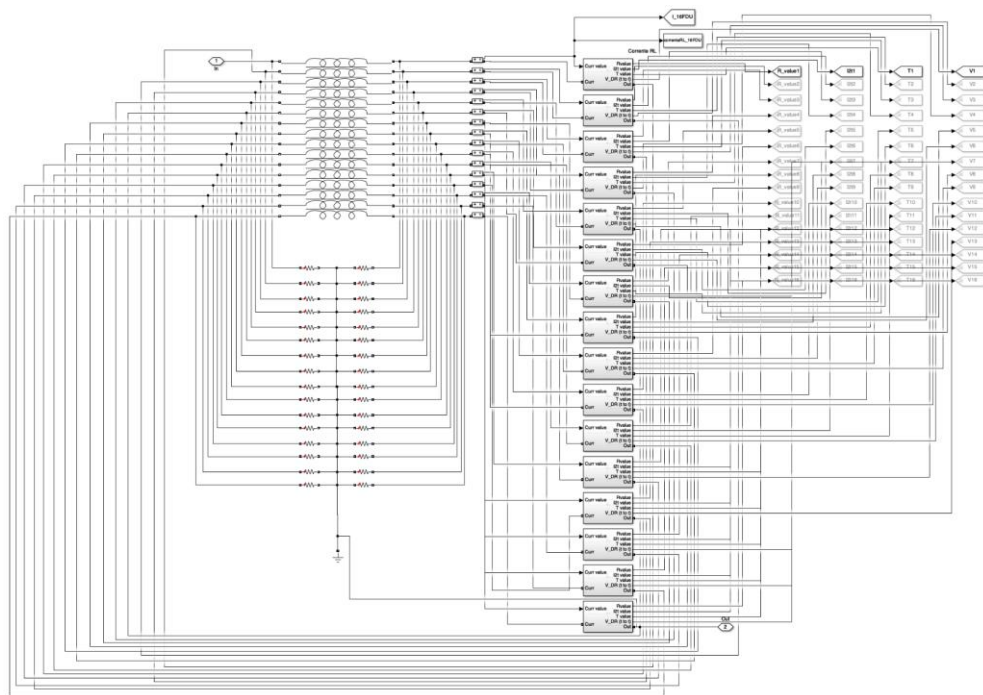


Figure 196: Detail of 16 FDU simulation block

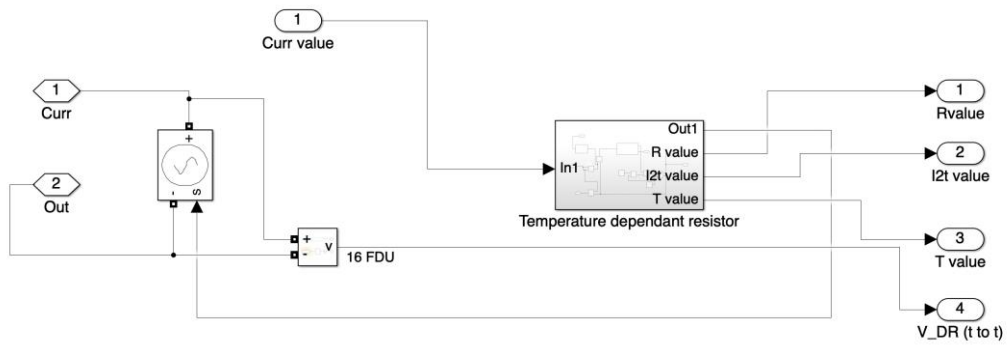


Figure 198: Detail of Temperature dependant resistor

6.5.4 Final Matlab-Simulink model results

In the following figures are reported all the trend parameters according to the model described in the previous section and as a result of the optimization tool on Simulink.

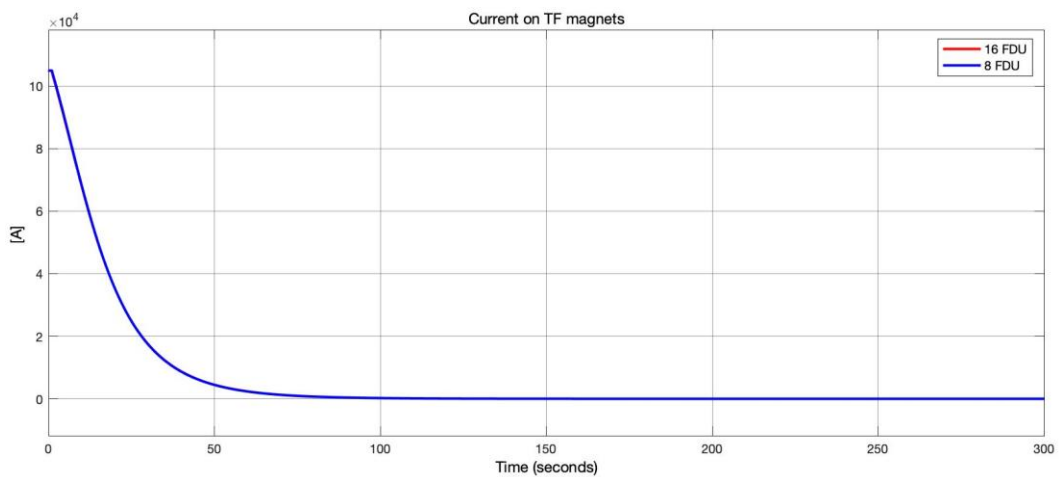


Figure 199: Current on TF magnets of DTT 16 and 8 FDU's (overlapped)

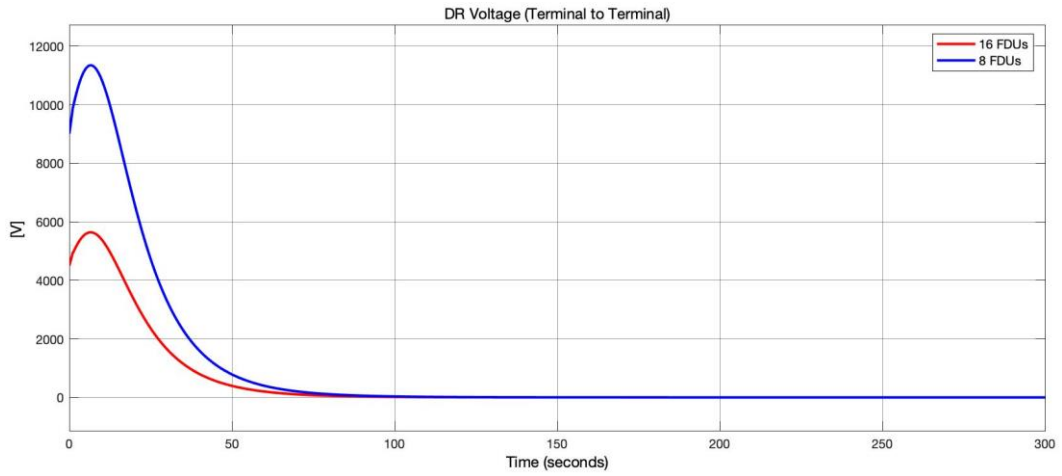


Figure 202: DR voltage Terminal to Terminal 16 and 8 FDUs

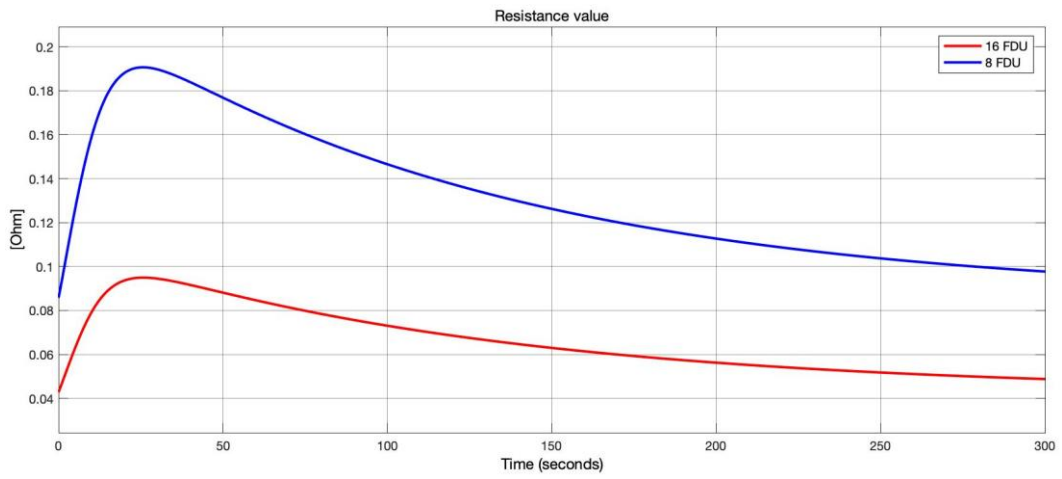


Figure 201: Resistance value during the discharge 16 and 8 FDUs

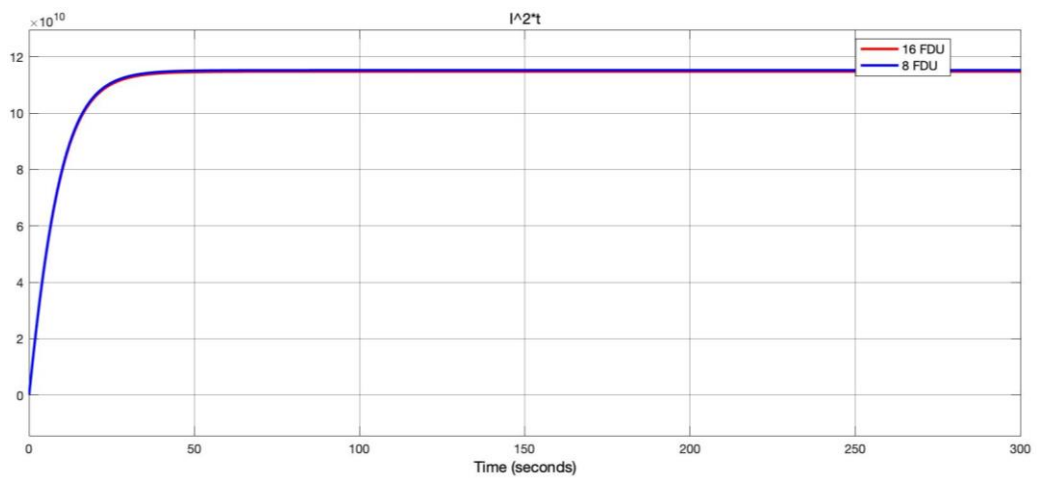


Figure 200: Specific energy through for 16 and 8 FDUs expressed in $[A^2t]$

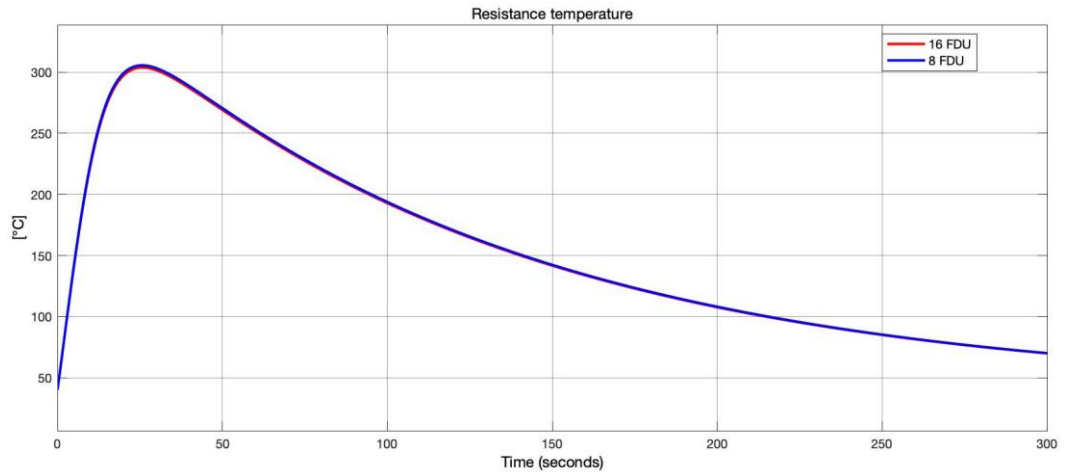


Figure 203: Temperature of the resistors during the discharge

As it can be seen from Figure 203, one of the major limits of the simulation (the maximum temperature) is respected with the parameters explained before.

6.5.5 Discharge of TFC with Varistor study

It was also conducted a small study related to the discharge of one TFC with varistor technology.

In particular the parameters used are the following:

Table 20: Varistor parameters

Parameter	Description	Value	Unit
L_{TF}	Equivalent inductance of one TFC	1.41	H
I_{nom}	Nominal current	105	kA
t_{delay}	Delay time after triggering command of the varistor	1.1	s
t_{BPS}	BPS opening time	0.1	s
β	Varistor coefficient	0.39	-
α	$\frac{1}{\beta}$	-	-
K	Varistor coefficient	49.5	-

Varistors are different than resistors, in particular varistors have a voltage dependent resistance with bidirectional path of the current with a power law relationship which is [43]:

$$I = K \cdot V^\alpha$$

Where all the parameters are described in the previous table.

Typically, varistors are either made from SiC or ZnO, in particular the last typology finds applications in high-energy applications and are commonly used as energy extraction method for inductive loads.

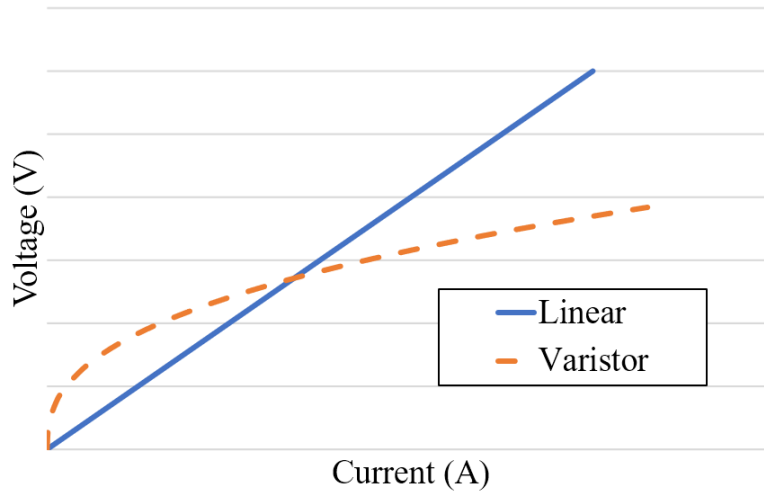


Figure 204: Example of VI responses for linear resistors and varistors [43]

The general model with one TFC of DEMO and a varistor is implemented as the following figure:

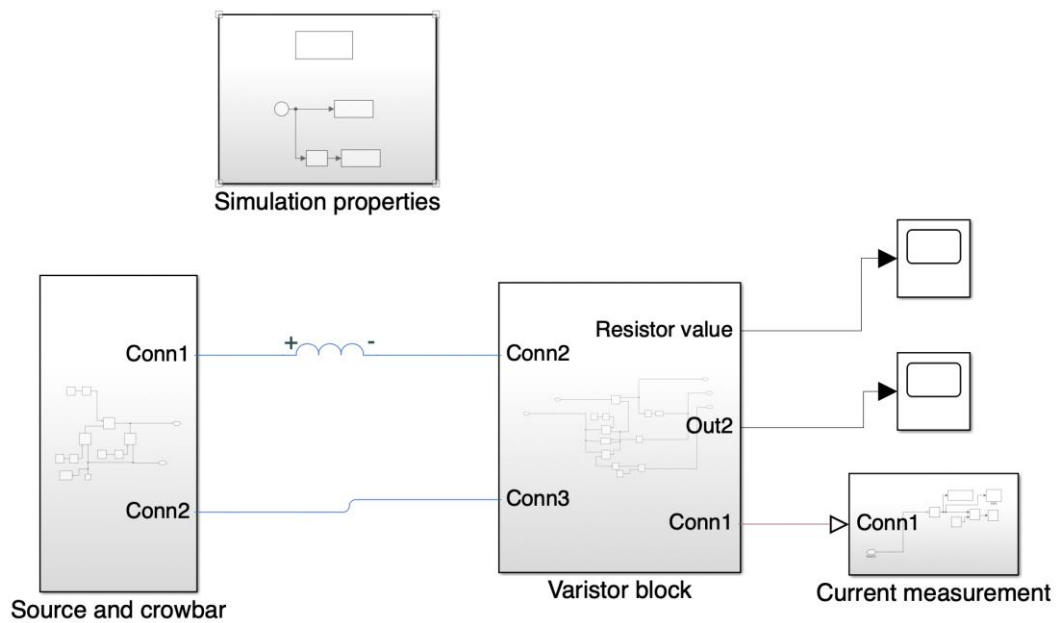


Figure 205: Varistor block simulation model on Matlab-Simulink

The varistor block is simulated according to the previous parameters and following the behavior accordingly to the power law.

In the following figure is reported a detailed screenshot of the model:

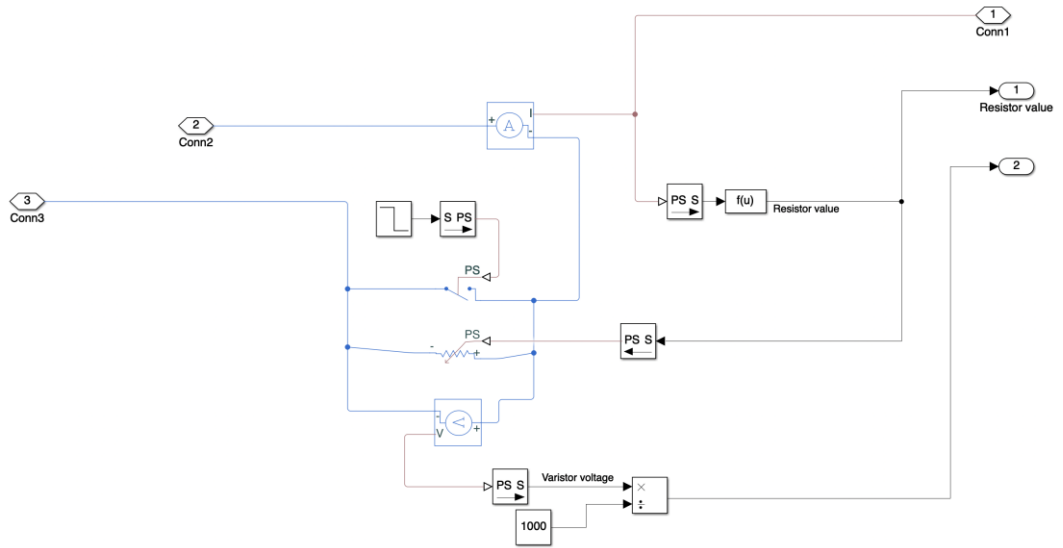


Figure 206: Detailed model for Varistor simulation of DEMO

As regarding the results, the following figures represent the main parameters like voltage terminal to terminal to the varistor, resistance value during the discharge of the varistor, specific energy through and current on the TFC:

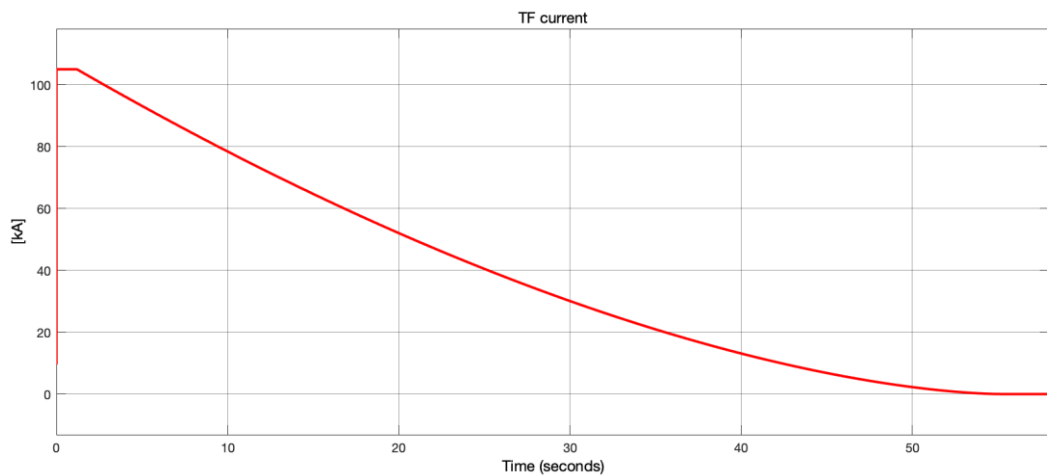


Figure 207: TFC current on DEMO during discharge with varistor

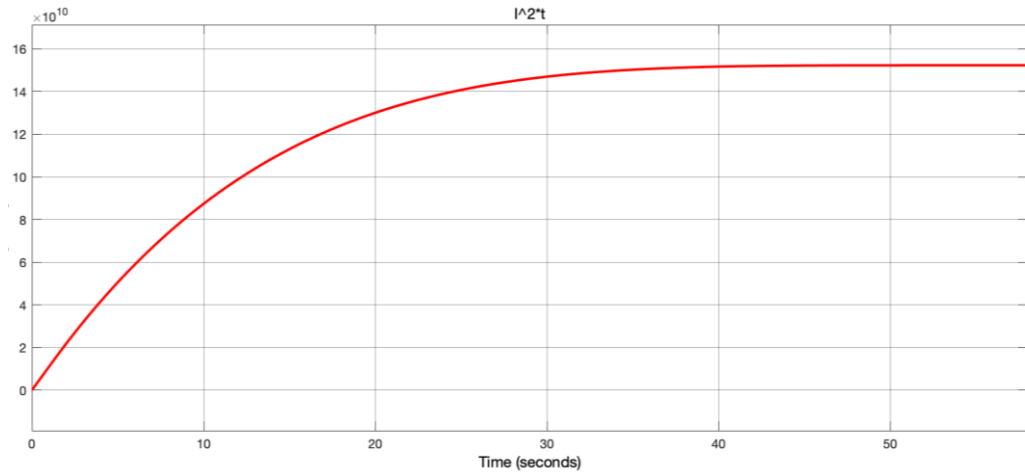


Figure 208: Specific energy through during discharge on one TFC of DEMO with varistor expressed in $[A^2 s]$

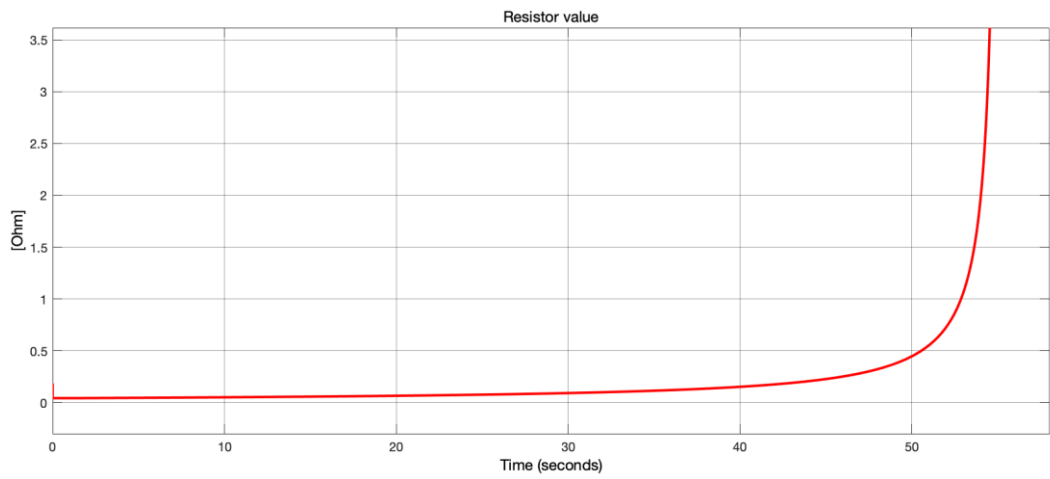


Figure 210: Resistance value of the varistor during TFC discharge of DEMO

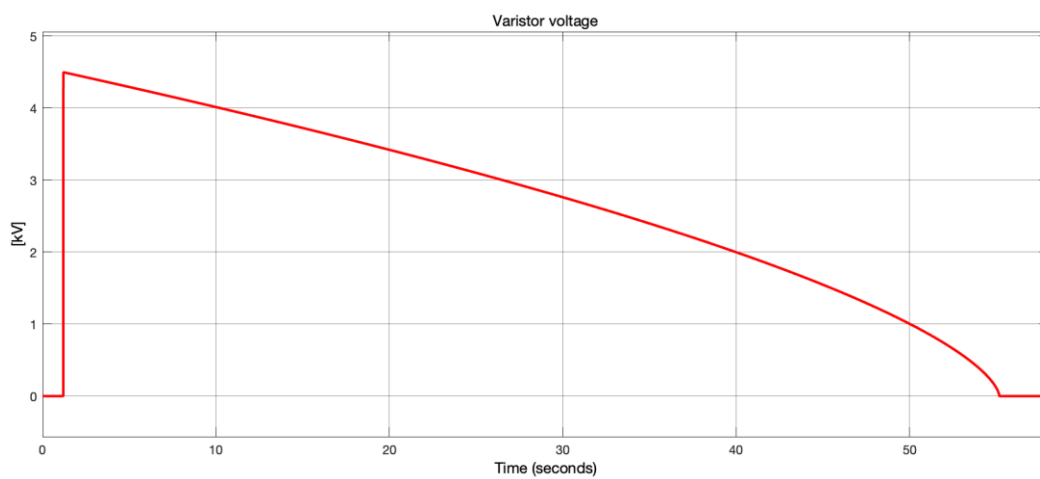


Figure 209: Voltage across varistor terminals during discharge of one TFC of DEMO

7 Conclusions

The study conducted throughout the PhD was carried out in order to have an accurate model on Matlab-Simulink that could be used for the study of DTT Fast Discharge Units.

The model has been developed in order to be as elastic and adaptable as possible and, therefore, can be used for future studies together with other components also of Multiphysics in order to evaluate different aspects of DTT plasma scenario operation.

For this purpose, a survey of the scientific literature was conducted in order to better understand what was present at the beginning of the PhD course and it can be said with certainty that the work carried out is innovative in the scientific sector of reference, namely the Fast Discharge Units for nuclear fusion reactors.

The modeling work was subsequently refined at ITER Organization which contributed to the development of a model similar in substance but different from the point of view of the parameters used and the studies conducted (i.e., a fault analysis according to different configurations).

The result obtained from this three-year research is consistent with the initial expectation and will allow, through appropriate adaptations of the model, to deepen different aspects of this technology by canceling or limiting many of the risk factors related to partial or total damage to the superconducting magnets of a nuclear fusion reactor.

A recommendation for further future research could be to further expand the level of detail of the model by implementing it with precise data relating to what will then be the construction characteristics of the machine in such a way as to have a more precise answer of the moment (currently the parameters of the model are based on assumptions that, however precise, they may not reflect maximum accuracy that adheres to reality).

The technology proposed for DTT's FDUs also demonstrates how, in addition to the passive discharge standard model, an active discharge model with better electrical and thermal performance can be implemented and the choice of one particular model in to be defined according to economic and physical characteristics of the Tokamak under study.

Bibliografia

- [1] C. R. Lopes, G. Ala, G. Zizzo, P. Zito e A. Lampasi, «Transient DC-Arc Voltage Model in the Hybrid Switch of the DTT Fast Discharge Unit,» *EEEIC Conference*, 2021.
- [2] C. R. Lopes, C. Terlizzi, R. Romano, G. Ala, G. Zizzo, P. Zito, S. Bifaretti, V. Bonaiuto e A. Lampasi, «Conceptual Design of the Grounding System of the DTT Experimental Facility,» *Melecon conference*, 2022.
- [3] C. R. Lopes, P. Zito, C. Fiamozzi Zignani, G. Messina, L. Morici, G. Tomassetti, A. Lampasi, G. Ala e G. Zizzo, «Design Optimization for the Quench Protection of DTT's Superconducting Toroidal Field Magnets,» *Symposium of Fusion Technology SOFT 2020*, 2020.
- [4] C. R. Lopes, P. Zito, A. Lampasi, G. Ala, G. Zizzo e E. Riva Sanseverino, «Conceptual Design and Modeling of Fast Discharge Unit for Quench Protection of Superconducting Toroidal Field Magnets of DTT,» *Melecon 2020*, 2020.
- [5] G. Messina, C. R. Lopes, P. Zito, A. Di Zenobio, C. Fiamozzi Zignani, A. Lampasi, L. Morici, G. Ramogida, G. Tomassetti, G. Ala e G. Zizzo, «Transient Electrical Behaviour of the TF Superconducting Coils of Divertor Tokamak Test Facility During a Fast Discharge,» *IEEE Transactions on Applied Superconductivity*, 2022.
- [6] A. Lampasi, C. R. Lopes, M. Manganelli, S. Pipolo e P. Zito, «Power Supply Systems for the DTT Superconducting Magnets,» *Melecon 2022*, 2022.
- [7] C. R. Lopes e P. e. a. Zito, «Conceptual Design and Modeling of Fast Discharge Unit for Quench Protection of Superconducting Toroidal Field Magnets of DTT,» *2020 IEEE 20th Mediterranean Electrotechnical Conference (MELECON)*, pp. 623-628, 2020.

- [8] P. Zito, G. Tomassetti, G. Messina, L. Morici, C. Fiamozzi Zignani, A. Lampasi, G. Ala, G. Zizzo e C. R. Lopes, «Conceptual Design and Modeling of the Toroidal Field Coils Circuit of DTT,» *Melecon 2020*, June 2020.
- [9] «ITER,» [Online]. Available: <https://www.iter.org/proj/inafewlines>.
- [10] T. Donné, W. Morris, X. Litaudon, C. Hidalgo e et al., *European Research Roadmap to the Realisation of Fusion Energy*, Munich, Germany, 2018.
- [11] [Online]. Available: <http://www.tokamak.info>.
- [12] A. A. Harms, K. F. Schoepf, G. H. Miley e D. R. Kingdon, *Principles of Fusion Energy*, World Scientific, 2002.
- [13] [Online]. Available: <https://www.science.org/content/article/fusion-power-may-run-fuel-even-gets-started>.
- [14] S. Blundell, *Superconductivity: a very short introduction*, New York: Oxford University Press Inc., 2009.
- [15] M. Maciejewski, *Automated, object-oriented simulation framework for modelling of superconducting magnets at CERN*, Ginevra, 2014.
- [16] H. M. B. Serieiro, «Use of Superconductors in the Magnetic Circuit of Electric Generators Adapted to Renewable Energy Sources».
- [17] «MIT technology review,» 10 December 2018. [Online]. Available: [https://www.technologyreview.com/s/612559/the-record-for-high-temperature-superconductivity-has-been-smashed-again/..](https://www.technologyreview.com/s/612559/the-record-for-high-temperature-superconductivity-has-been-smashed-again/)
- [18] R. Timmer, «Numerical Modeling of Superconducting YBCO Tapes,» 2015, Twente University, Enschede (Netherlands).
- [19] J. V. Nugteren, «Normal Zone Propagation in a YBCO Superconducting Tape,» University of Twente, 2012..
- [20] M. d. o. Physics, «Superconductivity: The Meissner Effect, Persistent Currents and the Josephson Effects,» 7 February 2018.

- [21] Y. Wakatsuki, «CNN,» 19 October 2016. [Online]. Available: <https://edition.cnn.com/2015/04/21/asia/japan-maglev-train-world-record/index.html>.
- [22] «JT-60SA Glossary,» [Online]. Available: <https://www.jt60sa.org/wp/glossary/#glossary-n>.
- [23] J.-6. a. EU, JT-60SA Research Plan Research Objectives and Strategy Ver. 4.0, Naka, Japan, 2018.
- [24] «JT-60SA Home page,» [Online]. Available: <https://www.jt60sa.org/wp/>.
- [25] «EuroFusion,» [Online]. Available: <https://www.euro-fusion.org/devices/jet/jets-salient-features/>.
- [26] Jet Joint Undertaking, UK, 1997.
- [27] «FTU official page,» [Online]. Available: <http://www.fusione.enea.it/FTU/index.html.it>.
- [28] E. i. document, «DTT Plant Integration Document vers. 3.2,» Frascati (Italy), August 2nd 2022.
- [29] ENEA, Divertor Tokamak Test facility Interim Design Report, Frascati (Rome), 2019.
- [30] E. Superconducting Magnets department, «DTT TF Coil Description,» Frascati , 2020.
- [31] D. S.c.a.r.l., «DTT Vacuum Vessel and Ports: Design Description Document,» Frascati (Italy), 2021.
- [32] I. Organization, «ITER Research Plan within the Staged Approach,» 17 September 2018. [Online]. Available: https://www.iter.org/doc/www/content/com/Lists/ITER%20Technical%20Reports/Attachments/9/ITER-Research-Plan_final_ITR_FINAL-Cover_High-Res.pdf. [Consultato il giorno 22 September 2022].
- [33] I. Organization, «ITER Organization official website,» [Online]. Available: <https://www.iter.org/mach/magnets>.

- [34] I. Organization, «ITER Organization Machine,» [Online]. Available: <https://www.iter.org/mach>.
- [35] S. Chen, Q. Wang, Y. Dai, Y. Lei e K. Kim, «Development of Digital Quench Detection and Dumping Circuit with Constant Voltage System for SMES,» *IEEE Transactions and Applied Superconductivity*, vol. 20, n. 3, July 2010.
- [36] R. Ammerman, T. Gammon, P. Sen e J. Nelson, «DC-arc models and incident energy calculations,» *IEEE Transaction on industry applications*, vol. 46, n. 5, September/October 2010.
- [37] R. Ammerman, T. Gammon, P. Sen e J. Nelson, «DC-arc models and incident-energy calculations,» *IEEE Transaction on Industry applications*, vol. 46, n. 5, Settembre/Ottobre 2010.
- [38] G. Ala, P. Buccheri e M. Inzerillo, «A Model to Simulate EM Switching Transients in Electric Power Distribution Substations,» *15th International Conference on Electricity Distribution CIRED-99*, 1999.
- [39] E. Gaio, A. Maistrello, L. Novello, M. Matsukawa, K. Shimada, F. Burini, G. Taddia e S. Tenconi, «Final Tests of the Four Switching Network Units Procured by the European Union for JT-60SA,» *Fusion Engineering and Design*, vol. 124, pp. 163-168, 2017.
- [40] N. S. S. C. (KTA), «Design of Nuclear Power Plants Against Damaging Effects from Lightning,» Germany 2009,2011.
- [41] P. D. Edwing, R. A. Kisner, K. Korsah, M. R. Moore, J. B. Wilgen e R. T. Wood, «Regulatory Guidance on Lightning Protection in Nuclear Power Plants,» Washington DC, 2005.
- [42] P. Zito, C. R. Lopes, A. Lampasi, S. Pipolo e M. Manganelli, «Internal document, Deliverable PES-T.05.02-T001-D001,» 2022.
- [43] T. e. a. Galvin, «Experimental Examples of Quench Protection with Varistors to Reduce Quench Voltages and Hot-Spot Peak Temperatures,» *IEEE Transactions on Applied Superconductivity*, vol. 32, n. 6, pp. 1-5, Sept. 2022.

- [44] «Science direct,» [Online]. Available: <https://www.sciencedirect.com/topics/mathematics/inertial-confinement>.
- [45] K. Mitsuru, K. Lackner e M. Quang Tran, *Fusion Physics*, Vienna: IAEA, 2012.
- [46] «Wikipedia,» [Online]. Available: https://en.wikipedia.org/wiki/Nuclear_fusion.
- [47] S. Blundell, *Superconductivity: a very short introduction*, New York: Oxford University Press Inc., 2009.
- [48] E. T. f. t. arXiv, «MIT Technology Review,» 10 Dicembre 2018. [Online]. Available: <https://www.technologyreview.com/s/612559/the-record-for-high-temperature-superconductivity-has-been-smashed-again/>.
- [49] A. K. Sahoo, «Modeling and Simulation of Superconducting Magnetic Energy Storage Systems,» *International Journal of Power Electronics and Drive Systems*, 2015.
- [50] R. Timmer, «Numerical modeling of Superconducting YBCO tapes,» Twente University, Enschede (Paesi Bassi), 2015.
- [51] J. V. Nugteren, «Normal Zone Propagation in a YBCO Superconducting Tape,» University of Twente, 2012.
- [52] M. d. o. Physics, *Superconductivity: The Meissner Effect, Persistent Currents and the Josephson Effects*, 7 Febbraio 2018.
- [53] Y. Wakatsuki, «CNN,» 19 Ottobre 2016. [Online]. Available: <https://edition.cnn.com/2015/04/21/asia/japan-maglev-train-world-record/index.html>.
- [54] C. G. Theiler, *Basic Investigation of Turbulent Structures and Blobs of Relevance for Magnetic Fusion Plasmas*, Lausanne, 2011.
- [55] A. Jardin, «Analysis of Divertor Profiles for Testing Physics Assumptions,» 2014.
- [56] L. Wittenberg, «The cost of tritium production in a fusion reactor,» *Fusion Technology; ISSN 0748-1896*, vol. 21, pp. 886-8790, 1992.

- [57] [Online]. Available:
<https://www.fusion.qst.go.jp/rokkasyo/en/project/blanket.html>.
- [58] [Online]. Available:
<https://news.newenergytimes.net/2022/01/08/lithium-lithium-everywhere-and-none-to-use-for-fusion-reactors/>.
- [59] H. Schau e S. Glaser, «Approaches for calculating LV DC arc flash parameters,» *55th International Universities Power Engineering Conference (UPEC), IEEE Xplore 2020*, 2020.
- [60] G. Ala, P. Buccheri e M. Inzerillo, «A model to simulate EM switching transients in electric power distribution substations,» *15th International Conference on Electricity Distribution CIRED-99*, 1999.
- [61] E. Gaio, A. Maistrello, L. Novello, M. Matsukawa, K. Shimada, F. Burini, G. Taddia e S. Tenconi, «Final tests of the four switching network units procured by the European Union for JT-60SA,» *Fusion Engineering and Design*, vol. 124, pp. 163-168, 2017.
- [62] «International Standard, IEC62305: Protection against lightning,» 2010.
- [63] I. Organization, «ITER Research Plan within the Staged Approach,» 17 September 2018. [Online]. Available:
https://www.iter.org/doc/www/content/com/Lists/ITER%20Technical%20Reports/Attachments/9/ITER-Research-Plan_final_ITR_FINAL-Cover_High-Res.pdf.
- [64] A. F., «TF Coils Self and Mutual inductances,» 2022.
- [65] B. S., «SDDD for SN, FDU, DC Busbars and Instrumentation.,» 2019.
- [66] M. S., «TF FDU Current Commutation Unit FAT procedure 7LFSWX,» 2020.
- [67] ENEA, «Divertor tokamak test facility interim design report,» Raffaele Martone (CREATE), Raffaele Albanese (CREATE), Flavio Crisanti (ENEA), Piero Martin (RFX) and Aldo Pizzuto (ENEA), Frascati (Roma), 2019.

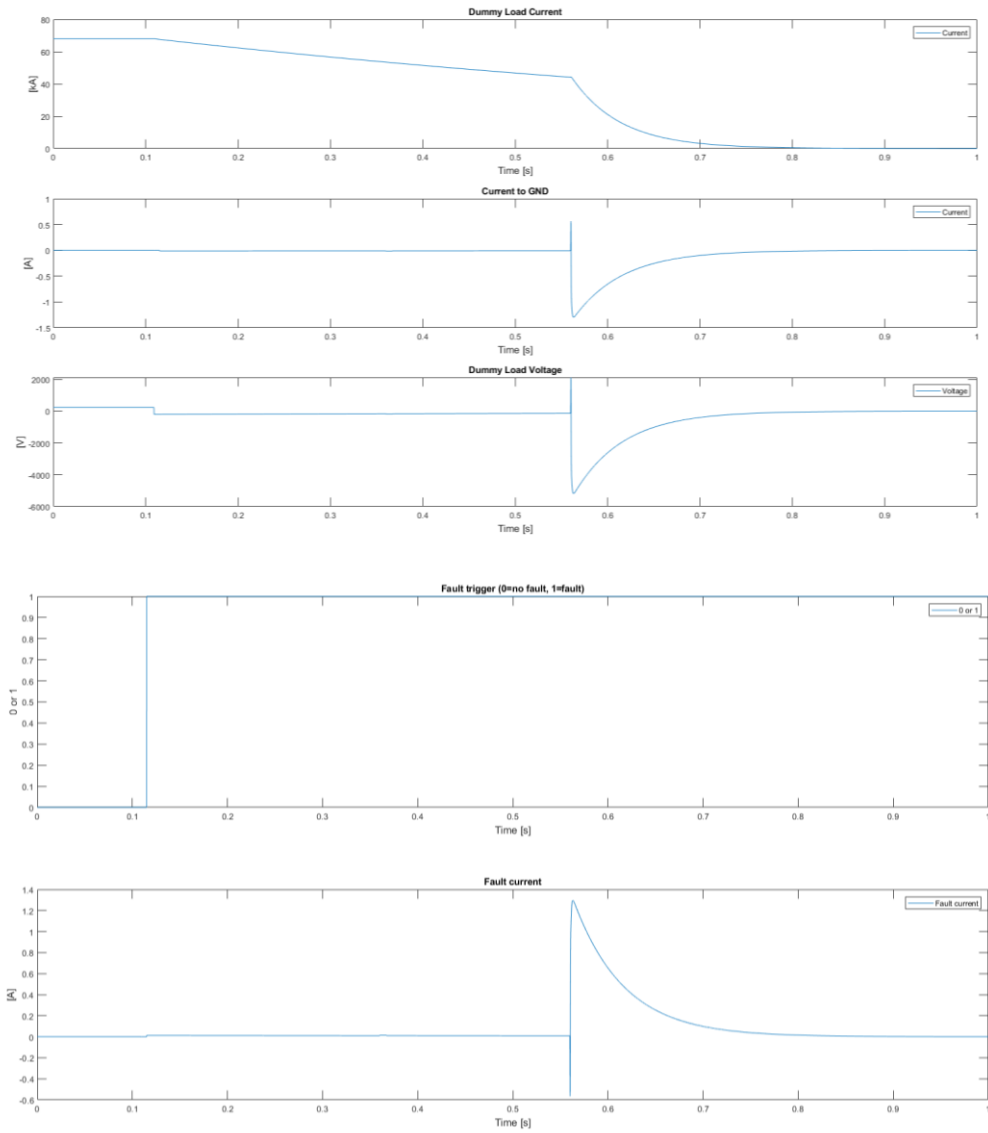
- [68] EFDA, «Fusion electricity: a roadmap to the realisation of fusion energy,» 2012.
- [69] «European Research Roadmap to the realisation of Fusion Energy,» [Online]. Available: https://www.euro-fusion.org/fileadmin/user_upload/EUROfusion/Documents/2018_Research_roadmap_long_version_01.pdf.
- [70] «ITER home page,» [Online]. Available: <https://www.iter.org>.
- [71] «DTT facility,» [Online]. Available: <https://www.dtt-project.enea.it>.
- [72] M. Maciejewski, «Automated, object-oriented simulation framework for modelling of superconducting magnets at CERN,» Ginevra, 2014.
- [73] S. Blundell, «Superconductivity: a very short introduction,» Oxford University Press Inc., New York, 2009.
- [74] «Superconductivity: the Meissner Effect, persistent currents and the Josephson effects,» 2018.
- [75] B. Fridman, «Capacitor bank for fast discharge unit of iter facility,» D. V Efremov Institute of Electrophysical Apparatus, St. Petersburg, Russia, 2011.

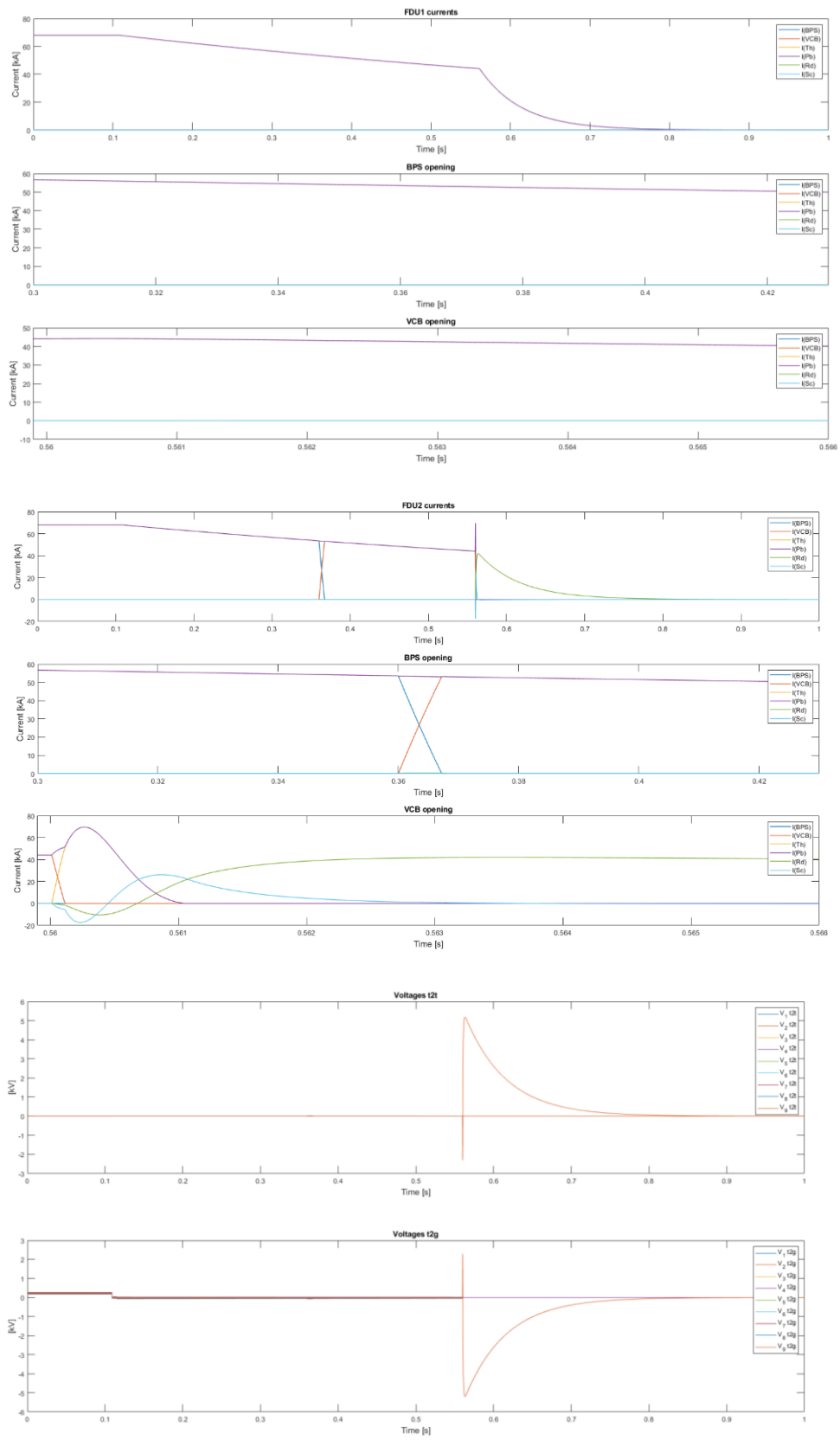
8 Appendix

In this appendix are reported all the results for each Scenario related to Section Fault analysis of FDUs in DL configuration.

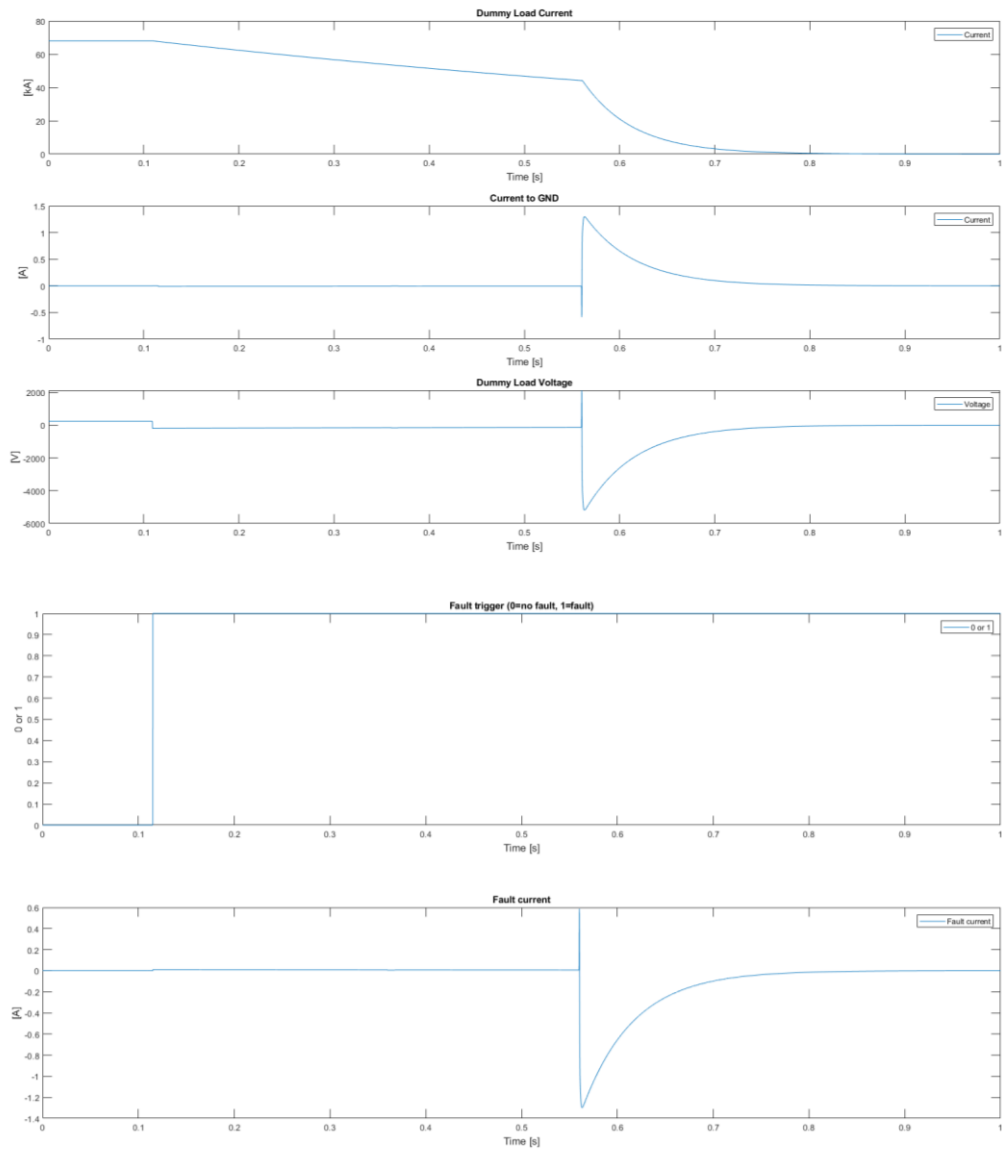
8.1 Scenario 1

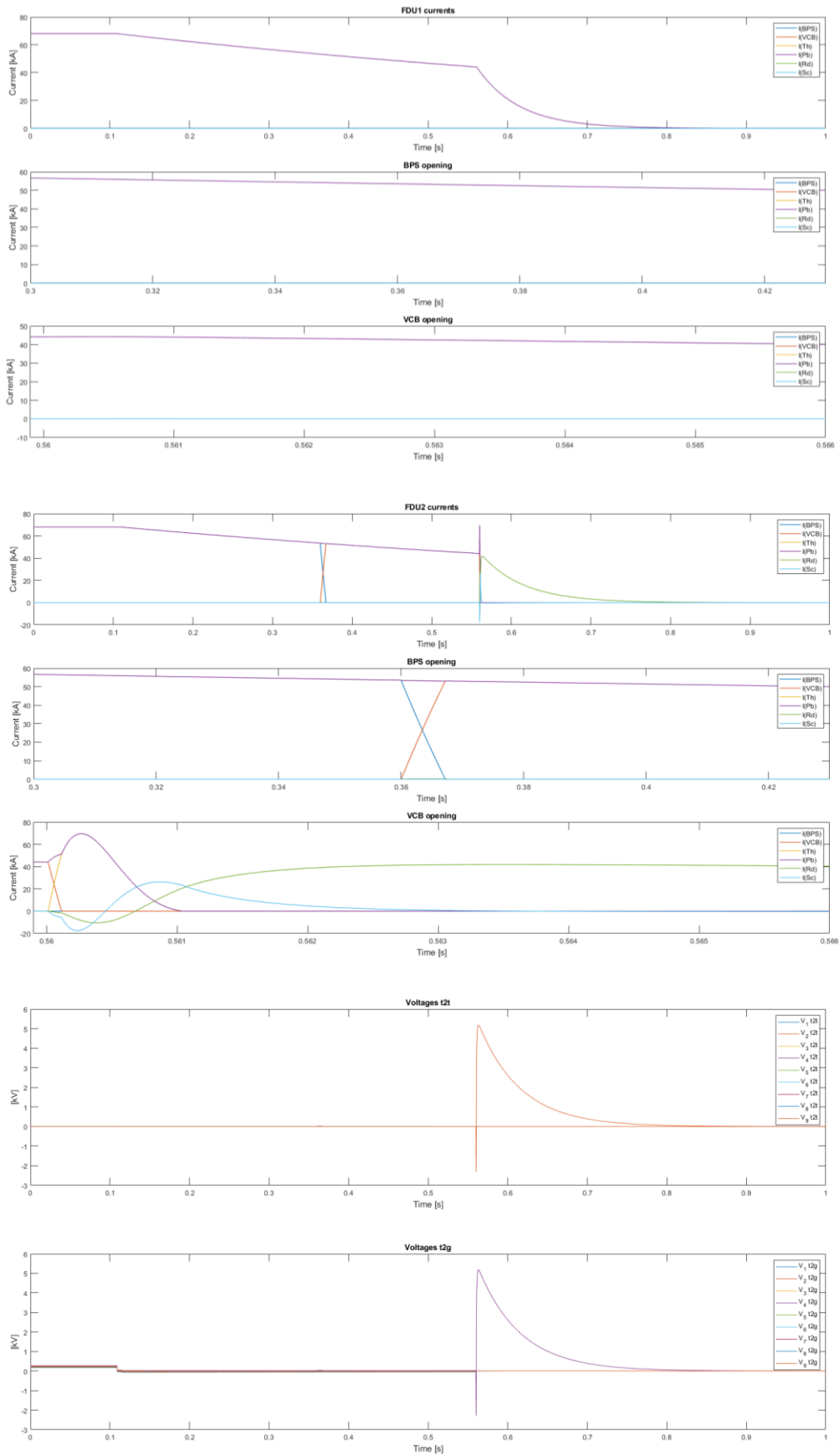
8.1.1 Simulation 1





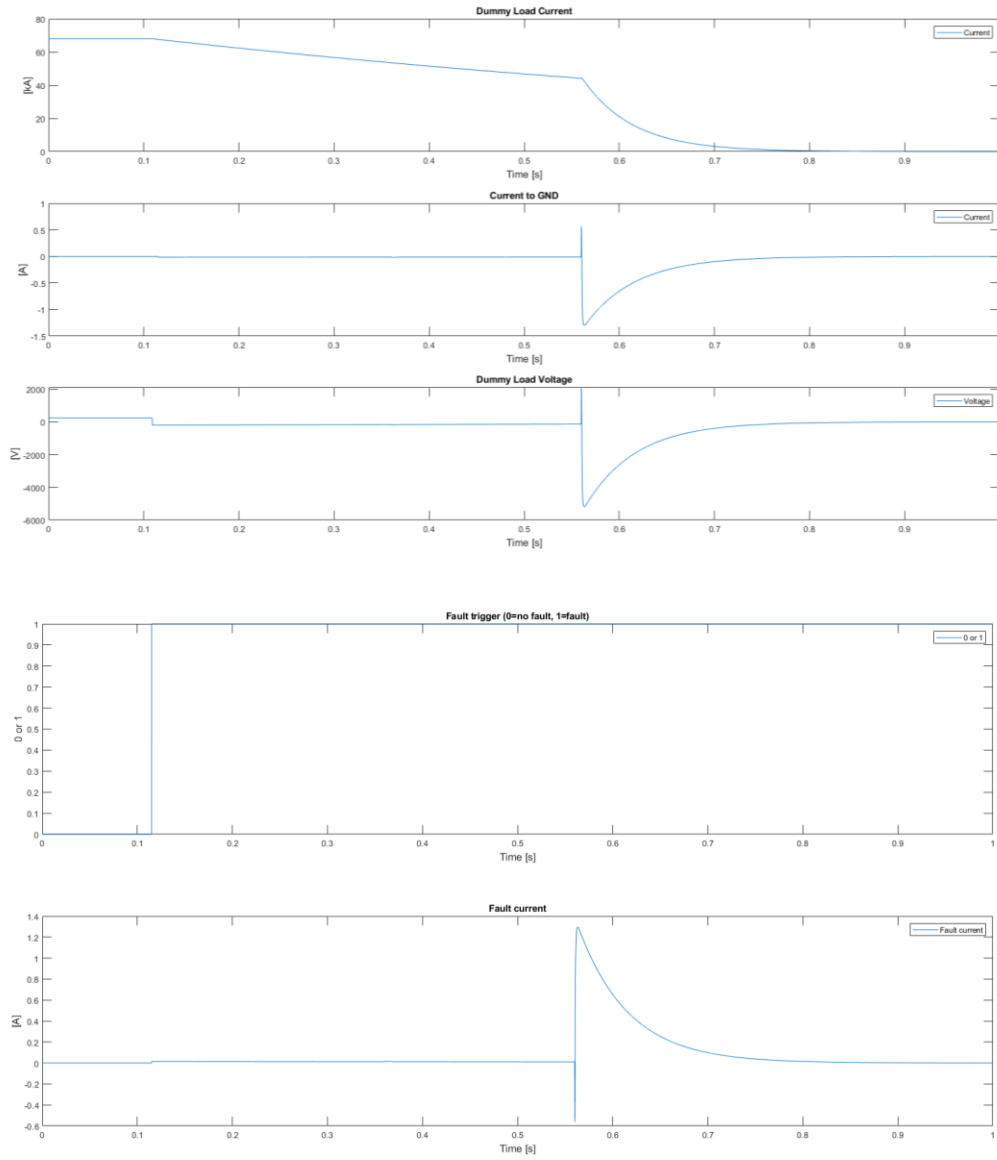
8.1.2 Simulation 2

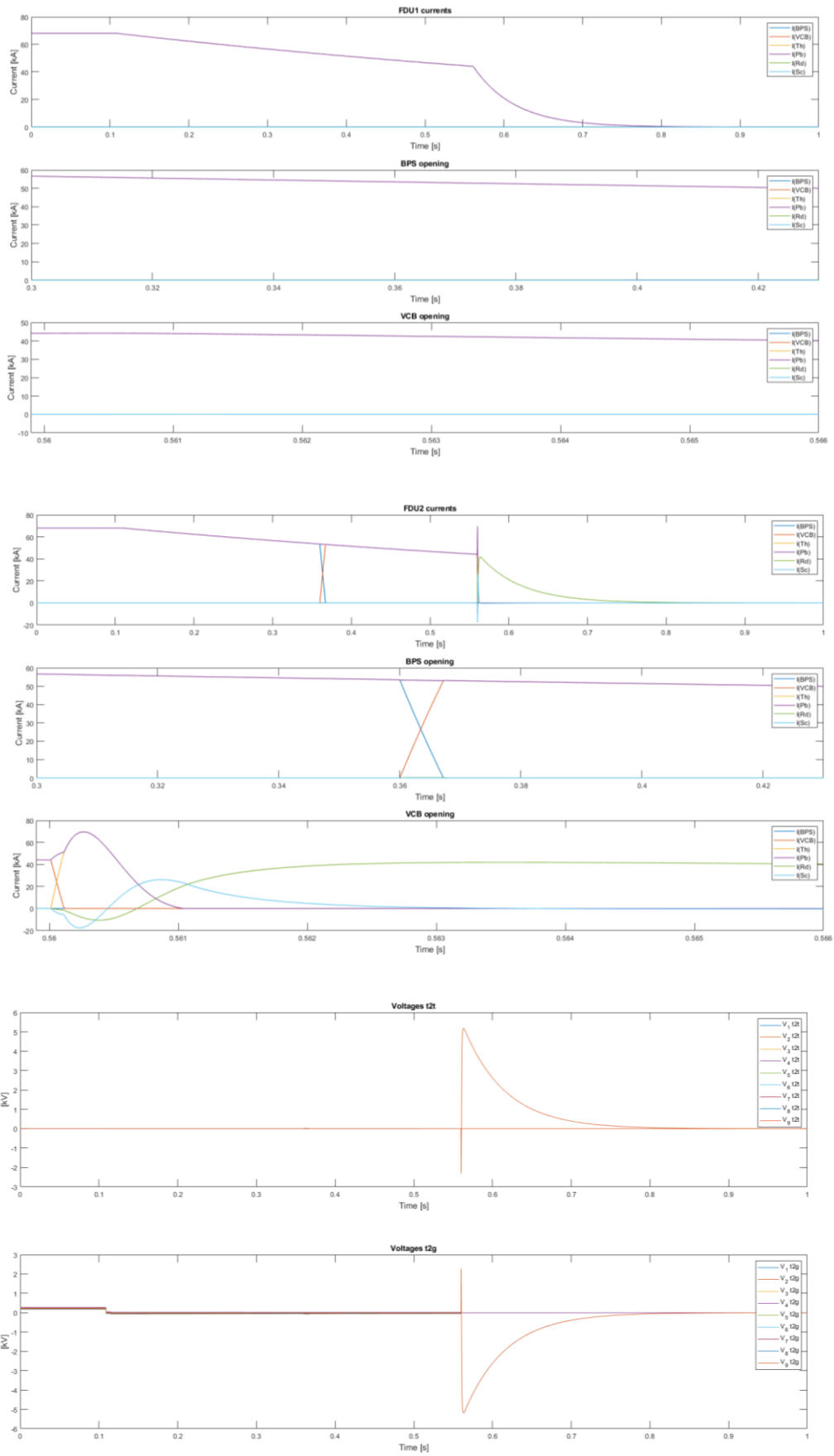




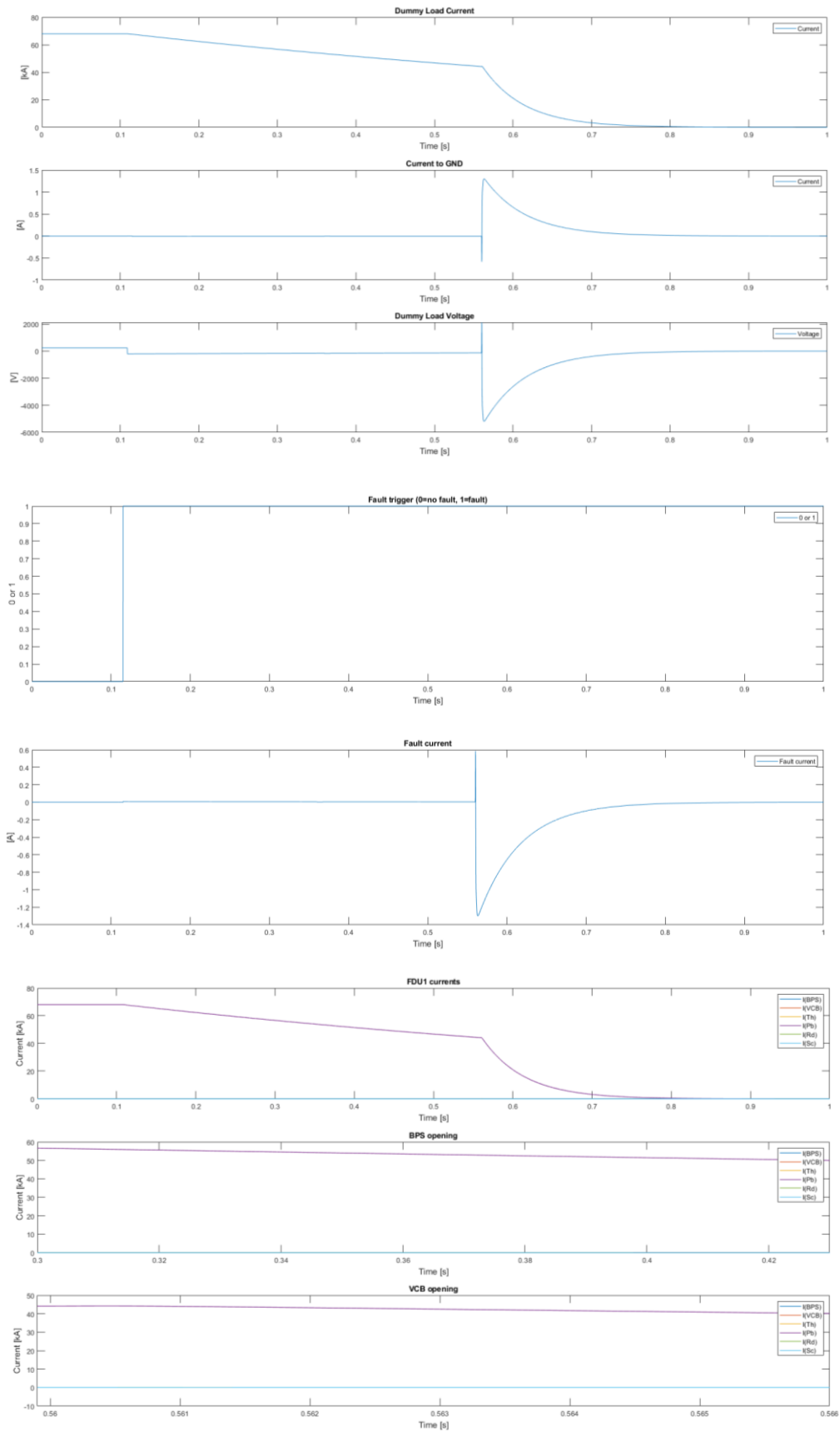
8.2 Scenario 2

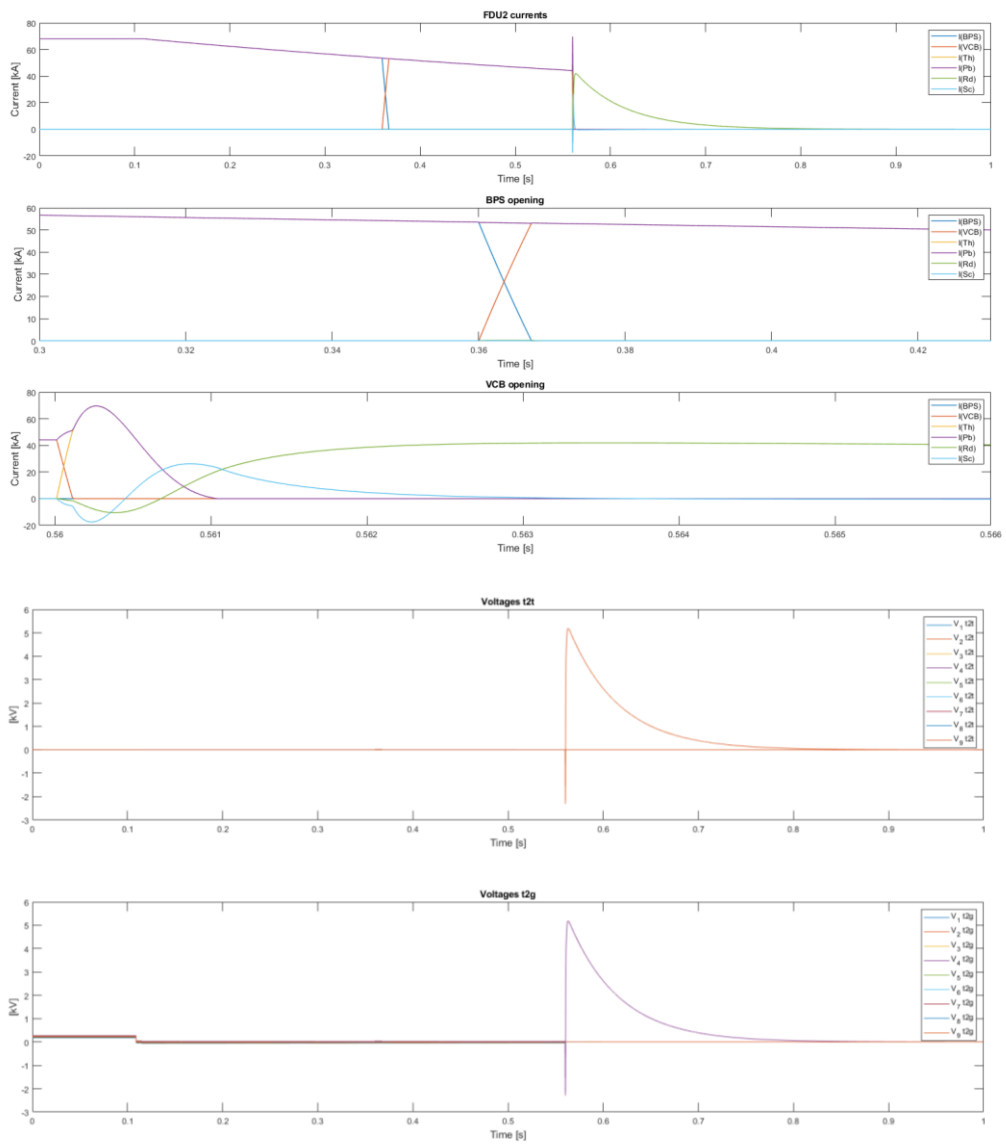
8.2.1 Simulation 1



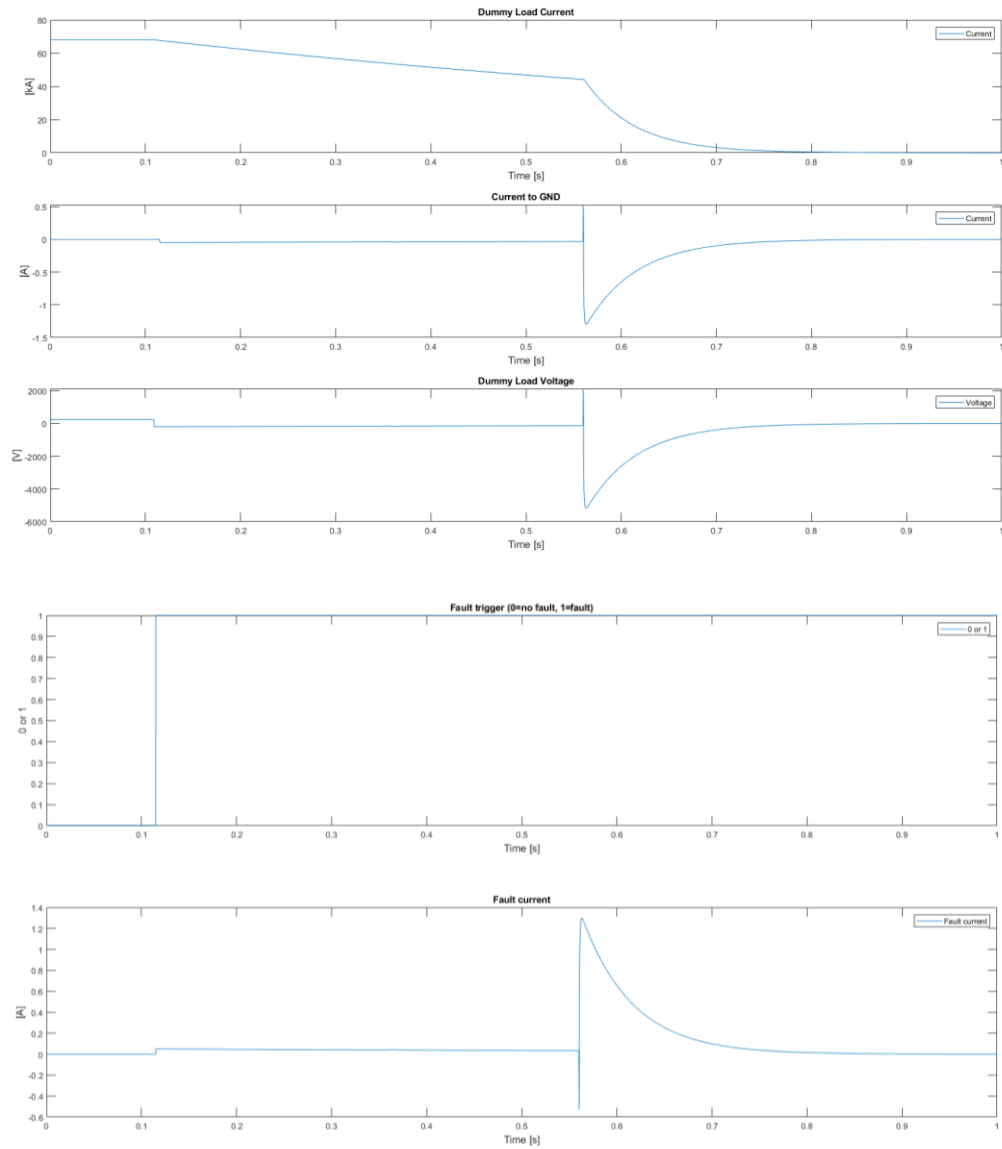


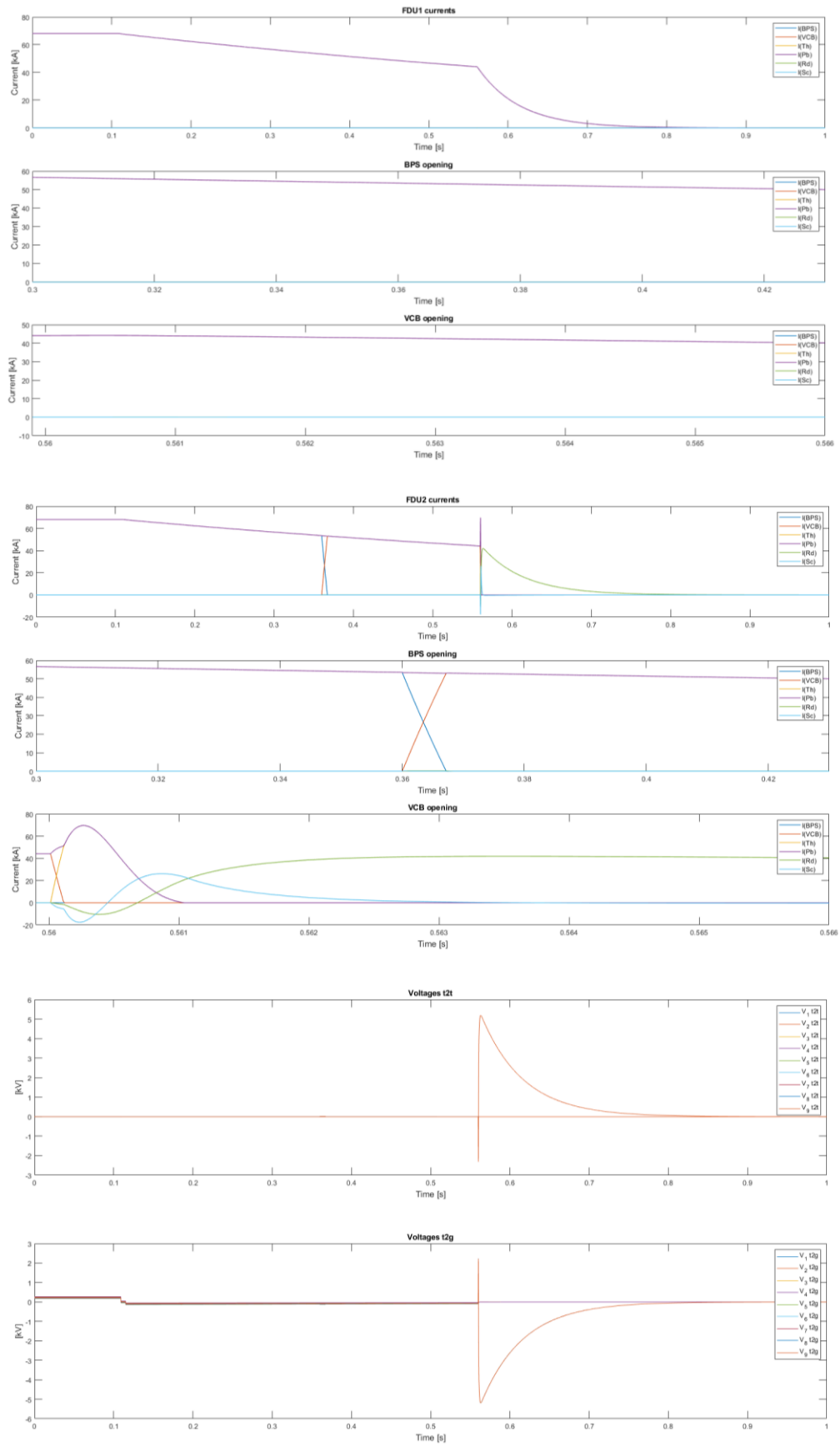
8.2.2 Simulation 2





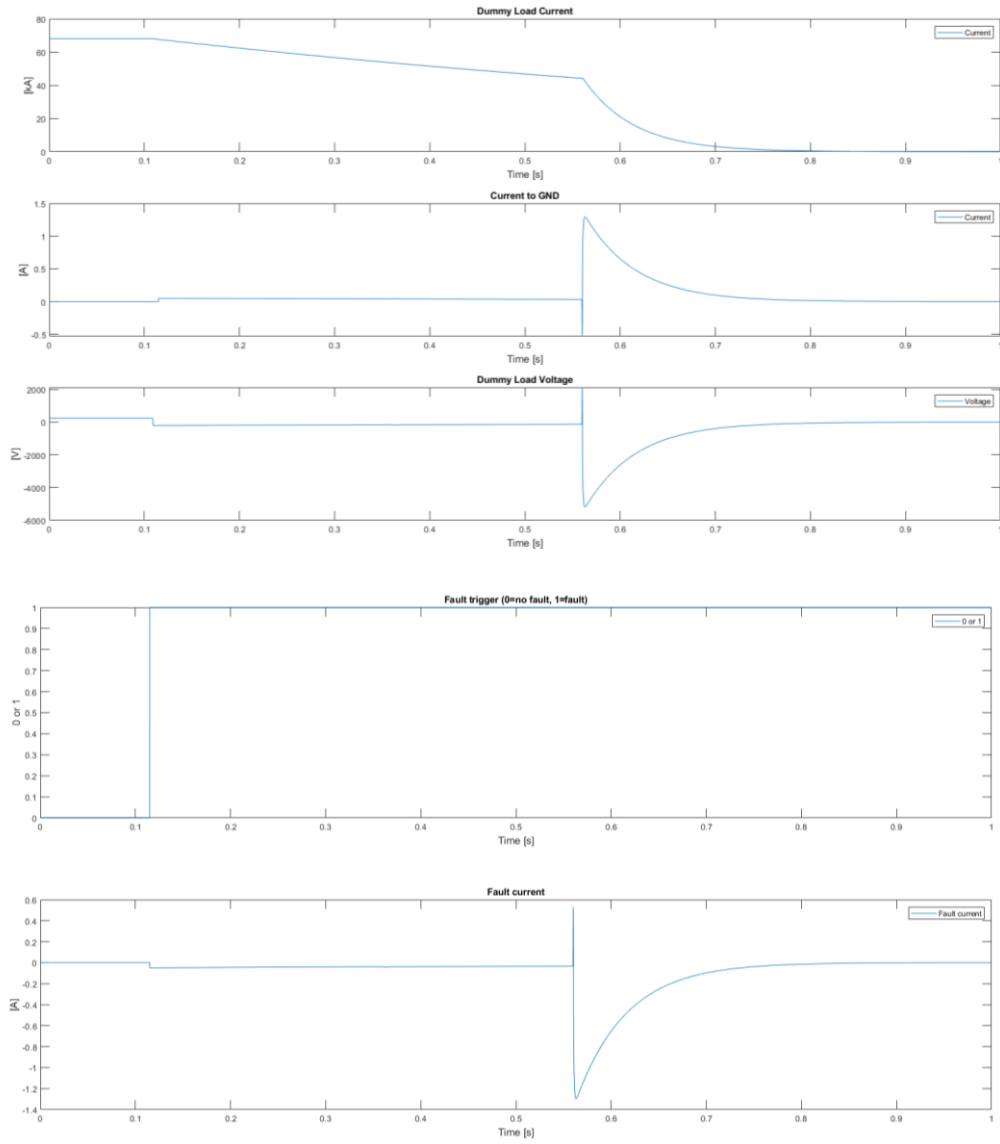
8.3 Scenario 3

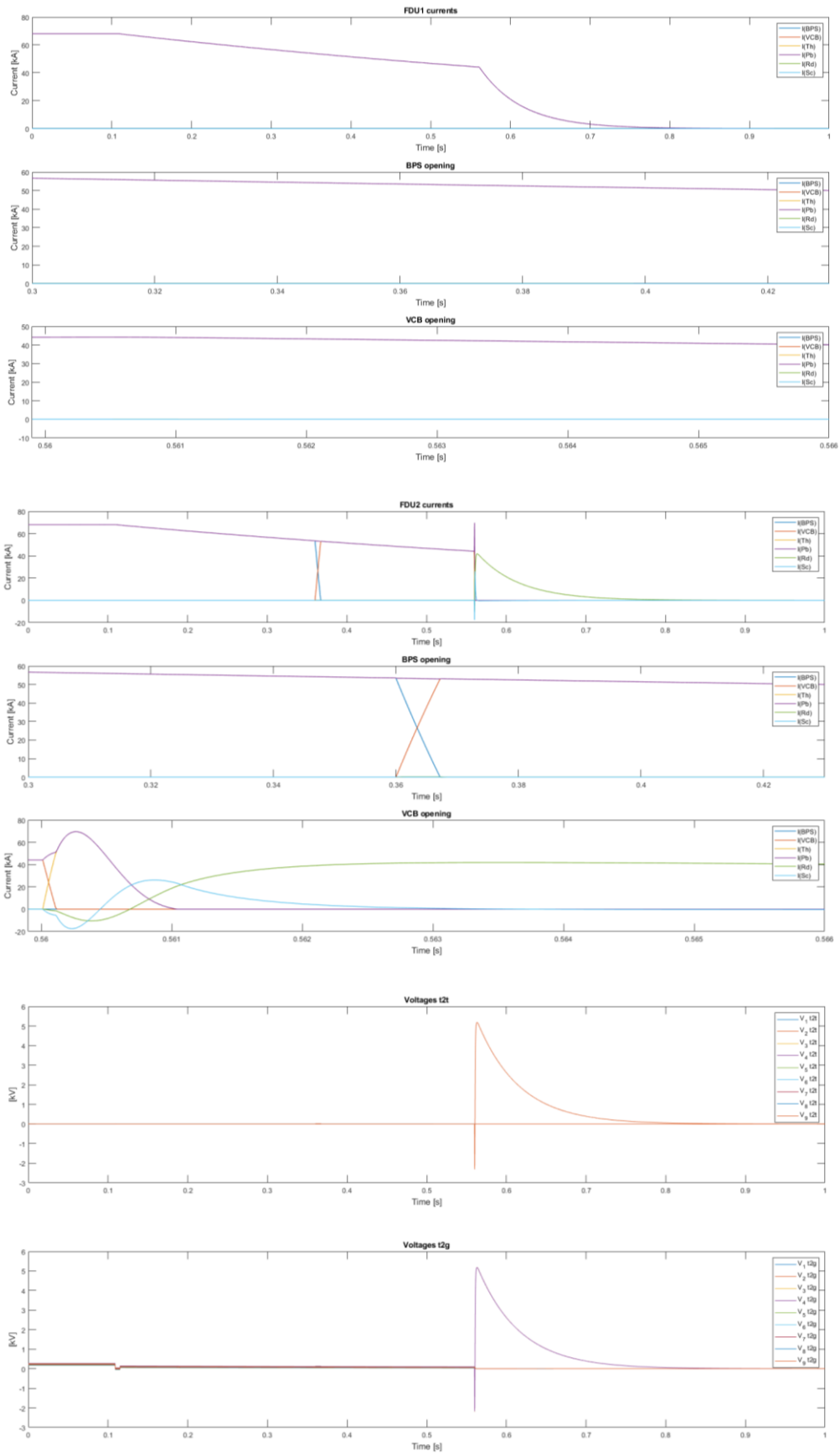




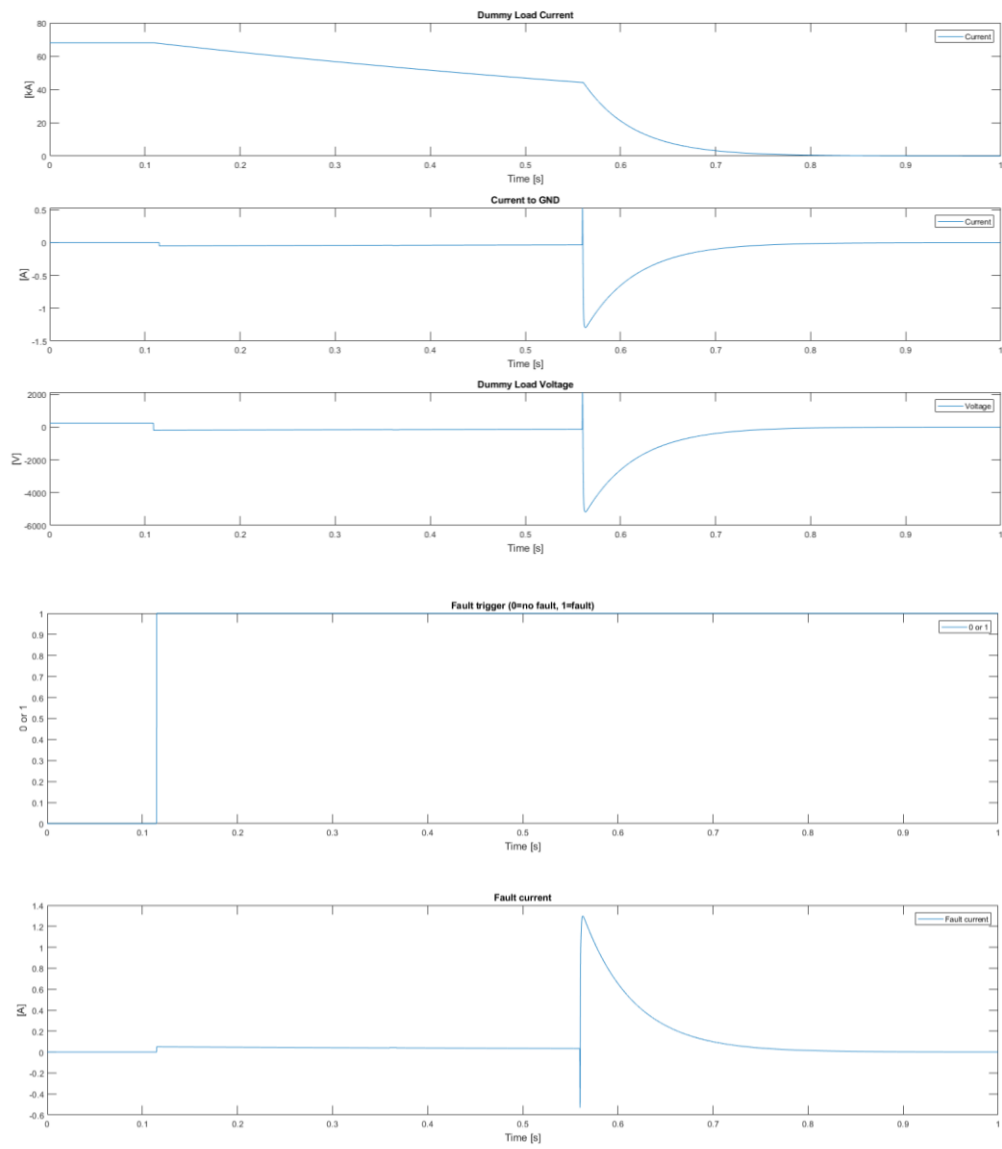
8.4 Scenario 4

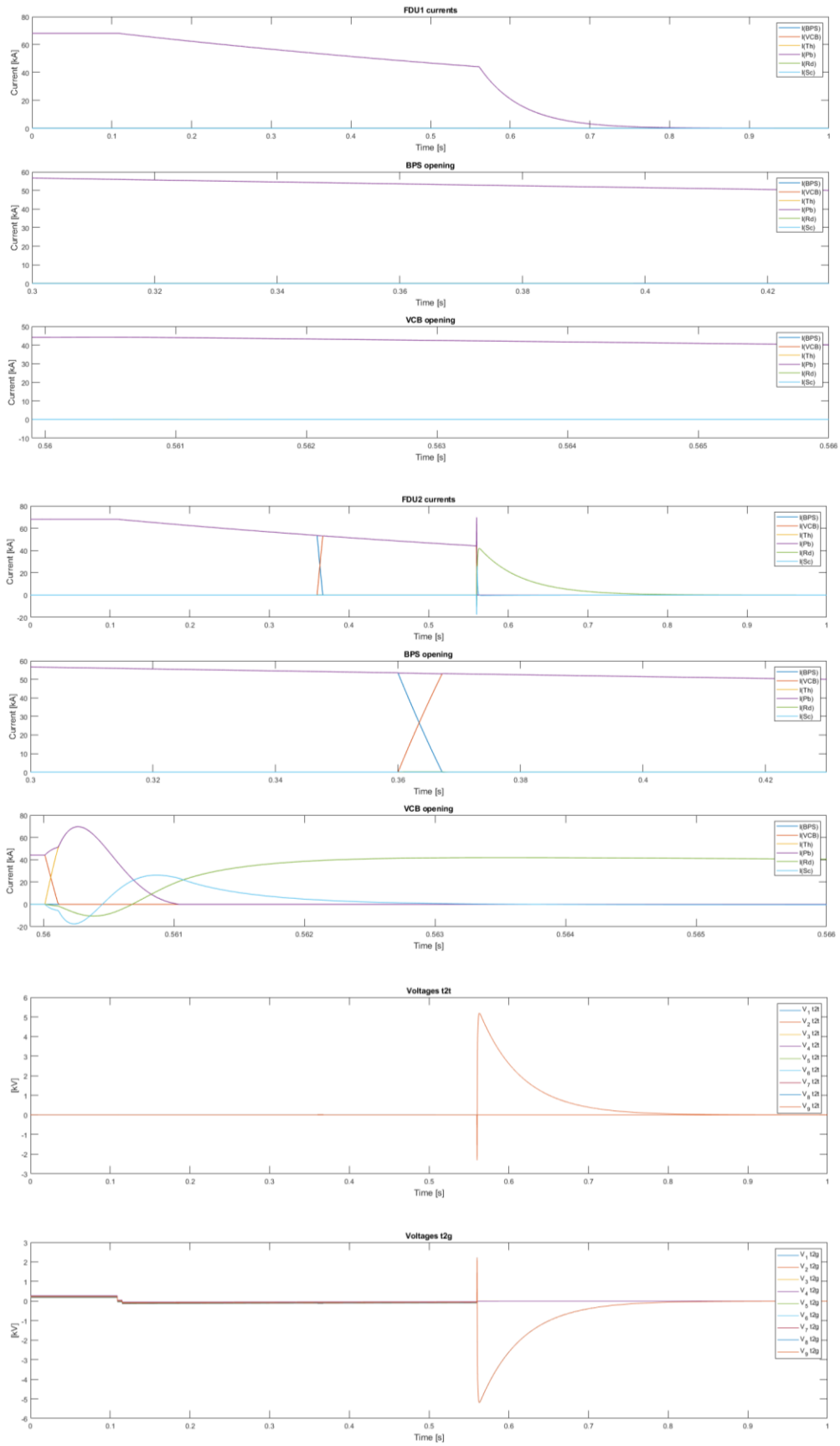
8.4.1 Simulation 1





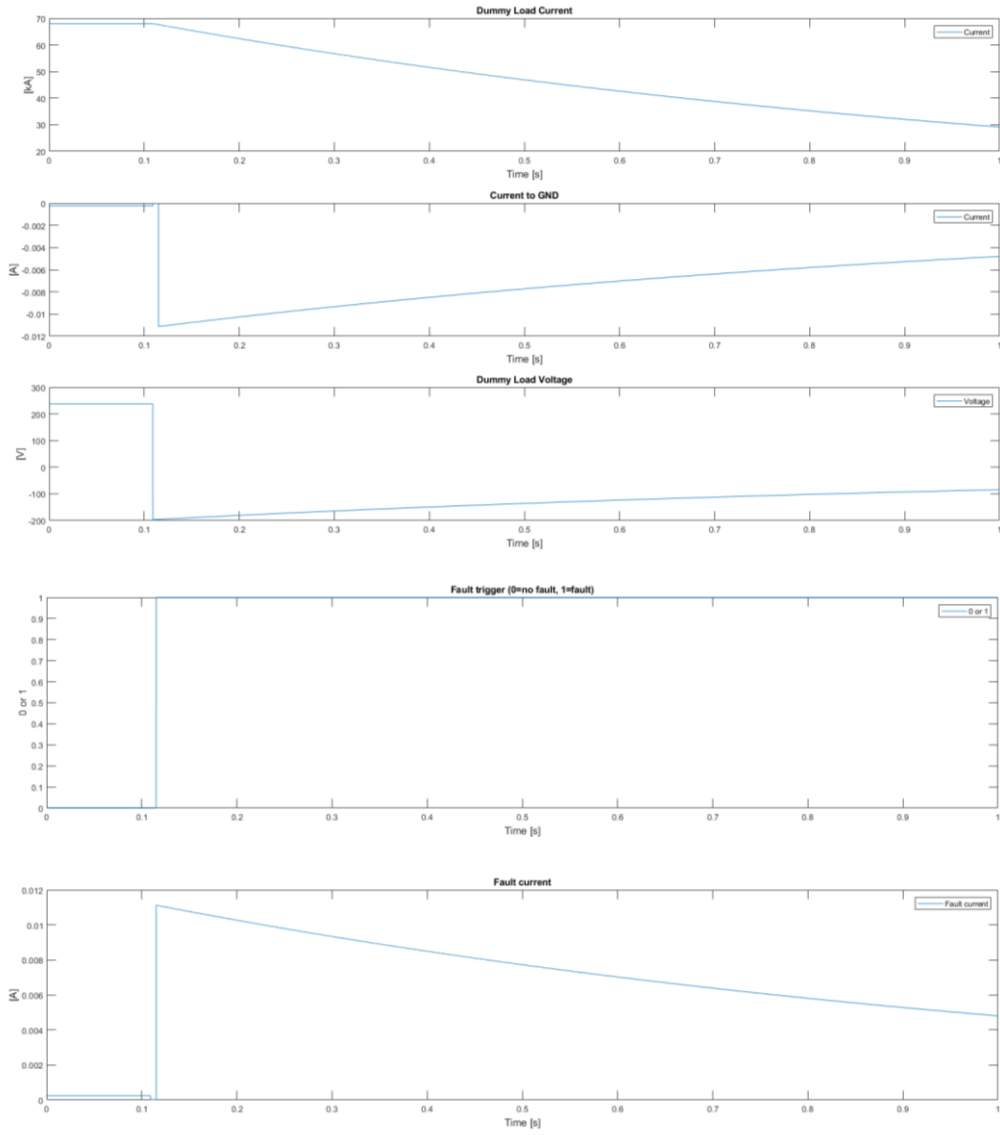
8.4.2 Simulation 2

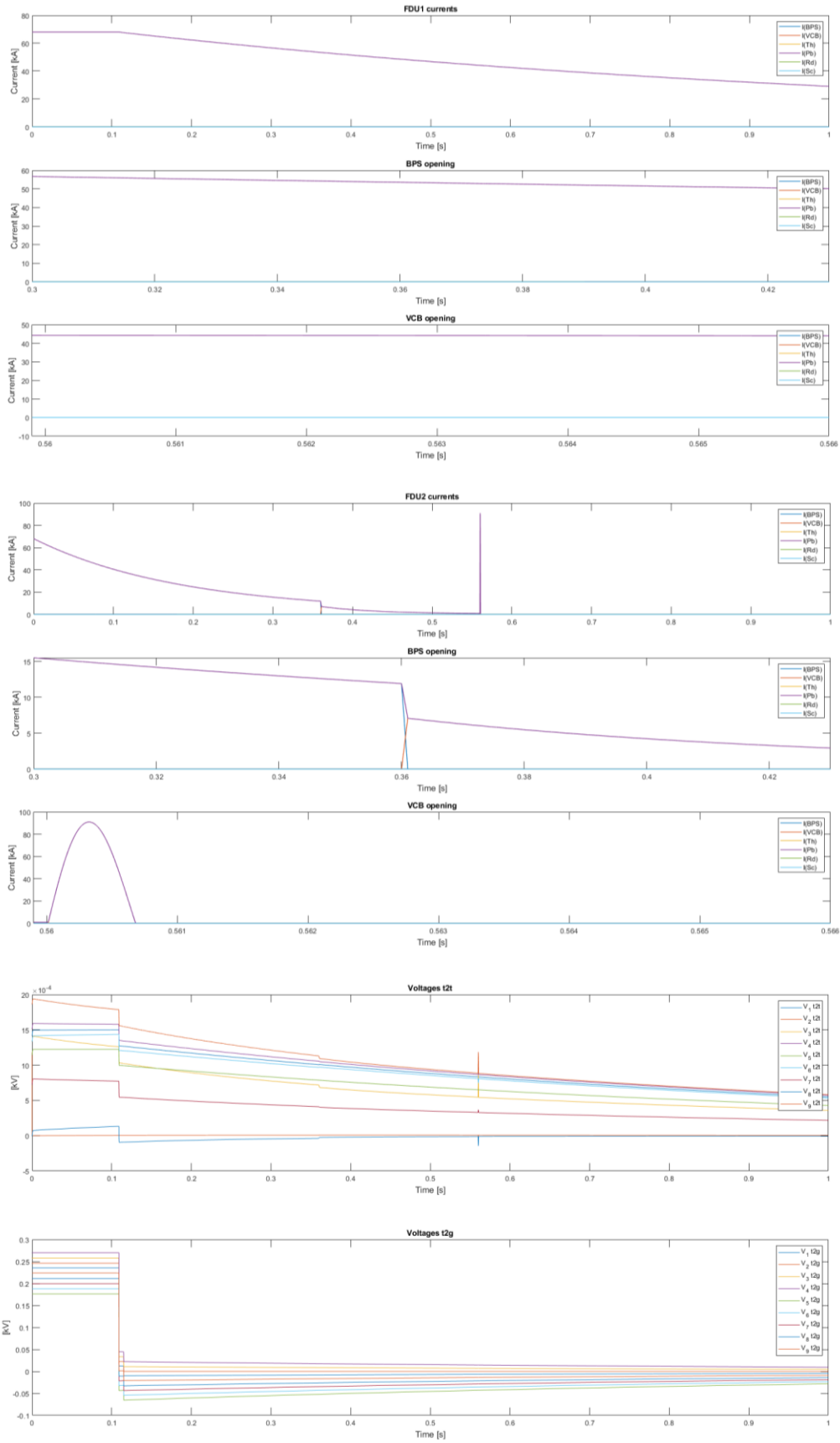




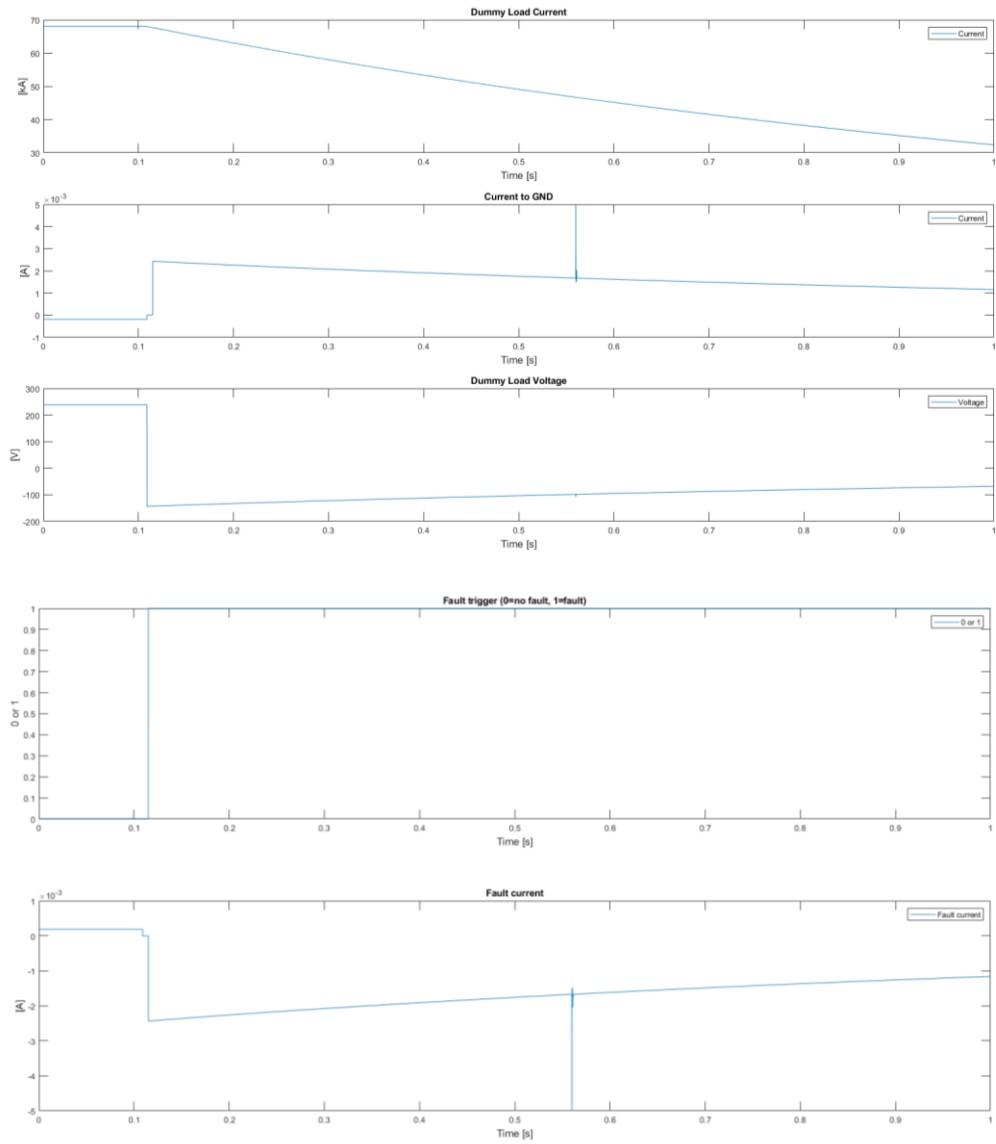
8.5 Scenario 5

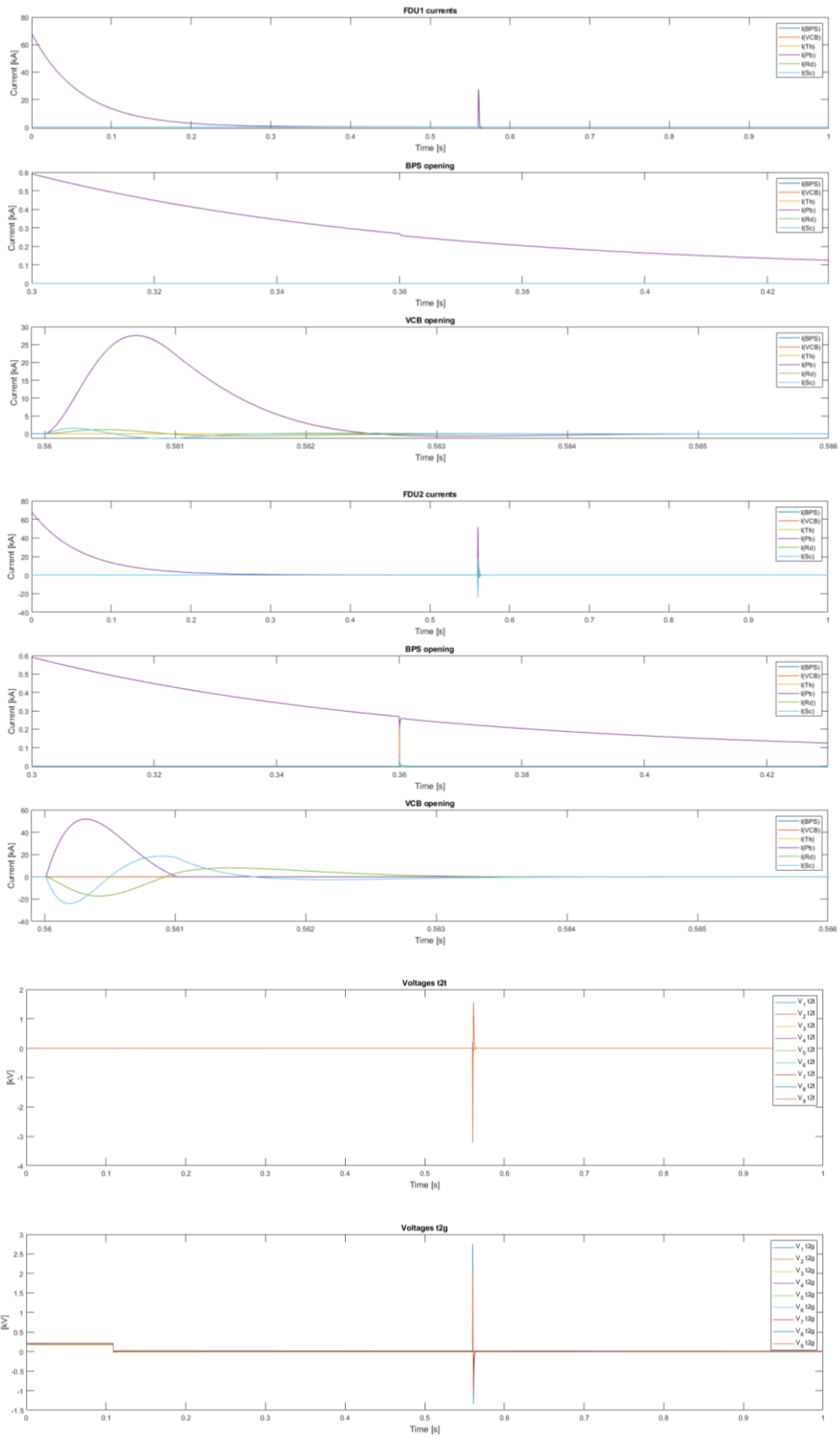
8.5.1 Simulation 1





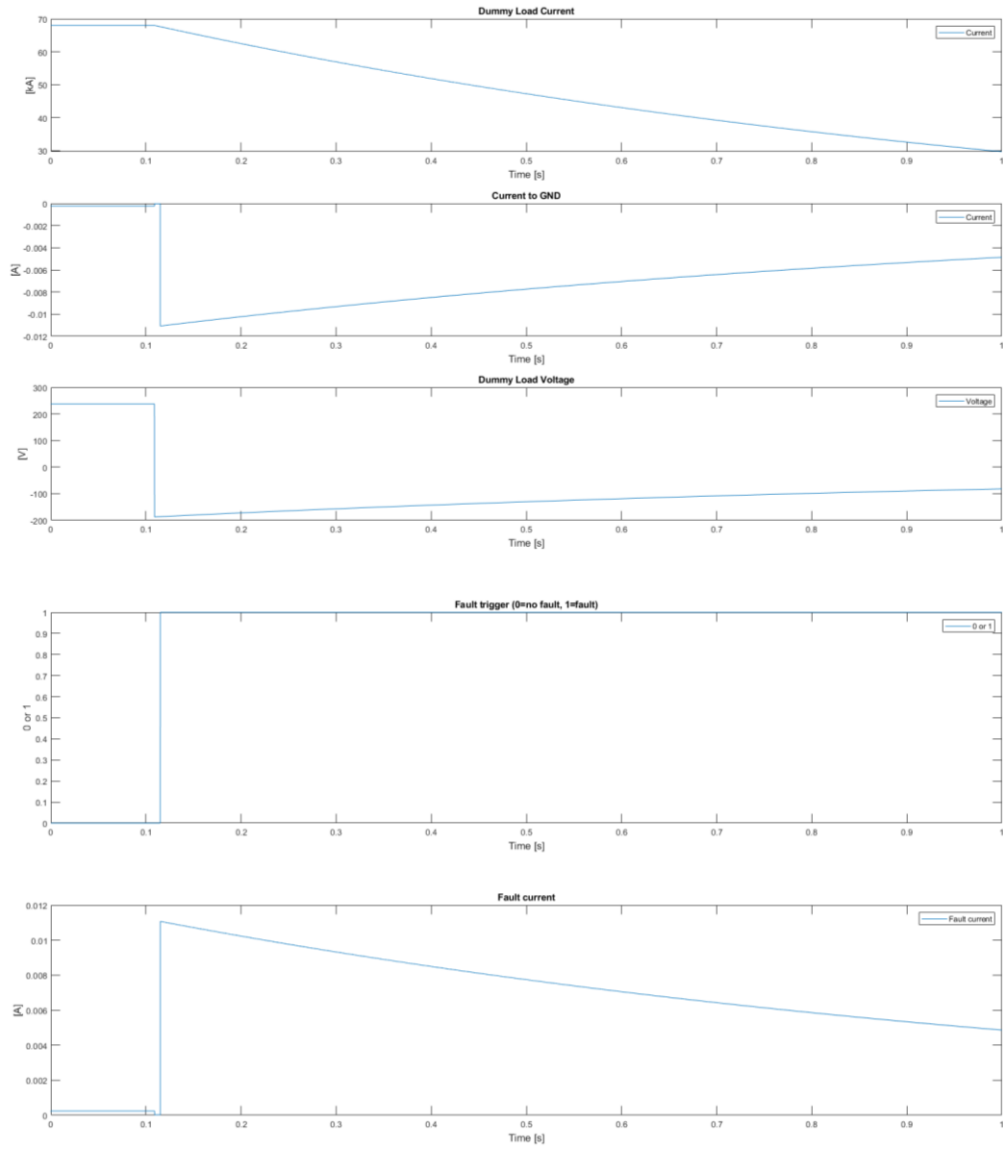
8.5.2 Simulation 2

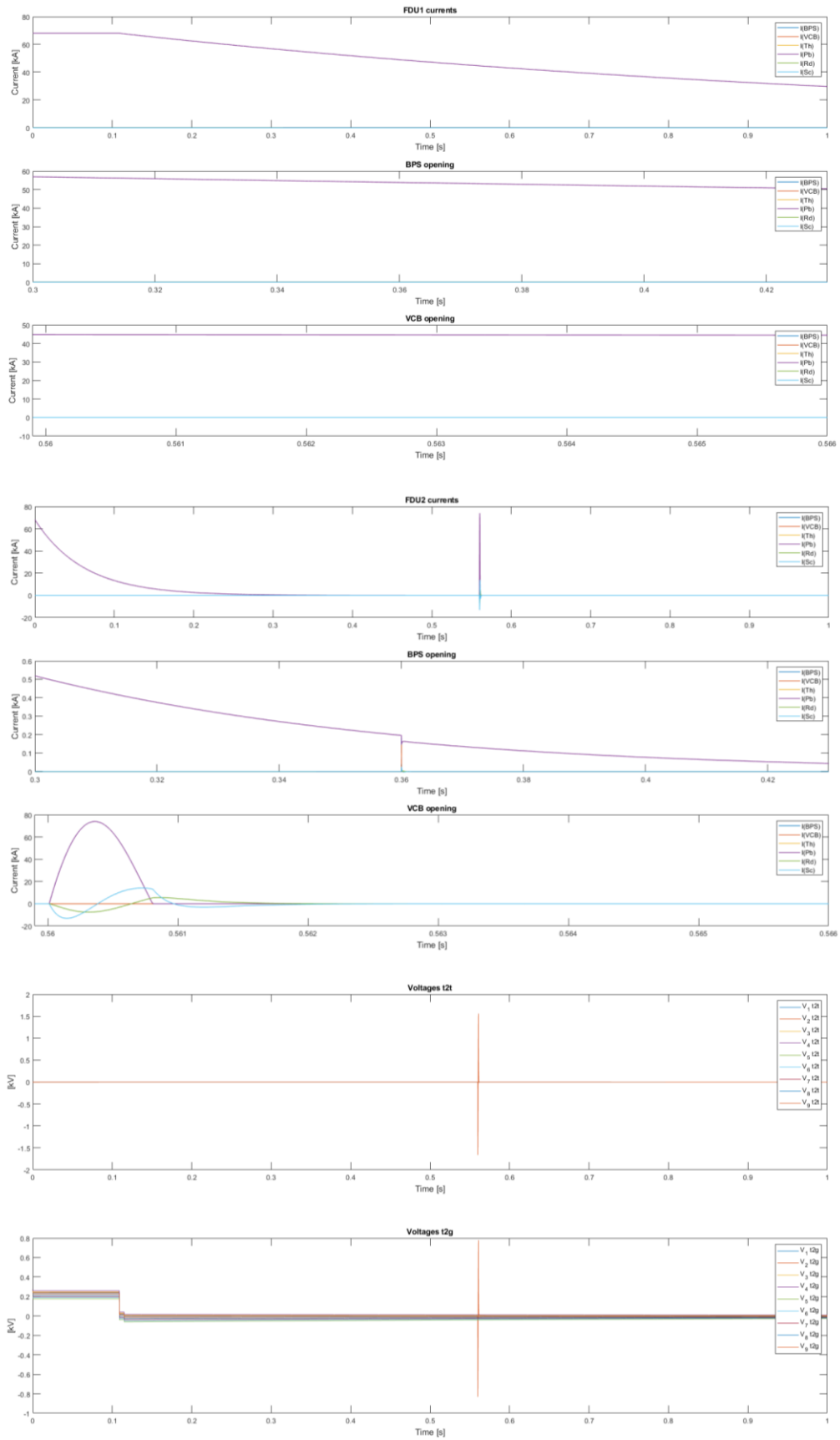




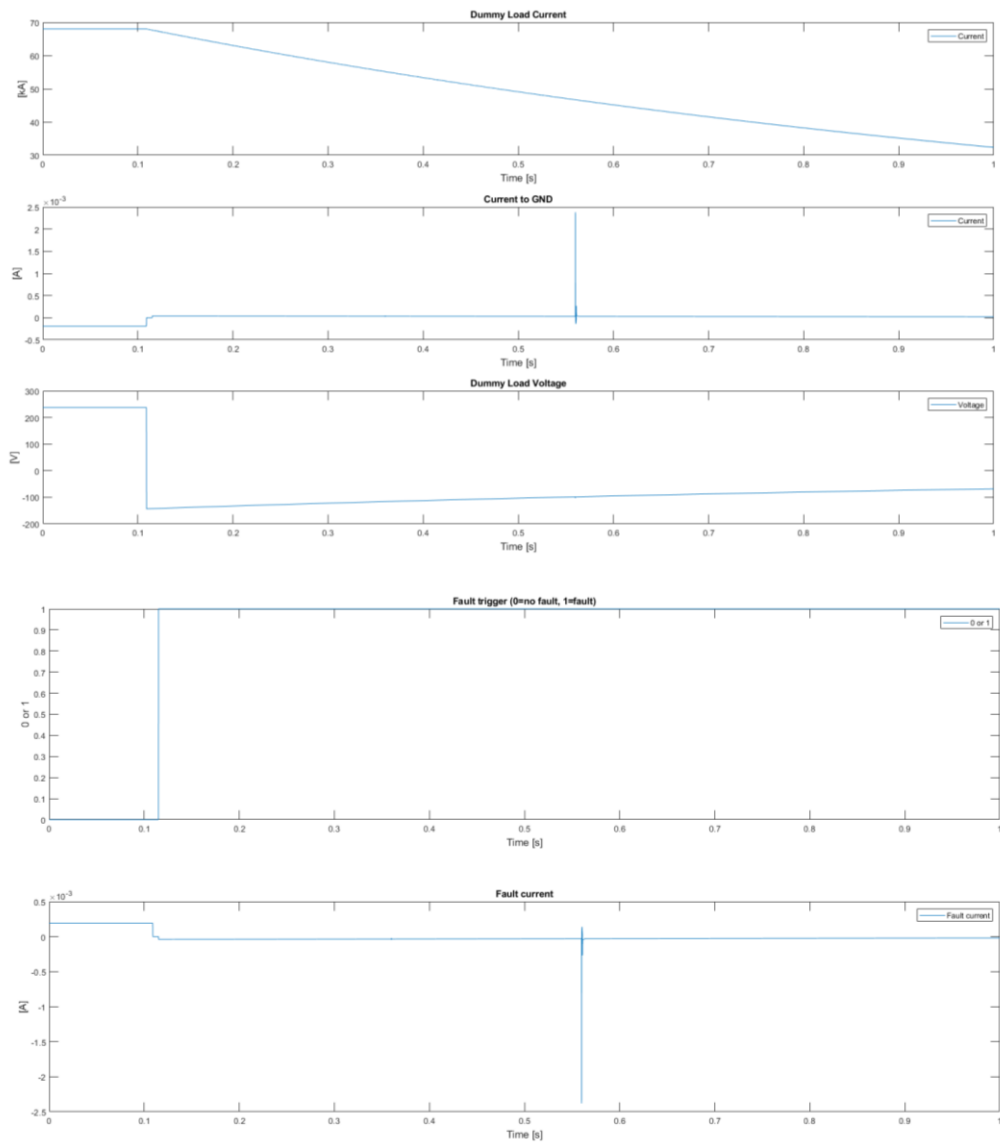
8.6 Scenario 6

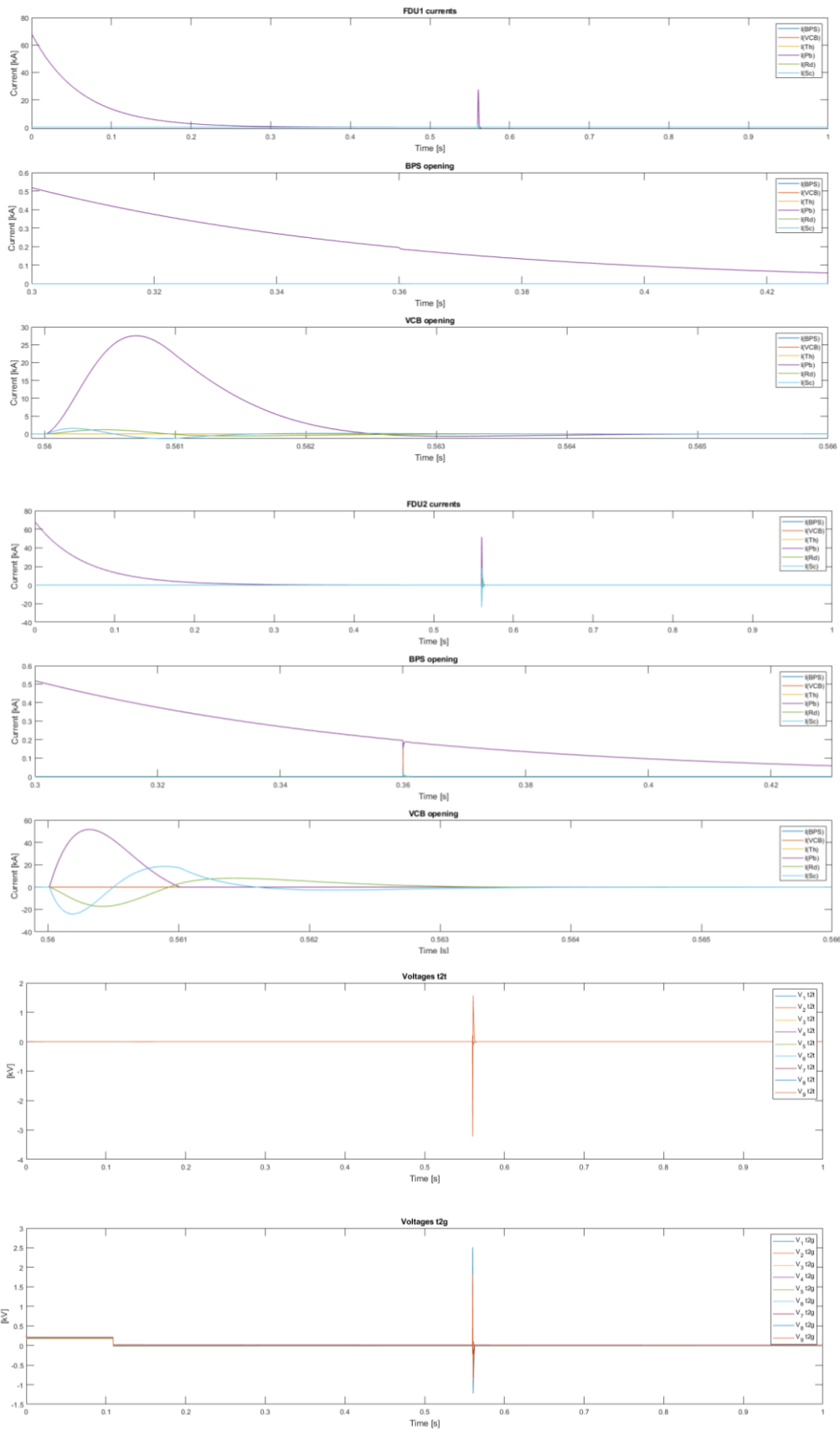
8.6.1 Simulation 1



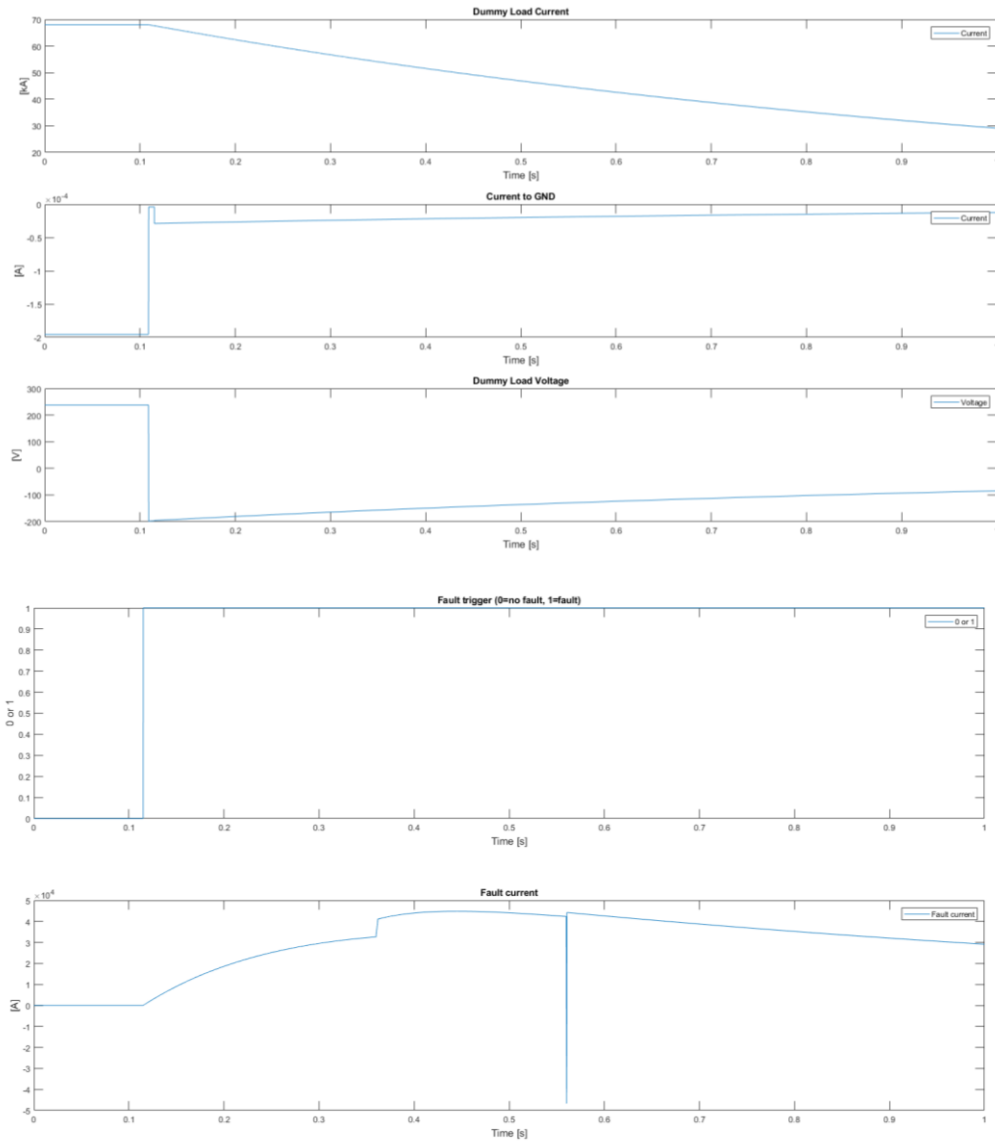


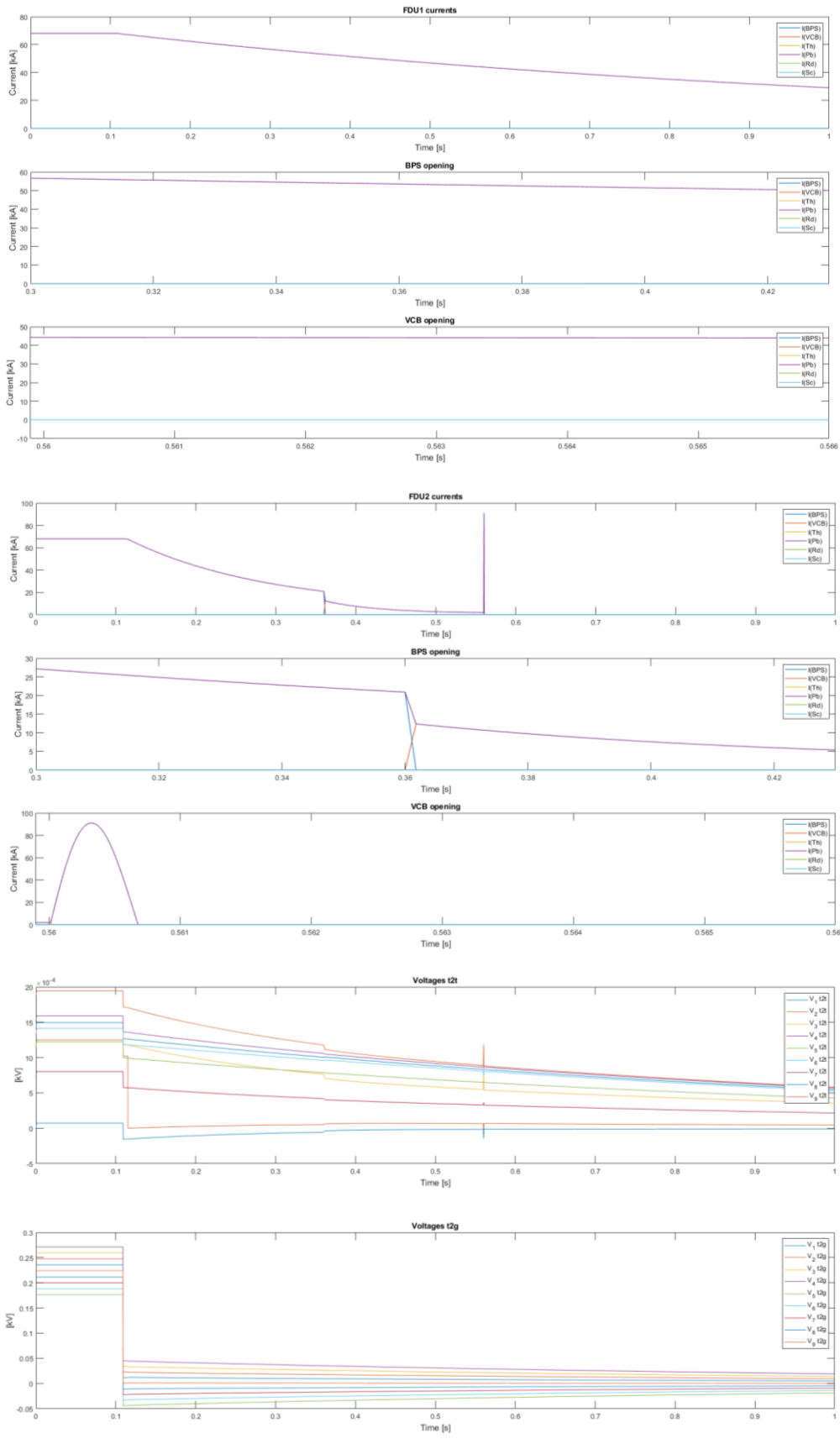
8.6.2 Simulation 2



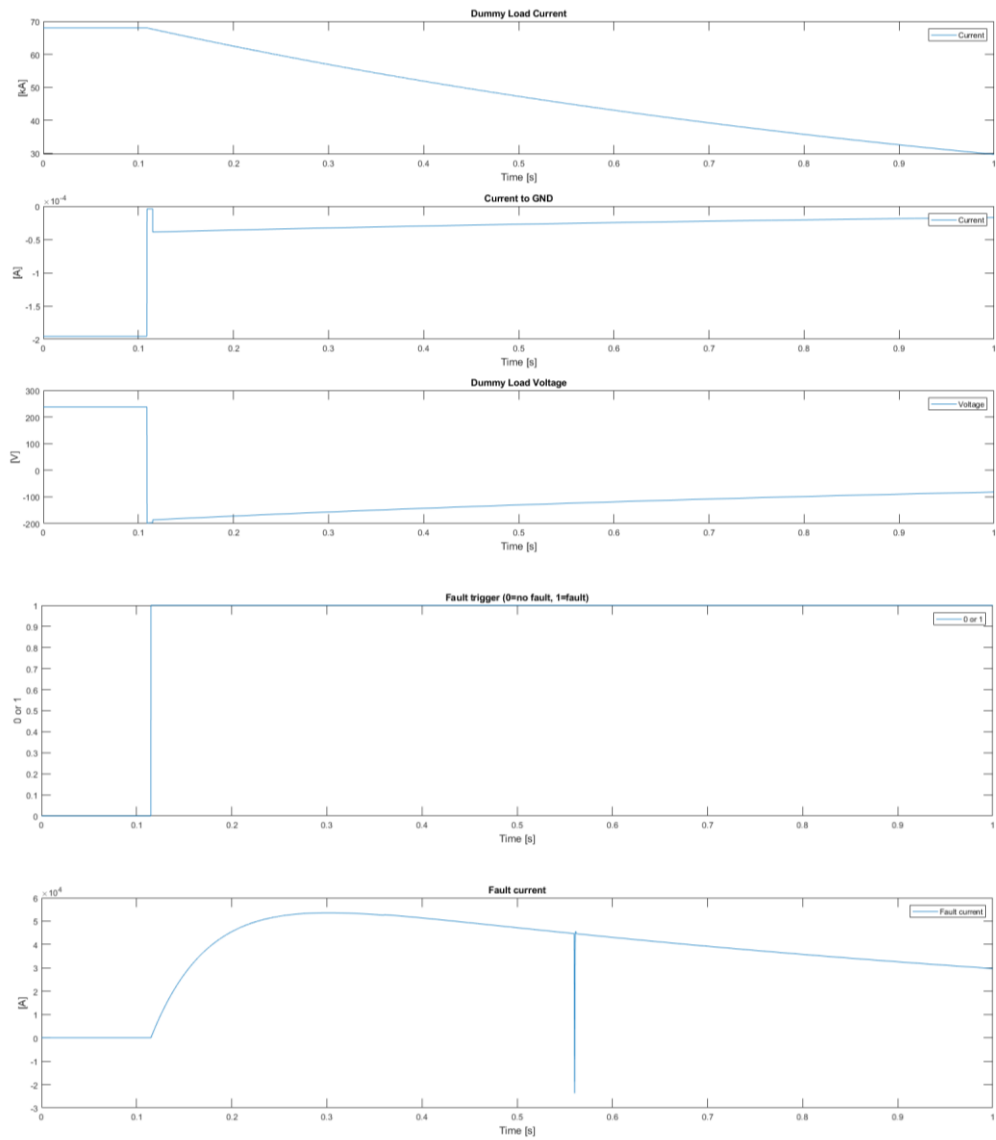


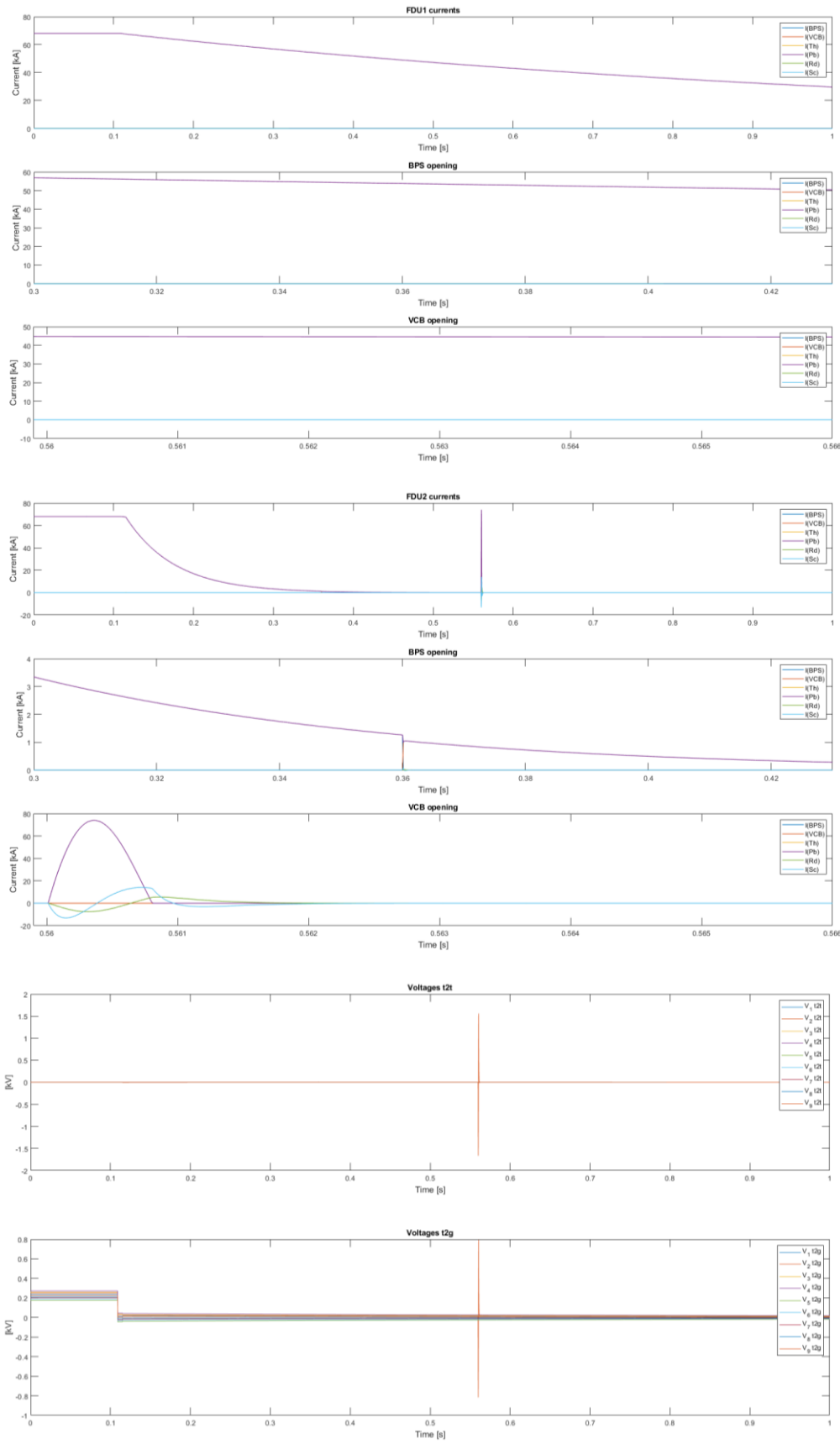
8.7 Scenario 7



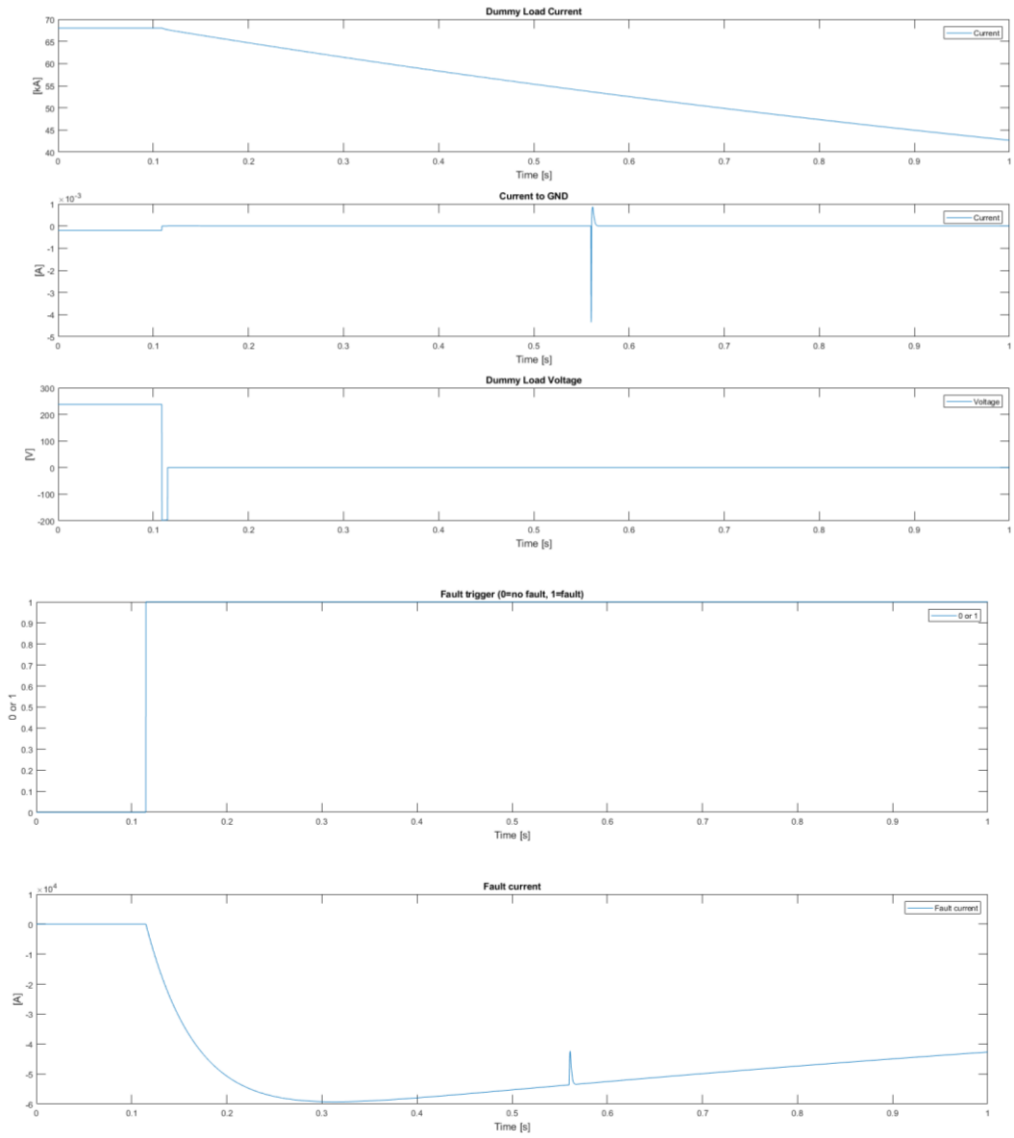


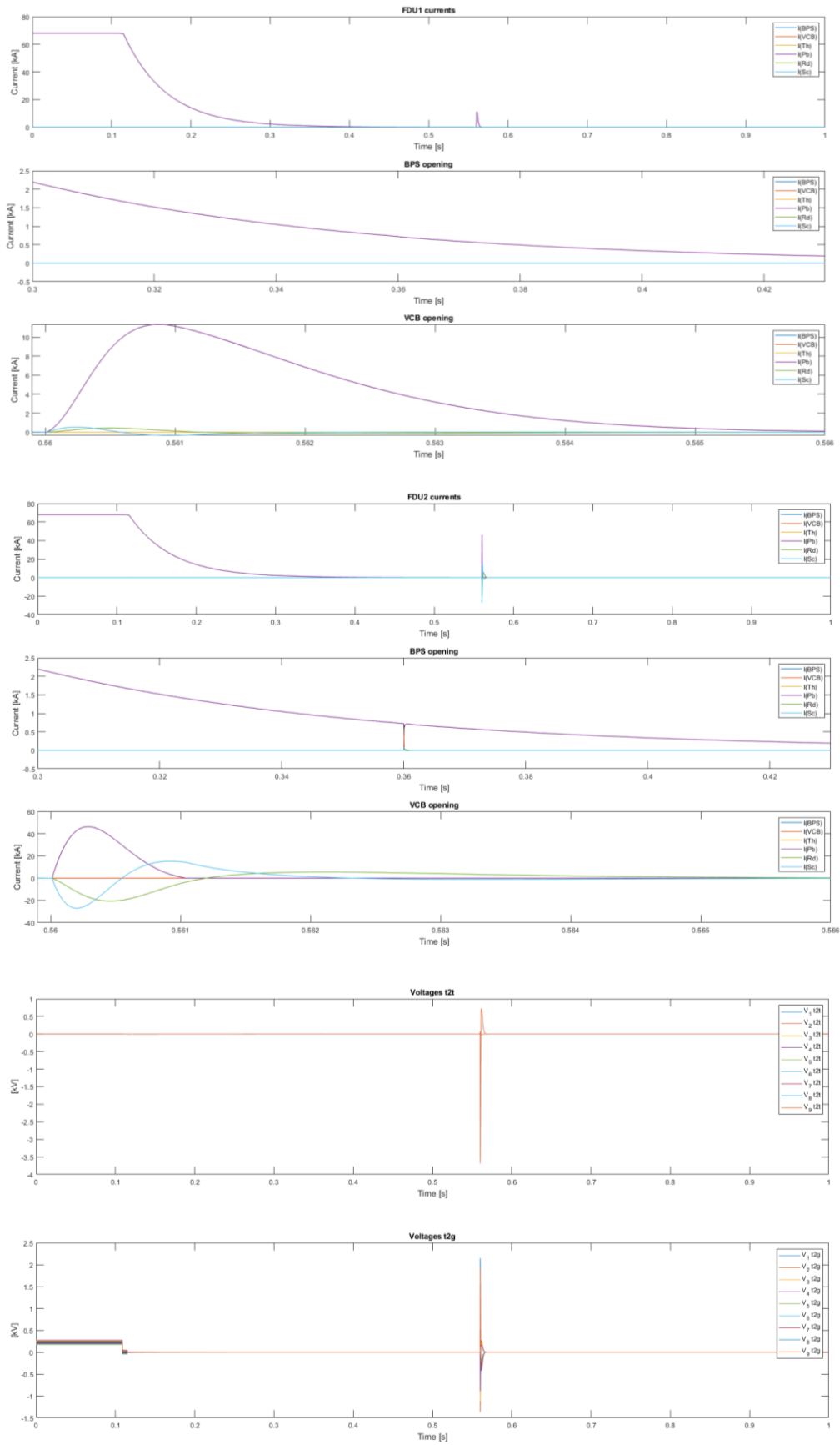
8.8 Scenario 8



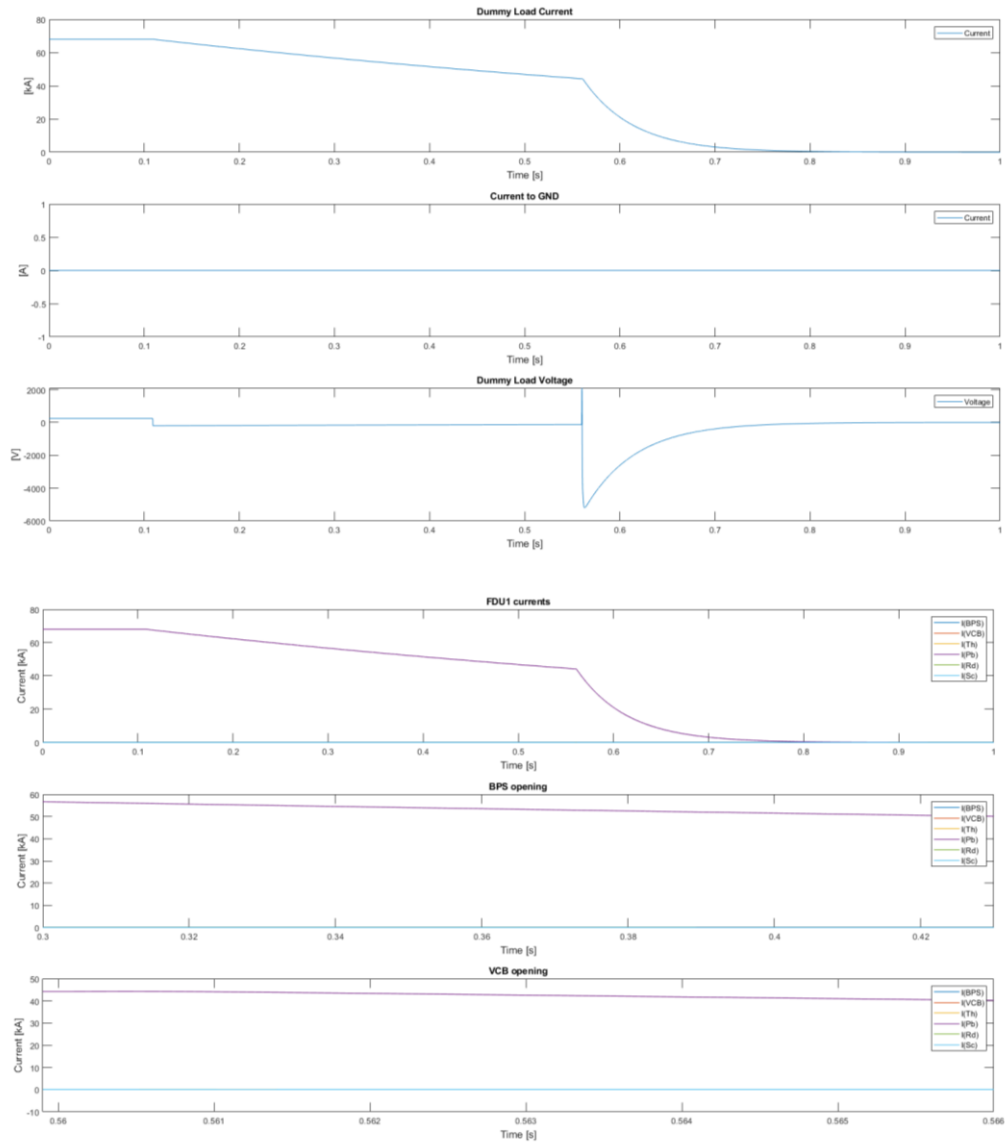


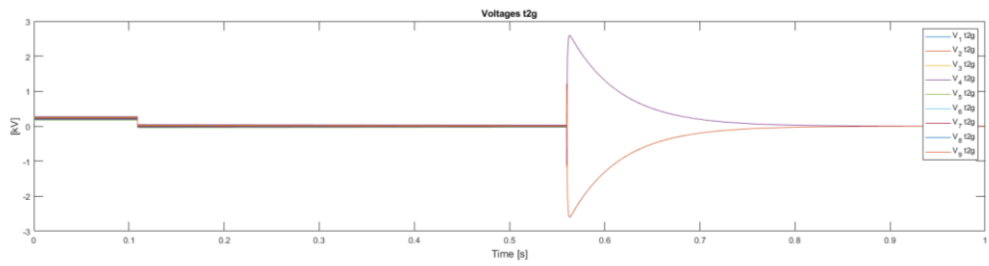
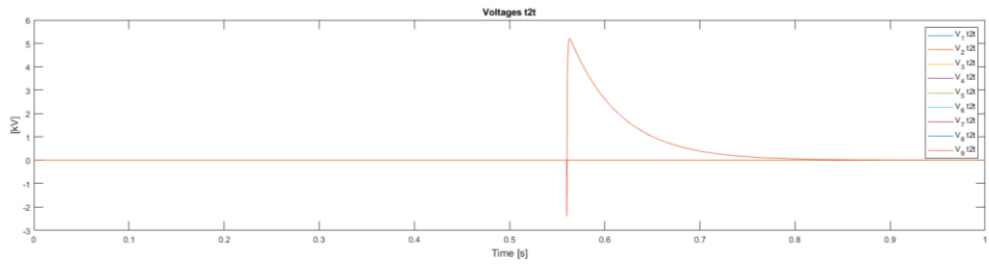
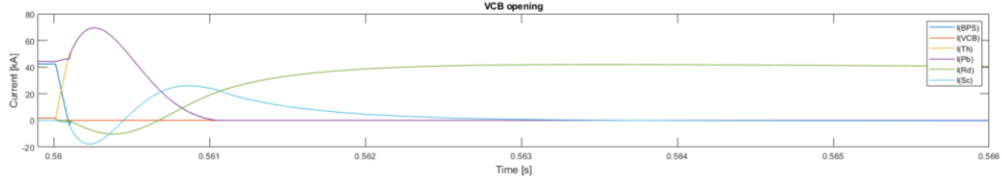
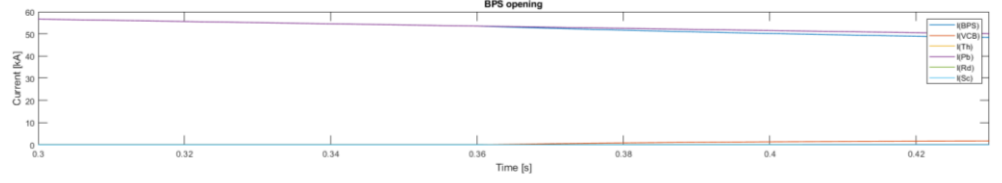
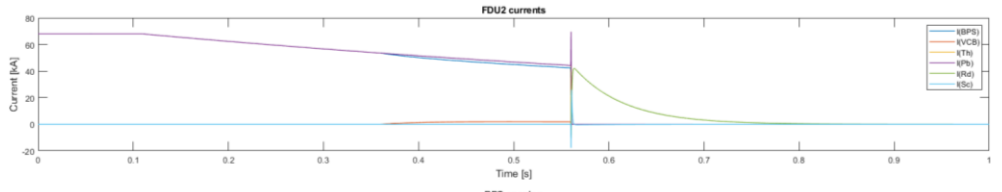
8.9 Scenario 9





8.10 Scenario 10





8.11 Scenario 11

